In search of the Box-Anomaly with the WASA facility at COSY

Dissertation zur Erlangung des Grades

Doktor der Naturwissenschaften

am Fachbereich für Mathematik und Naturwissenschaften

der Bergischen Universität Wuppertal

vorgelegt von

Christoph Florian Redmer

geb. in Essen

Jülich, im März 2010

Zusammenfassung

Der Zerfallskanal $\eta \to \pi^+\pi^-\gamma$ des η Mesons ist sensitiv für Beiträge der Box-Anomalie. Bisher sind nur wenige Messungen differentieller Verteilungen dieses Zerfallskanals veröffentlicht worden und die Messungen mit der größten statistischen Signifikanz sind nicht effizienzkorrigiert. Der Vergleich dieser Messungen mit theoretischen Vorhersagen weist Unstimmigkeiten zwischen verschiedenen Messungen auf, die mit der fehlenden Effizienzkorrektur in Verbindung gebracht werden. Mit dem WASA Detektor am Speicherring COSY wurde eine neue Messung des Zerfallskanals $\eta \to \pi^+\pi^-\gamma$ durchgeführt. Nach Untergrundabzug steht ein Datensatz von 13738 ± 136 Ereignissen des Zerfallskanals zur weiteren Analyse zur Verfügung. Basierend auf diesem Datensatz wurden die differentiellen Verteilungen der Teilchen im Endzustand untersucht. Die Winkelverteilung der Pionen kann durch P-Wellen Wechselwirkung beschrieben werden. Im Rahmen der Fehler sind Beiträge höherer Bahndrehimpulse, wie etwa der Ladungssymmetrie verletzende D-Wellenbeitrag, vernachlässigbar. Die Form des Energiespektrums der Photonen im Ruhesysten des η Mesons zeigt eine starke Abweichung von der Vorhersage des einfachsten eichinvarianten Matrixelementes auf. Die Abweichung wurde auch in den früheren Messungen beobachtet. Im Gegensatz zu diesen Messungen wurden in der hier vorgestellten Messung auch Photonenenergien unter $50\ MeV$ registriert. Zusätzlich deutet die Achsenaufteilung der Histogramme auf eine um einen Faktor 2 bessere Auflösung in der Photonenenergie hin. Die Form der Energieverteilung wird durch eine Rechnung des Vector Meson Dominance Modelles, die als Erweiterung des einfachsten Matrixelementes benutzt wird, gut beschrieben.

Abstract

The decay mode $\eta \rightarrow \pi^+\pi^-\gamma$ allows to study the box anomaly. Experimental data on differential distributions are scarce and of low statistic. Additionally, the largest samples have not been corrected for efficiency. Recent theoretical interpretations yield ambiguous results. Using the WASA facility at COSY, a new measurement has been done. A background subtracted sample of 13738 ± 136 events of the decay $\eta \rightarrow \pi^+\pi^-\gamma$ has been obtained. Differential distributions of the particles in the final state have been studied after being corrected for efficiency. The pion angular distribution can be described by P-wave interaction. Evidence for contributions of higher angular momenta, such as a C-violating D-wave contribution, is not found. The investigation of the photon energy spectrum in the η rest frame reveals a strong disagreement with the simplest gauge invariant matrix element. This was also observed by previous measurements. In contrast to previous measurements of the photon energy line shape, the obtained spectrum also covers the region below 50 MeV photon energy and the bin width, which is matched with the resolution of the variable, is smaller by a factor of 2. The line shape of the distribution is found in agreement with VMD calculations which are used as an unitarized extension of the simplest matrix element.

Contents

Introduction

The Standard Model of elementary particle physics embodies the current knowledge of elementary particles and their interactions. Quarks and leptons form the basic constituents of matter and gauge bosons mediate the fundamental forces acting between them. The photon is the mediator of the electromagnetic force, the $W^{\pm}$- and Z-bosons mediate the weak force and the gluons are the exchange particles of the strong force. Electromagnetic and weak interactions are unified in the electroweak interaction described by the Glashow-Weinberg-Salam theory.

Quantum Chromo Dynamics (QCD) is the theory of the strong force, using quarks and gluons as degrees of freedom. The coupling of QCD is momentum dependent. At larger momenta, which correspond to short distances the coupling is small and the methods of Perturbation Theory can be applied. For intermediate and low momenta the coupling of QCD is large, so that perturbative calculations cannot be performed. Here, the quarks are confined to hadrons, the relevant degrees of freedom in the low energy regime of QCD. The behavior of the coupling is referred to as asymptotic freedom.

Effective field theories, which incorporate the symmetries of QCD can be used to describe and study the low energy regime of QCD. A general symmetry of QCD, if the three light quarks u, d, and s are considered massless, is the chiral symmetry $SU_L(3) \times SU_R(3)$. This symmetry is spontaneously broken to $SU_V(3)$, giving rise to an octet of massless Goldstone bosons, which can be identified with the pseudoscalar π, K, and η mesons. Due to the mass of the quarks chiral symmetry is explicitly broken. The low energy regime can be described by the methods of Chiral Perturbation Theory, which uses the Goldstone bosons as relevant degrees of freedom. Expansions are done in the powers of momenta of the mesons. At each order of the calculations free parameters of the theory have to be introduced in order to restore the renormalizability. Chiral Perturbation

Theory is used successfully to describe the low energy regime of QCD in a model independent way.

The η meson plays an important role in the understanding of the low energy regime of QCD. High precision measurements of differential distributions and decay rates allow to test the predictions of Chiral Perturbation Theory. This work is dedicated to the anomalous sector of QCD, which is manifested in the radiative decay of the pseudoscalar mesons.

Chapter 1 summarizes the theoretical aspects and the results of previous measurements of the decay $\eta \to \pi^+\pi^-\gamma$, giving the motivation for this work.

Chapter 2 introduces the COSY accelerator and the WASA facility, the relevant experimental setup for this work.

Chapter 3 describes analysis tools and common routines of event reconstruction, such as calibration, track finding, particle identification and energy reconstruction.

Chapter 4 illustrates the analysis, performed to extract the decay $\eta \to \pi^+\pi^-\gamma$.

Chapter 5 presents the results of the studies, including an estimate of the systematic uncertainties.

Chapter 6 gives a summary of this work and an outlook.

Chapter 1

Theory and Motivation

1.1   The η meson

The η meson was discovered in 1961 [P$^+$61]. It is characterized by the quantum numbers $I^G(J^{PC}) = 0^+(0^{-+})$ and a life time of $(5.0 \pm 0.3) \cdot 10^{-19}s$. Zero spin and negative parity make the η meson part of the light pseudoscalar meson nonet, along with $\pi^0, \pi^+, \pi^-, K^0, \bar{K}^0, K^+, K^-$, and η'.
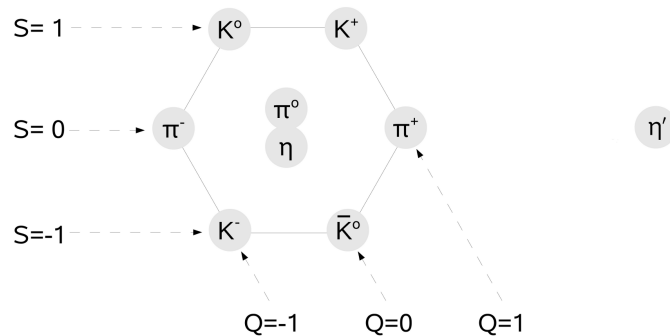
Figure 1.1: Multiplet of pseudoscalar mesons according to $SU(3)$ flavor symmetry group

In the quark model mesons are quark-antiquark systems. The three lightest quarks u, d, and s allow for 9 $q\bar{q}$ combinations. Because of the approximate $SU(3)$

flavor symmetry of these quarks the mesons can be organized in an octet and a singlet:

$$3 \otimes \bar{3} = 8 \oplus 1 \tag{1.1}$$

In Fig. 1.1 the octet and singlet states are depicted in a multiplet picture. Here, the mesons are ordered according to strangeness S along the vertical axis, according to the isospin projection I_3 along the horizontal axis, and according to charge Q along the diagonal.

The physically observed particle η is a combination of the octet and singlet states η_8 and η_1. The combination is described by a mixing angle θ:

$$\eta = \eta_8 \, cos(\theta) - \eta_1 \, sin(\theta) \tag{1.2}$$

The size of the mixing angle has to be determined experimentally. From the quark content of the pure SU(3) states the content of the η meson can be described as:

$$\eta_8 = \frac{1}{\sqrt{6}}(u\bar{u} + d\bar{d} - 2s\bar{s}) \tag{1.3}$$

$$\eta_1 = \frac{1}{\sqrt{3}}(u\bar{u} + d\bar{d} + s\bar{s}) \tag{1.4}$$

$$\eta = \frac{1}{\sqrt{2}}(u\bar{u} + d\bar{d})cos(\alpha) - s\bar{s} \, sin(\alpha) \qquad [\text{A}^+08] \tag{1.5}$$

Here, the mixing angle $\alpha = \frac{\pi}{2} - \theta_i + \theta$ is related to the angle θ by the ideal mixing angle $tan(\theta_i) = \frac{1}{\sqrt{2}}$, for which the $u\bar{u} + d\bar{d}$ and $s\bar{s}$ terms decouple. The mixing angle was established experimentally to be $\theta = -15.5°\pm1.3°$ [BES99]

A striking feature of the η meson is that all decays modes via the strong and electromagnetic interactions are forbidden in the lowest order. The decay into two pions cannot occur due to P and CP invariance. The decay into four neutral pions is forbidden for the same reasons. G - parity conservation does not allow the decay into three pions. The electromagnetic decay $\eta \to \pi^0\gamma$ is forbidden by the conservation of angular momentum and C invariance. Also, the η meson cannot decay via $\eta \to \pi^0\pi^0\gamma$ or $\eta \to \pi^0\pi^0\pi^0\gamma$ because of charge symmetry invariance. The decay $\eta \to \pi^+\pi^-\gamma$ may occur because it involves the chiral anomaly, but at a suppressed rate due to the limited phase space. The decay will be discussed in more detail in Section 1.2.1. The first allowed decay mode of the η meson is the second-order electromagnetic transition $\eta \to \gamma\gamma$. In Tab. 1.1 the most prominent decay modes are summarized.

Decay Mode	Branching Ratio
$\eta \to \gamma\gamma$	$39.30 \pm 0.20\%$
$\eta \to \pi^0\pi^0\pi^0$	$32.56 \pm 0.23\%$
$\eta \to \pi^+\pi^-\pi^0$	$22.73 \pm 0.28\%$
$\eta \to \pi^+\pi^-\gamma$	$4.60 \pm 0.16\%$
$\eta \to e^+e^-\gamma$	$(7.0 \pm 0.7) \cdot 10^{-3}$

Table 1.1: Most prominent decay modes of the η meson. The branching ratios are taken from [A$^+$08].

The η meson is an eigenstate of C and CP transformations. Due to the blocking of first order processes, rare decay modes become experimentally accessible. Thus, investigations of suppressed, symmetry violating decay modes are possible. This makes the η meson a valuable laboratory to test the symmetries of QCD.

1.2 The decay mode $\eta \to \pi^+\pi^-\gamma$

$\eta \to \pi^+\pi^-\gamma$ is the fourth strongest decay mode of the η meson, with a branching ratio of $4.60 \pm 0.16\%$ [A$^+$08]. The conservation laws of the quantum numbers constrain the dynamics of the decay products. As a pseudoscalar meson the η has spin $J = 0$. The photon has spin $J = 1$. To satisfy angular momentum conservation the two pion system has to be in a state of angular momentum $J = 1$. Similar conclusions can be drawn from the charge symmetry invariance. The photon and the η meson are eigenstates of the charge symmetry transformation with the eigenvalues $C = -1$ and $C = +1$, respectively. Due to C invariance the $\pi^+\pi^-$ system must have $C = -1$. The charge symmetry of a two body system is calculated according to $(-1)^J$, where J is the relative angular momentum of the system. Thus, C invariance demands odd values of angular momentum.

1.2.1 The box anomaly

The anomalies of QCD, which were found in current algebra as divergent Axialvector-Vector currents [Adl69, BJ69, Bar69] are important in the understanding of the process $\eta \to \pi^+\pi^-\gamma$. Fig. 1.2 illustrates the two anomalies, relevant for the η

decay with Feynman graphs: The AVV-anomaly (a), describing the coupling of
two vector mesons and a pseudo scalar meson and the VAAA-anomaly (b) which
describes the coupling of three pseudo scalar mesons and a vector meson. The
terms are referred to as triangle anomaly and box anomaly, referring to the shape
of the Feynman graphs. The decay mode $\eta \to \pi^+\pi^-\gamma$ allows to study the box
anomaly term, but the signal is obscured by resonant processes involving the
triangle anomaly. Both terms are contained in the Wess-Zumino effective action
which handles the anomalies of QCD [WZ71].

(a) AVV　　　　　　　　　　　　　(b) VAAA
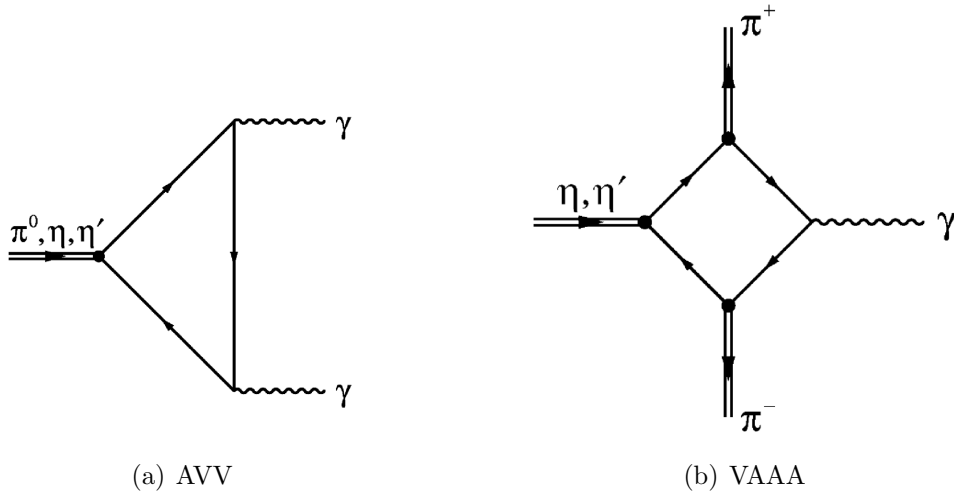
Figure 1.2: Feynman graphs for the triangle and box anomalies of QCD

It was shown by Witten [Wit83] that in an effective field theory of hadrons,
in which the $SU(3)_L \times SU(3)_R$ symmetry is spontaneously broken to $SU(3)_V$,
the Wess-Zumino term is an essential part of the chiral Lagrangian. In order to
incorporate all symmetries of QCD, the effective Euler-Lagrange equation has to
be – at leading order in the momentum expansion – of the form

$$\partial^\mu(\frac{1}{2}F_\pi^2 U^\dagger \partial_\mu U) + \lambda\epsilon^{\mu\nu\alpha\beta}(U^\dagger\partial_\mu U)(U^\dagger\partial_\nu U)(U^\dagger\partial_\alpha U)(U^\dagger\partial_\beta U) = 0 \qquad (1.6)$$

with F_π being the pion decay constant, λ being a constant factor, $\epsilon^{\mu\nu\alpha\beta}$ is the total
anti-symmetric tensor in four dimensions and $U = \exp\frac{i}{F_\pi}\sum_{j=1}^8 \lambda_j^a\phi_j^a$, where λ^a
are the generators of SU(3) and ϕ^a are the Goldstone boson fields. In the absence
of the second term, the equation is not only invariant under the naive parity
operation $x \leftrightarrow -x$ but also under the operation $U \leftrightarrow U^{-1}$, which is equivalent to
$\phi \leftrightarrow -\phi$. Neither the naive parity nor the latter operation, which counts modulo

two of the number of Goldstone bosons $(-1)^{N_B}$, is not a symmetry of QCD. In order to obtain a Lagrangian which incorporates only the appropriate symmetries an additional term is needed, which is odd under the naive parity operation and even in the number of pion fields. Eq. 1.6 is violating the naive parity as well as $(-1)^{N_B}$, but it is invariant under the combined operations $x \leftrightarrow -x$, $U \leftrightarrow U^{-1}$. The parity operation of QCD corresponds to the combined operations because of the Goldstone bosons being identified with the pseudoscalar mesons.

The Lagrangian resulting from this additional term corresponds to the Wess-Zumino effective action and is referred to as Wess-Zumino-Witten Lagrangian Γ_{WZW}. It can only be written in a closed form in 5 dimensions, to which the four dimensional space time is a boundary, and integrated via the Stokes theorem [Wit83]

$$
\begin{aligned}
\Gamma_{WZW} &= \frac{iN_c}{240\pi^2} \int_M d\Sigma^{ijklm} Tr\left((U^\dagger\partial_i U)(U^\dagger\partial_j U)(U^\dagger\partial_k U)(U^\dagger\partial_l U)(U^\dagger\partial_\mu U)\right) \\
&= -\frac{N_c}{240\pi^2 F_\pi^5} \int dx^4 Tr(\phi^a\partial_\mu\phi^a\partial_\nu\phi^a\partial_\alpha\phi^a\partial_\beta\phi^a)\epsilon^{\mu\nu\alpha\beta} + \text{ higher orders}
\end{aligned}
$$

(1.7)

Here, N_c is the number of colors. In the chiral limit, the lagrangian describes the process $K^+K^- \to \pi^+\pi^-\pi^0$, referred to as quintangle anomaly. If the Lagrangian is coupled to a photon field $A\mu$, it has the form [Hol02]

$$
\begin{aligned}
\Gamma_{WZW}(UA_\mu) = \Gamma_{WZW}&(U) \\
&+ \frac{N_c e}{48\pi^2}\epsilon^{\mu\nu\alpha\beta} \int d^4x A_\mu Tr(Q(R_\nu R_\alpha R_\beta + L_\nu L_\alpha L_\beta)) \\
&- \frac{iN_c e^2}{48\pi^2}\epsilon^{\mu\nu\alpha\beta} \int d^4x F_{\mu\nu} A_\alpha Tr\Big(Q^2(R_\beta + L_\beta) \\
&+ \frac{1}{2}(QU^\dagger QUR_\beta + QUQU^\dagger L_\beta)\Big)
\end{aligned}
$$

(1.8)

with Q being the quark charge matrix, $F_{\mu\nu}$ being the electromagnetic field strength tensor defined as $F_{\mu\nu} = \partial_\mu A_\nu - \partial_\nu A_\mu$, and R_μ and L_μ are defined as $(\partial_\mu U^\dagger)U$ and $U\partial_\mu U^\dagger$, respectively. The first term is independent of the photon field and again corresponds to the quintangle anomaly. The second term, containing one photon and three Goldstone bosons, agrees with the QCD VAAA box anomaly and the third term corresponds to the QCD triangle anomaly, with one Goldstone boson and two photons. Thus, the effective action Γ_{WZW} precisely describes the

effects of QCD anomalies in low-energy processes with photons and Goldstone bosons [Wit83].

In the chiral limit the amplitude of the decay mode $\eta \to \pi^+\pi^-\gamma$ is determined by the box anomaly term of Γ_{WZW}. The decay amplitude of the physical η particle is calculated as [Hol02]:

$$\mathcal{A}_{\eta \to \pi^+\pi^-\gamma}(0,0,0) = \frac{eN_c}{12\sqrt{3}\pi^2 F_\pi^3} \left(\frac{F_\pi}{F_8} \cos\theta - \sqrt{2}\frac{F_\pi}{F_0} \sin\theta \right) \epsilon^{\mu\nu\alpha\beta} \varepsilon_\mu^* p_{+\nu} p_{-\alpha} k_{\gamma\beta}$$

(1.9)

with F_0 and F_8 being the decay constants of the singlet and octet η states, θ being the mixing angle, $p_\pm$ and k being the momenta of the pions and the photon, respectively , and ε^* being the polarization of the photon. The resulting rate $\Gamma_{\eta \to \pi^+\pi^-\gamma}^{(0)} = 35.7\ eV$ [Hol02] is almost a factor of two lower than experimental value $\Gamma_{\eta \to \pi^+\pi^-\gamma}^{(exp)} = 60 \pm 4\ eV$ [A$^+$08]. Additionally, a shift in the experimental spectrum of the squared invariant mass of the two pions $s_{\pi\pi}$ towards larger invariant masses is observed (see Section 1.2.2). The significant difference results from the dynamic range of the η decay $m_{\pi\pi}^2 \leq s_{\pi\pi} \leq m_\eta^2$, which is well above the chiral limit of $s_{\pi\pi} = 0$. Thus, it is important to include final state interactions, which is done by unitarized extensions of the Γ_{WZW}.

A realistic description can be obtained by matching the result of the low energy limit with a Vector Meson Dominance (VMD) model [Pic92, PR93]. The decay amplitude is modified with a form factor:

$$\mathcal{A}_{\eta \to \pi^+\pi^-\gamma}(s_{\pi\pi}) = \mathcal{A}_{\eta \to \pi^+\pi^-\gamma}(0,0,0) \times \left(-\frac{1}{2} + \frac{3}{2}\frac{s_{\pi\pi}}{m_\rho^2 - s_{\pi\pi}} \right)$$

(1.10)

with m_ρ being the mass of the ρ meson. The decay rate obtained from this ansatz is $\Gamma_{\eta \to \pi^+\pi^-\gamma}^{VMD} = 62.3\ eV$ [Hol02], which is in good agreement with the experimental value.

A better agreement between the results of Chiral Perturbation Theory and experiment is achieved by including pion loop corrections and terms of momenta up to the order $\mathcal{O}(p^6)$. The decay rate is $\Gamma_{\eta \to \pi^+\pi^-\gamma}^{(\mathcal{O}(p^6)+1\text{-loop})} = 47\ eV$ [BBC90].

The calculations of the Vector Meson Dominance model shown above, do not match the results of the loop corrections [Hol02]. In order to introduce final state interactions in a form which matches the one-loop chiral corrections and the vector dominance results, Holstein postulated the structure

$$\mathcal{A}_{\eta \to \pi^+\pi^-\gamma}(s, s_{\pi\pi}) = \mathcal{A}_{\eta \to \pi^+\pi^-\gamma}(0,0) \times \left(1 - c + c\frac{1 + as_{\pi\pi}}{D_1(s_{\pi\pi})} \right)$$

(1.11)

where $D_1(s_{\pi\pi})$ is the Omnes function, which is defined in terms of the P-wave $\pi\pi$ scattering phase shifts. The parameters a and c are fixed to $c = 1$ and $a = \frac{1}{2m_\rho^2}$. The decay rate calculated with this approach $\Gamma^{N/D}_{\eta\to\pi^+\pi^-\gamma} = 65.7 \ eV$ is compatible with the experimental value.

Recent calculations are conducted in the framework of the Chiral Unitary Approach [BN04, BN07]. Here, the results of the one-loop corrections of the chiral Lagrangian are matched with a Bethe-Salpeter equation with coupled channels. The Bethe-Salpeter equation satisfies unitarity constraints and generates resonances dynamically through the iteration of meson-meson interactions. The free parameters of this approach are fixed by a fit to the experimental data. The decay rate $\Gamma^{CUA}_{\eta\to\pi^+\pi^-\gamma} = 60.9^{+1.1}_{-1.2} \ eV$ [BN07] is in good agreement with the experimental value.

A different ansatz has been performed by Benayoun et al. [BDD$^+$03]. The anomalies of QCD are evaluated in the framework of Hidden Local Symmetries [BKY88, FKT$^+$85], where vector mesons are accounted for as degrees of freedom together with pseudoscalar mesons and contact terms. The Lagrangian describing the decay $\eta \to \pi^+\pi^-\gamma$ consists of a resonant term and a contact term, which contains the box anomaly term. The decay rate calculated from this approach $\Gamma^{HLS}_{\eta\to\pi^+\pi^-\gamma} = 56.3 \pm 1.7 \ eV$, is in agreement with the experimental value. In the absence of the contact term, the rate would be larger by a factor of two which is interpreted as a strong indication of the box anomaly.

The different approaches to include final state interactions, which have been summarized in this section, predict decay rates which are in agreement with the experimental value. In addition to the decay rate, the line shape of the invariant mass spectrum of the two pions $s_{\pi\pi}$ is calculated. It is more sensitive to the description of final state interactions than the decay rate and allows to draw more detailed conclusions on the agreement of experiment and theory. A comparison of the predictions with experimental distributions is done in Section 1.2.2, where the available experimental data on the decay $\eta \to \pi^+\pi^-\gamma$ are discussed.

1.2.2   Previous Measurements

The decay mode $\eta \to \pi^+\pi^-\gamma$ has been the subject of various investigations. Tab. 1.2 provides an overview of the experiments, the reconstructed number of events, and the focus of the investigations. The statistically most significant measurements are found in [G+70, L+73, T+72, J+74]. Here, pion beams and hydrogen targets were used to produce η mesons. The focus of the investigations includes the determination of the branching ratio, the test of charge symmetry violation, and the measurement of the Dalitz plot distributions.

Experiment	Events	Focus
Crawford et al. [CP66]	33	BR, DP, CV
Litchfield et al. [L+67]	160	BR
Baltlay et al. [B+67]	509	BR
Cnops et al. [C+68]	1088	DP
Gormley et al. [G+70]	7257	DP, BR
Thaler et al. [T+72]	36155	CV
Layter et al. [L+73]	18150	DP
Jane et al. [J+74]	34680	CV
CLEO Collab. [L+07]	900	BR

Table 1.2: Previous measurements of the decay mode $\eta \to \pi\pi\gamma$, the acquired statistics and the focus of the investigations. Branching ratio (BR), Dalitz plot distributions (DP), and charge symmetry violation (CV).

The absolute branching ratio of $4.60 \pm 0.16\%$ in [A+08] is a fit to the results of the individual measurements listed in Tab. 1.2. However, the result of the CLEO collaboration is excluded. In this recent measurement of the prominent η decays a relative branching ratio of $R_{BR} = \frac{\Gamma(\eta\to\pi^+\pi^-\gamma)}{\Gamma(\eta\to\pi^+\pi^-\pi^0)} = 0.175 \pm 0.007 \pm 0.006$ has been found, which is deviating by more than three standard deviation from other measurements.

As discussed above, the two pion system in the decay $\eta \to \pi^+\pi^-\gamma$ allows for testing the charge conjugation symmetry. Two observables have been established to quantify the amount of C-violation. One observable is the left-right-asymmetry parameter which is calculated according to $A_{\pm} = \frac{N_+ - N_-}{N_+ + N_-}$, where N_+ and N_- are defined as the number of events in which the momentum of the π^+ in the η rest
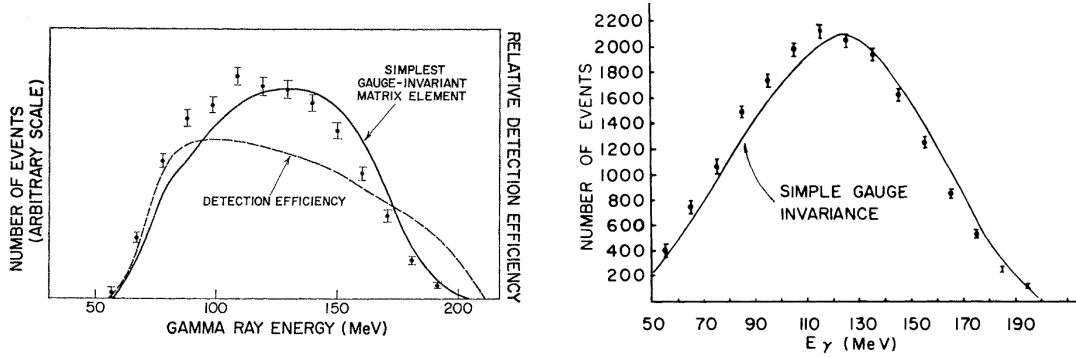
Figure 1.3: The photon energy distribution in the η rest frame published by Gormley et al. [G+70] (left) and Layter et al. [L+73] (right). Both experimental distributions are not corrected for efficiency. Instead, the prediction of the simplest matrix elements, shown with a solid line, have been folded with the efficiency. In the spectrum of Gormley et al. the efficiency is shown.

frame is larger than the momentum of the π^- and vice versa. The current value of $A_{\pm} = (0.9 \pm 0.4) \cdot 10^{-2}$ [A+08] is averaged from the measurements quoted in Tab. 1.2. Another observable is the strength of a D-wave contribution, which is given by the parameter β in the fit of the angular distribution of the pions with the function $\frac{d\Gamma}{d(\cos(\theta))} = A \cdot \sin^2(\theta) \cdot (1 + \beta \cdot \cos^2(\theta))$. A D-wave contribution introduces even relative angular momenta between the two pions, which are forbidden due to C-invariance. The current value, averaged from the measurements quoted in Tab. 1.2 is $\beta = -0.2 \pm 0.7$ [A+08]. The result of Thaler et al. is excluded from this average. The value of $\beta = 0.12 \pm 0.06$ [T+72] would be in favor of a D-wave contribution, but it is interpreted as an interference of P-wave and F-waves.

Four of the measurements listed in Tab. 1.2 studied the Dalitz plot distributions of the decay system. Here, the two statistically most significant results of Gormley et al. [G+70] and Layter et al. [L+73] will be discussed in more detail. In Fig. 1.3, the spectra of the photon energy in the η rest frame of both measurements are shown. The spectra are presented in the range of $50 \ MeV \leq E_\gamma \leq 200 \ MeV$ with a binning of $10 \ MeV$. Additionally, the distributions are compared to the shape predicted by the simplest gauge invariant matrix element, which is shown in Eq. 1.9. The simplest matrix element is not in agreement with either of the distributions, which show a shift towards lower photon energies. A better agreement is reported for a purely ρ-dominant matrix element, without the contact term due

to a contribution of the box anomaly. It must be noted, that both experimental distributions are not corrected for efficiency. Instead, the model prediction has been folded with the efficiency. In case of Gormley et al. [G+70] the detection efficiency is shown explicitly, as can be seen in the left panel of Fig. 1.3.

The theoretical approaches presented in Section 1.2.1 have been compared with the experimental distribution with respect to the prediction of the photon energy line shape. Fig. 1.4, taken from [Hol02], shows a comparison of three approaches with the data of Gormley et al. [G+70]. In the left panel, the data are compared to the Vector Meson Dominance result (see Eq. 1.10) shown with a dashed line, and to the approach using the one-loop corrections and an Omnes function to describe final state interactions (see Eq. 1.11), shown with a solid line. In the right panel, this approach is compared to the result of the one-loop corrections without an additional model to describe final state interactions, shown with a dot-dashed line.
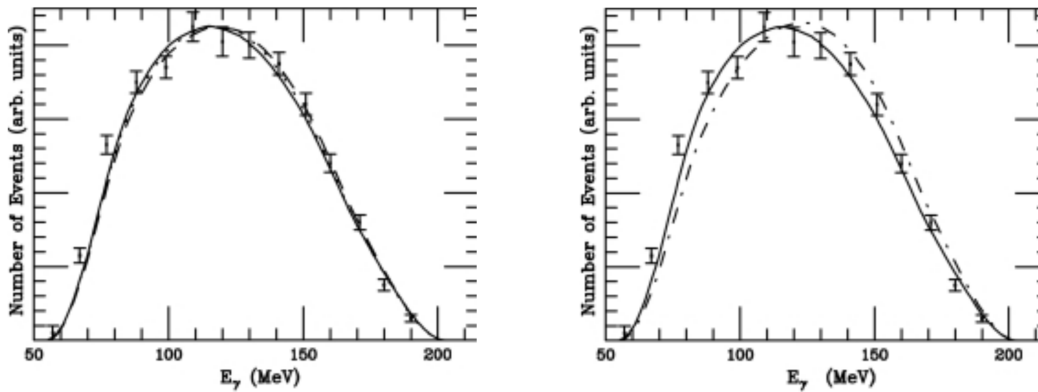
Figure 1.4: Comparison of the photon energy spectrum of Gormley et al. [G+70] with different theoretical approaches. The solid line corresponds in both cases to the ansatz which combines the one-loop corrections with an Omnes function to include final state interactions. It is compared with the prediction of the vector meson dominance model, illustrated by the dashed line in the left panel, and with the one-loop corrections without further models, illustrated with the dot-dashed line in the right panel. The results of Vector Meson Dominance and the ansatz including the Omnes function are in good agreement. The one-loop corrections are shifted towards higher photon energies, illustrating the necessity of the inclusion of final state interactions.

The Vector Meson Dominance model and the approach including the Omnes function, describe the data similarly well. One-loop corrections by themselves,

are not able to reproduce the shape of the experimental distribution, showing the necessity of unitarized extentions of the chiral Lagrangian.

A fit of the Chiral Unitary Approach to both experimental spectra is shown in Fig. 1.5. The solid black line shows the best fit and the blue band indicates a 1σ confidence region. The figures are taken from [BN07]. Both experimental distributions can be described individually by the model resulting in a $\chi^2 \simeq 1$ of the fit. However, in an attempt to fit both data sets simultaneously a χ^2 value close to 1 cannot be achieved. This is interpreted as an inconsistency between the two data sets, which cannot be recovered due to unknown systematic errors of the measurements and an additional systematic error which is introduced by the extraction of efficiency corrections.
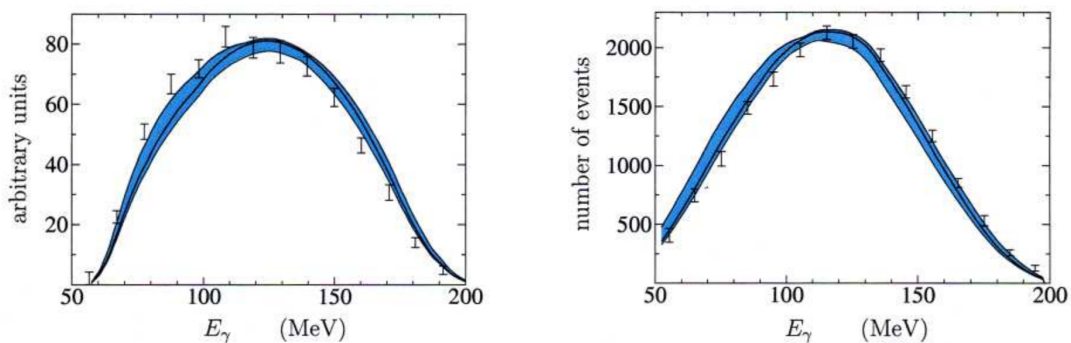
Figure 1.5: The photon energy distributions of Gormley et al. [G+70] (left) and Layter et al. [L+73] (right) are fitted with the calculations of the Chiral Unitary Approach. The solid line corresponds to the best fit and the blue band shows the 1σ confidence band. The plots are taken from [BN07].

A similar discrepancy is reported from the comparison of the approach using Hidden Local Symmetries [BDD+03] with both of the experimental distributions. The model was fitted to the experimental distribution with and without the contact term of the Lagrangian that accounts for the box anomaly contribution. Fig. 1.6, taken from [BDD+03], illustrates the result of the fit. The agreement of the model prediction and the data is expressed by the χ^2 value of the fit. In the left panel of Fig. 1.6 the photon energy spectrum of Gormley et al. is shown, which is in better agreement with the model when the fit is performed taking into account the box anomaly contribution, as shown by the solid line ($\chi^2 = 5.5$). Without this contribution the fit, illustrated with a dotted line, results in a

$\chi^2 = 12.3$. The photon energy spectrum of Layter et al., shown in the right panel of Fig. 1.6, results in larger χ^2 values of the fit. However, the model prediction without the contribution of the box anomaly is favored by a $\chi^2 = 10.7$ compared to a $\chi^2 = 26.7$ in case of a box anomaly contribution. The discrepancy between the two data sets is attributed to the missing efficiency corrections, which have been extracted from the published data sets [G+70, L+73] in a model dependent way [BDD+03].
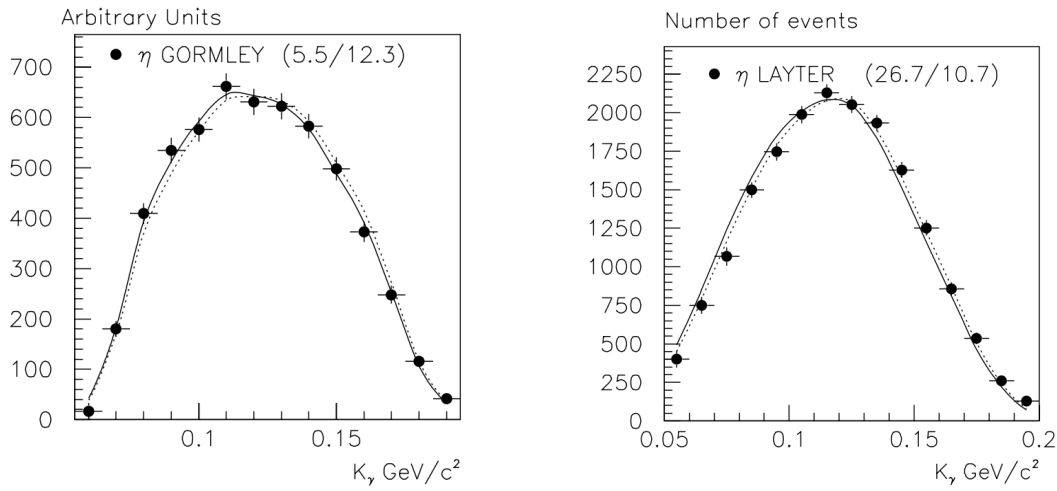
Figure 1.6: The photon energy distribution in the η rest frame of Gormley et al. [G+70] (left) and Layter et al. [L+73] (right) is compared to the model prediction based on the Hidden Local Symmetry approach [BDD+03]. Both spectra are fitted with (solid line) and without (dotted line) the contact term of the Lagrangian accounting for the box anomaly contribution. The χ^2 values of the fit, shown as numbers in the plots in the form (With contact term/without contact term), favor the box anomaly contribution in case of Gormley et al., but disfavor it in case of Layter et al.

1.3   Motivation for this measurement

The anomalies of QCD form a fundamental part of the Chiral Perturbation Theory, the effective field theory of hadrons. The decay mode $\eta \rightarrow \pi^+\pi^-\gamma$ allows to test the anomalous sector and especially the box anomaly. However, experimental data are scarce and suffer from low statistics. Additionally, the statistically most

significant measurements have been published without efficiency corrections. Instead, the efficiency was folded with the models used for comparison.

The recent comparison of the available data with different theoretical models shows the importance of properly included final state interactions. However, there are ambiguities in the theoretical interpretation of the two statistically most significant measurements, which can be partly attributed to the missing efficiency corrections.

A new measurement of the decay mode $\eta \rightarrow \pi^+\pi^-\gamma$ with high statistical significance is necessary to settle the ambiguities. The aim of the present work is to provide a kinematically complete measurement of the η decay and a careful extraction of the differential distributions, in order to gain further insight into the anomalous sector of QCD.

Chapter 2

The WASA facility at COSY

The Wide Angle Shower Apparatus (WASA) is a detector setup designed to study the production of light mesons in hadronic interactions and their decays. It includes an electromagnetic calorimeter and a drift chamber located in the field of a superconducting solenoid to detect and identify charged as well as neutral particles. A pellet target system was developed to provide target densities of $\geq 10^{15} \frac{atoms}{cm^2}$ allowing for luminosities in the order of $10^{32} cm^{-2} s^{-1}$. The capability of the WASA detectors to cope with a high particle flux in combination with the pellet target system is mandatory for the investigation of rare processes. In order to pursue a physics program focussed on rare leptonic decays, all detector components have been optimized for the detection of dileptons. The material budget close to the interaction region was dimensioned to minimize the probability for conversion of photons.

WASA was first proposed in 1987 [KZ87]. The facility was installed at the CELSIUS storage ring at the TSL in Uppsala, Sweden [B+08] and operated until the shutdown of the accelerator in 2005. It was then transferred to the COSY accelerator in Jülich, Germany. Higher beam energies, as well as the availability of polarized beams allow for an enhanced physics program, focussing on symmetries and symmetry breaking [A+04].

After successful installation and commissioning in the fall of 2006 WASA has been taking data since April 2007.

2.1 The COSY storage ring

The COler SYnchroton is a storage ring of 184 m circumference, situated at and maintained by the Forschungszentrum Jülich [M+97, Mai97]. It provides unpolarized and polarized proton and deuteron beams in the momentum range of 0.6 to 3.7 GeV/c. This allows to produce and study hadrons up to a mass of 1030 MeV/c, which includes the Φ-meson. The layout of the facility is shown in Fig. 2.1.
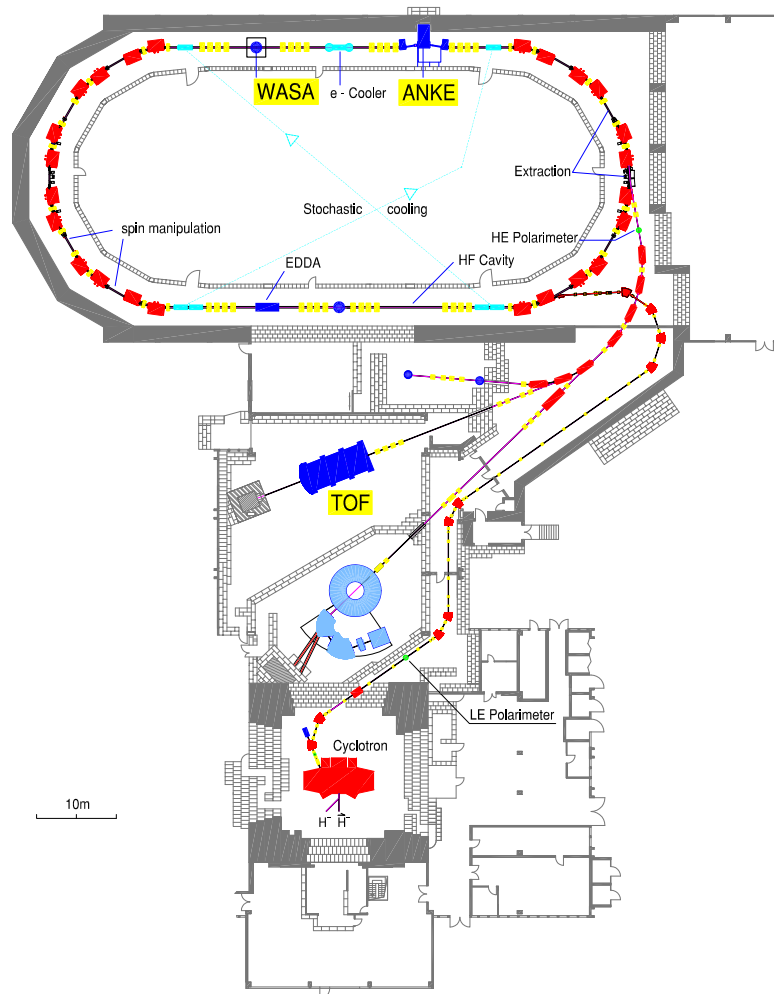
Figure 2.1: Floor plan of the COSY accelerator complex. The internal and external experimental setups are highlighted. The WASA detector is mounted upstream of the electron cooler.

The COSY ring has the shape of a race track with two straight sections. In

the straight sections the tools for beam cooling and monitoring are situated. Additionally, four internal experimental setups can be accommodated, one of which is the WASA detector. There is also the possibility to extract the beam and deliver it to external experiments.

An isochronous cyclotron serves as preaccelerator to COSY. It is fed by either unpolarized or polarized H^- and D^- sources, respectively. The ions are accelerated up to energies of 45 MeV. The injection into the COSY ring is carried out as stripping injection using a 20 $\mu g/cm^2$ carbon foil which removes both electrons from the ions. In this way up to 10^{11} particles can be stored in the ring, yielding typical luminosities of 10^{31} $cm^{-2}s^{-1}$ for internal experiments. In combination with the pellet target system of the WASA facility (see section 2.2) luminosities of 10^{32} $cm^{-2}s^{-1}$ are feasible.

The particle beams can be phase space cooled by means of electron cooling at injection energies and by stochastic cooling at higher energies [P$^+$00]. This results in a high momentum resolution of the beam of up to $\Delta p/p \approx 1 \cdot 10^{-4}$. Beam life times of maximally one hour have been achieved during an internal experiment. In addition to the cooling of the beam, a barrier bucket cavity [GRS09] can be used, to compensate for the mean energy loss in beam target interactions. This is of special importance in case of a target thickness of $\geq 10^{15} \frac{atoms}{cm^2}$, as used by the WASA facility. Here, beam cooling by itself is not sufficient to recover the energy loss in the beam target interactions [GRS09]. Typical life times of the beam are on the order of a few minutes.

2.2   The Pellet Target

Studies of rare processes make a number of demands on the target system of the experimental setups. The Pellet Target System has been especially developed for the WASA facility to fulfill these requirements. It provides a stream of frozen droplets of hydrogen or deuterium, called pellets. A target thickness of $10^{15} \frac{atoms}{cm^2}$ has been achieved. Thereby, luminosities on the order of 10^{32} $cm^{-2}s^{-1}$ are possible. At the same time, the target is suited for internal experiments at storage rings allowing for reasonable beam life times on the order of few minutes. The dimension of the target in the interaction region is small. The pellets have a diameter on the order of 35 μm. This has two advantages. The small size reduces the

probability for secondary interaction inside the target. At the same time, there is a well defined interaction point enhancing the angular resolution. The target station is set up such that most of the structural material is located outside of the detector. Only a thin tube is used to guide the pellets into the scattering chamber. In the interaction region itself a containment of the target is not necessary. This is an important prerequisite for 4π detection. The full geometrical coverage of the detector is possible by the minimization of the structural material. Fig. 2.2 illustrates the target system and its connection to the scattering chamber and the COSY beam tube, respectively.
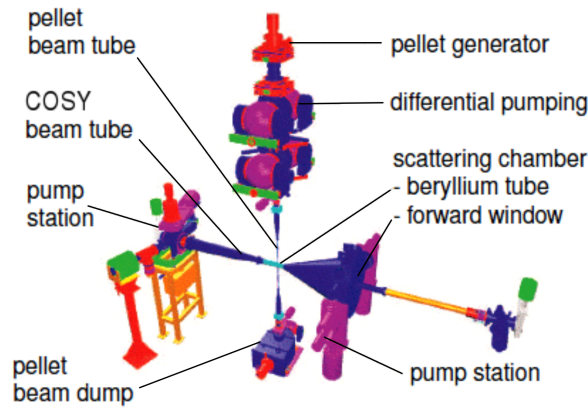
Figure 2.2: Schematic view of the Pellet Target System

The pellet generator is located above the Central Detector. Here, liquefied gas of high purity is pressed through a thin glass nozzle into the droplet formation chamber. In this chamber, pressure and temperature are adjusted such that the conditions are close to the triple point of the target material. The nozzle is vibrating, breaking up the liquid jet into individual, equally spaced droplets. While passing through the chamber, the surface of the droplets freezes by evaporation and the liquid droplets become solid spheres, the pellets.

The pellets are accelerated up to velocities of $100\ m/s$ by the flow of the carrier gas, when conducted into vacuum via a thin glass tube, the vacuum injection capillary. A skimmer is used to collimate the pellet beam before it can enter the pellet beam tube. This is a $2\ m$ long tube of $7\ mm$ diameter, guiding the pellets to the interaction region. Here, the pellet beam has a size of $2-4\ mm$.

The pellet rate at the interaction point is determined by the frequency of the

Pellet size	$\approx 35 \mu$m
Pellet frequency	
at nozzle	$70 kHz$
at interaction point	$5000 - 12000 s^{-1}$
Pellet velocity	$60 - 100 \ m/s$
Pellet stream divergence	$\sim 0.04°$
Pellet stream diameter at beam	$2 - 4 \ mm$
Effective target thickness	$> 10^{15} \text{cm}^{-2}$

Table 2.1: Performance of the WASA Pellet Target System.

nozzle in the generator. Typical frequencies are on the order of 70 kHz. However, due to beam collimation at the skimmer and turbulences during the vacuum injection the pellet rate becomes irregular. On average, rates of a few thousand pellets per second pass the interaction point. Tab. 2.1 summarizes the target properties during the beam time of October 2008, in which deuterium pellets were used.

After the interaction with the ion beam of COSY, the pellets are deposited in the pellet beam dump. Here, a stack of metal plates coated with charcoal is used to decelerate and retain the pellets. Turbo pumps remove the gas of the evaporating pellets.

The operation using deuterium needs regular breaks in which the nozzle is heated up to evaporate blockage due to frozen materials. The reason for the blocking has not been clarified yet. Fig. 2.3 shows the ratio of operation and re-generation during the beam time in October 2008. As can be seen, it was possible to increase the duty factor of the target. In the beginning the nozzle was heated up to room temperature in order to remove blocking. Later it was observed that a temperature of 160 K is fully sufficient. This allowed to reduce the time for the target regeneration from approximately 12 to only 3 hours.
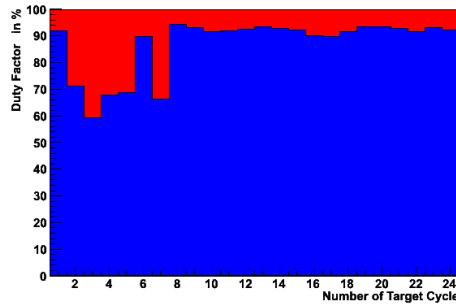
Figure 2.3: Duty factor of the pellet target during the production run in October 2008. The operation with deuterium pellets requires the nozzle to be heated up at regular intervals in order to remove blocking.

2.3 The WASA detector

The WASA detector is a 4π detection system designed to study decays of light, unflavored mesons and their production in hadronic interactions. The detector is divided into two major parts. The Forward Detector, covering polar angles from 3 to 18 degrees and the Central Detector covering polar angles from 20 to 169 degree. The Forward Detector is designed to reconstruct recoil particles to tag on meson production via the missing mass technique. The Central Detector is used to reconstruct the mesons or the particles originating from their decay.

A cross section of the complete WASA detector is shown in Fig. 2.4. The individual components of the Central and Forward Detector are described in the following sections.

2.3.1 Coordinate System

Positions in the WASA setup are either described in cartesian coordinates (x, y, z) or in spherical coordinates (r, θ, ϕ). Either of the descriptions is based on a right-handed coordinate system with the Z-axis oriented along the beam axis. The origin is located in the interaction point of COSY beam and pellet target.

This definition results in a positive X-axis pointing horizontally outwards to the outside of the COSY ring and a positive Y-axis pointing vertically upwards.
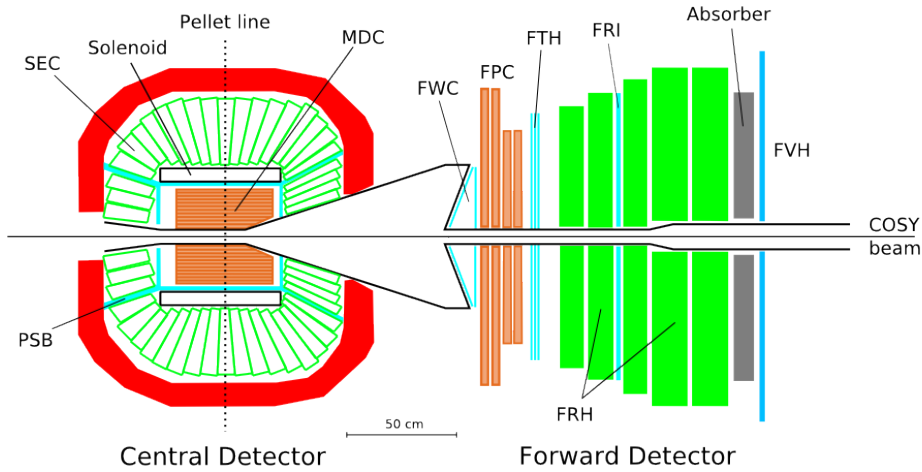
Figure 2.4: Cross section of the WASA detector. The setup is divided into two parts. The Central Detector consists of a Mini Drift Chamber (MDC) operated in the field of a superconducting solenoid, a Plastic Scintillator Barrel (PSB) to distinguish charged from neutral particles, and an electromagnetic calorimeter (SEC). The Forward Detector consist of the Forward Proportional Chamber (FPC), the Forward Range Hodoscope (FRH) and a set of thin scintillator hodoscopes: The Forward Window Counter (FWC), the Forward Trigger Hodoscope (FTH) the Forward Range Intermediate hodoscope (FRI), and the Forward Veto Hodoscope (FVH) which is installed behind an removable iron absorber.

The polar angle θ is the angle measured from the Z-axis and the azimuthal angle ϕ is measured in the XY-plane starting from the X-axis.

2.3.2   Central Detector

The Central Detector surrounds the scattering chamber and the interaction point. The straw chamber in the magnetic field and the electromagnetic calorimeter allow the measurement of momentum and energy of charged as well as neutral particles. Plastic scintillators allow the discrimination between charged and neutral particles on the trigger level. The amount of passive material close to the interaction region is kept at a minimum in order to reduce the probability of secondary interactions like photon conversion. The scattering chamber, shown in Fig. 2.5, is made from 1.2 mm thin beryllium and the total thickness of the

solenoid corresponds to only 0.18 radiation lenghts. In the following section the individual components of the Central Detector are described.

2.3.2.1 Mini Drift Chamber

The Mini Drift Chamber is assembled from 1738 straw tubes. Each straw tube is made from $25\mu m$ thin aluminized Mylar and a sensing wire of 20 μm gold plated tungsten stretched with a tension of 40 g. The tubes are arranged in 17 layers with an increasing tube radius from the inner to the outermost layers. In the inner five layers the tubes have a radius of 2 mm, followed by six layers of 3 mm tube radius. The tubes in the six outer layers have a radius of 4 mm.

Every second layer is aligned along the beam axis. They are interleaved by eight layers, which are skewed with angles of 6 to 9 degrees, resulting in an hyperboloid shape of the tubes in the radial direction. The five innermost layers have different lengths, due to the conical shape of the scattering chamber. This results in an asymmetry with respect to the pellet beam tube.

As can be seen from Fig. 2.6, in each layer the individual tubes are held in place by plates forming semi-rings. The plates are made from an aluminum-beryllium alloy (50% Al / 50% Be). The semi rings are joined around the beam pipe. The fully assembled chamber is enclosed in a cylindrical cover made of 1 mm thick Al-Be alloy.

The straw tubes are operated as proportional drift tubes. A mixture of argon and ethane ($80\% Ar$ / $20\% C_2H_6$) is used as drift gas. When ionizing particles cross, free electron ion pairs are generated in the tubes along the trajectory. A precise reconstruction of the trajectory of a traversing particle is possible by measuring the drift time of the electrons. The Mini Drift Chamber is situated in the magnetic field of the superconducting solenoid and the momentum of the particle can be determined form the curvature of the trajectory. A more detailed description of the construction and the operation of the Mini Drift Chamber can be found in [Jac04].

2.3.2.2 Plastic Scintillator Barrel

The Plastic Scintillator Barrel is a cylindrical detector surrounding the central drift chamber. It consists of a barrel part and a forward and backward end cap.

Figure 2.5: The central scattering chamber, made from 1.2 mm beryllium.
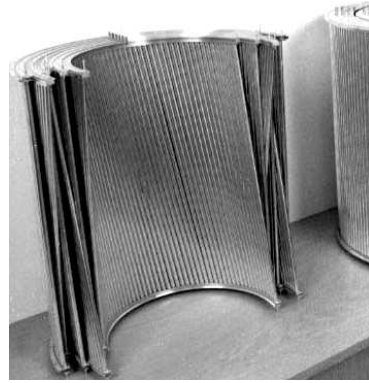
Figure 2.6: Half-shells of the Mini Drift Chamber before assembly.
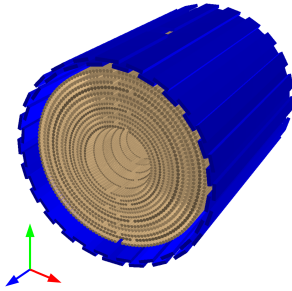
Figure 2.7: 3D view of the Mini Drift Chamber mounted inside the central part of the Plastic Scintillator Barrel.
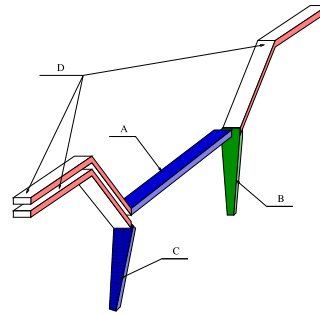
Figure 2.8: One full sector of the Plastic Scintillator Barrel, the elements of the backward (C), central (A) and forward (B) part are connected to light-guides (D).
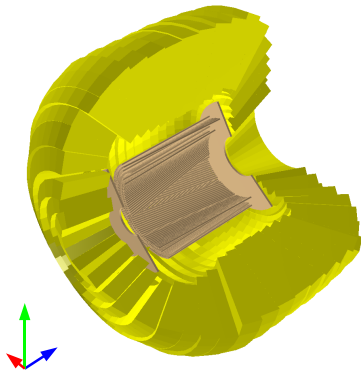
Figure 2.9: Cross sectional drawing of the calorimeter. The positions of the Plastic Scintillator Barrel and the Mini Drift Chamber are indicated.
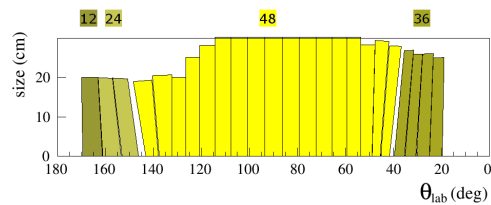
Figure 2.10: Polar angle coverage of the calorimeter. The numbers above the sketch indicate the number of crystals per calorimeter ring.

Each part is made from 8 *mm* thick BC408 plastic scintillator. The forward and backward parts are assembled from 48 trapezoidally shaped elements. The edges of the individual elements are inclined, so that there is a small region of overlap for neighboring elements. In this way gaps between elements are avoided which would decrease the detection efficiency. While the forward endcap is perpendicular to the beam axis, the backward part is inclined by 30 degrees, forming a conical surface.

The elements of the central part are rectangular bars. As indicated in Fig. 2.7, the elements are assembled such that they overlap on each side by 6 *mm* with the neighboring elements. Two of the elements are cut into halves, leaving space for the pellet beam tube. The central part of the Barrel consists of a total of 50 elements.

The 146 elements are read out individually by photomultiplier tubes. Fig. 2.8 shows one section of the complete Plastic Scintillator Barrel with light guides attached to the elements. These are necessary to transport the scintillation light to the outside of the iron yoke, where photomultiplier tubes can be used. More details on the construction and the design of the Plastic Scintillator Barrel can be found in [Jac04].

The fast signals of the plastic scintillators are used to discriminate charged from neutral particles on the trigger level. In the offline analysis the information on the energy deposits are used for the identification of charged particles (See Section 3.4).

Due to aging effects of the scintillator material, the elements of the central part of the Plastic Scintillator Barrel have been refurbished in 2008 [Pod09].

2.3.2.3   Superconducting Solenoid

The superconducting solenoid provides the magnetic field, needed to determine momenta of charged particles with the Mini Drift Chamber. It is placed inside the calorimeter, surrounding the drift chamber and the Plastic Barrel. In order to allow for high sensitivity and accuracy of energy measurements in the calorimeter, the wall thickness of the solenoid and its cryostat was minimized. It corresponds to 0.18 radiation lengths. The solenoid is cooled with liquid Helium and operated at 4.5 *K*. The axial magnetic field can be provided with flux densities up to 1.3 *T*

in the interaction region. Measurements of the magnetic field strength with a hall probe have been compared to simulations of the magnetic flux in order to establish a map of the magnetic field. Fig. 2.11 shows the density distribution of the magnetic flux for a coil current of 667 A, which corresponds to 1.3 T in the interaction region. The field in the volume of the Mini Drift Chamber is uniform within 20% of the average value of the field strength of 1.22 T [A$^+$04].
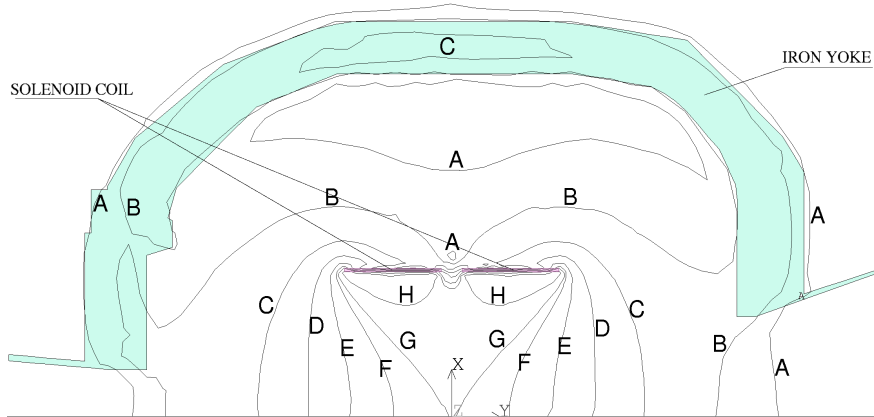
Figure 2.11: Calculated distribution of the magnetic flux density for a coil current of 667 A. Contour maxima are indicated by lines marked A - H, where: $A = 0.10$ T, $B = 0.25$ T, $C = 0.50$ T, $D = 0.75$ T, $E = 1.00$ T, $F = 1.20$ T, $G = 1.30$ T, $H = 1.5$ T [A$^+$04]

The field of the solenoid is confined by a return yoke made from iron with low carbon content. The field outside of the yoke is negligible. This is important for the operation of photomultiplier tubes. A detailed description of the solenoid can be found in [Rub99].

2.3.2.4   Scintillating Electromagnetic Calorimeter

The Calorimeter, as shown in Fig. 2.9, is the outermost active component of the Central Detector. It is assembled from 1012 sodium doped cesium iodide ($CsI(Na)$) crystals. The crystals, arranged in 24 rings, cover polar angles from 20 to 169 degrees, which corresponds to 96% of the full solid angle. The gaps arise from the forward and backward openings of the scattering chamber and the openings needed for the pellet beam tube and the liquid helium supply of the solenoid.

The Calorimeter consists of a central part and two end caps, which differ in crystal size, as can be seen from Fig. 2.10. Between the central part and the end caps there are small gaps, due to the light guides of the Plastic Barrel. The trapezoidally shaped crystals with lengths from 20 to 30 *cm* correspond to ~ 16 radiation lengths and ~ 0.8 hadronic interaction lengths.

The crystals are read out individually by photomultiplier tubes. Long light guides are used, so that the readout is done outside of the iron yoke. Here, the photomultiplier tubes are not affected by the field of the solenoid. The signals are sufficiently fast to be used for triggering. More details on the construction and the design of the calorimeter can be found in [Koc04].

The Calorimeter provides energy and angular information, which is essential for the reconstruction of photons and charged particles. The energy resolution for photons is described by $\frac{\Delta E}{E} = \frac{5\%}{\sqrt{E/GeV}}$. For stopped charged particles the energy resolution is $\sim 3\%$. The stopping power of the crystals is 190 MeV for charged pions, 400 MeV for protons, and 450 MeV for deuterons [B$^+$08]. The angular resolution of the calorimeter has a lower limit which is defined by the crystal size. A single crystal covers $\sim 5°$ of the polar and $\sim 7.5°$ of the azimuthal angle. The position of an electromagnetic shower is reconstructed as the energy weighted average of the contributing crystals (see Section 3.3.2), taking into account the lateral expansion of the shower. For photons and electrons the lateral expansion scales with the Molière radius R_M, calculated as

$$R_M = X_0 \cdot \frac{E_S}{E_C} = 3.57 \ cm \tag{2.1}$$

where $X_0 = 1.86 \ cm$ is the radiation length of $CsI(Na)$, $E_C = 11.05 \ MeV$ is the critical energy and $E_S = 21.2052 \ MeV$ is the scale energy [A$^+$08]. Thus, depending on the energy of the incident photons and electrons, the angular resolution of the Calorimeter is equal or better than the granularity of the crystals. The angular and energy resolution will be discussed in more details in Section 4.5.2.

2.3.3 Forward Detector

The Forward Detector of the WASA facility is designed to detect ejectiles in the polar angular range of 3 to 18 degree. It consists of a set of plastic scintillator detectors providing energy information and a straw tube tracker used for the

precise measurement of angles. The fast signals of the plastic scintillators are used on the trigger level, exploiting both energy and angular information.

2.3.3.1   Forward Window Counter

The first subdetector of the Forward Detector in beam direction is the Forward Window Counter (FWC). It is located directly in front of the paraboloidal stainless steel window of the scattering chamber. The two layers of the detector are made from 3 mm thick BC408 plastic scintillator material. Each layer is divided into 24 elements individually read out by XP3112 photomultiplier tubes. The first layer is inclined by 80 degree with respect to the beam axis, to be as close to the exit window as possible. The second layer is perpendicular to the beam axis, mounted in front of the supporting steel cross of the window, as shown in Fig. 2.12. The layers are shifted by half an element with respect to each other, resulting in an effective granularity of 48 elements.

The Window Counter is essential for trigger decisions. Coincident hits at the same azimuthal angle in the subsequent detectors are used to suppress events which are not originating from the interaction region. Due to the relatively high energy loss in the Window Counter compared to protons and pions, ^{3}He can be distinguished effectively on the trigger level. Fig. 2.18 shows two correlation plots of the energy deposits in the first layer of the Range Hodoscope (see Section 2.3.3.4) and the first layer of the Trigger Hodoscope (see Section 2.3.3.3). For both plots, the same data sample, taken with a low bias trigger during the beam time in September 2009, was analyzed. The low bias trigger demands at least one hit in the first layer of the Range Hodoscope. In the left panel, a coincidence with the trigger on a low energy hit in the Window Counter is demanded in the analysis. The right panel shows the correlation when there is a coincidence with a high energy hit in the Window Counter. The thresholds of the trigger conditions correspond to 0.1 MeV and 3.1 MeV, respectively. As can be seen, protons and deuterons are predominant when triggering with the low threshold. Their contribution is suppressed by more than two orders of magnitude for the high threshold.
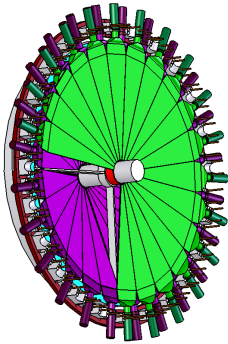
Figure 2.12: Forward Window Counter, a quarter of the second layer (green) is removed to show the structure.
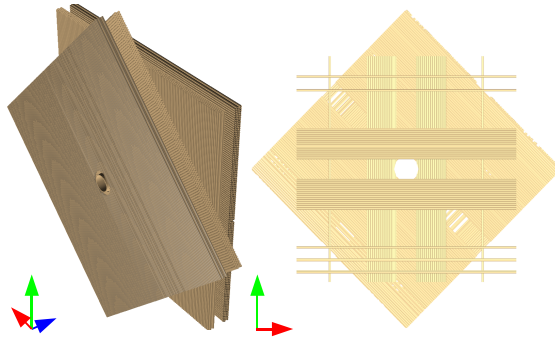
Figure 2.13: 3D view (left) and upstream view (right) of the Forward Proportional Chamber. Here, straws are removed to show the structure.
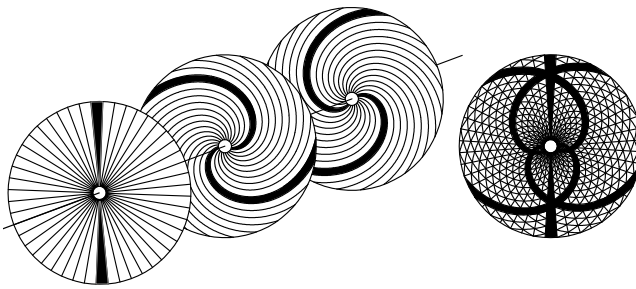
Figure 2.14: The three layers of the Forward Trigger Hodoscope hit by two particles (left). The intersection of the elements defines pixels as indicated in the projection of the planes (right).
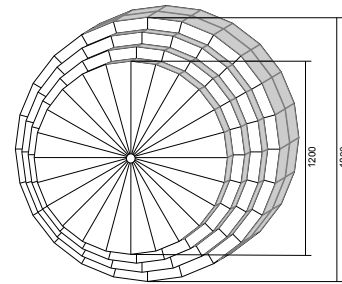
Figure 2.15: Forward Range Hodoscope, dimensions are given in mm.
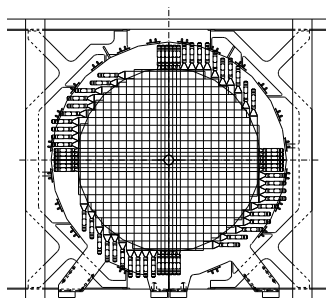
Figure 2.16: Forward Range Intermediate hodoscope.
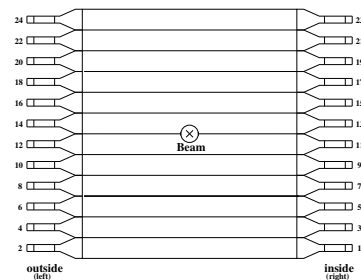
Figure 2.17: Forward Veto Hodoscope
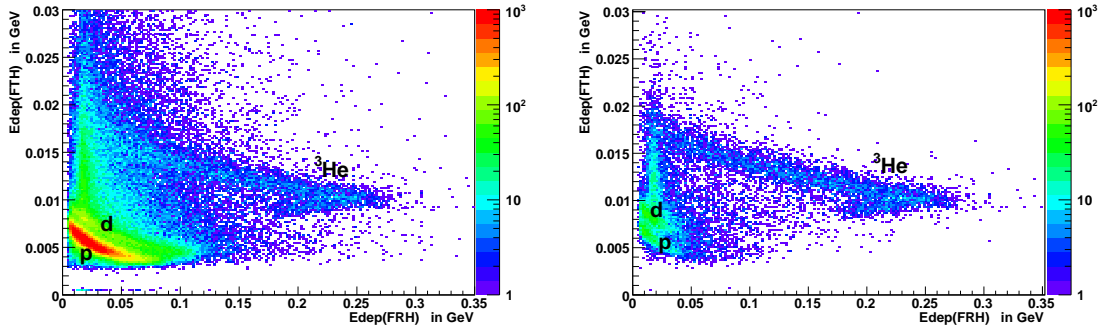
Figure 2.18: The correlation plots of the energy deposits in the Forward Trigger Hodoscope and the Forward Range Hodoscope illustrate the selection of ^{3}He on the trigger level. A trigger condition, which demands a high energy deposit ($> 3.1\ MeV$) in the Forward Window Counter (right) reduces the contributions of protons and deuterons in the data by more than two orders of magnitude. For comparison, the correlation is shown with the standard threshold of 0.1 MeV (left). The data analyzed here, were taken during the beam time in September 2009, in which η mesons were produced in the reaction $pd \rightarrow {}^3$He η. In this beam time an additional threshold on the energy deposits in the Trigger Hodoscope of 3 MeV was used.

2.3.3.2   Forward Proportional Chamber

The Forward Proportional Chamber (FPC) is a straw tube tracker, used to determine scattering angles with high precision in the offline analysis. The straw tubes are drift tubes of 8 mm diameter. Each tube is made from 26 μm thick aluminized Mylar and a sensing wire of 20 μm stainless steel stretched with a tension of 40 g. The drift gas is a mixture of argon and ethane in the proportion 80% Ar / 20% C_2H_6.

The detector is divided into four independent modules. Each module is assembled from four layers of 122 straw tubes. The layers are shifted by one tube radius with respect to each other. This results in a hexagonally closed packing structure. In the left panel of Fig. 2.13 the orientation of the four modules is illustrated. The first and second module in beam direction are rotated by +45 and −45 degrees respectively with respect to the X-axis. The third and fourth module are aligned along the X and Y axis. The orientation of the individual straw tubes is shown explicitly in the right panel of Fig. 2.13. Here, an upstream view through the FPC is given. The modules are shown with a reduced number of tubes to illustrate the

structure.

2.3.3.3 Forward Trigger Hodoscope

The Forward Trigger Hodoscope (FTH) is made from 3 layers of 5 mm thin BC408 plastic scintillators. The first layer is divided into 48 sectors. The second and third layer are divided into 24 elements shaped as Archemedian spirals. The direction of rotation of the elements is clockwise in the second layer and counterclockwise in the third layer. The elements of the three layers are read out individually by EMI/THORN 9954B photomultiplier tubes.

As shown in Fig. 2.14, the special geometry results in a pixel structure of the detector, where each pixel is formed by a unique combination of elements. The Trigger Hodoscope provides the hit multiplicity as well as azimuthal and polar angles on the trigger level.

Prior to the installation at the COSY ring as well as in the operation during the detector commissioning it was confirmed that the scintillators of the Forward Trigger Hodoscope suffered from severe aging effects [Red06, Pau07]. This resulted in detection inefficiencies. Thus, in 2008 the scintillators have been replaced.

Before and after the replacement the detection efficiency of the scintillators was studied. The analysis was performed using elastically scattered protons selected from data taken in the production runs of April 2007 and November 2008. In these beam times η mesons were produced in proton-proton collisions. The data samples used for the efficiency studies were picked up by a low bias trigger which is used for monitoring purposes. It does not involve any information of the Trigger Hodoscope. The trajectories of the protons have been identified in the Forward Detector by demanding hits in all consecutive layers of the Window Counter and the Range Hodoscope (see Section 2.3.3.4) at the same azimuthal angle. The angular information given by the granularity of the Window Counter and the Range Hodoscope, respectively, has been refined using the Forward Proportional Chamber. From the identified crossing point of the tubes in the different modules azimuthal as well as polar angles were determined. The coordinates extracted from the straw tube tracker allowed to calculate the number of the element in each layer of the Trigger Hodoscope which must have been hit by the reconstructed proton. The ratio of reconstructed tracks with a hit in the Trigger Hodoscope to

the total number of reconstructed tracks is taken as measure for the detection efficiency.

In Fig. 2.19 the results of the analysis are shown. For each layer of scintillators the efficiency is presented as a function of the track coordinates. The histograms in polar coordinates provide an upstream view on each detector layer.

In all six histograms identical regions of apparently low efficiency are visible. Besides the hole for the beam pipe in the center and the outer edge of the detector this results also from the support structure of the window of the scattering chamber. The steel cross along the X and Y-axis stops or deflects particles. In the three plots illustrating the status of April 2007 additional lines of low efficiency divide the area into 12 azimuthal bins. This structure originates from gaps between the elements of the old Window Counter which was still in use at that time. It consisted only of one layer with twelve elements and was replaced in the summer of 2007.

The detection efficiency in the first layer of the Trigger Hodoscope is almost uniform. On average it is 98% in April 2007 as well as in November 2008. Only in small, well defined regions does the efficiency drop to values of about 90%. These regions show up as straight, radial lines with equal azimuthal distances. This loss of efficiency is caused by gaps between the individual elements. In order to have space for wrapping material the scintillators were machined 200 μm smaller on each side. The average efficiency could be slightly improved by a very careful mechanical readjustment of the individual elements.

In the second and third layer the detection efficiency was less homogeneous in April 2007. From Fig. 2.19 it is easily seen that in three elements of the second layer the detection efficiency dropped down to approximately 80%. The loss is not uniform along the element. It increases with increasing distance to the photomultiplier tubes. In both, the second and the third layer the efficiency is smallest in the area close to the beam tube. This indicates that the detection efficiency depends on the light collection efficiency which was shown to have deteriorated by aging effects of the material [Red06]. From the status of November 2008 as shown in Fig. 2.19 it is visible that after the renewal the efficiency of both layers is almost homogeneous. The average detection efficiency is increased to approximately 98%. Regions of lower efficiency are restricted to gaps between the individual elements.

First Layer, April 2007   First Layer, November 2008

Second Layer, April 2007   Second Layer, November 2008

Third Layer, April 2007   Third Layer, November 2008
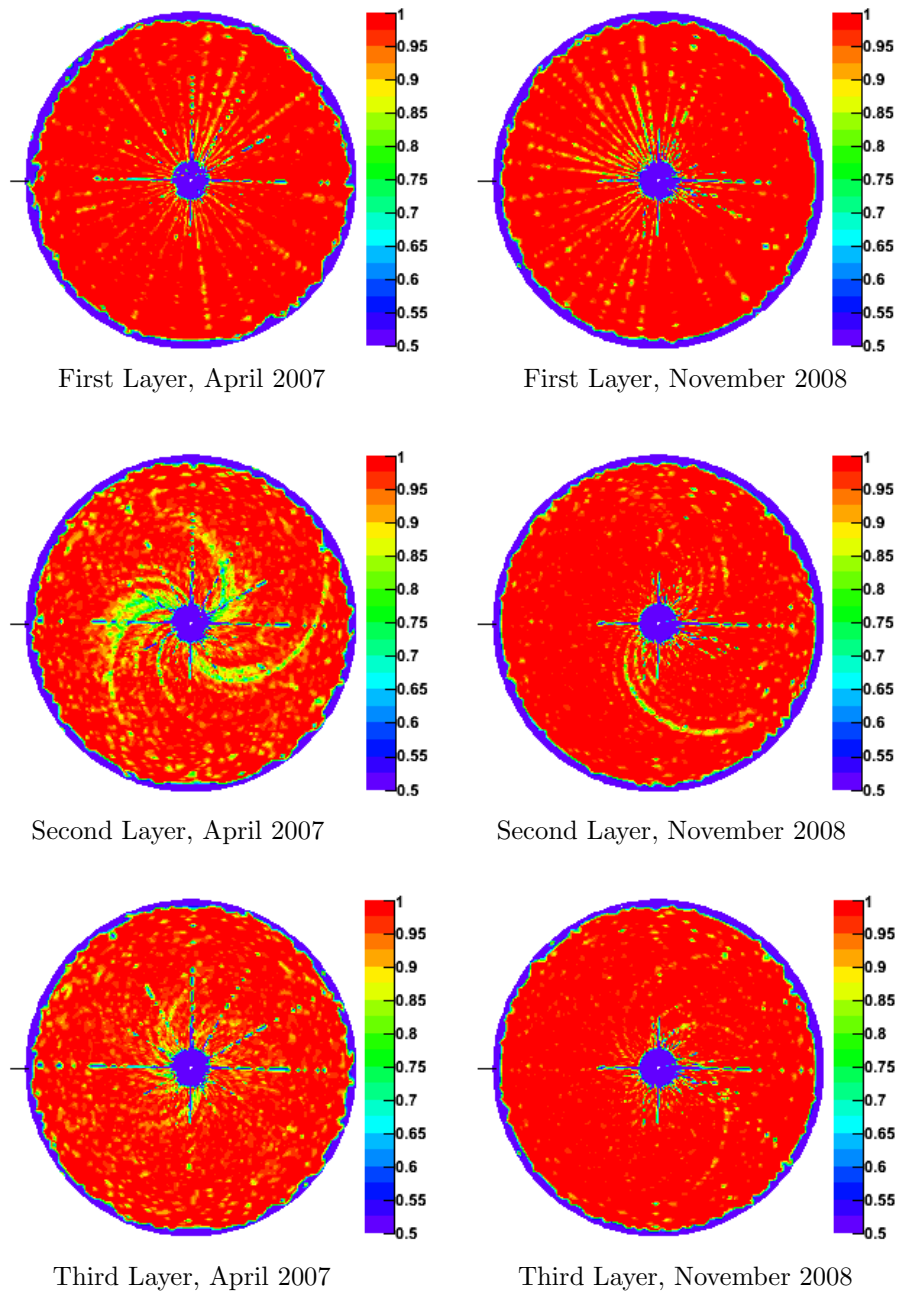
Figure 2.19: Comparison of the Trigger Hodoscope efficiency before and after the renewal. The efficiency of each detector layer is presented in a polar plot, showing an upstream view of the layer.

In addition to the detection efficiency also the light collection efficiency was studied. Since the protons reconstructed in the analysis are close to minimum ionizing, their energy loss in the detector is constant. The amount of scintillation light should be the same independent of the track coordinates. Thus, the protons form a good tool to study the light collection efficiency. The dependence of the light output on the scattering angle is taken as a measure for the uniformity.
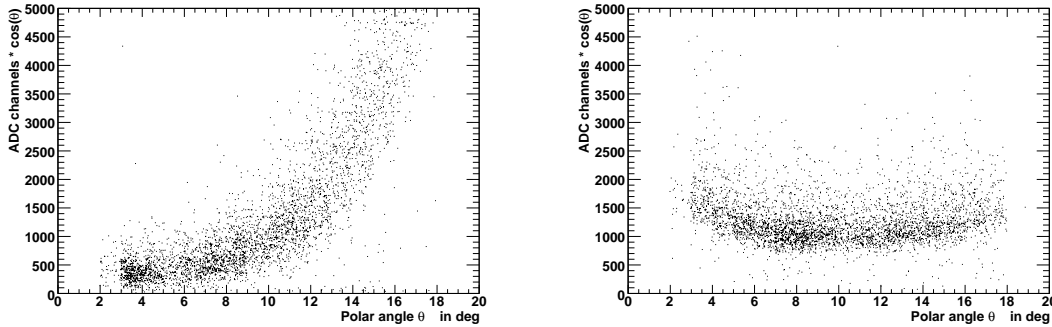
Figure 2.20: The light output of the old elements of the Trigger Hodoscope showed a strong position dependence due to aging effects (left). After the renewal of the scintillators, the uniformity of the light output is improved and only depending on the geometry of the detector elements (right). Here, element 11 in the second plane of the Trigger Hodoscope has been analyzed.

In Fig. 2.20 the light output for one element in the second layer of the Trigger Hodoscope is shown as a function of the scattering angle. The left panel shows a strong position dependence of the signals obtained from the production run in April 2007. While the light output is large at large scattering angles, i.e. close to the photomultiplier tubes, it is very small for hits close to the beam pipe. Here, the signals are even close to the threshold of the discriminators. This leads to a decrease in the detection efficiency caused by signals below the threshold. The right panel shows the same distribution obtained with the replaced scintillator in November 2008. A position dependence of the light output is visible, but it is small. An obvious difference between the two measurements is the light output from signals at low angles. In the previous case it is flat and close to threshold. In the renewed element it rises significantly almost up to the level of the light output at large angles. This behavior is expected due to the shape of the elements which has a focussing effect. In the old elements the effect was masked by the increased attenuation of the material due to aging effects.

The renewal of the Forward Trigger Hodoscope brought an essential improvement for the detection efficiency and the light collection efficiency of the detector. This does not only increase the selectivity of trigger conditions involving the signals of the Trigger Hodoscope but also improves the energy reconstruction and particle identification in the Forward Detector.

2.3.3.4 Forward Range Hodoscope

The Forward Range Hodoscope (FRH) is the essential component for the reconstruction of kinetic energies of particles ejected into the Forward Detector. It consists of 5 layers made from plastic scintillator BC400. The first three layers have a thickness of 110 mm, whereas the last two have a thickness of 150 mm. Each of the layers is assembled from 24 elements, read out individually by XP2412 photomultiplier tubes. The Range Hodoscope is illustrated in Fig. 2.15.

For stopped particles an energy resolution of approximately 3% can be achieved. Tab. 2.2 summarizes the stopping power of the Range Hodoscope for different particle species. For higher incident energies the resolution worsens, which will be discussed in more detail in Section 4.5.2.

Apart from the energy reconstruction, the Range Hodoscope is crucial for the identification of particles and it delivers fast signals for the first level trigger.

Particle	Stopping Power
π	200 MeV
p	360 MeV
d	450 MeV
^3He	1000 MeV
^4He	1100 MeV

Table 2.2: Stopping power of the FRH for different particles.

2.3.3.5 Forward Range Intermediate hodoscope

The Forward Range Intermediate hodoscope (FRI) is a two-layered scintillator hodoscope. It is installed between the second and third layer of the Range Hodoscope. Each of its layers is made from 32 rectangular elements. Following a

cartesian geometry, the elements of the first layer are aligned horizontally and those of the second layer vertically. This allows for an additional position sensitivity within the Range Hodoscope. To compensate for high count rates close to the beam pipe, the elements close to it have only half the width compared to those at larger distances. Fig. 2.16 shows a schematic view of the detector. More detailed information about the design and performance of this hodoscope can be found in [Pau06].

2.3.3.6   Forward Veto Hodoscope

The very last active element of the forward detector is the Forward Veto Hodoscope (FVH). It is made from twelve horizontally aligned bars of plastic scintillator. Each bar is 2 cm thick and 13.7 cm wide and read out from both sides via XP2020 photomultiplier tubes. A drawing of the detector is shown in Fig. 2.17. The purpose of the Veto Hodoscope is the detection of particles punching through the Range Hodoscope and, if used, the absorber (see Section 2.3.3.7). Depending on the reaction, the signals from the Veto Hodoscope can be used as a veto, enhancing the selectivity of the trigger.

In the fall of 2008 a second layer has been installed. It is located further downstream in front of the first COSY quadrupole after the WASA setup. It is planned to be used as a stop detector for Time-Of-Flight measurements. This will improve the energy resolution of the Forward Detector for high-energy particles [Zie08].

2.3.3.7   Forward Range Absorber

The Forward Range Absorber is a passive absorber of variable thickness. It is made from 5 mm thick iron plates that can be stacked up to a total thickness of 10 cm. The absorber is located between the Range Hodoscope and the Veto Hodoscope and mounted on a rail system to be moved in or out. Slower protons originating from the production of η mesons are stopped in the iron, while faster protons can punch through. Their signal in the Veto Hodoscope can be used as a veto signal to enhance the trigger efficiency. The absorber was originally designed considering η production in pp collisions at 1360 MeV beam energy, therefore it covers only the polar angles up to 13 degrees.

2.3.4   The Light Pulser Monitoring System

A light pulser system is used in order to monitor the stability of the gain of the photomultiplier tubes. Deviations of the detector response to the light pulses are attributed to changes in the gain. Two different light pulse generators are used for organic and inorganic scintillators. The pulses for the crystals in the electromagnetic calorimeter are generated by a xenon Flash Tube. For the plastic scintillator detectors three LED based light pulse sources are used. From the pulse generators the signals are transmitted via a network of optical fibers to the photomultiplier tubes. The stability of the light pulser signals is monitored directly via photodiodes. They serve as reference signals to which the detector response to the light pulse is normalized. This information is used in the offline analysis to correct for changes in the gain. A more detailed description of the light pulser monitoring system can be found in [ZR09].

2.4   Data Acquisition System

The upgraded data acquisition system of the WASA facility is based on the third generation of DAQ systems used in experiments at COSY [K$^+$06b] and has been designed to cope with the desired luminosities [H$^+$08]. The signal readout has been optimized and is hardware based by using FPGAs for event and buffer management. The digitizing modules work in a self-triggering mode, storing the data in buffers. The data acquisition system runs in common stop mode, which means that the trigger is coming after the data have been digitized. The buffer size in the digitizing modules is sufficient to bridge the trigger delay. Synchronization and readout follows the EMS framework [Z$^+$94]. The structure of the data acquisition system is illustrated in Fig. 2.21.

The design goal of the data acquisition system, a readout and conversion time of $\approx 20 \mu s$, has been reached [Wol08]. The event size and the writing speed of the hard disks of $\approx 80\ MB/s$ are the limiting factors. At a typical event size of $8\ kB$, event rates of $10\ kHz$ are managed at a life time of 80% of the system.
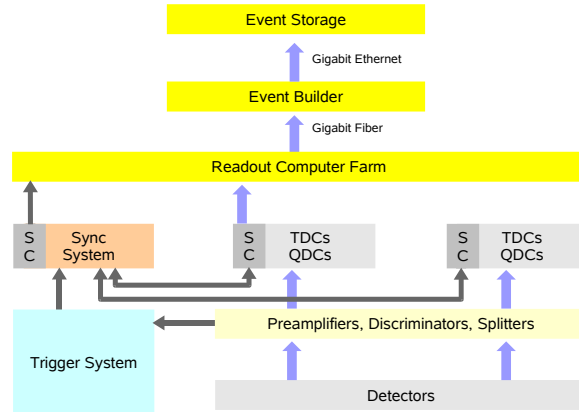
Figure 2.21: Schematic overview of the data acquisition system.

2.4.1   Signal Readout

The analog signals of the plastic scintillator detectors are split into two signal branches using passive splitters. One branch delivers the signals to Charge-to-Digital-Converters (QDC). In the other branch the signals are inputs to leading edge discriminators. The logic signals are used in the trigger system, described in Section 2.5. Additionally, the signals are recorded by Time-to-Digital-Converters (TDC).

The analog signals of the crystals in the calorimeter are split into two branches using active splitter boxes. One branch is input to QDCs. In the other branch analog sums are formed from groups of signals corresponding to 4×3 crystals in the forward part, 4×4 crystals in the central part, and 3×3 crystals in the backward part of the calorimeter. Dual threshold discriminators evaluate the sums, producing logic signals which are provided to the trigger system.

Front-end electronic modules based on the CMP16 ASIC [CMP] are used to amplify and discriminate the signals of both straw tube trackers. The signal processing is done close to the detectors to be less sensitive to noise induced from external electromagnetic fields. The output of the discriminator is transferred in LVDS to the TDCs.

2.4.2 Digitization

The Charge-to-Digital Converter (QDC) modules have 16 input channels each. The analog input signals of each channel are continuously sampled by Flash-ADCs. The evaluation of the digitized signals is done by FPGAs. In addition to charge integration, double pulse detection, time stamping by zero crossing detection, and pedestal subtraction is performed. For debugging purposes signal amplitude and baseline information can be obtained [H+08].

Due to the different shape of the fast signals of plastic scintillators and the comparably slow signals of the $CsI(Na)$-crystals in the calorimeter, two different types of QDCs are used:

SlowQDC with a sampling rate of 80 MHz for the signals of the calorimeter

FastQDC with a sampling rate of 160 MHz for the plastic scintillator detectors

The timing of the QDCs is sufficiently precise for the signals of the calorimeter. For the faster signals of the plastic scintillators TDCs are used for higher timing resolution. The readout of the straw chambers only utilizes TDCs. The different timing properties of the detectors demand the use of two different types of TDCs. Both modules provide 64 input channels each.

FastTDC are used for the timing of the signals from plastic scintillators. The modules are based on the GPX ASIC [TDC06, K+06a] with ECL input signals.

SlowTDC are used for the straw chambers. The modules are based on the F1 ASIC [TDC01] with LVDS input signals. The LVDS lines are also used to set the thresholds on the CMP16 boards.

The four different modules are equipped with FIFO buffers. The digitized information is marked with time stamps and stored in the buffer until a valid trigger is issued. The buffer size of 2 μs is sufficiently large to bridge trigger delays.

2.4.3 Synchronization

The individual digitization modules are grouped in 14 crates. Each crate is equipped with an optimized LVDS system bus [H+08]. It is used to manage the

crate wide module readout and synchronization via a system controller. The controller is also responsible for the communication of the crate with the DAQ and the data transfer to the readout computer farm.

A dedicated synchronization system [W$^+$05] was developed to control and synchronize the data flow. When the trigger system issues a trigger, the synchronization system generates an event number with a time stamp, which is distributed to all crates to start the readout of the digitizing modules. New triggers are blocked by the synchronization system as long as the modules are busy.

All crates are connected to a computerfarm via optical links. An event builder manages the readout of the individual data streams and writes them to a disc array. The data streams are stored in a cluster format, in which the packages sent by the crates are unsorted. Only a part of the data is sorted according to the event numbers and used for online monitoring. The decoding of the cluster format into events is part of the offline analysis software (see Section 3.1).

2.5   Trigger System

At the design luminosities of the WASA detector of $10^{32} cm^{-2} s^{-1}$ the data acquisition system has to cope with event rates on the order of 5 MHz. Thus, a selective trigger system is needed to reduce the initial amount of events by selecting only final states of interest. Fig. 2.22 gives a schematic overview of the trigger system used in the data acquisition system of the WASA detector.

The trigger decisions are based on multiplicities, coincidences, and track alignment in the plastic scintillator detectors as well as cluster multiplicities and energy sums in the electromagnetic calorimeter.

The signals of the plastic scintillator detectors are inputs to multiplicity units. Here, hits in adjacent elements stemming from the same particle are combined into clusters to calculate the cluster multiplicity per detector plane. A coincidence time window in the order of 20 ns is used to match neighboring hits into clusters. The multiplicity signals form a set of primary trigger conditions.

A more complex condition is referred to as Matching Trigger, in abbreviation *fhdwr*. The hit information in both layers of the Window Counter and in the first layers of Trigger and Range Hodoscope is tested for alignment. Hits in consecutive
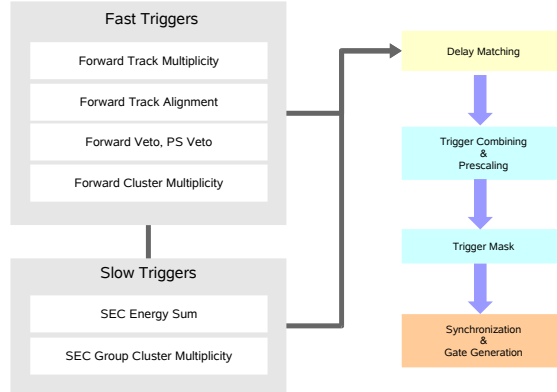
Figure 2.22: Schematic overview of the trigger system.

detector layers at the same azimuthal angle are considered as particle trajectories. The trigger signal is issued by a validated hit in the first layer of the Trigger Hodoscope. A hit is validated if it was found in coincidence with hits in one of the two layers of the Window Counter and a hit in the first layer of the Range Hodoscope at the same azimuthal angle. The efficiency of this trigger condition has been evaluated relative to a low bias trigger. Depending on the track multiplicities and the thresholds on the energy deposits in the Window Counter (see Section 2.3.3.1), the efficiency varies between $(98.7 \pm 0.6)\%$ and $(79.2 \pm 0.5)\%$ [Zhe09].

The information of the electromagnetic calorimeter is taken into account in terms of cluster multiplicity and energy sums. The analog signals are summed in groups of 9 to 16 crystals, as described in Section 2.4.1, dividing the calorimeter into hardware clusters. The summed signals are evaluated by a dual threshold discriminator giving logic signals for low and high energy deposits. Coincident hits in the elements of the Plastic Scintillator Barrel, validated by timing and the geometrical overlap with the crystals, are used to discriminate charged hits from neutral hits. Finally, the cluster multiplicity is established by calculating the number of charged or neutral groups with low and high energy deposits, respectively. The analog sums of individual groups of crystals can be further summed to evaluate the total energy deposit in the electromagnetic calorimeter or its subsections, e.g. left and right halves.

The individual delays of the primary triggers are matched in a programmable delay unit. In order to form more complex trigger conditions the primary signals are combined in coincidence matrices. Up to 32 different coincidence conditions can be included in the data stream. To balance the individual trigger rates the signals pass programmable scaling units. The scaler readout is added to the data stream. High rate triggers can optionally be prescaled to be included in the data stream for monitoring purposes. Finally, the triggers that are allowed to start the readout are selected via a mask and OR units.

The signals of the trigger logic are registered by a FastTDC. The information can be used in the offline analysis to study trigger efficiencies and to identify the trigger that initially started the acquisition.

2.6   Production of η mesons

At the WASA facility at COSY η mesons are produced in proton-proton or proton-deuteron collisions. Both methods of production provide different advantages, while being complemetary in the investigations of the different decay modes of the η meson.

The production in proton-proton interactions is done at a beam energy of $T_{Beam} = 1400\ MeV$ [A$^+$04, Vla08, A$^+$09]. This corresponds to an excess energy of $Q = 60\ MeV$, where the production cross section is $9.8 \pm 1\ \mu b$ [C$^+$94]. The large cross section and the good geometric acceptance of the detector allow to study even rare processes like the decay mode $\eta \rightarrow e^+e^-$ with a branching ratio $< 2.7 \cdot 10^{-5}$. However, a large background contribution originates from multi-pion production. While the cross section for three-pion production at a beam energy of $T_{Beam} = 1400\ MeV$ is at the same order of magnitude as the cross section for η production [P$^+$07], the cross section for two-pion production is higher by a factor 20 for neutral pions and by a factor 100 for charged pions [S$^+$09]. The total count rate in proton-proton interactions demands selective triggers. An appropriate reduction of the event rates is only possible by restrictions put on the decay system of produced mesons. Decay modes with a distinctive signature are suited best for an investigation in this way, like the decay modes $\eta \rightarrow \pi^0\pi^0\pi^0$, $\eta \rightarrow \pi^+\pi^-e^+e^-$, $\eta \rightarrow\ e^+e^-e^+e^-$, and $\eta \rightarrow\ e^+e^-$.

The background from multi-pion production turns out to be problematic in the

investigation of several decay modes of the η meson, like $\eta \to \pi^0 \gamma \gamma$ [Cha08] and $\eta \to \pi^+ \pi^- \gamma$ [Red09].

The production of η mesons in proton-deuteron collisions is done via the reaction $pd \to {}^3\text{He} \, \eta$ at a beam energy of 1000 MeV. The excess energy amounts to $Q = 60 \; MeV$. At this energy the production cross section for the η meson is $0.412 \pm 0.016 \; \mu b$ [B$^+$02]. This is approximately 25 times lower than the production cross section in proton-proton interactions at the same excess energy. The disadvantage of a lower cross section is compensated by several aspects.

Helium ions can easily be identified by their energy loss in the Forward Detector on the trigger level. With simple and well defined trigger conditions a clean sample of $pd \to {}^3\text{He}X$ can be achieved. The trigger does not introduce any bias to the decay system of produced mesons, since the conditions are based only on the Forward Detector. This allows for measurements of the absolute branching ratio of different decay modes.

Compared to proton-proton interactions, the reaction $pd \to {}^3\text{He} \, X$ yields less background stemming from multi-pion production. The cross section for two-pion production is in the same order of magnitude as the cross section for η production [B$^+$06]. In proton-proton interactions the ratio is worse by at least a factor 20.

Another advantage compared to the production in proton-proton interactions is the lower center-of-mass velocity. It results in an increased acceptance for the decay products of the η meson in the Central Detector. This is of special importance for studies of Dalitz plot distributions.

Due to these advantages the production of η mesons in the reaction $pd \to {}^3\text{He}\eta$ is attractive for studies of not-so-rare decay modes. Especially for investigations of the modes for which multi-pion production is the most severe background, like $\eta \to \pi^+ \pi^- \gamma$, the topic of this work.

Chapter 3

Event Reconstruction

The data analysis comprises a number of stages from the decoding of the digitized information to a high level analysis including the comparison with simulations and the interpretation. The flow chart in Fig. 3.1 gives an overview of the analysis chain used in this work. This chapter addresses the tools used for event recon-
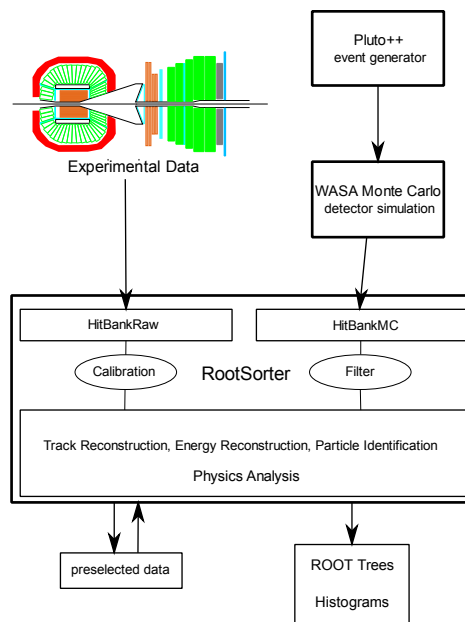
Figure 3.1: Flow chart of the analysis chain.

struction and simulation including a description of the reconstruction procedures, such as calibration, track finding, and particle identification.

3.1 Analysis Tools

3.1.1 RootSorter

Online as well as offline data analysis is performed within the RootSorter framework [HHM03]. The analysis environment is based on the ROOT data analysis framework [CER10] developed at CERN. The software is organized in a modular structure. Decoding, calibration of individual subdetectors, track and energy reconstruction are implemented in individual modules. High level analysis modules automatically load the necessary low level modules. In this way only the necessary parts of the software are used. New routines can be be added without changes in the existing code. A central data base provides individual decoding tables, geometry information and calibration constants for each run period. The parameter sets are selected by specifying either the date or the run number. User options allow to control further parameters of the analysis either by command line options or a configuration file.

Each analysis starts with the decoding of the detector information. Time and energy information from the individual detector elements is combined into hit objects which are stored in HitBanks. At this level, the handling of experimental data and data from a Monte Carlo simulation differs. Data from the experiment are stored in a RawHitBank to be calibrated. Monte Carlo data are stored into a MCHitBank. Instead of a calibration, the data is processed by filters which are steered to match the resolution of the Monte Carlo simulation to the actual resolution obtained from the experiment by applying smearing factors. This step is necessary, since the tools have not been aiming at simulating the physical resolution of the detectors (see Section 3.1.3). After calibration or filtering, data from experiment and simulation are handeled identically.

RootSorter provides prefabricated analyses which are designed for low level monitoring, e.g. during data taking. Specialized high level analyses for a dedicated physics case are designed by the user. A running analysis can be monitored from a standard ROOT session. Due to the server-client structure monitoring can be done remotely.

The analysis presented in this work is based on RootSorter Rev. 3122 compiled with ROOT v5.18.

3.1.2   Pluto++

Pluto++ is an event generator for hadronic interactions [F$^+$07]. It was originally designed for the HADES experiment [SBB$^+$95] and is entirely based on ROOT [CER10]. The generation of the homogeneous and isotropic phase space is based on the GENBOD [Jam68] routines. The implemented physics aspects include resonance production with mass-dependent Breit-Wigner sampling. The calculation of partial and total widths for resonances producing unstable particles is performed recursively in a coupled-channel approach. For elementary reactions, angular distribution models for selected channels have been included, based on the parametrization of existing data. Among these are the following aspects of the decay modes of the η meson:

For the decay mode $\eta \to \pi^+\pi^-\pi^0$ a matrix element has been implemented based on the parametrization of the Dalitz plot distributions measured by the Crystal Barrel collaboration [A$^+$95]. The decay mode $\eta \to \pi^+\pi^-\gamma$ is implemented with the simplest gauge invariant matrix element including p-wave interactions of the pions according to $|M^2| \sim k^2 q^2 sin^2\theta$. Here, k denotes the photon momentum in the rest frame of the η meson. q and θ are defined as the momentum of either pion and the angle between π^+ and γ, both in the rest frame of the two pions. To generate the Dalitz decay $\eta \to e^+e^-\gamma$ a form factor is implemented to describe the mass dependence of the decay width.

A flexible user interface allows to include further angular distributions, correlations, and branching ratios. Furthermore it is possible to include detector effects such as acceptance and efficiency by filters. In the context of this work the software version v5.32 has been used.

3.1.3   WASA Monte Carlo

The WASA Monte Carlo software is based on the GEANT3 package [CER93], developed at CERN. Detector elements and support structures are described in terms of geometrical volumes filled with appropriate materials. The magnetic field of the solenoid is included via a field map. Parameter files allow to control the simulation and to adjust it according to the experimental situation.

The simulation of an event starts with a set of four-momentum-vectors, provided by an external event generator. It is also possible to use the internal gener-

ator to study the response of the detector system for single particle tracks. Each particle is propagated, simulating its interaction with either passive or active materials by taking into account energy loss, quenching effects, multiple Coulomb scattering, hadronic interactions, decays and other processes implemented into GEANT with available cross sections. The WASA Monte Carlo software does not contain the simulation of processes like light propagation in the scintillators, response of photo multiplier tubes, electronic noise or electron drift behavior in the gas detectors. Agreement between the simulated and the actual detector response in the experiment is achieved via smearing, applied by adjustable input filters of the data analysis program.

In addition to detector responses from the tracking, the WASA Monte Carlo software provides the initial four momenta of the particles as well as vertex positions. This allows for systematic studies of the quality of reconstruction procedures and efficiency calculations.

3.2 Calibration

3.2.1 Electromagnetic Calorimeter

The calibration of the electromagnetic calorimeter is optimized for the reconstruction of photons. Initial calibration constants have been obtained by measurements of cosmics muons and radioactive sources before in-beam operation [Koc04, Jan06]. For each run period an updated set of constants is derived based on the measurement of the two-photon decay of neutral pions.

Events with exactly two neutral tracks in the Central Detector are selected (see Section 3.3.2). The neutral tracks are regarded as photons and the invariant mass is calculated according to

$$
\begin{aligned}
M_{\gamma_1 \gamma_2} &= \sqrt{(E_{\gamma_1} + E_{\gamma_2})^2 - (\vec{P}_{\gamma_1} + \vec{P}_{\gamma_2})^2} \\
&= \sqrt{2k_1 k_2 E_{\gamma_1} E_{\gamma_2}(1 - cos\theta_{1,2})},
\end{aligned}
\tag{3.1}
$$

where E_{γ_1} and E_{γ_2} are the measured energies of the photons based on the preliminary calibration constants, $\vec{P}_{\gamma_1}$ and $\vec{P}_2$ are their momentum vectors, $\theta_{1,2}$ is their opening angle and $k_{1,2}$ are the calibration correction factors. The invariant mass
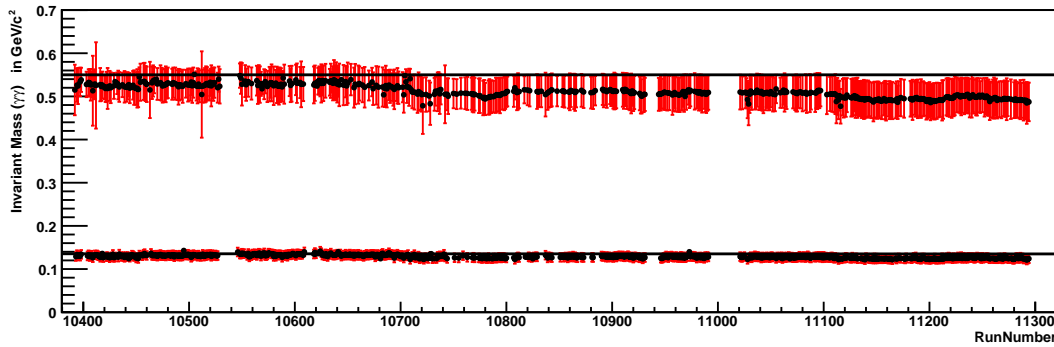
Figure 3.2: The absence of light pulser information results in a deviation of the reconstructed meson masses, which becomes worse due to gain drifts of the photomultiplier tubes. Here, the peak positions of π^0 and η mesons in the two-photon invariant mass of preselected data of the beam time in October 2008 is presented as a function of the run numbers of the beam time. The peak positions are extracted by a Gauß fit. The error bars indicate the width of the fitted distribution. The black lines show the actual meson masses.

is assigned to the central crystal of each cluster. It is assumed that the influence of the neighboring crystals averages out.

From the deviation of the invariant mass of the two photons to the mass of π^0, for each crystal of the calorimeter the calibration correction factor can be iteratively obtained according to

$$k = \frac{M_{\pi^0}^2}{M_{\gamma\gamma}^2}. \tag{3.2}$$

The calibration method implicitly corrects for shower losses and border effects.

The reference signals of the Light Pulser System (see Section 2.3.4) are used to correct for gain drifts during long production runs. In Fig. 3.2, the necessity of the light pulser corrections is illustrated with the peak positions of π^0 and η mesons in the two-photon invariant mass distribution. Here, data of the production run in October 2008 (see Section 4.1) have been analyzed. In the preselection of the raw data, the light pulser information was omitted (see Section 4.2). As a result, the reconstructed invariant masses of both mesons are smaller by 5% in the beginning of the beam time and the deviation increases up to 15% at the end of the beam time. The black lines in Fig. 3.2 indicate the actual meson masses of $m_{\pi^0} = 134.978 \ MeV/c^2$ and $m_\eta = 547.8 \ MeV/c^2$ [A$^+$08].

In order to compensate for the deviation, a linear correction has been extracted for each run of the beam time. The correction factor describes the averaged ratio of the reconstructed and actual meson masses.

3.2.2 Plastic Scintillators

The calibration of the plastic scintillator detectors comprises the conversion of ADC and TDC channels into energy and time scales, respectively. Several effects have to be taken into account that cause deviations from a simple linear transformation. Among these are the light collection efficiency of the detectors, the dependence of the scintillation efficiency on the particle species, and possible non linear effects in the response behavior of the photomultiplier tubes.
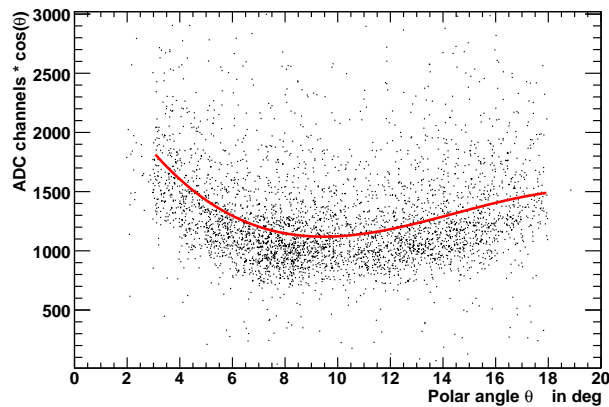
Figure 3.3: The light output of element 11 of the second layer of the Forward Trigger Hodoscope is parametrized as function of the scattering angle. The red curve shows the polynomial of third order which is used to describe the nonuniformity.

The uniformity of light collection efficiency depends on the geometrical shape of the detector elements. The light output of elastically scattered protons is used to parametrize the collection efficiency as a function of the scattering angle. The specific energy loss of the fast protons is fairly constant since they are close to minimum ionizing. Deviations from a constant light output of a detector element can be attributed to a non uniform collection efficiency. Fig. 3.3 shows the dependence of light output on the scattering angle for an element of the second

layer of the Trigger Hodoscope. The dependence is parametrized with a polynomial of third order, as shown with the red curve. It is used to correct for the nonuniformity of the light output of the element.

The conversion from ADC signals to deposited energy is achieved by comparison to Monte Carlo simulations. For every detector element the correlation of the light output corrected for nonuniformity with the light output of an element in the preceding layer is compared to the correlations of deposited energies in the corresponding elements in the simulation. From the bands in the correlation plot shown in the left panel of Fig. 3.4 five characteristic points can be defined. These points are:

Zero point (0)

Minimum ionizing point (1)

Punch-through point (3) , where the kinetic energy of the particle becomes larger than the stopping power of the current layer. Hence, the particle is punching through.

Equilibrium points (2),(4) , where the energy loss of particle punching through the current layer (2) is as large as the energy loss of a particle stopped in the current layer (4).

Maximum deposit point (5) in the current layer.

The one-dimensional projections of the correlation plots at these points are used to compare the measured light output to the deposited energy from simulations. As demonstrated in the right panel of Fig. 3.4, these points allow to determine the deviation of the conversion from light output to deposited energies from simple linearity. Nonlinearity can arise, for example, from non linear effects in the photomultiplier tubes and from quenching effects in the scintillator material. The latter can be described by Birk's formula [Leo94] and are taken into account in the simulations. It is therefore implicitly corrected by the comparison of measurement and simulation.
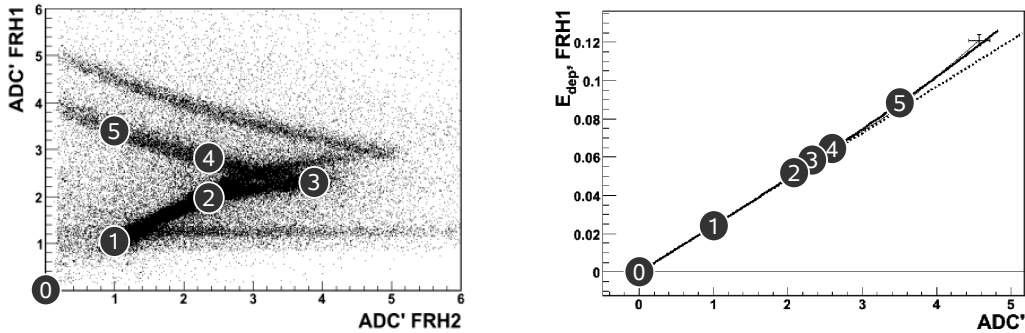
Figure 3.4: Nonlinearity corrections are obtained by comparing the correlation of the nonuniformity corrected light output of subsequent detector layers (left) at characteristic points (see text) to the correlation of the energy deposits from a Monte Carlo simulation (right). A fit to the points (solid curve) describes the calibration function. The dotted line indicates a linear correlation. The figures are taken from [Vla08].

3.2.3 Straw Tube Chambers

Straw Chambers, like the Mini Drift Chamber and the Forward Proportional Chamber achieve a high spatial resolution, because in addition to the known positions of the anode wires, the drift time of the electrons is measured. It is converted into drift distances. The drift distance is identified with the closest approach of a particle trajectory to the anode wire of a straw tube and, thus, is an important information in the track reconstruction. The conversion uses a Time-to-Distance relation which is a parametrization of the drift velocity. A general definition of the drift velocity can be given as

$$\vec{v} = \mu|\vec{E}|\frac{1}{1 + \omega^2\tau^2}(\hat{E} + \omega\tau(\hat{E} \times \hat{B}) + \omega^2\tau^2(\hat{E} \cdot \hat{B})\hat{B}), \qquad (3.3)$$

with $\hat{E}$ being the unit vector along the direction of the electric field in a straw due to the voltage at the anode wire and $\hat{B}$ the unit vector along the direction of the magnetic field, here, the solenoidal field in the Central Detector. μ is the electron mobility in the gas, ω is the cyclotron frequency and τ is the mean time between collisions of the drifting electrons [A+08]. The Time-to-Distance relation depends on the mixture of the drift gas, the voltages applied to the anode wires, and the magnetic field in which the chamber is situated. Whenever any of these parameters is changed, a new Time-to-Distance relation must be derived. In the data analysis this is part of the calibration of the straw tubes. The procedures

for the calibration of both of the straw tube trackers consist of two steps. At first the starting point T_0 of the drift time measurement has to be established.

In the determination of T_0 the time reference of the individual TDCs, the trigger time and its jitter is eliminated by using the relative time between a straw tube and the nearest plastic scintillator. In case of the central drift chamber the relative time to the Plastic Scintillator Barrel is taken into account. For the Forward Proportional Chamber the time difference with respect to the Trigger Hodoscope is used. Individual values of T_0 are then determined by fitting a Fermi function to the time spectra of each tube.

The extraction of a Time-to-Distance relation from the drift time spectra is based on the following assumptions.

- the tubes are 100% efficient

- the measured signals are due to particle tracks (no noise)

- the tubes are uniformly irradiated $\left(\frac{dn}{dr} = \frac{N_{total}}{R_{Tube}} = const \right)$

with N_{total} being the number of events registered, and R_{Tube} being the distance between the sense wire and tube wall, i.e. the maximum drift distance.

Using these assumptions, the drift velocity can be written as

$$v(t) = \frac{dr}{dt} = \frac{dn}{dt}\frac{dr}{dn} = \frac{R_{Tube}}{N_{total}}\frac{dn}{dt}. \tag{3.4}$$

Integration of this formula yields the Time-to-Distance relation:

$$D(t) = R_{Tube} \cdot \frac{\int_{T_0}^{t} n(t)dt}{\int_{T_0}^{T_{max}} n(t)dt} \tag{3.5}$$

with $N_{total} = \int_{T_0}^{T_{max}} n(t)dt$ and T_{max} being the largest drift time.

Fig. 3.5 shows a measured drift time spectrum and the derived Time-to-Distance relation. The relation is linear apart from the regions close to the wire and close to the wall of the drift tube. The linearity of the relation is a feature of the drift gas mixture ($80\%Ar \,/\, 20\%C_2H_6$) in the straw tubes. The Time-to-Distance relation is used to convert measured drift times into drift distances, which are essential for the track reconstruction (See Section 3.3.2).
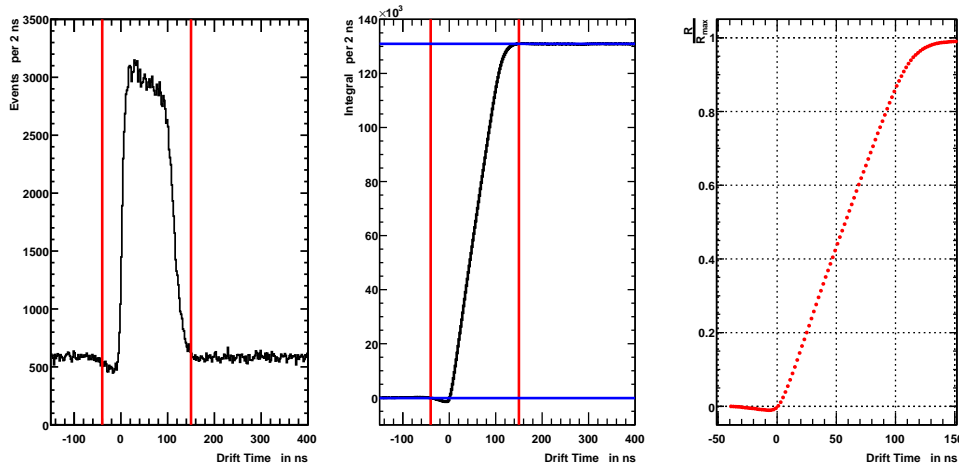
Figure 3.5: To derive the Time-to-Distance relation, the drift time spectrum (left), here, the average drift time of layer 13 in the Mini Drift Chamber, is integrated after the subtraction of a flat background. The red lines indicate the range of integration. In the central panel, the integrated drift time distribution is shown. After identifying the maximum drift range (blue lines), the distribution is parametrized and used as Time-to-Distance relation. The linearity of the relation is a feature of the drift gas mixture ($80\%Ar\,/\,20\%C_2H_6$).

3.3 Track Reconstruction

The reconstruction of particle trajectories is a basic step in the data analysis to obtain four-momentum vectors. Hits in individual subdetector elements originating from the same particle are combined to clusters. The clusters in the different subdetectors are merged into tracks. The methods used for cluster and track finding differ depending on the subdetectors. In the following sections the algorithms relevant for this work will be described.

3.3.1 Forward Detector

The track assignment in the Forward Detector begins with the formation of clusters from hits in adjacent elements of each subdetector layer. Here, only time coincident hits are assigned to a cluster, in order to ensure that the hits belong to the same particle. Angular and timing information of a cluster are calculated

as the average of the hit information contributing to it. The energy information is the sum of the energies deposited in the individual hits.

The reconstruction of charged tracks is based on the pixels of the Forward Trigger Hodoscope. Due to its special geometry (see Section 2.3.3.3) all pixels are formed by a unique combination of elements. In this way, the clusters in the three layers are checked for overlap. The average time of the hits contributing to a pixel is used as time of the track. The position of the pixel defines the coordinates of the track, assuming its origin in the origin of the WASA coordinate system (see Section 2.3.1), the beam-target interaction point.

(a) Azimuthal angle   (b) Polar angle
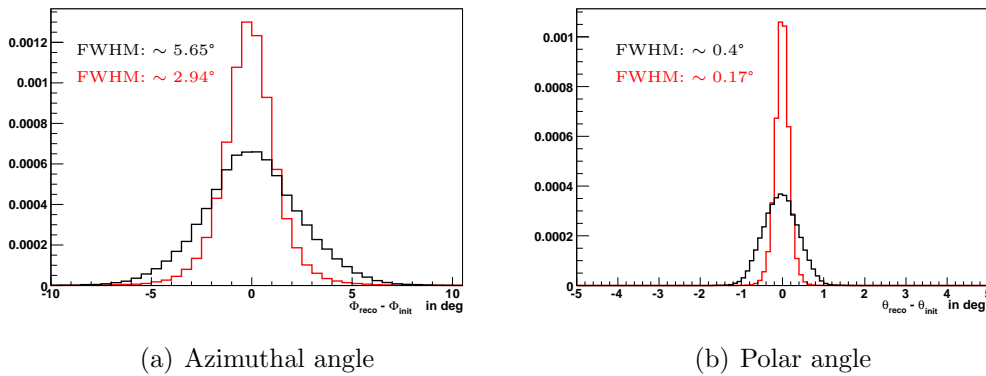
Figure 3.6: Comparison of the angular resolution achievable in the Forward Detector by using only the Trigger Hodoscope (black) or in addition the Forward Proportional Chamber (red) for track reconstruction. The resolution in azimuthal (a) as well as polar (b) angles is improved by approximately a factor 2 utilizing the Forward Proportional Chamber. Here, a Monte Carlo simulation of the reaction $pd \rightarrow {}^{3}\text{He}\ \eta(\eta \rightarrow \pi^{+}\pi^{-}\gamma)$ was used to compare the initial and reconstructed coordinates of the helium ion.

The angular information from the Trigger Hodoscope is refined using the Forward Proportional Chamber. Here, only the position of the sensing wires is taken into account. In each detector module the tube is selected which is closest to the coordinates given by the Trigger Hodoscope. The crossing point of all wires is used to calculate the new track coordinates. The angular resolution is demonstrated in Fig. 3.6 by comparing the initial four-momentum coordinates given by the event generator with the reconstructed coordinates after a full Monte Carlo simulation. Due to the higher granularity of the Forward Proportional Chamber

already with this procedure, called binary mode, an improvement by a factor 2 is visible. Including the drift distance information is expected to further improve the resolution. This is currently under evaluation [Hej09].

Finally, the cluster information of Window Counter, Range Hodoscope, and Veto Hodoscope is added to the tracks, depending on azimuthal overlap, time difference and a minimum amount of deposited energy. The information of the Forward Range Intermediate hodoscope has not been included in the track finding.

In the algorithm, it is assumed that charged particles are registered in the Trigger Hodoscope. Clusters in subsequent detector layers that are not overlapping with such pixels are merged into neutral tracks. For the present work, the reconstruction of neutral particles in the Forward Detector is not relevant.

3.3.2   Central Detector

The Central Detector consists of three different types of detectors. Each of these calls for a separate procedure to identify hits belonging to the same particle. In the following sections these algorithms are explained. Finally, the merging of the cluster information into tracks is described.

Mini Drift Chamber

From the trajectories of particles registered in the Mini Drift Chamber momentum and angular information of charged particles can be determined. This is done in two steps. First, pattern recognition techniques are applied to group hits, belonging to one particle, into tracklets, which are parametrized as helices. Then, a fitting routine is used to refine the parameters of each tracklet.

The algorithm used for pattern recognition is based on the assumption of a homogeneous magnetic field in the region of the drift chamber. In two steps, multi-model regression techniques are applied to fit helices to the hits. In the first step, the coordinates of the hits are projected onto the XY-plane. Taking into account the drift distance information, circles are fitted to the hits by minimizing the weighted sum of the distances to the center of each circle. In the second step, a straight line is fitted in the RZ-plane to all hits on a circle in the XY-plane. This fixes the six parameters necessary to describe a helix:

R_0 **and** Φ_0 , the polar coordinates of the axis of a helix in the X-Y plane

R , the radius of the helix

Q , the charge of the particle, which is determined from the curvature

θ , the dip angle of the helix

z_0 , the Z-coordinate of the closest approach of the helix to the origin

More details about this algorithm can be found in [KMPT97, Jac04]. Currently, three different algorithms are being developed. They are based on the Hough transformation, the minimum spanning tree method, and tracklet matching, respectively [Man04]. The development aims at an improved reconstruction efficiency for dilepton pairs.

At this stage of the reconstruction, parameters of the particles can be derived, which allow for a full reconstruction of final states albeit with limited precision. The momentum of the particle is calculated from the curvature of the helix under the assumption of a homogeneous magnetic field. Here, the nominal value of the field strength at the interaction point is used. However, as the magnetic field of the solenoid is not homogeneous (see Section 2.3.2.3), a systematic error is introduced. This is illustrated with the black curve in the right panel of Fig. 3.7, showing the relative difference of the reconstructed momentum of π^+ as a function of the scattering angle. The pions have been simulated with an initial momentum of 100 MeV/c. Depending on whether the pions have been emitted into the central region of the drift chamber or into the forward and backward regions, deviations of 5% up to 25% are observed. An improvement in the momentum reconstruction can be established by averaging the field strength along the particle trajectory using the map of the magnetic field. In the left panel of Fig. 3.7 the average value of the magnetic field strength is shown as a function of the reconstructed scattering angle and the deviations from homogeneity are visible. The red curve in the right panel of Fig. 3.7 displays the improvement in momentum reconstruction using the averaged field value. The deviations in the central region are below 2% and are reduced in the forward and backward region from 25% to 15%. The blue graph in the left panel illustrates the improvement of the momentum reconstruction by the track fit, which will be explained later on. Here, the deviations are below 1% independent of the scattering angle.
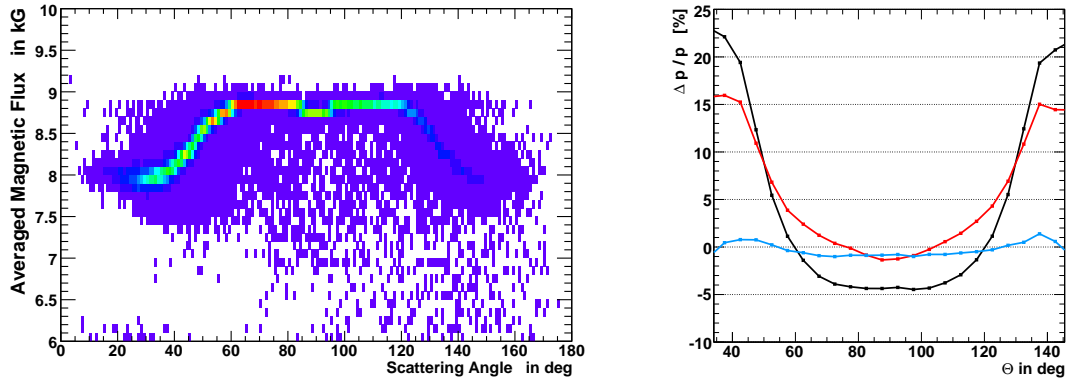
Figure 3.7: The assumption of a homogeneous magnetic field introduces a systematic error in the reconstructed momenta, as can be seen from the black curve in the right panel. Using the averaged magnetic field strength along a track reduces the systematic error significantly (red curve). The left panel shows the averaged magnetic field as a function of the scattering angle. A track fit, which takes into account the correct magnetic field strength at each point of the track, reduces the systematic error below 1% (blue curve).

Two more observables can be extracted from the helices, which are important for combining the information of the Mini Drift Chamber with other detector components. The first is the coordinate of the point, where the tracklet exits the drift chamber. These coordinates can be directly compared with the information of the Plastic Barrel. The second parameter is the direction in which the trajectory extends outside the chamber. It is calculated as the tangent to the helix at the point of exit. From both parameters, a hypothetical point of impact on the calorimeter surface is calculated.

The helices found by the pattern recognition are further processed by the final fitting routine. Using Kalman filter methods [Kal60], each tracklet is traced from the outer layers of the chamber back to the interaction region. The track parameters taken or derived from the pattern recognition result are used as initial values. The parameters are iteratively improved, taking into account energy loss and multiple Coulomb scattering in the detector material as well as the full map of the magnetic field. The result is the best estimate of the track parameters with a full covariance matrix at each point along the track. Important input parameters of the fit are the spatial resolution of the drift chamber and the mass of the particle. The latter is important for the multiple scattering and energy

loss calculations. By default the pion mass is used. In the analysis of final states with different particle species, like the decay mode $\eta \to \pi^+\pi^- e^+ e^-$, the fit has to be repeated after the particle identification with the correct masses in order to obtain optimal resolution.

The spatial resolution of the chamber can be deduced from the residual distributions of the fitting routine, calculated as the difference between measured drift distance and the distance of the fitted track to the sensing wire of a tube. The width of the residual distributions reflects the spatial resolution of the chamber, which is influenced by several factors. The chamber as well as the reconstruction routine have an intrinsic resolution. The intrinsic resolution is folded with the drift distance resolution, which is determined by the calibration. The residual distributions should be centered at zero. Shifts hint at systematic errors.

Figure 3.8: Residuals of the fitting routine. The individual distributions have been averaged per layer. Each distribution is represented by the result of a Gauß fit, showing its mean value and width. The data are shown in black and Monte Carlo simulations in red.
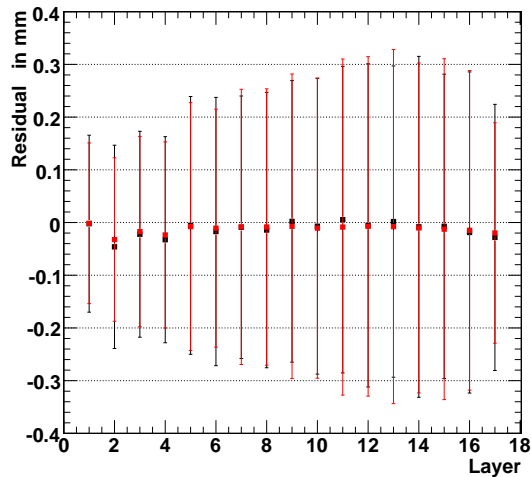
Fig. 3.8 shows the averaged residual distributions for each layer of the Mini Drift Chamber. The individual distributions are represented by the mean value and the width of a Gauß function fitted to the distributions. The residual distributions obtained from data taken in October 2008 (See Section 4.1) , shown by the black symbols, agree with the distributions obtained from the analysis of Monte Carlo simulations, shown in red. Agreement has been achieved by assuming a spatial resolution of the chamber of 325 μm, introduced by a Gauß smearing of the drift distances from the WASA Monte Carlo software.

The current reconstruction procedures do not include a vertex fit. A rough estimate on the vertex position can be deduced from helix parameters D_0 and

Z_0, which define the point of closest approach of each track to the origin of the coordinate system.

Plastic Scintillator Barrel

The elements in the Plastic Scintillator Barrel overlap to avoid efficiency losses. The overlap regions are well defined, resulting in a higher granularity than provided by single elements. If hits in the overlap region of two adjacent elements are assumed to stem from the same particle, they are merged into a cluster. The criteria for merging are a minimum deposited energy of $E_{min} = 0.5 \ MeV$ in each of the elements and a time difference smaller than $\Delta T_{max} = 10 \ ns$ between the hits.

The azimuthal angle of the cluster position is calculated as the average of its individual elements. The polar angle is fixed to the center of the detector planes, at 30 degree for the forward part, 90 degree for the central part and 140 degree for the backward part. The time information of the cluster is averaged from the contributing hits. The deposited energy assigned to a cluster is taken from the hit with the highest energy deposit.

Electromagnetic Calorimeter

Photons entering the crystals of the calorimeter produce electromagnetic showers. Depending on the energy of the photon, the shower can exceed the size of a single crystal. To reconstruct the incident photon, crystals belonging to the shower have to be identified. Their information is combined into clusters.

The algorithm used to perform the cluster finding is an iterative procedure. The hit with the highest energy deposit is taken as the central crystal of the first cluster. All neighboring elements with suitable hits are added to the cluster. The criteria are a time difference smaller than $50 \ ns$ and an energy deposit of at least $2 \ MeV$. Each added hit is checked for suitable hits in the neighboring crystals, which are again added to the cluster and checked for hits in the neighboring crystals. The procedure is repeated until all hits in neighboring crystals are found.

From the hits which have not been assigned to a cluster, the hit with highest energy deposit is taken as the central hit of the next cluster. This is repeated until all hits have been assigned to clusters.

The properties of each cluster are calculated from the properties of the contributing crystals. The individual energy deposits are summed up to the total energy deposit of the cluster. The time information is taken from the central hit. The position of the cluster is the mean value of the crystal positions, weighted by the deposited energies according to

$$\vec{X} = \frac{\sum_i w_i \vec{x_i}}{\sum_i w_i},\tag{3.6}$$

where the weights w_i are define as:

$$w_i = MAX\{0, W_0 + \ln \frac{E_i}{\sum_i E_i}\}.\tag{3.7}$$

The parameter W_0 has the value 5 [Vla08].

Track Assignment

The current algorithm for track assignment is optimized to find as many tracks as possible, independent of the energy or the charge of a particle as well as of the inefficiencies of single subdetectors. From the presence or absence of hits in the three components of the Central Detector, one can think of eight possible combinations leading to either charged or neutral tracks. Here, neutral tracks are defined by the absence of hits in the detectors sensitive for charged particles, the drift chamber and the plastic scintillator.

In Tab.3.1 all possible combinations are listed. To be able to reconstruct four-momenta it is necessary to identify the particles. In the case of charged particles, the available methods (see Section 3.4) require the information of at least two detectors per track. Solitary clusters from the Mini Drift Chamber as well as from the plastic scintillators will be omitted from further analysis.

The algorithm used for the track reconstruction starts with the evaluation of charged tracks. After all possible combinations for charged particles have been checked, the remaining signals of the calorimeter will be assigned to neutral tracks.

In the first step all combinations of clustered hits in the Mini Drift Chamber and the Plastic Scintillator Barrel are checked. The condition for two clusters to belong to one track is purely geometrical. In Fig. 3.9, the azimuthal distance between the cluster position in the Plastic Barrel and the exit coordinate of the

Detector Combination	Explanation
MDC, PSB, SEC	Charged, punching through to the calorimeter, registered in all detectors
MDC, PSB	Charged, stopped in the PSB or the solenoid
MDC, SEC	Charged, punching through to the calorimeter, undetected in the PSB
PS, SEC	Charged, punching through to the calorimeter, undetected in the MDC
MDC	Charged, stopped inside the MDC
PSB	Charged, stopped in the PSB or the solenoid, undetected in the MDC
SEC	Neutral
None	No track can be reconstructed

Table 3.1: List of possible hit combinations in the subdetectors of the Central Detector that result in tracks.

tracklet in the drift chamber (see Section 3.3.2) is plotted. From the width of a Gauß fit to the distribution, a maximum allowed difference of 10° is chosen as a condition for matching. For the polar angles it is only checked, whether the exit coordinate of the drift chamber coincides with the angular region covered by an element of the Plastic Scintillator Barrel.
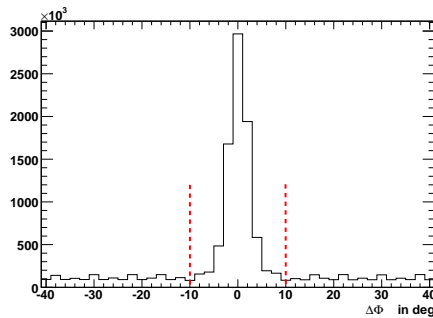
Figure 3.9: Difference of the azimuthal angles of the exit coordinate of the drift chamber tracklets and the clusters in the Plastic Scintillator Barrel. The red lines indicate the conditions under which the information of drift chamber and Plastic Barrel are assigned to one track.

For every matching combination it is tested if a cluster in the calorimeter is found, which belongs to the same track. Proper matching is ensured by checking

conditions on the clusters of the calorimeter and the drift chamber as well as the Plastic Barrel.

To test the matching between clusters from the Mini Drift Chamber and the calorimeter, the tracklet reconstructed within the chamber is extrapolated to the calorimeter. The extrapolation is straight and has to be tangential to the tracklet at the exit coordinate. The intersection of the track with the calorimeter surface is used as a hypothetical impact position of the charged particle. This impact position is compared to the measured cluster positions in the calorimeter. Fig. 3.10 shows the distribution of the opening angle between calculated and measured positions. Up to a maximum opening angle of 20° between the clusters of the drift chamber and the calorimeter is assumed to have originated from the same track.
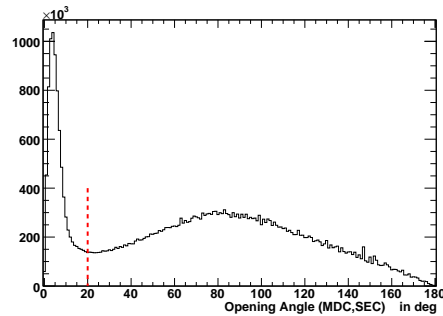
Figure 3.10: Distribution of the opening angle between the cluster position extrapolated from the drift chamber information and the position measured in the calorimeter. The red line indicates the condition under which the information of the drift chamber and the calorimeter are assigned to one track.

In order to check if clusters in the Plastic Barrel and the calorimeter belong to the same track, the angular distance as well as the time difference of the clusters is evaluated. Due to the geometry of the Plastic Barrel elements, a condition on the azimuthal angle is the most restrictive. The left panel of Fig. 3.11 shows the distribution of azimuthal distance of any combination of clusters. From the width of a Gauss fit to the distribution, a maximum distance of 20° is allowed for hits from the same track. Additionally, the polar angle of the cluster in the calorimeter has to be found in the angular range covered by the Plastic Barrel element. In the right panel of Fig. 3.11 the time difference between clusters in the calorimeter and the Plastic Scintillator Barrel is shown. The width of this distribution is about

25 *ns*. It is governed by the time resolution of the calorimeter. The time window to accept two clusters to be from the same track is chosen accordingly.
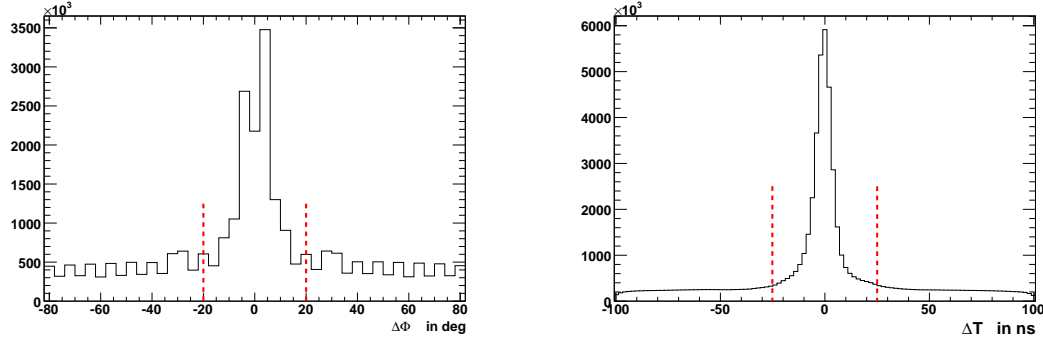
Figure 3.11: The difference of the azimuthal angles (left) and the time difference (right) of the clusters in the Plastic Barrel and in the Calorimeter are criteria for the track assignment. The red lines indicate the conditions under which the information of the Plastic Barrel and the Calorimeter are assigned to one track.

After the first step in the track reconstruction, all clusters in the Mini Drift Chamber have either been merged to form tracks or were identified as solitary. In a second step, the remaining clusters in the Plastic Scintillator Barrel are tested for possible combinations with the remaining clusters of the calorimeter. After this step, all possible charged tracks have been identified. In the last step of the track reconstruction, all remaining clusters in the calorimeter are assigned to neutral tracks.

3.4   Particle Identification

In the case of neutral particles, neutrons and photons have to be discriminated. In the Forward Detector both particle types could be reconstructed by secondary particles originating from interactions with the detector material, such as the photoeffect, Compton scattering, pair production and nuclear interactions. Currently, neutral particles are not reconstructed from the Forward Detector. In the Central Detector all neutral tracks are treated as photons.

Thus, in both the Forward Detector and the Central Detector particle identification is only an issue for charged particles. The procedures in the analysis

software make use of the specific energy loss described by the Bethe-Bloch formula [Leo94]. In the following, the application of the procedures for the different parts of the setup is described.

3.4.1   Forward Detector

The multi-layer structure of the Forward Detector is designed to use the $\Delta E - E$-technique. The energy loss in one detector layer is compared to the energy deposited in the subsequent layers. Different particle types end up in separate structures in the energy loss correlation plots. Depending on the kinetic energies of the particles, different subsets of detector layers can be compared. Fig. 3.12 demonstrates the particle identification in the analysis of proton-proton interactions at a beam energy of $T_b = 1400 \ MeV$ and proton-deuteron induced reactions at a beam energy of $T_b = 1000 \ MeV$.
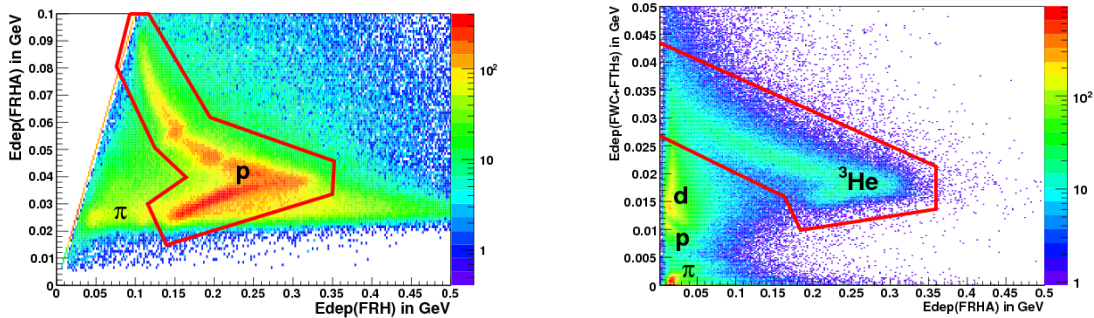
Figure 3.12: Particle identification in the Forward Detector is done using the ΔE-E technique. The correlation of the energy deposits in the first layer of the Range Hodoscope with the total energy deposit in the Range Hodoscope is used to identify the recoiling protons in pp induced interactions (left). The correlation of the summed energy deposit in the Window Counter and the Trigger Hodoscope with the energy deposits in the first layer of the Range Hodoscope is used to identify ^{3}He in pd induced interactions. The red lines indicate conditions to select protons and ^{3}He,respectively.

The left panel of Fig. 3.12 shows the deposited energy in the first layer of the Forward Range Hodoscope as a function of the total deposited energy in the Forward Range Hodoscope. The visible band is assigned to protons either stopping in or punching through the detector. The structures in the upper branch

of the band are due to passive material between the layers of the Forward Range Hodoscope. Most of the pions that are emitted into the Forward Detector are minimum ionizing and only seen at low energy deposits.

In the right panel of Fig. 3.12 the summed energy deposits in both layers of the Window Counter and the first layer of the Trigger Hodoscope is presented as a function of the energy deposited in the first layer of the Range Hodoscope. The bands of $p, d,$ and ^{3}He are clearly visible. Again, most of the pions are minimum ionizing. Due to the trigger conditions (see Sec. 4.1) the proton and deuteron distributions are suppressed.

The selection of a certain particle species is performed with conditions of the correlation of the energy deposits. The red lines in Fig. 3.12 indicate conditions to select protons and ^{3}He, respectively. The identification and selection of helium ions will be further discussed in the Sections 4.2 and 4.3.

3.4.2 Central Detector

The track reconstruction with the Mini Drift Chamber in the magnetic field of the superconducting solenoid provides momenta and charge state of the particles. Combined with the information on deposited energy in the Plastic Scintillator Barrel and the calorimeter particle identification can be performed. Three different correlations are used to separate leptons from pions and protons. Their applicability depends on the momenta of the particles.

In the $\Delta E - p$ - method, the specific energy loss of the particles in the Plastic Scintillator Barrel is studied as a function of the particle momenta and the charge state. For the calculation of the specific energy loss it has to be taken into account that particles in a magnetic field move on curved trajectories. Hence, their path in the Plastic Scintillator Barrel has not only a component depending on $d\theta$ but also on $d\phi$. The left panel of Fig. 3.13 shows the correlation plot of momentum and specific energy loss for a Monte Carlo simulation of the decay $\eta \to \pi^+\pi^-\pi^0$ with the subsequent Dalitz decay $\pi^0 \to e^+e^-\gamma$. Pions and leptons form separate structures, which can be selected by conditions on the correlation of momentum and energy loss as indicated with red lines in Fig. 3.13. For momenta above 130 MeV/c the structures of $\pi^\pm$ and $e^\pm$ merge, making the reliable particle identification with the $\Delta E - p$ - method impossible. In this momentum range the energy information of the calorimeter has to be taken into account.
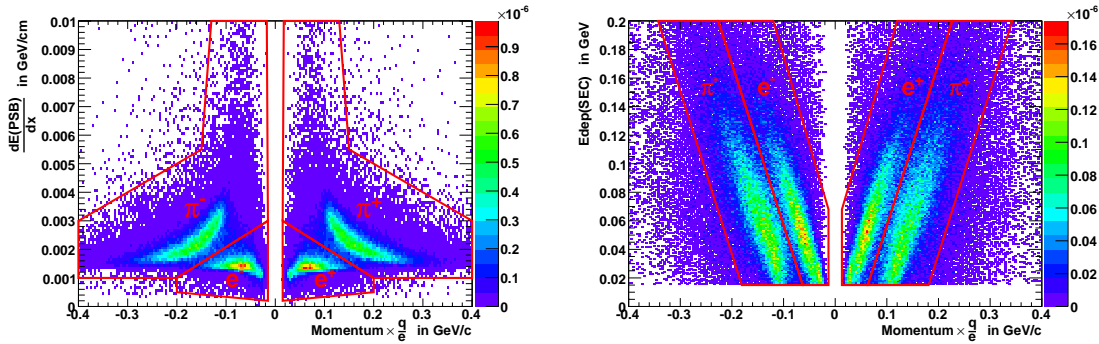
Figure 3.13: Particle identification in the Central Detector is done using the $\Delta E - p$ method (left) or the $E - p$ method (right). The energy loss in the Plastic Scintillator Barrel and in the calorimeter is studied as a function of momentum and charge state of the particles. Here, both methods are demonstrated with a Monte Carlo Simulation of the reaction $\eta \to \pi^+\pi^-\pi^0$ with the subsequent decay $\pi^0 \to e^+e^-\gamma$. The red lines indicate possible conditions to select particles of a certain type.

This is done in the $E - p$ - method. Here, the correlations of energy deposits in the calorimeter and the particle momenta are studied. The right panel of Fig. 3.13 displays the correlation plot. Electrons can be recognized due to their direct correlation of momentum and deposited energy. Like photons, they create electromagnetic showers depositing their total energy in the calorimeter. Pions produce separate bands at lower deposited energies. Again, the red lines indicate conditions on the correlation of momentum and deposited energy which can be used to select a certain particle type.

The purity and the efficiency of the methods described above depend on the applied conditions, on the quality of the calibration of the involved detectors and of the event sample. In order to illustrate the methods a Monte Carlo simulation was analyzed, which has the same amount of $\pi^\pm$ and $e^\pm$ in the final state. In the experimental data pions are present with much higher abundance, so that the structures due to leptons are hardly to be seen prior to a careful event selection. This will be discussed in more detail in Section 4.4.1.

A third possibility of particle identification in the Central Detector is the $\Delta E - E$-technique. It is independent of the drift chamber, using only the information on deposited energy in the Plastic Scintillator Barrel and the calorimeter. Similar to the $\Delta E - p$ - method, the applicability of this method is limited by the

plastic scintillator. To separate leptons from pions, it is only useful at momenta below $130MeV/c$. For higher momenta, the energy deposits in the thin plastic scintillators become constant and indistinguishable. Protons can be identified, due to the higher ionization density, which is successfully used in the analysis of the reaction $dd \rightarrow {}^3\text{He}\,p\pi^-$ [KMS09].

3.5   Energy Reconstruction

For stopped particles the deposited energy should correspond to the kinetic energy. Due to passive material from wrapping and support structures of the detectors and inefficiencies in the scintillation process, such as quenching, the kinetic energy of the particle cannot be measured directly.

In the Central Detector only the energy reconstruction of photons depends on the energy deposited in the detector material. The conversion of deposited energies into kinetic energies is done implicitly in the calibration (see Section 3.2.1). The momenta of charged particles are determined from the curvature of the tracks in the magnetic field of the solenoid. Energy deposits in the detectors are used for particle identification (see Section 3.4).

The reconstruction of particles emitted into the Forward Detector requires corrections to convert the deposited energy into kinetic energy. These conversion parameters have been derived from Monte Carlo simulations. Making use of the full description of the detector setup in the WASA Monte Carlo software (see Section 3.1.3), single particle tracks are simulated uniformly covering the acceptance region of the Forward Detector. To extract the conversion parameters, the relative difference of the reconstructed deposited energy and the initial kinetic energy is parametrized as a function of the deposited energy.

The parameter sets have to be generated depending on scattering angles and the plane in which the particle stopped, since the amount of active as well as passive material depends on the number of detector layers traversed and on the polar angle of the track. The ionization losses and the stopping power as well as the scintillation efficiency depend on the mass and the charge of a particle. The full number of parameter sets has to be produced for each particle type.

This method of energy reconstruction is also applicable for particles which did not stop in the detector or which underwent nuclear interactions with the detector

material. In the latter case the last detector layer in the track is determined, in which the particle lost energy only due to ionization. It is then considered as a particle that did not stop in the preceding subset of detectors. Hence, for each subset of detectors the conversion parameters have to be derived for particles that have not been stopped, again depending on scattering angle and particle type. The accuracy of this approach is strongly dependent on the excess energy of the particle compared to the stopping power of the detector.

Another source of uncertainty arises from the classification of particles as stopped in or punched through the detector. This is done using $\Delta E - E$- plots of the potential last detector layer and the preceding ones. The highest uncertainty arises from the region around the punch-through point. In this region the bands of stopped and exiting particles merge. A reliable selection is hardly possible. This can cause artifacts in the reconstructed kinetic energy distributions.

Currently, the parameter sets have been derived for protons and ^{3}He. In Fig. 3.14 the parametrization used for the reconstruction of protons is shown. A detailed overview on the performance can be found in [Pau06].

For the analysis discussed in Chapter 4, the kinetic energy of helium ions has to be reconstructed. All ^{3}He ions stemming from the reaction of interest $pd \rightarrow {}^3\text{He}\,\eta$ are stopped the first layer of the Range Hodoscope. Instead of the full parameter set, a single equation is sufficient. Eq. 3.8 describes the kinetic energy of ^{3}He as a function of deposited energy in the scintillators and the scattering angle θ. The parameters have been derived for deposited energies given in units of $[GeV]$. The accuracy of this method of reconstruction is discussed in Section 4.5.2.

$$E_{kin}(E_{dep}, \theta) = (c_0 + c_1 \cdot E_{dep} + c_2 \cdot E_{dep}^2 - c_3 \cdot E_{dep}^3) \cdot (a_1 - a_2 \cdot cos(\theta)) \qquad (3.8)$$

with:

$c_0 = 0.199876 \qquad a_1 = 1.42133$

$c_1 = 0.640187 \qquad a_2 = 0.364951$

$c_2 = 1.60489$

$c_3 = 2.28946 \qquad$ [Bas09]
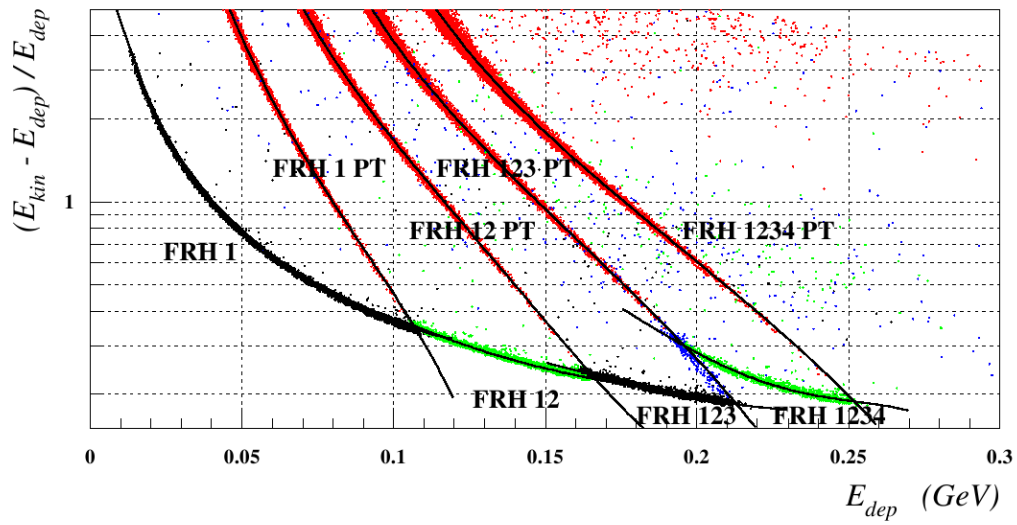
Figure 3.14: Correlation of the deposited energy and the relative difference of deposited and kinetic energy for Monte Carlo generated protons of kinetic energies between 0 and 1 GeV [Pau06]. The lower branches show stopped particles, whereas the branches labelled with "PT" correspond to particles punching through the given sets of detector layers. The black graphs illustrate the parametrization of the corresponding bands.

Chapter 4

Analysis of $\eta \rightarrow \pi^+\pi^-\gamma$

4.1   Run Information

The data analyzed in this work, were taken during a production run of four weeks in October 2008. A proton beam with a momentum of $1.7\,GeV/c$ ($T = 1.003\,GeV$) impinging on a deuterium pellet target was used to produce η mesons in the reaction $pd \rightarrow {}^3\mathrm{He}\,\eta$. Table 4.1 summarizes the conditions during data taking.

   In Fig. 4.1 the scaler readout of a typical cycle during data taking is displayed. The cycles of the accelerator in this beam time had a length of $100\ s$. Data are accepted during the flat top period after the beam has been accelerated to the desired energy and is stored in the ring. After the acceleration, at a time in the cycle of $t_c = 3.4\ s$ the high voltages of the detectors are ramped up to the normal operation level. During the acceleration and the dumping of the beam the detector voltages are ramped down in order to protect the wire chambers and photomultiplier tubes from high currents. At $t_c = 7\ s$ the vacuum shutters for the target system open. Simultaneously, the acquisition system starts recording data. The cycle length was chosen such that the beam current is reduced by a factor 2 at the end. At $t_c = 91\ s$ the shutters at the target close and the pellet stream is blocked until the next cycle reaches the region of the flat top. The data taking continues until $t_c = 93\ s$. Then the acquisition system is stopped and the detector voltages are ramped down before the beam is dumped. The two additional seconds of data taking in each cycle allow for an estimate of the amount of reactions stemming from interactions of the proton beam with the rest

beam momentum	1.7 GeV/c
beam energy	1.003 GeV
beam particles	protons
particles in flat top	$5 \cdot 10^9$
target material	deuterium pellets
pellet rate	$7 - 10\ kHz$
current in solenoid	589 A
field strength at interaction point	0.85 T
experiment trigger	$fwHea1\,|\,fwHeb1\,|\,fHedwr1$ (see text)
trigger rate at $t_c = 30\ s$	$\sim 1\ kHz$
total data taking time	722 h
time for target regeneration	167 h
cycle length	100 s
data taking within cycle	86 s
DAQ life time	90%
effective data taking time	430 h

Table 4.1: Overview of the run parameters for the production run performed in October 2008.

gas in the scattering chamber. The changes of the beam current and the trigger rates over the cycle are displayed along with the pellet rate in Fig. 4.1. From the ratio of issued and accepted trigger signals the lifetime of the data acquisition system is measured to be 90%.

Helium ions have a distinctive signature in the Forward Detector, which can be identified on the trigger level. The experiment trigger was set up to select events with at least one track in forward direction with a high energy loss in the Window Counter. This was achieved by the Matching Trigger (see Section 2.5) combined with a high threshold on signals of the Window Counter *fHedwr1*. To increase the selectivity of the trigger, it was demanded in coincidence with hits
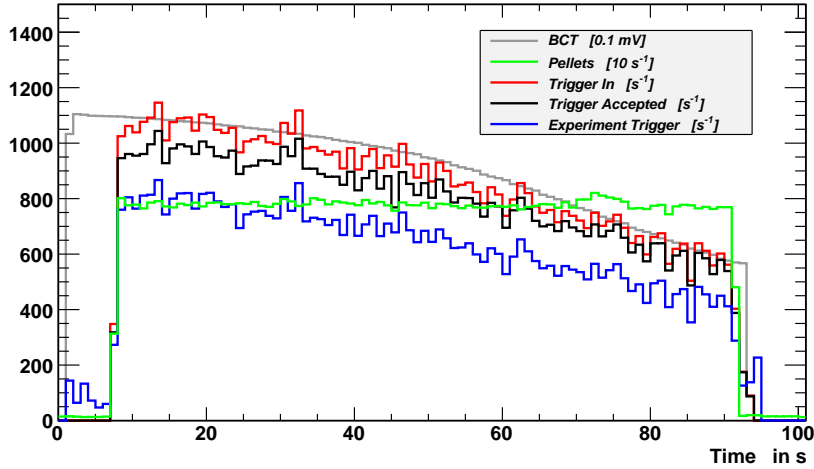
Figure 4.1: Scaler readout of a typical cycle during the beam time. The beam intensity is provided by a beam current transformer (BCT) in mV. Here, it is scaled up by a factor 10. The pellet rate is given in Hz, scaled down by a factor 10. The rates of the experiment trigger, all triggers offered to (TriggerIn) and accepted by (TriggerAccepted) the DAQ are given in Hz. All observables are displayed as a function of time in the cycle.

in both layers of the Window Counter. It was possible to reduce the event rate with the experiment trigger to $\sim 1\ kHz$, while the rate in single elements of the Forward Range Hodoscope was in the order of $1\ MHz$. The rate is well below the capability of the data acquisition system, so that the life time was in the order 90%. The trigger conditions only put restrictions on the recoil particle in the Forward Detector without introducing bias on the decay system of the mesons.

In the beginning of the beam time the Barrier Bucket technique was used to compensate for the mean energy loss of the COSY beam in the beam target interactions. Later another method was introduced which allowed for longer beam life times without compensation of the energy loss. This was achieved by changing the beam orbit. At the beginning of the cycle the beam was moved outward by a change of 4‰ in the COSY dipoles. Due to the energy loss in the interaction with the pellet target the radius of the orbit decreases during the cycle. The life time of the beam is increased by making full use of the acceptance of the COSY ring. Since the WASA detector is located at a dispersion-free section of the accelerator, the overlap of beam and target was not affected by this method. The gain in beam

lifetime is displayed in the left panel of Fig. 4.2. Here, the beam current for a cycle with the Barrier Bucket cavity switched on and for a cycle using the increased acceptance is plotted. In the latter case, illustrated with the red histogram, the beam current at the end of the cycle is almost a factor 2 higher compared to the situation when the barrier bucket method is used.
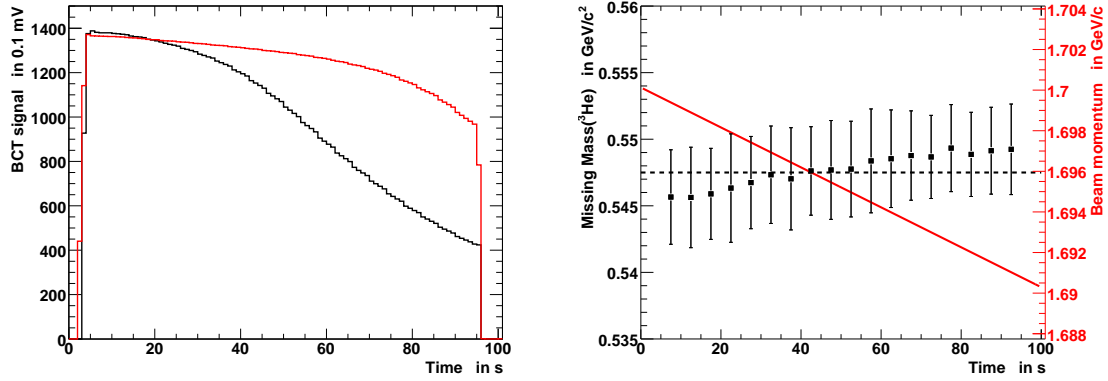
Figure 4.2: The comparison of the beam intensity during a cycle (left) with energy loss compensation (black histogram) and a changing beam orbit due to energy loss (red histogram) shows an improvement by a factor 2 at the end of the cycle. The life time of the beam is improved on the expense of a time dependence of the beam momentum, as can be seen from the peak position of the η signal in the missing mass calculated from ^{3}He as a function of time in the cycle (right). The error bars indicate a 1σ band from the fit of the η signal. Here, the missing mass is calculated assuming a constant beam momentum of 1696 MeV/c. The dashed line indicates the mass of the η meson. The extracted time dependence of the beam momentum is shown with the red graph.

The time dependence of the beam momentum due to the energy loss is illustrated in the right panel of Fig. 4.2. Here, the signal of the η meson in the missing mass calculated from the reconstructed helium ions is shown as a function of the time in the cycle. ^{3}He can be easily identified and an inclusive missing mass distribution can be calculated (see Section 4.2). The inclusive spectrum is fitted with a Gauß function combined with a polynomial of sixth order to describe the η peak on a continuous background. The right panel of Fig. 4.2 shows the peak position of the fitted Gauß distribution with error bars corresponding to the width of the distribution. Comparing the beginning and the end of the cycle, a relative shift of the peak position by 3 MeV is observed. The absolute deviation of the peak position from the η mass, which is shown by the dashed line, is due

to the assumption of a constant beam momentum of 1696 MeV/c in the analysis, which underestimates the actual beam momentum in the beginning of the cycle and overestimates it in the end of the cycle. The red graph in the right panel of Fig. 4.2 shows a linear fit to the beam momenta, which have been extracted from the scattering angle of ^{3}He at different cycle times. It is used to correct for the time dependence of the beam momentum in the data analysis.

4.2   Preselection

A preselection has been performed in order to keep only the events in which a helium ion can be identified in the Forward Detector [Zło09]. Based on the online calibration, the correlation of the averaged energy deposits in both layers of the Window Counter and the first layer of the Trigger Hodoscope with the energy deposit in the first layer of the Range Hodoscope is studied for each reconstructed track. In the correlation plot, shown in the left panel of Fig. 4.3, the structure associated with ^{3}He is clearly visible and well separated from structures originating from protons and deuterons. The red lines in Fig. 4.3 indicate the condition on the energy deposits of a track to be identified with ^{3}He. Saving each event containing at least one helium candidate provides a sample of $pd \to$ ^{3}HeX for further studies. The initial amount of data is reduced to 11.3%. The information of the light pulser system is not included in the preselected data. In order to correct for the gain drifts of the during the beam time, illustrated in Fig. 3.2, correction factors have been derived for the calibration constants of the calorimeter, as described in Section 3.2.1.

For the selected events the missing mass was calculated from the reconstructed helium four-momentum vector according to

$$
\begin{aligned}
MM_X(^3\text{He}) &= \sqrt{(P_{Beam} + P_{Target} - P_{3_{\text{He}}})^2} \\
&= \sqrt{(E_{Beam} + m_d - E_{3_{\text{He}}})^2 - (\vec{p}_{Beam} - \vec{p}_{3_{\text{He}}})^2}.
\end{aligned}
\tag{4.1}
$$

The resulting missing mass spectrum in Fig. 4.3 shows a pronounced peak at the mass of the η meson on a continuous background. A fit of the peak area yields a total number of $(10.89\pm0.01)\cdot10^6$ events, in which the η meson has been produced and tagged with the Forward Detector. The full width at half maximum of the signal is 8.31 MeV/c^2.
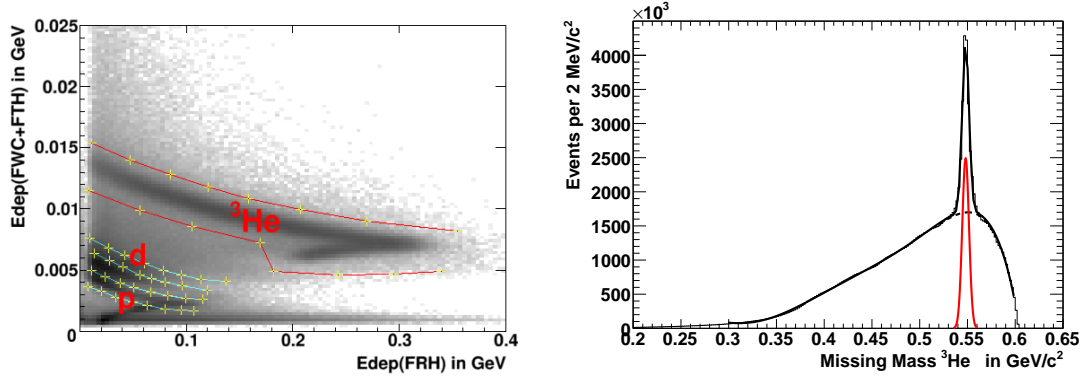
Figure 4.3: ^{3}He ions are identified by the correlation of the averaged energy deposits in the Window Counter and the first layer of the Trigger Hodoscope with the energy deposits in the first layer of the Range Hodoscope (left) [Zło09]. Events having at least one track with energy deposits in the region enclosed with the red lines are kept by the preselection. The blue lines indicate the regions in which stopped protons and deuterons are found. The inclusive missing mass spectrum $pd \rightarrow {}^3\text{He}X$ of the preselected data (right) shows a pronounced peak at the η mass. It contains $(10.89 \pm 0.01) \cdot 10^6$ events.

The number of reconstructed mesons corresponds to the average luminosity during data taking according to:

$$\mathcal{L} = \frac{N}{\sigma \cdot \epsilon} \; , \tag{4.2}$$

where N is the number of reconstructed events, σ is the production cross section and ϵ is the reconstruction efficiency. A summary of the calculations is shown in Tab. 4.2.

Monte Carlo simulations show an efficiency of 70% for the reconstruction of ^{3}He. This includes an estimate on the loss of efficiency by nuclear interactions with the detector material [Zło09], which has not yet been implemented in the WASA Monte Carlo software. From the total cross section of η production of 412 nb [B$^+$02] an integrated luminosity of $3.8 \cdot 10^{37} \; cm^{-2}$ can be calculated. Target regenerations, the structure of the COSY cycles and the dead time of the data acquisition system reduced the real time of the experiment of 722 hours to an effective time of data taking of 430 hours (See Tab. 4.1). The resulting average luminosity of the production run is $2.45 \cdot 10^{31} \; cm^{-2}s^{-1}$.

η mesons tagged with FD	$(10.89 \pm 0.01) \cdot 10^6$
efficiency	70%
production cross section	$412 \pm 16 \ nb \ \ [\text{B}^+02]$
integrated luminosity	$3.8 \cdot 10^{37} \ cm^{-2}$
average luminosity	$2.45 \cdot 10^{31} \ cm^{-2}s^{-1}$

Table 4.2: Average luminosity during data taking estimated from the number of tagged η mesons.

4.3 Event Selection

The reaction $pd \to {}^3\text{He}\,\eta$ with the subsequent decay $\eta \to \pi^+\pi^-\gamma$ has four tracks in the final state. Three of them are charged, one is neutral. The helium ion, which is the recoil particle from the meson production is reconstructed from a charged track in the Forward Detector. The decay products of the η meson are detected in the Central Detector. For the reconstruction of the decay mode, one neutral from a photon and two charged tracks of opposite polarity are necessary.

The selection of tracks in the Forward Detector starts with conditions based on the geometry of the setup. Only tracks with scattering angles from $3°$ to $18°$ are taken into account. This cut is necessary, since the track finding in the Forward Detector is based on the Forward Trigger Hodoscope (Section 3.3) which has a larger acceptance in the polar angle.

Additional conditions validate the trigger conditions (See section 4.1). Events of interest must have energy deposits in both layers of the Forward Window Counter, the first layer of the Trigger Hodoscope, and in the first layer of the Range Hodoscope.

The $\Delta E - E$ method has been used to distinguish tracks belonging to helium ions from those originating from other particles, as described in section 3.4. Fig. 4.4 shows the correlation of the sum of deposited energies in the Window Counter plus the first layer of the Trigger Hodoscope with the deposited energy in the first layer of the Forward Range Hodoscope. The band assigned to ${}^3\text{He}$ is visible. Above the red line in Fig. 4.4 tracks are accepted as helium.
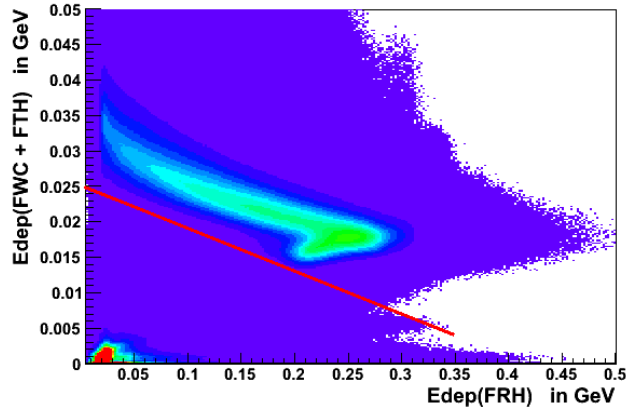
Figure 4.4: $\Delta E - E$-plot in the Forward Detector showing the correlation of the summed energy deposits in the Window Counter and the Trigger Hodoscope with the energy deposits in the first layer of the Range Hodoscope. Track with energy deposits above the red line are accepted as ^{3}He. The absence of proton and deuteron structures in the plot is due to the preselection (see Section 4.2).

Further restrictions can be deduced by considering the kinematics at the center of mass energy of $\sqrt{s} = 3.416 \; GeV/c^2$, yielding ^{3}He in the final state. Fig. 4.5 shows the correlation of kinetic energy and scattering angle of helium corresponding to η, single, and multi-pion production. Additionally, the acceptance regions of the Forward Range Hodoscope are marked in terms of angular acceptance and stopping power. It can be seen that helium ions originating from the production of η mesons are stopped in the first layer of the Range Hodoscope. Due to higher excess energies, the recoiling ^{3}He of other final states can reach the second layer, as shown by the punch through region of the helium band in Fig. 4.4. Thus, the exclusion of helium candidates depositing energy in the second layer reduces background contributions.

The tracks in the Forward Detector that fulfill the conditions are identified with ^{3}He. Their kinetic energy is derived from the deposited energies as described in Section 3.5. The information allows to reconstruct the four-momentum-vector of the helium particles.

The decay products of the meson are identified in the Central Detector. Tracks originating from the decay products have to be correlated in time with the helium candidates. Fig. 4.6 shows the time difference between the helium ions and
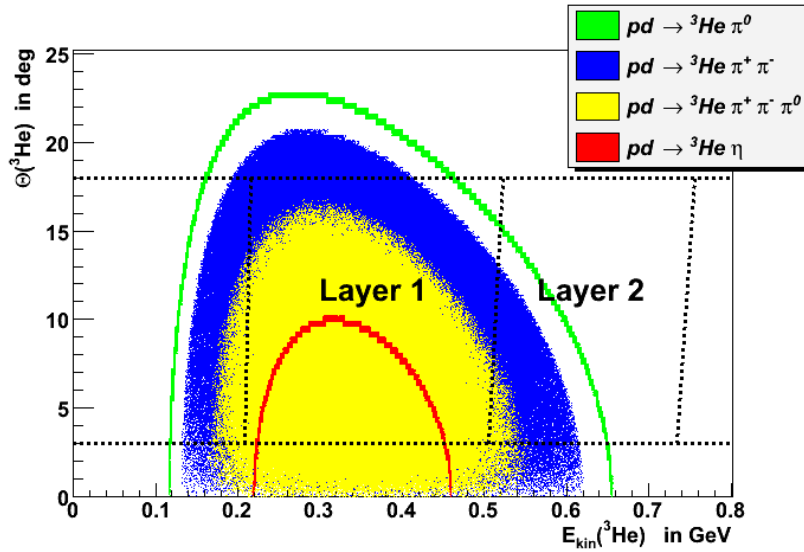
Figure 4.5: Correlation of kinetic energy and scattering angle of ^{3}He for different possible reactions at the CMS energy of $\sqrt{s} = 3.416\ GeV/c^2$. The horizontal, dashed lines mark the angular acceptance of the Forward Detector. The vertical, dashed lines illustrate the stopping power of the first and second layer of the Range Hodoscope.

the tracks in the Central Detector. The prompt peak due to coincident tracks is prominent in both distributions. The red lines in Fig. 4.6 indicate the time window in which tracks are accepted as coincident. The width of the time windows corresponds to the 3σ range of a Gauß fit to the individual distributions. For charged tracks it has a width of 25 ns and for neutral tracks a width of 45 ns.

The tracks have to fulfill additional criteria depending on their assignment to either neutral or charged particles. Tracks of charged particles must be registered by all three subdetectors of the Central Detector. This requirement allows to use all possibilities of particle identification discussed in Section 3.4. As a drawback, this condition introduces a threshold on particle momenta. Pions need at least a momentum of approximately 80 MeV/c to reach the calorimeter. Another criterion for the selection of charged tracks was introduced in order to suppress tracks originating from products of secondary interactions or photon conversion in the beam tube. It implies a condition on the vertex position. As the current version of the analysis software package does not yet include a vertex fit, the decision is made on a track by track basis evaluating the helix parameters of the drift chamber reconstruction. If a track is closer to the beam axis than $D_0 = 35\ mm$ in

(a) Charged tracks (CDC)

(b) Neutral tracks (CDN)
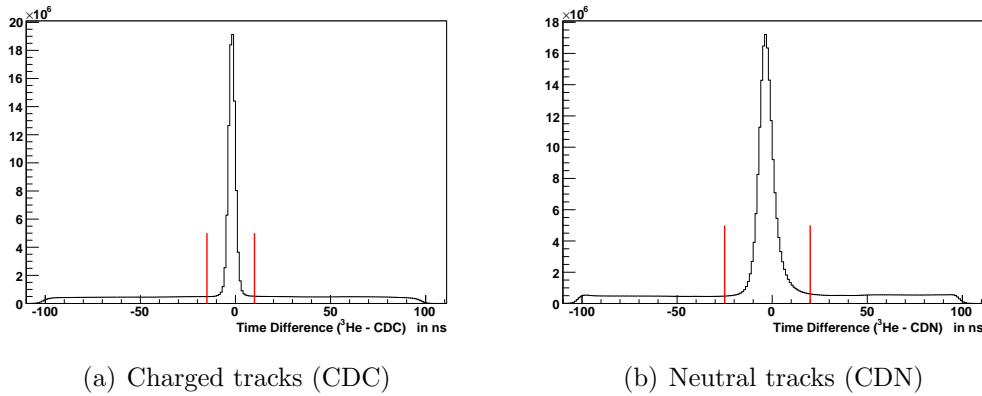
Figure 4.6: Time correlation of charged (a) and neutral (b) tracks in the Central Detector with the ^{3}He track in the Forward Detector. The marked regions of 25 ns (CDC) and 45 ns (CDN) width show the time windows to accept tracks. They have been determined as the 3σ range of a Gauß fit to the distributions.

the XY plane, it is taken into account for further analysis. The distance reflects the radius of the beam pipe.

Tracks assigned to neutral particles are required to have a minimum energy deposit of 20 MeV in the calorimeter. This threshold was chosen to suppress signals not originating from particles but from noise or artifacts in the reconstruction.

To select event candidates for the decay $\eta \rightarrow \pi^+\pi^-\gamma$ only those events are accepted which have two charged and one neutral track in the Central Detector, correlated with a helium ion. The two charged tracks have to have opposite polarity. To create four-momentum vectors all charged tracks are assumed to be pions. The neutral tracks are assigned to photons.

This selection is refined by additional restrictions based on momentum and energy conservation. For each event the total missing four-momentum vector is calculated according to

$$P_{miss} = P_{Beam} + P_{Target} - P_{3_{\mathrm{He}}} - P_{\pi^+} - P_{\pi^-} - P_\gamma. \tag{4.3}$$

In Fig. 4.7 the absolute value of the missing momentum is presented as a function of the missing energy. The resulting distribution is asymmetric. Its maximum is located at small, negative values of energy. Long tails extend, especially in the direction of negative values of missing energy, along the diagonals of equal momentum and energy. The excess to negative values indicates that in the reconstruction

four-momenta have been overestimated. The diagonal structures suggest the photons to be the source of wrong reconstruction. However, the distribution is not concentrated at the line of equal energy and momentum. It approaches this line asymptotically, which hints at massive particles.
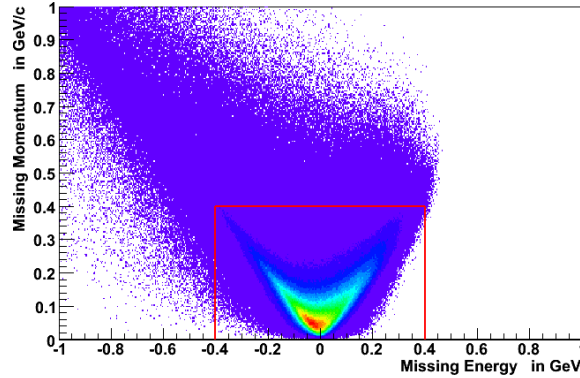
Figure 4.7: Missing momentum as a function of missing energy of all event candidates. The excess to negative values indicates that in the reconstruction four-momenta have been overestimated. The red lines indicate the condition, which is used to refine the event selection.

A constraint on energy and momentum conservation is used to exclude events as indicated by the red lines in Fig. 4.7. Events with a deviation of more than $400~MeV$ from energy conservation or more than $400~MeV/c$ from momentum conservation are rejected. Studies using Monte Carlo simulations show that this condition rejects approximately 2.3% of the signal events.

For the selected event candidates, the missing mass was calculated from the ^{3}He. The resulting distribution is shown in the left panel of Fig. 4.8. It can be seen from the shape of the spectrum that a large amount of background is still inherent in the event sample. The missing mass spectrum has been fitted with distributions from Monte Carlo simulations for the background reactions. The main contribution is due to multi-pion production. Further background reactions and possible methods to suppress their contributions are discussed in Section 4.4. Details about the fit of the data with Monte Carlo distributions can be found in Section 4.6.

In the right panel of Fig. 4.8 the invariant mass distribution of the $\pi^+\pi^-\gamma$ system is shown. Here only the events are taken into account for which the missing
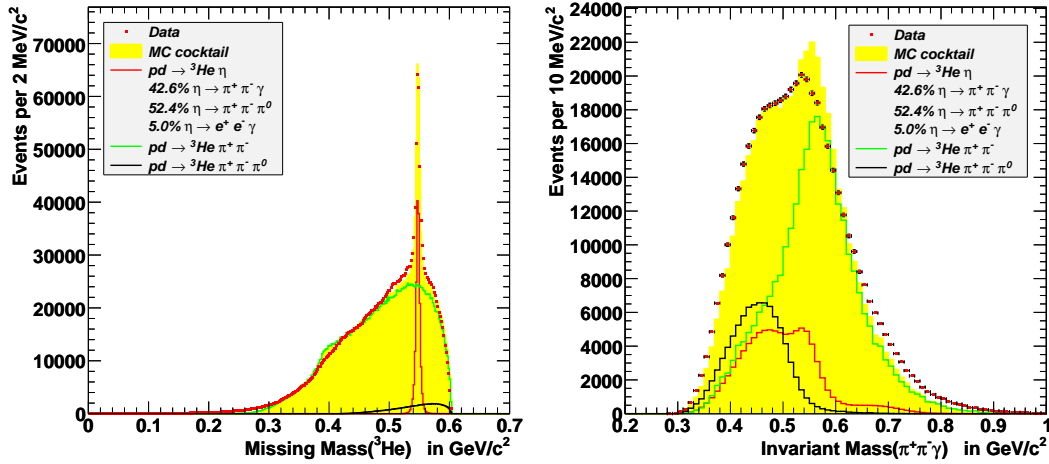
Figure 4.8: The missing mass (left) and invariant mass distribution (right) for the selected $\eta \to \pi^+\pi^-\gamma$ candidate events. Here, the invariant mass distribution is shown only for events with missing mass between 535 MeV/c^2 and 560 MeV/c^2. Both distributions are presented with a histogram fit of Monte Carlo distributions to illustrate the contributions of individual channels. Two-pion production is dominating.

mass calculated from ^{3}He is found in the range 535 $MeV \leq M_x(^3\text{He}) \leq 560\ MeV$, the region of the η mass. The resulting spectrum shows a broad, continuous distribution ranging from 280 MeV, the rest mass of two pions, up to approximately 800 MeV. At the η mass a small peak can be seen, which can be attributed to the channel $\eta \to \pi^+\pi^-\gamma$. A fit with distributions obtained from the analysis of Monte Carlo simulations suggests that the signal is almost completely overshadowed by contributions of three pion production and the decay mode $\eta \to \pi^+\pi^-\pi^0$ at lower invariant masses and by two-pion production at higher invariant masses. Next steps in the analysis chain concentrate on the reduction of signals originating from background reactions.

4.4 Background Channels

The missing mass spectrum shown in Fig. 4.8 reveals the amount of events in the selected sample originating from background channels. The continuous shape of the distribution outside of the region of the η signal indicates multi-pion production as the most severe source of background. In particular, the contribution of

two-pion production is observed. The lower edge of the spectrum is approximately at 280 MeV/c^2, which corresponds to the mass of two pions. In the event selection one photon has been requested and two-pion production can only contribute, if the neutral cluster is a fake signal. The appearance of additional neutral clusters in close to the reconstructed impact point of a charged particle is referred to as hadronic splitoff [Bur92, Gib98, Koe03].

Final states with three pions can contribute, if one of the two photons from the decay of a neutral pion was not detected. An important source of this background is the hadronic decay mode of the η meson $\eta \to \pi^+\pi^-\pi^0$. In contrast to other sources of multi-pion production it cannot easily be identified because it contributes to the η peak in the missing mass distribution of ^{3}He.

Further background may arise from inefficiencies in the particle identification. Here, the Dalitz decay $\eta \to e^+e^-\gamma$ and the two-photon decay of the η meson can contribute because they have the same topology of tracks. In the latter case one of the photons has to undergo conversion in the detector material.

In the following sections, the methods used for background suppression are discussed. Each method was optimized with respect to its statistical significance, which is calculated according to

$$\text{Significance} = \frac{N_{sig}}{\sqrt{N_{sig} + N_{bkg}}} \qquad , \qquad (4.4)$$

where N_{sig} and N_{bkg} are the numbers of signal and background events, respectively. It describes the relative amount of events in the sample stemming from the signal reaction.

4.4.1   Misidentified particles

For the selected events, particle identification as discussed in Section 3.4 turns out not to be useable. As can be seen in Fig. 4.9, the regions attributed to leptons are covered by the tails of the dominant pion distribution. A distinct structure that could be attributed to leptons is not visible. Correlated conditions on momentum and deposited energy, as proposed in Section 3.4 will merely decrease the reconstruction efficiency of the signal channel. Instead, pions will be identified indirectly, based on energy and momentum conservation.
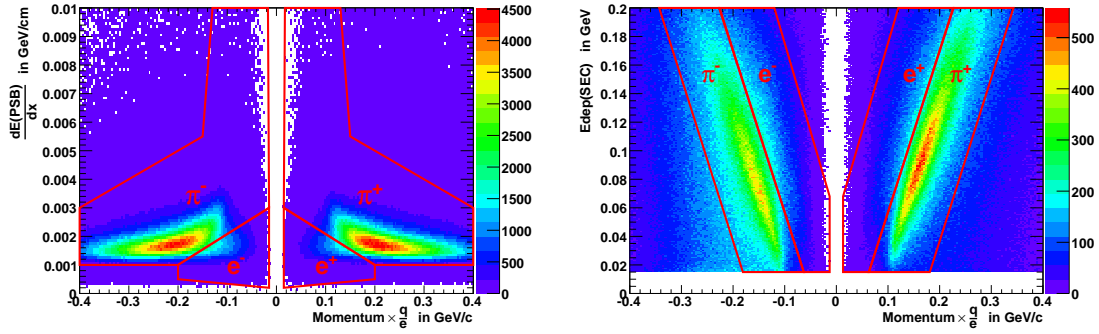
Figure 4.9: Due to the large abundance of pions in the selected data, particle identification in the Central Detector based on the correlation of momentum and energy loss in the Plastic Scintillator Barrel (left) or calorimeter (right) is not usable. Potential signatures of leptons are covered by the tails of the pion distributions. The conditions discussed in Section 3.4, as shown with the red lines, merely reduce the reconstruction efficiency by cutting into the pion distribution.

In the left panel of Fig. 4.10 the distribution of the squared missing mass of the ^{3}Heγ-system is shown. For events of the decay mode $\eta \to \pi^+\pi^-\gamma$ this distribution is equivalent to the invariant mass distribution of the two pions and has to fulfill the condition $2m_\pi \le M(^3\text{He}\gamma) < m_\eta$. To apply this condition, the resolution of the experimental setup has to be taken into account. This is done by evaluating the statistical significance using Monte Carlo simulations. Here, the Dalitz decay $\eta \to e^+e^-\gamma$ is considered to be the most important source of background events. In the right panel of Fig. 4.10, the significance of a condition on a minimum missing mass of the ^{3}Heγ-system is displayed. The maximum significance is reached by rejecting events with missing masses lower than $240~MeV/c^2$. This is the condition used in the analysis, as indicated by the dashed line in the left panel of Fig. 4.10.

The Monte Carlo simulations have been used to estimate the efficiency of the applied condition. The contribution of the Dalitz decay of the η meson is reduced by 86.45%. The reconstruction efficiency of the signal channel $\eta \to \pi^+\pi^-\gamma$ is only reduced by 0.39%.
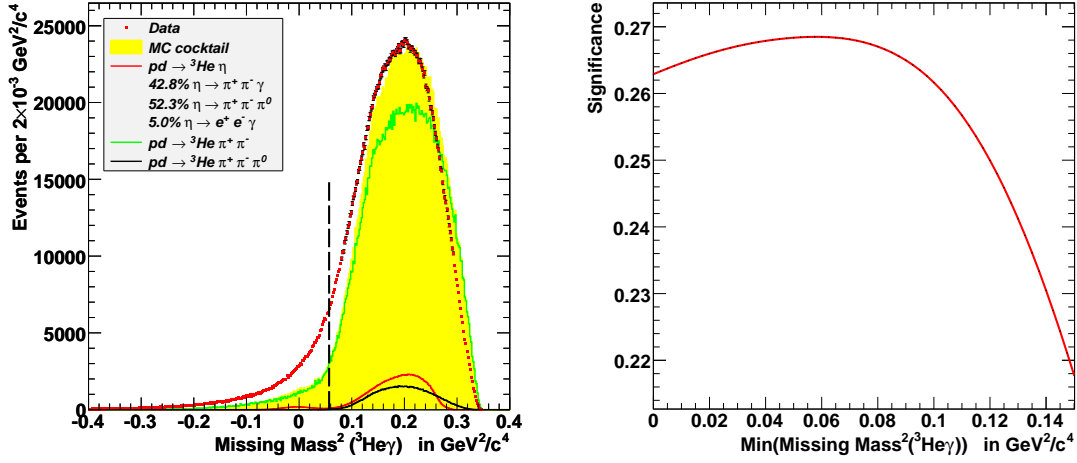
Figure 4.10: Events with two pions in the final state have to have missing masses of at least two times the pion rest mass ($(2m_\pi)^2 = 0.0779 \ GeV^2/c^4$) in the missing mass distribution of the ^{3}Heγ-system (left). The dashed line indicates the condition chosen to reject events stemming from background reactions. The condition has been selected with respect to its statistical significance (right).

4.4.2   Three-pion final states

The relative amount of background due to three-pion final states can be estimated by comparing the acceptance and the cross sections with the signal channel. Requiring that one of the two photons of the π^0 decay remains undetected, the geometric acceptance for the decay mode $\eta \to \pi^+\pi^-\pi^0$ is 12%. This is almost six times lower compared to the acceptance of the decay $\eta \to \pi^+\pi^-\gamma$, which is 70% (for details, see Section 4.7). However, the branching ratio of the three pion final state is five times larger [A+08]. Thus, the ratio of signal and background stemming from the η meson is almost one-to-one, which is consistent with the result of the fit with Monte Carlo distributions shown in Fig.4.8. An estimate of the contribution of the direct three pion production is more difficult. The geometric acceptance can be estimated to be 11%, but published data on the production cross section are available at higher excess energies only [S+10]. At the center-of-mass energy of $\sqrt{s} = 3.416 \ GeV/c^2$ it can be expected to be of similar size as the cross section of η production [Kup09]. Thus, the contribution to the selected data sample is about the same as from the η decay mode.

The contributions of the three pion final states can be identified by making use of momentum and energy conservation. If the reconstructed single photon stems from the decay of a neutral pion, a clear signal of the π^0 should be visible in the missing mass spectrum of the $^3\text{He}\pi^+\pi^-$ system.
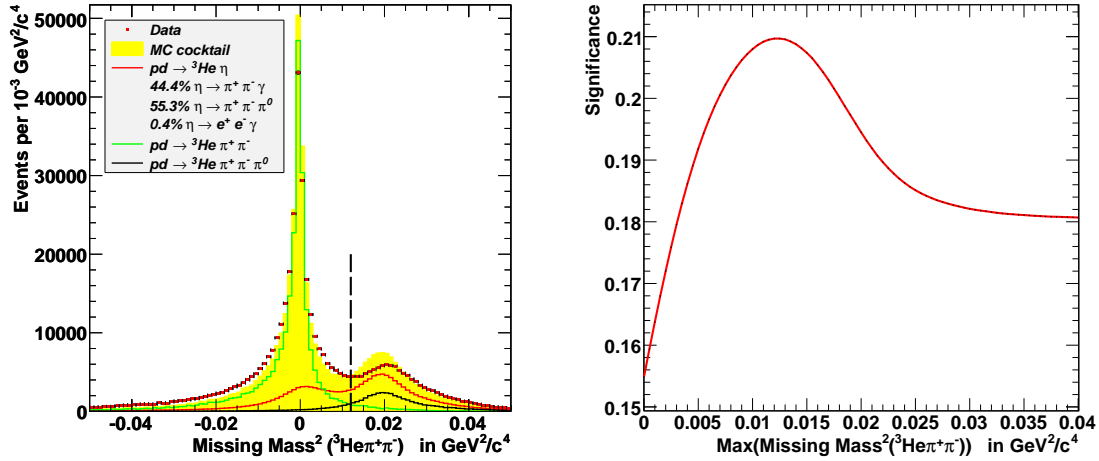
Figure 4.11: Contributions of three-pion final states are identified by the peak at the squared mass of π^0 in the missing mass distribution of the $^3\text{He}\pi^+\pi^-$ system (left). The dashed line indicates the condition to reject events attributed to background. The condition has been optimized with respect to its statistical significance (right).

In the left panel of Fig. 4.11, the missing mass distribution displays two peaks. The first peak, containing the majority of events, is located at mass zero. It originates from events without additional particles or an additional massless particle in the final state. These events stem from the background reaction $pd \to {}^3\text{He}\pi^+\pi^-$ and the signal channel $\eta \to \pi^+\pi^-\gamma$. A second peak corresponding to the three-pion final states is located at the squared π^0 mass of 0.019 GeV^2/c^4. It has a width of $\sigma = 0.012\ GeV^2/c^4$. To suppress the contribution of three-pion final states, all events with a squared missing mass of the $^3\text{He}\pi^+\pi^-$ system larger than 0.0125 GeV^2/c^4 are rejected. The condition, indicated with a dashed line in the left panel of Fig. 4.11, has been optimized considering its statistical significance. Based on Monte Carlo simulations, the significance has been determined using direct three-pion production as well as the decay of the η meson into three pions as possible background channels. In the right panel of Fig. 4.11 the significance is illustrated. The maximum is visible at 0.0125 GeV^2/c^4, the condition applied

in the analysis.

Along with the significance the efficiency of the condition has been studied. As can be seen from the missing mass distribution, the condition removes part of the distribution not originating from final states with three pions. Thus, a loss of events of the signal channel is to be expected. The studies of Monte Carlo simulations show that the reconstruction efficiency of the decay mode $\eta \rightarrow \pi^+\pi^-\gamma$ is reduced by 20.41%. The suppression of events stemming from final states involving three pions is larger by a factor of 4. Approximately 79.40% of the direct pion production as well as the decay mode of the η meson are rejected. The effect is best seen, by comparing the invariant mass distributions of the $\pi^+\pi^-\gamma$ system before (Fig. 4.8) and after applying the condition discussed here (Fig. 4.14). The background at lower masses is significantly reduced.

4.4.3   Hadronic Splitoffs

A shower in the calorimeter can spread in a manner which cannot be retrieved by the search patterns used in the reconstruction (See section 3.3.2). The remaining signals will be reconstructed as additional particles. This effect is referred to as splitoff. To discriminate this effect in hadron induced showers from those induced by photons the term hadronic splitoff is used.

Hadronic splitoffs feature small deposited energies and they are located in the vicinity of the impact point of a charged particle in the calorimeter. In Fig. 4.12 the correlation of the energy of each photon candidate and its distance to the nearest charged track is shown. The distance is represented by the opening angle between the showers of the photon and the charged pion in the calorimeter. A strong enhancement at smallest values of energy and angles is clearly visible. In order to reduce the background originating from hadronic splitoffs, a condition following the hyperbolic relation

$$E_\gamma > \frac{A}{\sphericalangle(\gamma, \pi)} \tag{4.5}$$

where E_γ is the photon energy in GeV and $\sphericalangle(\gamma, \pi)$ is the opening angle between photon and pion in degrees. The parameter A is chosen according to the statistical significance. For different values of A the distribution of missing mass calculated from ^{3}He was fitted by a polynomial of fourth order and a Gauß distribution
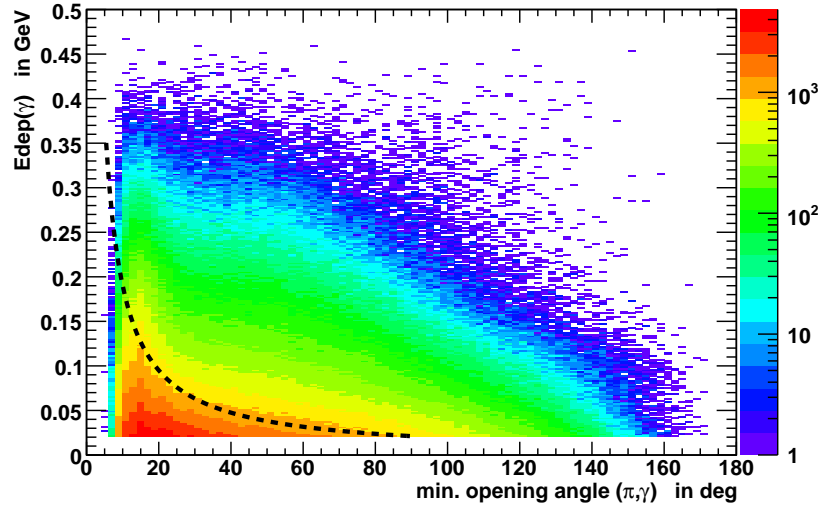
Figure 4.12: The deposited energy of the photon candidate is plotted as a function of the opening angle between the photon cluster and the impact point of the closest charged rack. A strong enhancement at smallest energies and angles is observed, which is attributed to background caused by hadronic splitoffs. The dashed curve indicates the condition, chosen to suppress this background.

to describe the background and the signal, respectively. The integral of either functions in the range of $530\ MeV$ to $560\ MeV$ yields the corresponding number of signal and background events. In the left panel of Fig. 4.13, the dependence of the significance on the parameter A is shown.

The maximum significance is found at a value of $A = 3.4\ GeV \times deg$. From the correlation of the signal and background efficiencies, shown in the right panel of Fig. 4.13, it can be seen that this condition removes about 70% of the continuous background and reduces the signal efficiency by 21%. However, the events of the signal decay $\eta \to \pi^+\pi^-\gamma$ are only affected in case of small invariant masses of $\pi^\pm\gamma$ pairs. A reduction of the reconstruction efficiency due to this condition results in unpopulated regions in the Dalitz plot, which cannot be recovered by efficiency corrections. This will be discussed in more detail in Section 5.1.4 and 5.2. Here, a less restrictive condition is chosen. For a hyperbolic relation, following $E_\gamma > \frac{1.9\ GeV \times deg}{\sphericalangle(\gamma,\pi)}$, the contribution of two-pion production to the selected events is still reduced by 54% and only 9% of the initial η mesons are rejected. The dashed curve in Fig 4.12 illustrates the condition. Events with entries in the region below
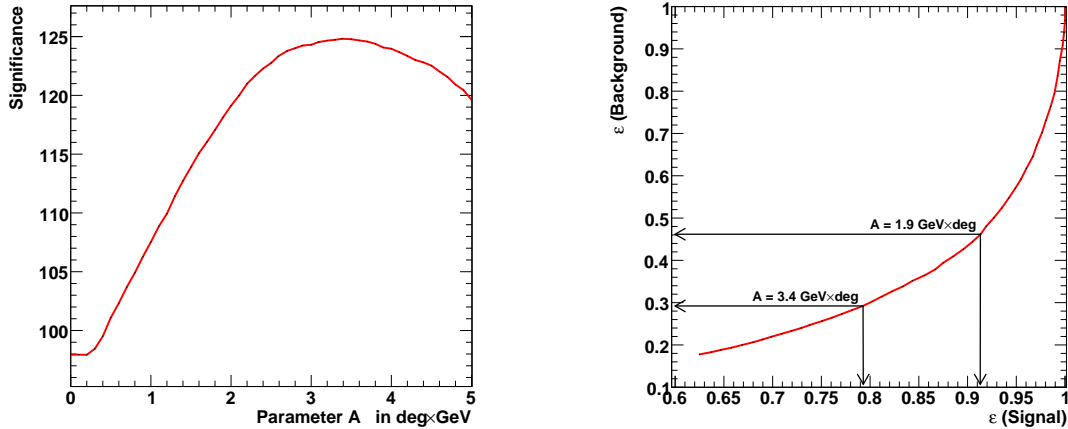
Figure 4.13: The significance of the condition to suppress hadronic splitoffs (left) is calculated from the number of events in the η peak in the missing mass of ^{3}He and the continuous background below the peak. The maximum significance is found for a parameter $A = 3.4 \; GeV \times deg$. For each tested parameter the correlation between the efficiency and background is plotted (right). The correlation plot is used to select a less restrictive condition in order to prevent efficiency gaps.

the curve are rejected as hadronic splitoffs.

Using the WASA Monte Carlo software, the effects of the condition on the individual decay modes has been evaluated. The reconstruction efficiency of the signal decay $\eta \to \pi^+\pi^-\gamma$ is reduced by only 1.85%. The contribution of the Dalitz decay of the η meson is reduced by 2.01%. The largest effect was found for the decay mode into three pions. The reconstruction efficiency was reduced by 9.09%.

Conclusions

In the left panel of Fig. 4.14 the missing mass distribution calculated from ^{3}He is shown. Here, all conditions discussed above have been applied. Compared to the distribution shown in Fig. 4.8, the continuous background due to multi-pion production has been reduced. Considering the full η peak as signal events, the signal-to-background ratio of 0.38 stayed the same. The improvement is seen when fitting the data points with the distributions of Monte Carlo simulations of the individual reactions. The peak at the mass of the η meson is now dominated

by events of the signal decay $\eta \to \pi^+\pi^-\gamma$. The contribution was increased from 48.2% to 67.3%.
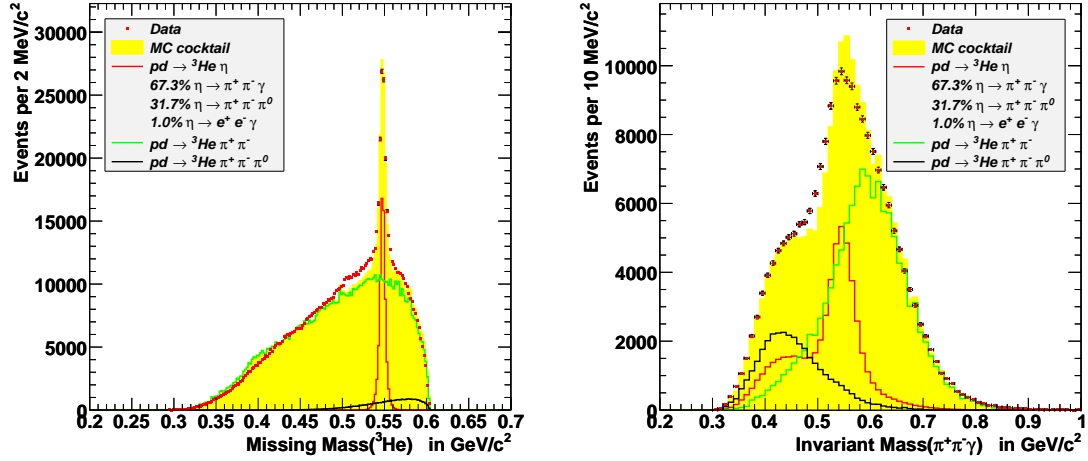
Figure 4.14: The missing mass (left) and invariant mass (right) distribution after the application of the conditions discussed above. Background from multi pion production and $\eta \to \pi^+\pi^-\pi^0$ has been significantly reduced, but is still covering the signal of $\eta \to \pi^+\pi^-\gamma$ in the invariant mass. Here, only the events with a missing mass between $535\ MeV$ and $560\ MeV$ are shown. Both distributions are presented with a histogram fit of Monte Carlo distributions to illustrate the contributions of individual channels.

The effect of the conditions can be seen in the right panel of Fig. 4.14. Here, the invariant mass calculated from π^+, π^- and γ is displayed. Only those events have been taken into account, in which the missing mass calculated from the ^{3}He is in the range of 535 and 560 MeV/c^2. This region approximately corresponds to a 3σ range of a Gauß fit to the η peak in the missing mass distribution. The spectrum shows a peak on top of a broad distribution. The peak is located at the mass of the η meson, but it has a tail towards higher masses. The histogram fit with Monte Carlo distributions reveals that the peak can be attributed to the decay $\eta \to \pi^+\pi^-\gamma$. However, it is overlaid by the contribution of $pd \to {}^3$He $\pi^+\pi$, which is not only responsible for the high energy tail of the spectrum but also constitutes the largest part of the background. The extension of the invariant mass distribution towards lower masses is due to events stemming from the remaining contribution of three-pion final states. This includes the decay mode $\eta \to \pi^+\pi^-\pi^0$.

It must be stated that the conditions do not provide sufficient constraints to

separate signal from background. A kinematic fit will provide optimal resolution and further means to suppress background events. The kinematic fit is described in the next section.

4.5 Kinematic Fit

The kinematic fit is a least square fit with constraints. The kinematic observables of all particles are varied in order to match the constraints of the working hypothesis. The amount of variation is limited by the experimental resolution. This results in an improved resolution of the fitted quantities and a restriction of each event to the allowed phase space. Constraints, such as the mass of intermediate particles, are exactly fulfilled. As a measure of agreement with the constraints the χ^2 distribution of the fit and the corresponding probability distribution are evaluated.

4.5.1 Application in the Analysis

For the reaction $pd \rightarrow {}^3\text{He}\,\pi^+\pi^-\gamma$ five constraints are possible. Four arise from energy and momentum conservation. A fifth constraint demands that the pions and the photon are decay particles of the η meson. The condition on the invariant mass of the three decay particles according to $(P_{\pi^+} + P_{\pi^-} + P_\gamma)^2 = M_\eta^2$ would be exactly fulfilled turning the fitted invariant mass distribution into a delta function. In the energy range considered here, cross sections and differential distributions of the identified background channels are not known. Thus, the invariant mass distribution of the $\pi^+\pi^-\gamma$ system has to be used for background subtraction and is not used as a constraint of the fit.

The measurement of the working hypothesis is kinematically complete. Each particle is described by its kinetic energy E_{kin}, the polar angle θ and the azimuthal angle ϕ. The errors are derived from Monte Carlo simulations as a double differential parametrization. Section 4.5.2 provides a detailed description of the error parametrization. The target is implemented as a deuteron at rest, whereas the beam is implemented as a proton either with a momentum of 1.7 GeV/c or with a momentum depending on the time of the event in the cycle, as discussed in Section 4.1. In the kinematic fit, the variables of beam and target are fixed. This

provides 12 parameters that can be used in the fit, which is applied as a $4C$-Fit, constrained only by overall momentum and energy conservation.

One of the reasons for using a kinematic fit, is to achieve a better suppression of background from hadronic splitoffs. The rejection of events with a small photon energy deposit together with a small distance between reconstructed showers as discussed in Section 4.4.3 has not been sufficient to clearly separate signal from background (see Fig. 4.14). The kinematic fit will be applied twice for each event, using different hypotheses. The reaction of interest, $pd \to {}^3\text{He}\,\pi^+\pi^-\gamma$, and the background reaction, $pd \to {}^3\text{He}\,\pi^+\pi^-$, will be tested, ignoring the measured photon as potential hadronic splitoff. The confidence levels of both fits are compared, taking the hypothesis with the higher confidence level as the most probable reaction. An analogous procedure can be applied to reduce the contribution of three pion final states. Similar methods have been used successfully in the data analysis of the Crystal Barrel experiment at LEAR [Mey95].

4.5.2 Error Parametrization

The errors can be estimated from Monte Carlo simulations by comparing the reconstructed values of kinetic energy, azimuthal and polar angle to the initial values given by the event generator. A prerequisite for this approach is the proper description of the experimental resolution by the simulation. This can be adjusted by smearing of the simulated observables.

The errors of the kinetic energies are parametrized by the relative difference of the reconstructed (E_{reco}) and initial values (E_{init}), and the absolute difference is used for the errors of the angles:

$$\Delta E = \frac{E_{reco} - E_{init}}{E_{reco}}$$
$$\Delta \theta = \theta_{reco} - \theta_{init}$$
$$\Delta \phi = \phi_{reco} - \phi_{init}$$

The resulting distributions are fitted by Gauß distributions. The mean value is sensitive to systematic deviations. The width $\sigma(\Delta E, \Delta \theta, \Delta \phi)$ is the resolution of the kinematic variable, its error.

Systematic studies of the error distributions depend on kinetic energy and scattering angle. This is taken into account by a double differential parametrization.

In Tab. 4.3 the sizes of the intervals in kinetic energy and polar angle, for the
parametrization, are listed. The interval size of the polar angle is chosen with
respect to particle types and the detectors involved in their reconstruction. The
errors of photons are not parametrized in equidistant angular intervals. The polar
angle is represented by 24 bins, which correspond to the calorimeter rings. Errors
are assigned to the ring in which the central crystal of the reconstructed cluster is
located. This prevents artifacts originating from the different crystal sizes, which
dominate the angular resolution of low energy photons.

Particle	Interval Size of	
	E_{kin} in MeV	θ
^{3}He	50	$1°$
π^+	50	$2°$
π^-	50	$2°$
γ	50	crystal size

Table 4.3: Step size of E_{kin} and the polar angle θ used to parametrize the errors.

In binary reactions like $pd \to {}^3\text{He}\,\eta$ the values of scattering angles and kinetic
energy are correlated and do not cover the full phase space. To avoid undefined
regions, high statistics samples of single ^{3}He, π^+, π^- and photons are generated.
The particles have energies and angles equally distributed in the range of the geo-
metric acceptance of the Forward and Central Detector. The reconstruction uses
methods and conditions identical with the actual analysis. Figure 4.15 illustrates
the extracted errors of E_{kin}, θ and ϕ. The values can be found in Appendix A.

As can be seen from Figure 4.15(a), the relative error of the kinetic energy of
^{3}He hardly depends on the scattering angle. It rises almost linearly with increasing
kinetic energy from 0.76% at 250 MeV up to 2.5% at 600 MeV. The error of
the azimuthal angle is independent of the energy and decreases approximately
exponentially with increasing scattering angles from $\Delta\phi = 2.5°$ to $0.5°$ as the
scattering angle increases from $\theta = 3°$ to $18°$.

The errors extracted for positive and negative pions show a similar behavior.
At scattering angles in the range of $40°$ to $140°$, the errors of the kinetic energy
as well as of azimuthal angles depend only on the kinetic energy. The relative
error of the kinetic energy increases from 8.5% to 25.7%. The error of azimuthal
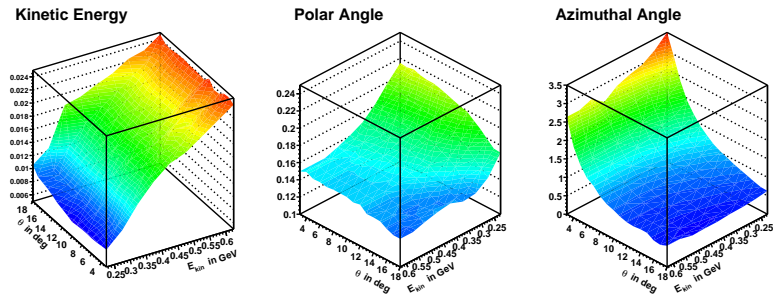
(a) Measurement errors of ^{3}He
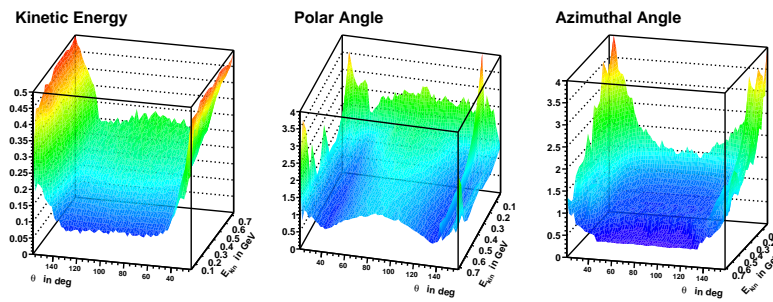
(b) Measurement errors of π^+
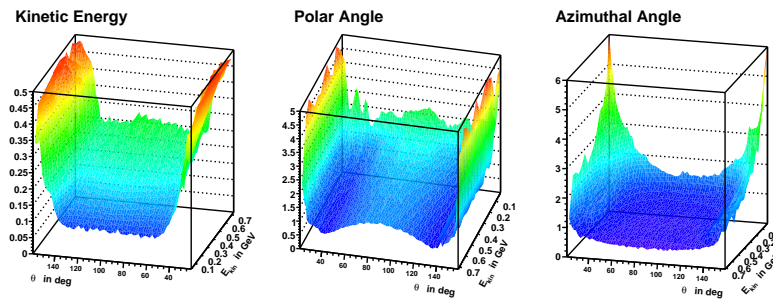
(c) Measurement errors of π^-
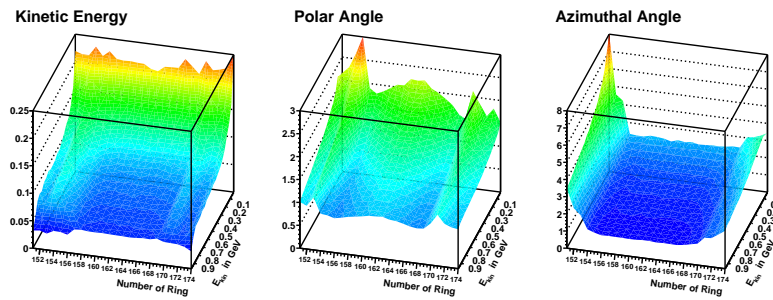
(d) Measurement errors of photons

Figure 4.15: Errors distributions of E_{kin}, θ and ϕ of the final state particles.

angles decreases from 1.55° to 0.48° with increasing energies. The errors of polar angles depend on the kinetic energy of the pions as well as on the polar angle itself. With increasing energies the error decreases. For scattering angles of 90° the error $\Delta\theta$ is largest and decreases towards minimum values at angles of 40° and 140°. At a kinetic energy of 50 MeV the error in polar angles is 2.8° and 1.8°, respectively. At a kinetic energy of 700 MeV the size of the error has decreased to 1.3° and 0.66°, respectively.
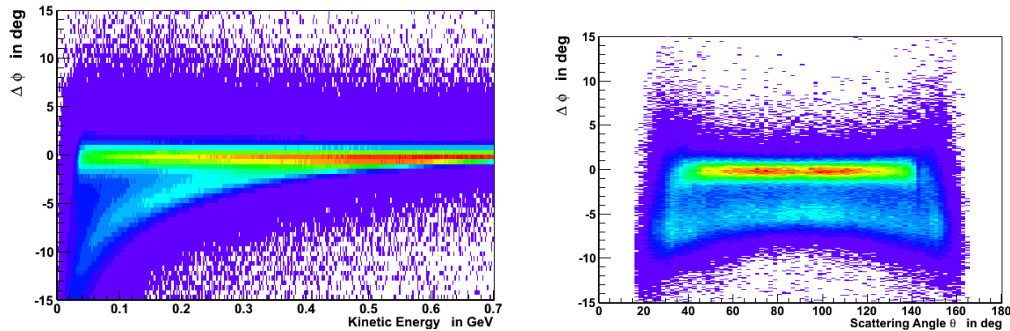
Figure 4.16: The error of the azimuthal angle of low energy charged pions shows a second structure which is depending on the kinetic energy (left). For a fixed kinetic energy (here, $E_{kin} = 150\ MeV$) the structure does hardly depend on the polar angle (right).

For polar angles smaller than 40° and larger than 140° the errors of all three kinematic variables of the pions increase. The regions correspond to the forward and backward end of the Mini Drift Chamber, where the number of layers which can contribute to a track decreases and, consequently, the errors of measurement increase. In the analysis, the error distributions are limited to errors of 30% for kinetic energies and 3° for either angle. As a result, the χ^2_{kf} value of the kinematic fit will be large or the fit will not converge for events with pions reconstructed in this region.

As illustrated in the left panel of Fig. 4.16, the correlation of kinetic energy and the error in azimuthal angles is ambiguous. At low energies two structures are visible. One is without a systematic offset, the other shows an offset which increases with decreasing energies. From the right panel of Fig. 4.16 it can be seen for the kinetic energy of 150 MeV that the systematic error is approximately independent of the polar angle. The structure might indicate an issue of the track reconstruction in the drift chamber (see Section 3.3.2), when dealing with tracks of

low energy particles. For the parametrization, the structure showing a systematic offset was ignored. This might lead to large χ^2_{kf} values of the kinematic fit and low probabilities.

The errors of the photon reconstruction are shown in Fig. 4.15(d). The error in kinetic energies decreases with increasing energy according to $\frac{\Delta E}{E} = \frac{5\%}{\sqrt{E/GeV}}$. At the borders between backward and central part as well as forward and central part slight deviations are visible. The errors of polar and azimuthal angle both decrease with increasing energies. Large electromagnetic showers of high energetic photons allow a better position determination (see Section 3.3.2). The different number of crystals as well as the different crystal sizes in the forward and backward endcaps of the calorimeter cause larger errors of the reconstructed angles as in the central part.

The error distributions of the kinematic variables of photons have large tails. These tails cannot be described by the Gauß fit, used for the parametrization. For a part of the analyzed events, this will lead to large χ^2_{kf} values of the kinematic fit and thus low values of probability are assigned.

The errors of the kinematic variables are implemented by piecewise bi-linear interpolation of neighboring bins. First, the contribution of the polar angle is interpolated then the kinetic energy.

Systematic deviations need to be corrected before application of the kinematic fit in order to avoid distortion of the results. A typical example of a systematic deviation is the azimuthal angle of ^{3}He, measured in the Forward Detector. The reconstruction of the angles assumes a straight track from the vertex, but the forward going particles traverse the magnetic field of the solenoid. Thus, their trajectories are curved close to the vertex. Fig. 4.17 shows this deviation as a function of polar angle and kinetic energy of the ^{3}He.

The effects of the Lorentz force are clearly visible. For a constant magnetic field the deviation of the azimuthal angle is calculated according to:

$$d\phi = 0.3 \frac{z\,B\,l}{p\,cos(\theta)} \qquad [\text{A}^+08] \tag{4.6}$$

where z is the charge of the particle, B is the magnetic flux in Tesla, l is the longitudinal component of the particle trajectory in meters, and p is the particle momentum in GeV/c. The magnetic field of the solenoid is not constant, as shown

Figure 4.17: The error of the azimuthal angle of ^{3}He shows a systematic deviation which depends on the kinetic energy E_{kin} and the polar angle θ.
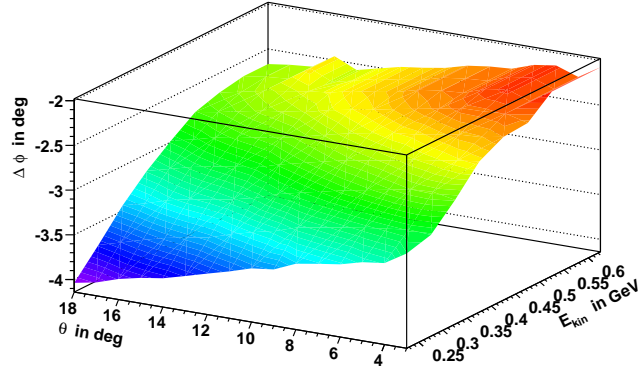
in Fig. 2.11, but equation 4.6 can be used to qualitatively judge the effect of the field on the trajectory of a particle.

The deviation from a straight track increases with increasing scattering angles θ. In this case the transverse component of the momentum, which is affected by the Lorentz force, increases. The deviation also increases with decreasing momenta. This can be seen from Fig. 4.17. The maximum deviation from a straight track in the parametrized kinematic range is at the kinetic energy of 200 MeV and a scattering angle of 18 degree. The azimuthal angle is decreased by 4.09 degrees. At the highest kinetic energy of 600 MeV and lowest scattering angle of 3 degrees the angle is only decreased by 2.04 degrees. Thus, this systematic error is parametrized depending on the kinetic energy and polar angle of the ^{3}He.

4.5.3   Performance

As described in Section 4.5.1 only energy and momentum conservation have been implemented as constraints, providing four degrees of freedom for the kinematic fit. For each event the result is evaluated on the basis of the χ^2_{kf} value of the fit and its probability. The probability for the best fit to have a value χ^2_{kf} with N degrees of freedom for the expected hypothesis is given by:

$$P(\chi^2_{kf}, N) = \frac{1}{\sqrt{2^N \Gamma(\frac{1}{2}N)}} \int_{\chi^2}^{\infty} e^{-\frac{1}{2}t} t^{\frac{1}{2}(N-1)} dt \qquad (4.7)$$

If the proper hypothesis is selected and the errors are correctly described the distribution of the probability should be uniform between 0 and 1 [A+08].
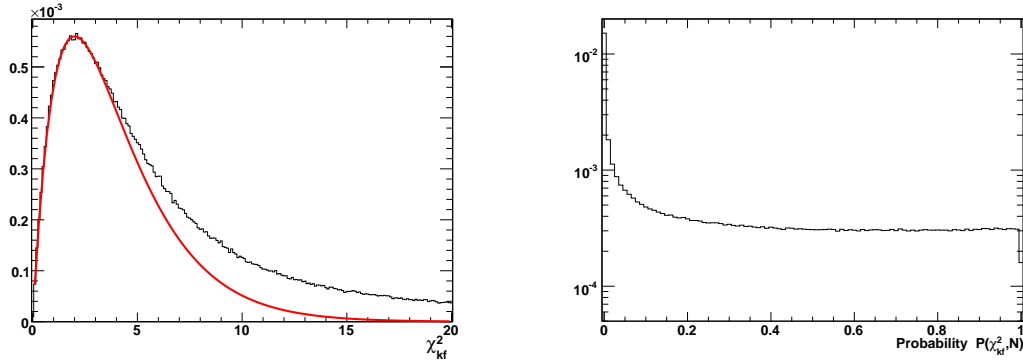
Figure 4.18: χ^2_{kf} distribution (left) and probability distribution $P(\chi^2_{kf}, N)$ (right) obtained from the analysis of a Monte Carlo simulation of $pd \rightarrow {}^3\mathrm{He}\eta$ with the subsequent decay $\eta \rightarrow \pi^+\pi^-\gamma$. The comparison with the theoretical χ^2_{kf} distribution for four degrees of freedom (red curve) shows an enhanced tail at large values of χ^2_{kf}. It is reflected in the strong population of the probability distribution $P(\chi^2_{kf}, N)$ at lowest probabilities.

The left panel of Fig. 4.18 shows the χ^2_{kf} distribution for a Monte Carlo simulation of the reaction $pd \rightarrow {}^3\mathrm{He}\eta$ with the subsequent decay $\eta \rightarrow \pi^+\pi^-\gamma$. The comparison with the theoretical χ^2_{th} distribution for four degrees of freedom, as illustrated with the red curve, shows an enhanced tail at higher values of χ^2_{kf}. In the right panel of Fig. 4.18, the corresponding probability distribution $P(\chi^2_{kf}, N)$ is displayed. The distribution is flat for values larger than 10%. The rise at lower probabilities corresponds to the events in the tail of the χ^2_{kf} distribution. The distribution would be uniform for the correct hypothesis and error estimation. Thus, events with $P(\chi^2_{kf}, N) > 10\%$ are selected corresponding to a reconstruction efficiency reduced by 43.7%. The deviation of the probability distribution from uniformity indicates wrongly estimated errors. This can be attributed to the issues of the error estimate of the charged pions that were reported in Section 4.5.2.

Fig. 4.19 shows the probability distribution for the data sample. The distribution is not uniform, but strongly peaked towards lower probabilities. This is due to the events from background channels for which the hypothesis of the fit was inappropriate. The experimental distribution is fitted with Monte Carlo distributions of the signal channel and the individual background channels. The distributions of the background channels are strongly peaked at lower values while the signal

Figure 4.19: Probability distribution $P(\chi^2_{kf}, N)$ obtained from the analysis of the selected data. The distribution is fitted with Monte Carlo distributions of the signal and all considered background channels. In contrast to the signal distribution, the probability distributions of the background channels are strongly peaked at lowest probabilities.
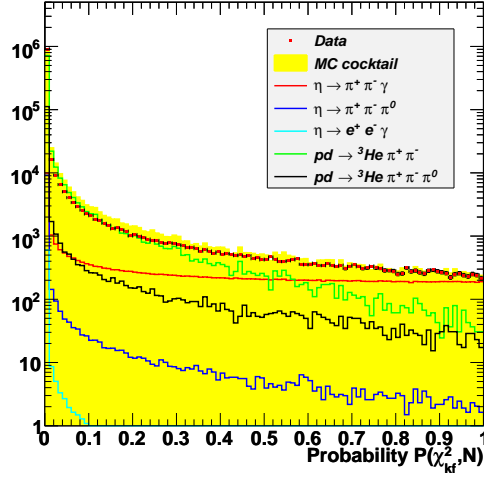
distribution is flat. The majority of events of the background channels is located at $P(\chi^2_{kf}, N) < 10\%$. Thus, the condition selecting the flat region of the probability distribution partly suppresses background contributions. The reduction of background is discussed in more details in Section 4.5.3.1.

The invariant mass spectrum of the $\pi^+\pi^-\gamma$ system after the kinematic fit is shown in Fig. 4.20. At this stage events with a probability $P(\chi^2_{kf}, N) < 0.1$ have been rejected. A sharp peak at the mass of the η meson is seen. The width of the signal is $\sigma = 3 \ MeV/c^2$, compared to the width of $\sigma = 29 \ MeV/c^2$ before, as indicated in Fig. 4.14. The fitted invariant mass is identical to the missing mass calculated from ^{3}He. The resolution is dominated by the missing mass resolution in the Forward Detector.

Figure 4.20: Invariant mass distribution of the $\pi^+\pi^-\gamma$ system after the kinematic fit and the rejection of events with $P(\chi^2_{kf}, N) < 0.1$. The distribution was fitted with Monte Carlo distributions of signal and background channels. The peak of the eta meson has a width of $\sigma = 3 \ MeV/c^2$. According to the histogram fit the contribution of the decay mode $\eta \to \pi^+\pi^-\pi^0$ to the signal peak is only 2.8%.
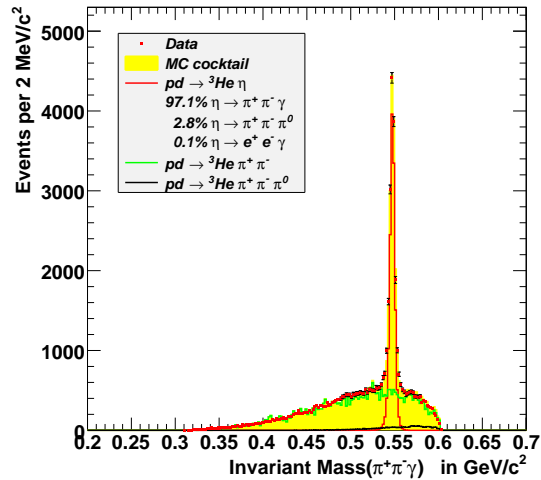
The constraint on the probability distribution reduces the contribution from background channels. The ratio of events in the η peak to the events in the continuous background distribution has increased from 0.38 in Fig. 4.14 to 1.77 in Fig. 4.20. The ratio was obtained by fitting a Gauß function plus a polynomial background in the mass range of 535 MeV/c^2 to 560 MeV/c^2.

A fit of the invariant mass spectrum with distributions obtained from an identical analysis of Monte Carlo simulations of signal and background channels has been performed. The contribution of the η meson is almost entirely described by the signal channel $\eta \to \pi^+\pi^-\gamma$. 2.9% of the signals in the peak can be attributed to background, where the contribution of the Dalitz decay is negligible. 2.8% of the background is contributed by the mode $\eta \to \pi^+\pi^-\pi^0$.

4.5.3.1   Background Reduction

In order to judge if an event belongs to the signal channel or to background reactions, each event was fitted twice with different hypotheses. The probability distribution of each fit can be used to classify the events as signal or background.

(a) $pd \to {}^3\mathrm{He}\,\eta(\to \pi^+\pi^-\gamma)$ (b) $pd \to {}^3\mathrm{He}\,\pi^+\pi^-$
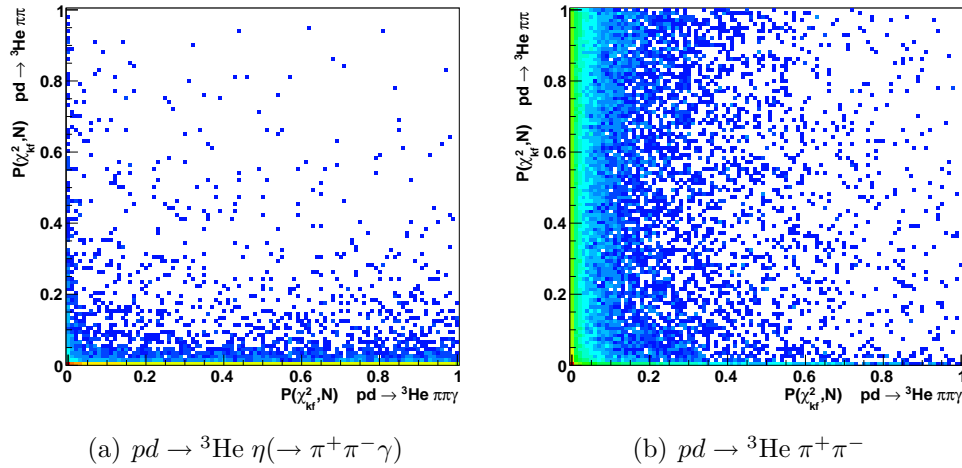
Figure 4.21: Correlation of the probability distributions for the hypotheses $pd \to$ ${}^3\mathrm{He}\,\pi^+\pi^-\gamma$ and $pd \to {}^3\mathrm{He}\,\pi^+\pi^-$ in the analysis of Monte Carlo simulations of $pd \to$ ${}^3\mathrm{He}\,\eta$, $\eta \to \pi^+\pi^-\gamma$ (left) and $pd \to {}^3\mathrm{He}\,\pi^+\pi^-$ (right). The Z-axis of both histograms is logarithmic.

Fig. 4.21 shows the correlation of the probability distributions for the hypotheses $pd \to {}^3\text{He}\,\pi^+\pi^-\gamma$ and $pd \to {}^3\text{He}\,\pi^+\pi^-$. The distributions have been obtained from the analysis of Monte Carlo simulations. In Fig. 4.21(a) it is shown that the η decay populates only the lowest probabilities for two-pion hypothesis. It can be clearly distinguished on the basis of the probability distribution. For events stemming from two-pion production the separation is not as clear. The probability distribution extends into regions of higher probabilities for the η decay. A condition on the probability distribution is introduced to accept only events from the region, where the distribution is uniform. Fig. 4.21(b) shows that the rejection of events with a probability lower than 0.1 for the hypothesis $pd \to {}^3\text{He}\,\pi^+\pi^-\gamma$ removes 95% of the two-pion contribution.
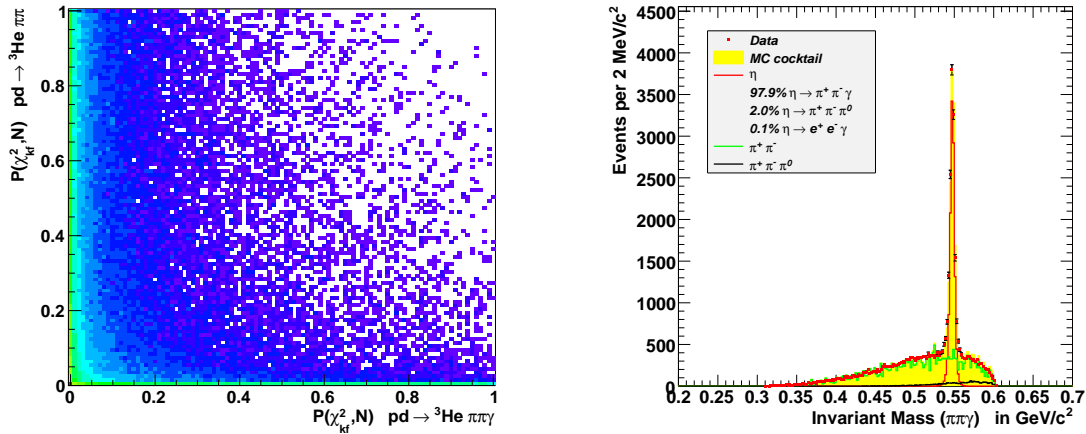
Figure 4.22: The correlation of the probability distributions for the different hypotheses of the kinematic fit illustrates the dominant background contribution of two-pion production in the data (left, Z-axis is logarithmic). Additional background suppression compared to the condition $P(\chi^2_{kf}, N) > 0.1$ can be achieved by rejecting the events with a higher probability for the background reaction. The resulting invariant mass distribution shows a signal to background ratio of 2.22 (right).

The correlation of the probabilities of the two different hypotheses of the kinematic fit for the data are shown in the left panel of Fig. 4.22. The visible structures are similar to Fig. 4.21. A large fraction of events is located at lowest probabilities for the decay mode $\eta \to \pi^+\pi^-\gamma$, but it is almost uniformly distributed in the probability distribution of the fit hypothesis of two-pion production. This is also reflected in the improved signal-to-background ratio of 1.77 show in Fig. 4.20.

The remaining background from multi-pion production is subtracted. This will be discussed in Section 5.1.3.

In order to test if further improvements of the signal-to-background ratio are possible, a method from the Crystal Barrel experiment at LEAR [Mey95] has been tested. The probabilities of the different hypotheses are compared on an event-by-event basis. The events for which the probability to match the hypothesis of two-pion production is larger are rejected. The resulting invariant mass distribution is shown in the right panel of Fig. 4.22. The additional condition on the probability distribution improved the signal-to-background ration from 1.77 to 2.22. The reconstruction efficiency of the decay mode $\eta \rightarrow \pi^+\pi^-\gamma$ is reduced by only 2.2‰. The additional condition on the probability distribution is not included in the analysis chain. The influence of this condition on the results of the analysis will be discussed in Section 5.2.

4.6   Comparison of Simulation and Data

For the decay mode $\eta \rightarrow \pi^+\pi^-\gamma$ and each background channel discussed in Section 4.4 samples of 10^7 events were generated. After a full detector simulation has been performed, each sample was analyzed with the same conditions as used in the data analysis. The experimental spectra are compared to Monte Carlo simulations, by fitting the sum of the simulated distributions to the experimental distribution. Individual scaling factors are determined for each Monte Carlo distribution.

The sum of Monte Carlo event weights of the generated samples of each reaction is normalized to 1. In this way, the sum of weights in the simulated distributions directly reflects the reconstruction efficiency. Since the events in the experimental distributions have the weight 1, the individual scaling factors reflect the efficiency corrected number of events of each contribution. The ratio of the scaling factors of different contributions corresponds to the ratio of the cross sections.

The only published cross section for $pd \rightarrow {}^3\text{He}\,X$ reactions at the center-of-mass energy of $\sqrt{s} = 3.416\ GeV/c^2$ is the cross section of $pd \rightarrow {}^3\text{He}\,\eta$ [B$^+$02]. The branching ratios of the decay modes can be fixed according to the PDG values [A$^+$08]. This leaves the cross sections of multi-pion production as free

parameters for the fit. In Tab. 4.4 the cross sections obtained from different fits are listed.

Distribution	Cross Sections in μb	
	$pd \to {}^3\mathrm{He}\pi^+\pi^-$	$pd \to {}^3\mathrm{He}\pi^+\pi^-\pi^0$
Fig. 4.8(a)	4.2	0.2
Fig. 4.8(b)	7.3	0.8
Fig. 4.14(a)	6.3	0.2
Fig. 4.14(b)	7.3	0.8
Fig. 4.19	4.3	1.4
Fig. 4.20	12.3	0.4

Table 4.4: Cross sections for multi-pion production obtained relative to the η production cross section by fitting the Monte Carlo distributions to the measured distributions.

The values for the cross section of two-pion production agree within factor of 3. Taking into account that the reconstruction efficiency for the reaction $pd \to {}^3\mathrm{He}\pi^+\pi^-$ is on the order of 0.5‰, this difference is still negligible. In order to judge if the result of the fit is reasonable it is compared to cross section measured at different energies. From measurements at the lower center-of-mass energies of $\sqrt{s} = 3.356~GeV/c^2$ a production cross section of $(5.1 \pm 0.5)~\mu b$ [B$^+$06] has been published. The value is compatible with the averaged results of the histogram fits.

The individual values of the cross section for three-pion production obtained from the fit vary by up to a factor of 7. For the reaction $pd \to {}^3\mathrm{He}\pi^+\pi^-\pi^0$, cross sections of $(1400 \pm 17 \pm 370)~nb$ at $\sqrt{s} = 3.608~GeV/c^2$ and of $(910 \pm 7 \pm 80)~nb$ at $\sqrt{s} = 3.655~GeV/c^2$ have been published [S$^+$10]. The values seem to be compatible with the averaged results of the histogram fit. However, the difference between the published cross section might indicate that the cross section at the center-of-mass energy of $\sqrt{s} = 3.416~GeV/c^2$ should be larger.

The histogram fit performed in this work relies on the correct description of the kinematics of the involved reaction channels and detector effects, like the hadronic splitoffs, in the Monte Carlo simulation. However, multi-pion production has been simulated assuming a homogeneous and isotropic populated phase space. Furthermore, the analysis chain is designed to suppress multi-pion production as

a source of background. To obtain reliable values of the multi-pion production cross sections a dedicated measurement and analysis should be performed.

4.7 Reconstruction Efficiency

The overall reconstruction efficiency is the product of the geometric acceptance, the detection efficiency, and the reconstruction efficiency of the analysis chain. The geometric acceptance of the setup is determined from the output of the event generator (see Section 3.1.2). Fig. 4.23 shows the correlation of the kinetic energy with the scattering angle for the particles in the final state of the reaction $pd \rightarrow {}^3\text{He}\eta$, $\eta \rightarrow \pi^+\pi^-\gamma$, generated with a beam momentum of $1.7\ GeV/c$. The geometric acceptance is the fraction of the events, where the scattering angles of all particles are found inside the sensitive ranges of the detectors, as indicated with the red lines in Fig. 4.23. Here, the geometric acceptance is found to be 70%, which requires the ${}^3\text{He}$ in the Forward Detector, and the decay products of the η meson in the Central Detector.
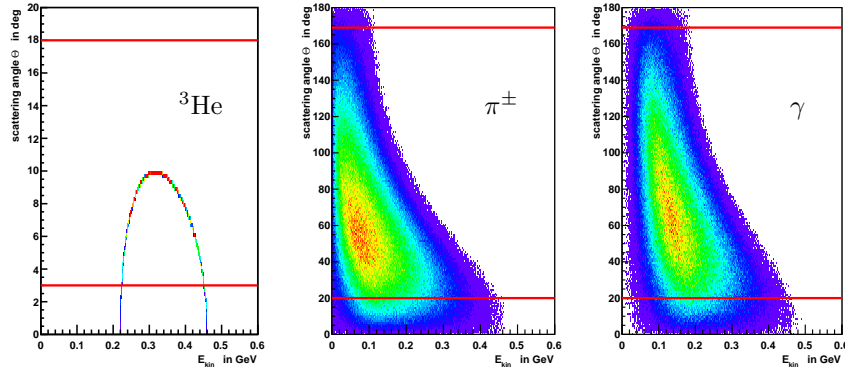
Figure 4.23: Correlation of kinetic energy with the scattering angle for all particles in the final state of the reaction $pd \rightarrow {}^3\text{He}\eta(\rightarrow \pi^+\pi^-\gamma)$. The red lines indicate the geometric acceptance of the WASA detector.

The reconstruction efficiency of the analysis chain is evaluated with the WASA Monte Carlo software. An event sample of the decay mode $\eta \rightarrow \pi^+\pi^-\gamma$ of 10^7 events was generated and tracked with the detector simulation. The output of the simulation was analyzed with the same program as the data. The efficiency

is calculated as the ratio of the number of events which fulfill the conditions and the total number of generated events. In Tab. 4.5 the efficiency of every analysis step is shown.

Condition	Efficiency
candidate selection	16.16%
energy and momentum conservation	97.79%
missidentified particles	99.61%
missed π^0	79.59%
hadronic splitoffs	98.15%
$P(\chi^2_{kf}, N) > 0.1$	56.26%
Total	6.92%

Table 4.5: Reconstruction efficiencies of the individual steps of the analysis chain presented in this chapter. The efficiency is determined from the analysis of a Monte Carlo simulation of $pd \to {}^3\mathrm{He}\,\eta$, $\eta \to \pi^+\pi^+\gamma$. The biggest drop in efficiency is caused by the event selection and by the cut on the probability distribution after the kinematic fit.

The biggest effect on the efficiency comes from the event candidate selection. The difference between the geometric acceptance and the efficiency of the track selection can be explained by the reconstruction of charged tracks in the Central Detector. Currently, only tracks which have been registered by all subdetectors are accepted. Allowing for all tracks in the analysis, which were registered in the drift chamber, increases the total number of tracks by 20%. The actual problem is the reconstruction efficiency of tracks in the central drift chamber. The pattern recognition (see Section 3.3) has an efficiency of about 80% for single tracks. The track fit which is applied on top of the recognized tracklets can reduce the efficiency by up to 50%. Improvements on the existing algorithms as well as new algorithms are being developed.

The loss of reconstruction efficiency by the individual conditions applied to suppress background have been discussed in the corresponding sections of this chapter. Generally, it can be stated that the gain in purity outweighs the loss of reconstruction efficiency.

Another sizable loss of reconstruction efficiency comes from the condition on the probability distribution of the kinematic fit $P(\chi^2_{kf}, N) > 0.1$. Ideally, this

condition would reject only 10% of the signal events, but, as can be seen from Tab. 4.5, almost 44% are rejected. Systematic errors in the reconstruction of the charged pions and error distributions, which do not have the shape of a Gauß distribution, result in an increased population of the probability distribution at values below 0.1. Different methods to improve the situation are under evaluation and not yet taken into account here.

The effects of the overall reconstruction efficiency on the results will be discussed in more detail in Section 5.1.4.

Chapter 5

Results

5.1   Dalitz Plot

The Dalitz plot [Dal53] is a tool to study the dynamics of three body systems, described by the 12 variables of the three four-momentum vectors. Kinematic constraints make some of the parameters redundant. Four parameters can be fixed by momentum and energy conservation. Three more parameters are fixed, if the three particles in the final state have been identified and their masses are known. Finally, without a preferred direction of the system, three more parameters are redundant. They correspond to the three Euler angles describing the orientation of the decay plane. This leaves two free parameters to describe the full dynamics of the final state. Correlations between the parameters are studied in the Dalitz plot.

The Dalitz plot represents the population of the available phase space. It is homogeneously populated in the absence of interactions between the particles. Resonances or interferences modify the population. Resonances produce band-like structures which are located at the mass of the resonance. The angular distribution of the resonance decay corresponds to the event distribution along the band. This feature allows to deduce quantum numbers from the Dalitz plot population.

5.1.1   Choice of Observables

A common way to present a Dalitz plot is the parametrization of the event distribution as a function of the squared invariant masses of two of the three particle combinations. In this work, the two combinations of $\pi^{\pm}\gamma$ are used.
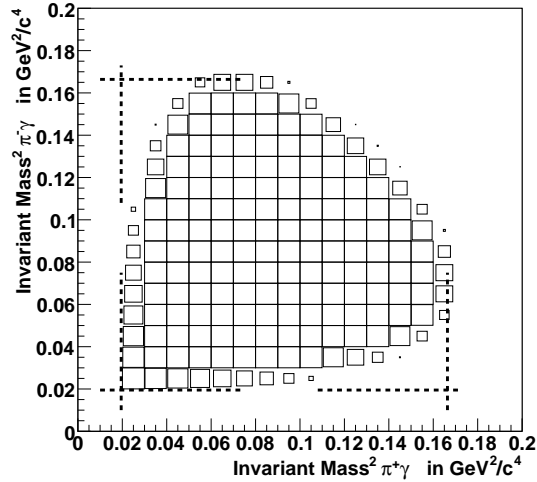
Figure 5.1: Dalitz plot showing the phase space of the decay $\eta \to \pi^+\pi^-\gamma$. The kinematically allowed region is marked with dashed lines. In this parametrization the distribution is symmetric with respect to the diagonal. Deviations from this symmetry can hint a C-violation (see text). The properties of the $\pi^+\pi^-$ system are inherent in the distribution perpendicular to the diagonal. The sharp edge at the lowest invariant masses is due to a massless particle (photon) in the final state.

Fig. 5.1 illustrates the phase space of the decay $\eta \to \pi^+\pi^-\gamma$ in the Dalitz plot. The dashed lines mark kinematic limits corresponding to the situations in which both particles of the respective combinations or the third particle is at rest. Here, the lower limit on both axis is defined by the squared rest mass of the charged pions $m_{\pi^{\pm}}$. The upper limits are defined by the squared difference of the η and $\pi^{\pm}$ masses $(m_{\eta} - m_{\pi^{\pm}})^2$. Because of the massless photon, the lower edge of the event distribution corresponds to the kinematic limits, while the upper limits are approached asymptotically, due to the third massive particle missing in the final state.

In this parametrization, the Dalitz plot is symmetric with respect to the diagonal. A deviation from this symmetry could be attributed to the violation of

C-invariance because it would mean a different behavior of particle and anti-particle. The event distribution perpendicular to the diagonal of the plot also contains the kinematic information of the $\pi^+\pi^-$ system, the third possible invariant mass combination.

For investigations of the box anomaly in the decay $\eta \to \pi^+\pi^-\gamma$ the invariant mass as well as the angular distribution of the $\pi^+\pi^-$ system are studied in order to disentangle resonant contributions due to final state interactions (see Section 1.2.1). Both distributions can be obtained as projections of the Dalitz plot. To be able to compare the results with previous measurements [G$^+$70, L$^+$73] a different representation of the Dalitz plot is used. Instead of invariant masses, the kinetic energies of the three particles in the rest frame of the η meson are used to describe the decay system. In this parametrization, the squared invariant mass of the two pions $s_{\pi^+\pi^-}$ is equivalent to the photon energy E_γ in the rest frame of the η meson. The relation is given by

$$E_\gamma = \frac{1}{2}\left(m_\eta - \frac{s_{\pi\pi}}{m_\eta}\right). \tag{5.1}$$

To study the angular distribution of the two-pion system, the angle of π^+ in the rest frame of the two pions is analyzed with respect to the direction of the photon. In terms of kinetic energies the angle can be expressed as:

$$cos(\theta_{\pi^+\gamma}) = \sqrt{\frac{s_{\pi\pi}}{s_{\pi\pi} - 4m_\pi^2}} \frac{T_+ - T_-}{|\vec{p}_+ + \vec{p}_-|} \tag{5.2}$$

where $T_\pm$ are the kinetic energies and $\vec{p}_\pm$ are the momenta of the pions in the η rest frame.

5.1.2   Resolution of the Observables

For the evaluation of Dalitz plot distributions it is necessary to know the resolution of the observables. A bias in the interpretation due to statistical fluctuations combined with inappropriate bin size can be prevented. The resolution is estimated using the WASA Monte Carlo software. For every event, the reconstructed value is compared to the one calculated from the event generator. The procedure is demonstrated in Fig. 5.2 for the case of the squared invariant mass of the two pions $s_{\pi\pi}$. In the left panel the distribution of the difference of reconstructed and

initial values for the squared invariant mass is shown. The width of the distribution is $\sigma = 0.00704 \; GeV^2/c^4$. To check for dependencies, the width was studied as a function of $s_{\pi\pi}$. This is shown in the right panel of Fig. 5.2. The resolution depends linearly on the squared invariant mass. The value of $\sigma = 0.00704 \; GeV^2/c^4$ corresponds to the resolution at largest invariant masses.
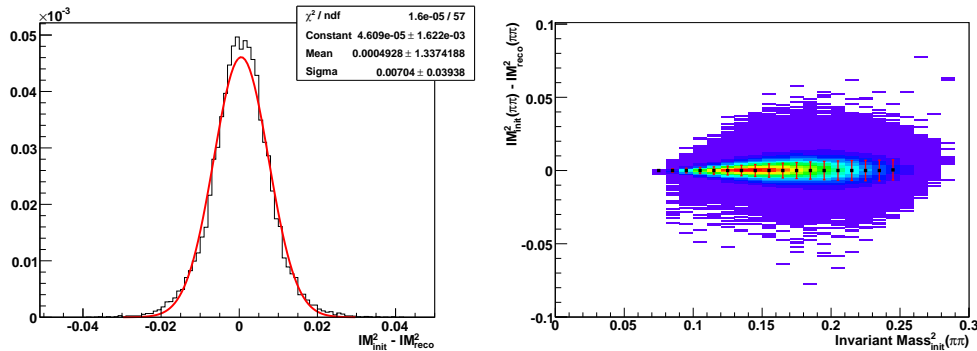
Figure 5.2: The resolution of $s_{\pi\pi}$ is studied from the difference of reconstructed and initial values in Monte Carlo simulations (left). Here, the distribution has a width of $\sigma = 0.00704 \; GeV^2/c^4$. To check for dependencies the resolution is studied as a function of $s_{\pi\pi}$ (right)

The resolution of the other variables has been obtained similarly. Tab. 5.1 summarizes the results. The error of the photon energy $E_\gamma(CMS_\eta)$ can be derived from the error of $s_{\pi\pi}$ by using Eq. 5.1. The relation is:

$$\sigma(E_\gamma) = \frac{0.5}{m_\eta} \cdot \sigma(s_{\pi\pi}) \tag{5.3}$$

This corresponds to the result of the Monte Carlo studies. The binning of the histograms in the following chapter is consistent with the respective resolutions.

5.1.3 Background Subtraction

At $\sqrt{s} = 3.418 \; GeV/c^2$, the center-of-mass energy of the present measurement, neither production cross sections nor differential distributions for the relevant background channels are published. Thus, a reliable description cannot be achieved with Monte Carlo simulations. Measurements at a lower center-of-mass energy of $\sqrt{s} = 3.356 \; GeV/c^2$ [B+06] report deviations of two-pion production from a homogeneous and isotropic phase space population. Thus, a model independent

Variable	Resolution
$s_{\pi\pi}$	$0.00704\,GeV^2/c^4$
$s_{\pi\gamma}$	$0.00439\,GeV^2/c^4$
$E_\gamma(CMS_\eta)$	$6.45\,MeV$
$cos(\theta_{\pi^+\gamma})$	0.0512

Table 5.1: Resolution of Dalitz plot variables

method of background subtraction has been chosen. It is based on a technique, previously used by the Crystal Barrel collaboration in the analysis of $\eta' \rightarrow \pi^+\pi^-\gamma$ [A+97].
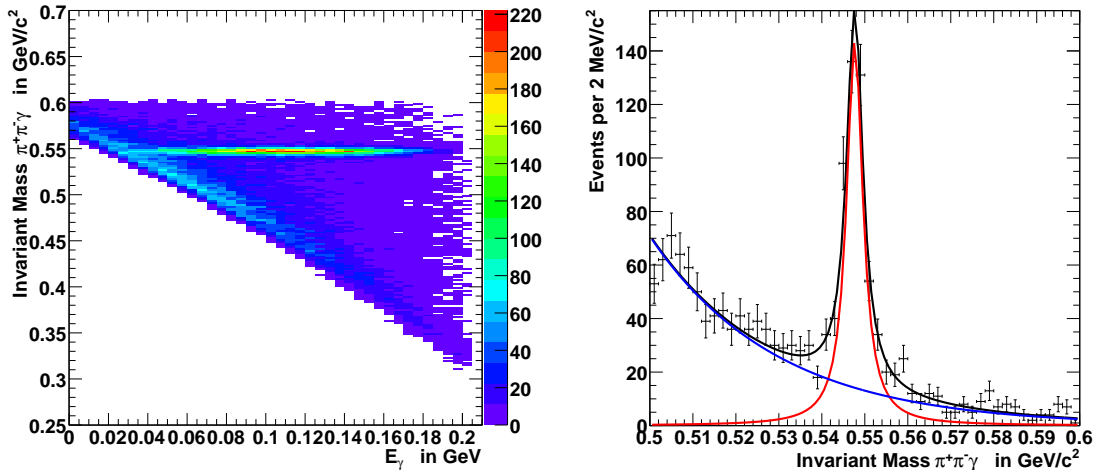
Figure 5.3: The continuous background is subtracted, by studying the distribution as a function of the invariant mass of the $\pi^+\pi^-\gamma$ system. The left panel illustrates the dependence for the photon energy E_γ. For each bin of the histogram, signal and background are fitted to extract the number of events stemming from the decay of the η meson. In the right panel the invariant mass is shown for $65\,MeV < E_\gamma \leq 70\,MeV$. Here, the background is fitted with an exponential function (blue) and the signal peak with a Lorentz function (red). The background-subtracted number of η decays in this range of E_γ corresponds to the integral of the signal curve.

Background is subtracted from a distribution by determining the contribution of the η-decay to the invariant mass of the reconstructed $\pi^+\pi^-\gamma$-system for each bin in the spectrum. In Fig. 5.3 this method is illustrated using the example of the photon energy in the rest frame of the η meson. The left panel shows the invariant mass as a function of the photon energy. Two enhancements are visible in the distribution. One is located at the mass of the η meson and is identified with the signal. The other one is found at small photon energies, along the lower edge of the kinematically allowed region of the distribution. This enhancement is due to background stemming from two-pion production. The signal content is extracted by studying slices of the two dimensional distribution. As an example, in the right panel of Fig. 5.3 the invariant mass of $\pi^+\pi^-\gamma$ is shown for photon energies in the range of $65\ MeV < E_\gamma \leq 70\ MeV$. The distribution is described by a Lorentz function on an exponential background. The peak is located at $547.65\ MeV$ which is the mass of the η meson and has a full width at half maximum of $4.57\ MeV$. The integral yields 435 ± 23 background-subtracted events from the total number of 1631 events in this photon energy bin.

This method of background subtraction accounts for contributions outside of the signal peak. Hence, it is best suited to remove background from multi-pion production. Background stemming from the η meson itself, like the contributions of the decay mode $\eta \to \pi^+\pi^-\pi^0$ will remain in the sample. This part can be subtracted with the help of Monte Carlo simulations, since the event generator applies a realistic model to generate this decay mode (see Section 3.1.2). The contribution of the decay mode $\eta \to \pi^+\pi^-\pi^0$ has been determined in Section 4.5.3 to be 2.8% of the events in the signal peak. It will be removed by subtracting Monte Carlo distributions, which have been scaled accordingly.

Dalitz Plot

Fig. 5.4 shows the measured Dalitz plot of the $\pi^+\pi^-\gamma$ system. In the left panel, the event distribution after the kinematic fit is illustrated. Here, all background is included which complies with the condition on the probability of the χ^2_{kf}. The populated region of the Dalitz plot exceeds the kinematically allowed region of the decay $\eta \to \pi^+\pi^-\gamma$, which is indicated by dashed lines in Fig. 5.4, at large values of invariant masses of the $\pi\gamma$ pairs. Since the η mass constraint has not been applied in the kinematic fit, the upper limit of the kinematically allowed region

is enhanced by the excess energy of $Q = 60\ MeV$. These limits are indicated by the dotted lines in Fig. 5.4. At low invariant masses of the $\pi\gamma$ pairs a strong enhancement in the population of the Dalitz plot can be seen. The inherent background is subtracted from each bin using the method described above. The signal content is extracted from the individual invariant mass distributions using a Lorentz function to describe the signal peak and an exponential function for the background.
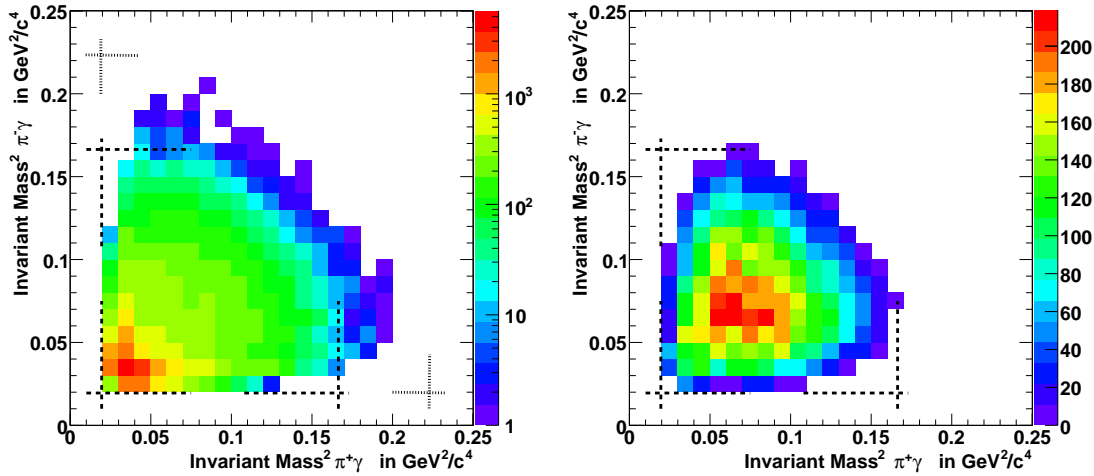
Figure 5.4: Measured Dalitz plot of the $\pi^+\pi^-\gamma$ system before (left) and after (right) background subtraction. The strong population of lowest invariant masses of $\pi\gamma$ before background subtraction corresponds to two-pion production as the strongest source of background. The kinematic limits of the η decay are illustrated with dashed lines. The dotted lines in the left panel show the limits of the available center-of-mass energy in the reaction $pd \to {}^3\mathrm{He}\ X$, which can be populated by background.

In the right panel of Fig. 5.4, the background-subtracted Dalitz plot is shown. The event distribution complies with the kinematic limits of the η decay. The strong enhancement at low invariant masses is removed. Instead, an enhancement at the center of the Dalitz plot is visible. It is symmetric with respect to the diagonal of equal invariant masses. The event distribution perpendicular to the diagonal is sensitive to the angular distribution of the $\pi^+\pi^-$ system. Assuming a uniform acceptance, the distribution decreases symmetrically from the center of the plot towards its borders. The shape matches an angular distribution described by $\frac{d\sigma}{d(cos(\theta))} \propto \sin^2(\theta)$. Thus, the Dalitz plot indicates the relative angular

momentum of the two pions to be $L = 1$. The acceptance correction is discussed in Section 5.1.4.

Pion Angular Distribution

The angular distribution of the π^+ in the rest frame of the two pions with respect to the photon is shown in Fig. 5.5. In the left panel of Fig. 5.5 the situation before background subtraction is illustrated. Here, the distribution has its maximum at large values of opening angles and decreases towards smaller values. At the smallest values the distribution increases again. The background subtraction is performed for each bin, as described above, using a Lorentz curve to describe the signal and a polynomial of fourth order to fit the background. The individual invariant mass distributions are shown in the Appendix B. The red histogram in the left panel of Fig. 5.5 indicates the continuous background removed in this way. The blue histogram shows the Monte Carlo distribution originating from the decay $\eta \to \pi^+\pi^-\pi^0$. It has been scaled according to 2.8% of the total η content and is subtracted from the data to account for the background in the η peak.
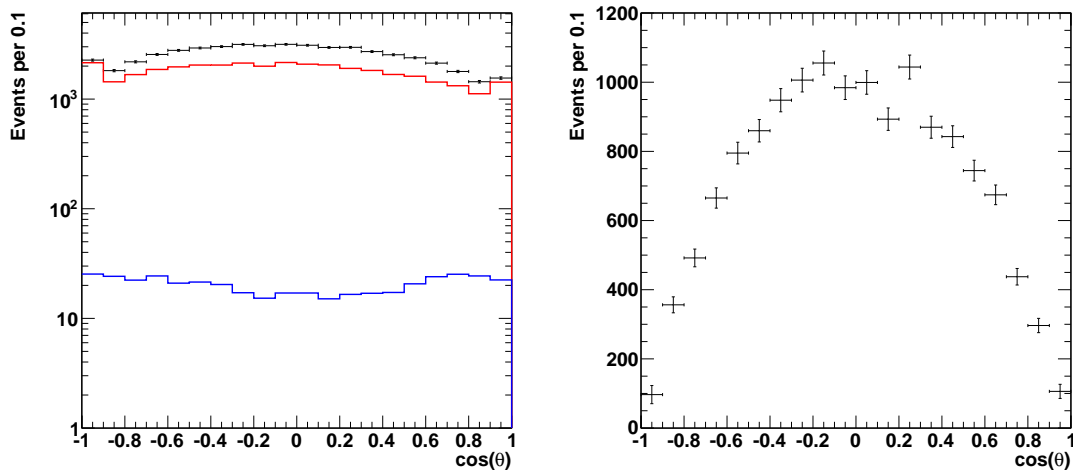
Figure 5.5: The pion angular distribution before background subtraction is shown in the left panel. The red histogram illustrates the continuous background and the blue histogram shows the background of $\eta \to \pi^+\pi^-\pi^0$ which is subtracted. The background-subtracted angular distribution is presented in the right panel.

In the right panel of Fig. 5.5 the distribution is shown after background subtrac-

tion. The relative amount of events removed as background is largest in the region of small opening angles between the photon and the pion. It can be assumed that these events stem from two-pion production since small opening angles were found as a characteristic feature of hadronic splitoffs (see Section 4.4.3). The shape of the background-subtracted distribution can be described by a polynomial of second order, which can be described by a $1 - x^2$ dependence. This corresponds to the observed event distribution in the Dalitz plot, and indicates a relative angular momentum of $L = 1$. This p - wave interaction between the two pions fulfills the requirement of odd angular momenta due to C-invariance (see Section 1.2) and was reported previously [G+70, L+73]. Before drawing final conclusions the distribution has to be corrected for efficiency.

Photon Energy

Fig. 5.6 shows the energy spectrum of the photons in the η rest frame. In the left panel the distribution is shown before background subtraction. The complete energy range up to the allowed maximum of 202.6 MeV is covered. Background is subtracted as described above, using a Lorentz curve on an exponential background to fit the invariant mass distributions of the individual bins in the range of 500 to 600 MeV/c^2. The individual invariant mass spectra can be found in Appendix B. The red histogram in the left panel of Fig. 5.6 shows the subtracted amount of continuous background. Additional background in the η peak is taken into account by subtracting the Monte Carlo distribution of the decay $\eta \to \pi^+\pi^-\pi^0$. Its contribution is shown with the blue histogram.

In the right panel of Fig. 5.6, the background-subtracted photon energy distribution is shown. It can be seen that the fraction of subtracted events is largest at energies lower than 120 MeV. Effects on the spectrum due to pion interactions are anticipated in this energy region. Thus, a careful background subtraction is essential. After the background subtraction the energy distribution starts at 25 MeV, indicating a reduced efficiency at low energies which will be discussed in detail in Sections 5.1.4 and 5.2.1. The distribution of the removed events suggests two-pion production as the major source of background. Low photon energies have been found as one of the characteristics of hadronic splitoffs discussed in Section 4.4.3. Before the background-subtracted photon energy distribution can be compared to model predictions it has to be corrected for efficiency effects.
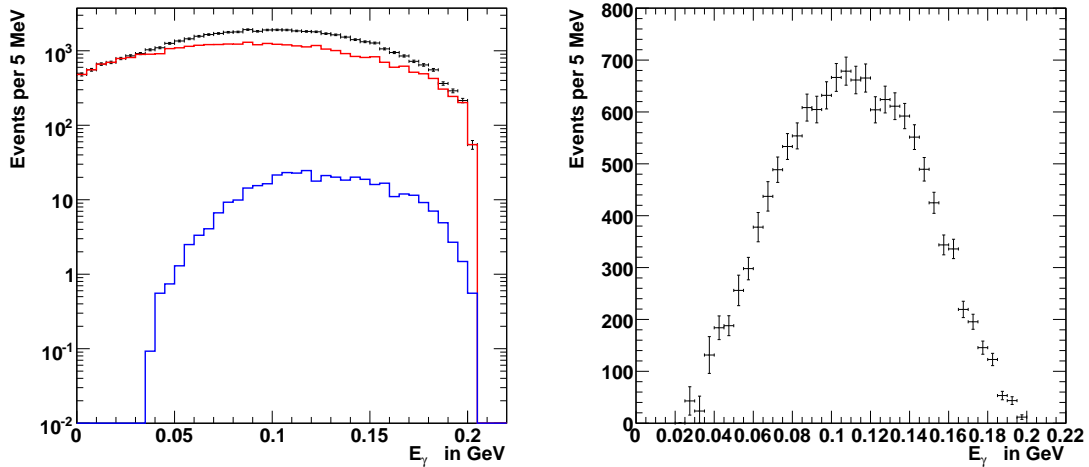
Figure 5.6: The energy distribution before background subtraction is shown in the left panel. The red histogram illustrates the continuous background and the blue histogram shows the background of $\eta \rightarrow \pi^+\pi^-\pi^0$ which is subtracted. The background-subtracted energy distribution is presented in the right panel.

Conclusion

The distributions show that the main background contribution originates from two-pion production. The model independent subtraction affected events with low photon energies and small opening angles between photon and pions. These properties are typical features of hadronic splitoffs, as demonstrated in Section 4.4.3.

The total number of reconstructed $\eta \rightarrow \pi^+\pi^-\gamma$ decays amounts to 13738 ± 136 events after background subtraction. With respect to the total statistics, this measurement is competitive with previous measurements discussed in Section 1.2.2. Before the spectra can be compared to theoretical distributions or previous measurements, the reconstruction efficiency has to be evaluated. This will be discussed in Section 5.1.4.

5.1.4   Efficiency Corrections

The shape of experimental distributions can be distorted by the limited acceptance, and the detection and reconstruction efficiency. To be able to draw conclusions about the underlying processes the distributions have to be corrected

for the overall efficiency. In Section 4.7, the geometric acceptance as well as the reconstruction efficiency have been discussed based on the detector simulation and event reconstruction.

The efficiency corrections are obtained by evaluating the fraction of initially generated events passing the analysis chain. In a realistic model of the physics processes all possible correlations should be included. If such a model is used to obtain the correction factors, it is sufficient to study the efficiency as a function of the distribution of interest. The applicability of this type of one-dimensional correction depends on the correctness of the model. To be independent of model assumptions, the corrections would have to be applied in every dimension of phase space.

One-dimensional efficiency correction

The simplest gauge invariant matrix element of the decay $\eta \to \pi^+\pi^-\gamma$ is chosen as the model for the one-dimensional acceptance corrections. It is described by $|\mathcal{M}^2| \sim k^2 q^2 sin^2\theta$, where k is the photon momentum in the η rest frame and q and θ are the momentum of either pion and the angle between the π^+ and the γ in the restframe of the two pions. The matrix element includes a p - wave interaction of the pions and, thus, fulfills the requirement of odd relative angular momenta of the two pions, which is imposed by C-invariance (see Section 1.2).

In the upper panels of Fig. 5.7 the background-subtracted experimental distributions are compared to the results of the analysis of Monte Carlo simulations of the signal decay based on homogeneous and isotropic phase space (blue histogram) and the simplest gauge invariant matrix element (red histogram). The Monte Carlo distributions have been normalized to the number of events in the experimental spectra. From the upper left panel it can be seen that the experimental angular distribution is, apart from the fluctuations in the region of $-0.1 \leq cos(\theta) \leq 0.4$, in agreement with the distribution of the matrix element. The phase space distribution fails to reproduce the distribution. In case of the photon energy, shown in the upper right panel neither of the Monte Carlo distributions are in agreement. Nevertheless, the distribution of the matrix element is similar in shape, but its center is shifted to higher photon energies. The phase space distribution differs in shape, but for energies lower 60 MeV it is in agreement with the experimental distribution.
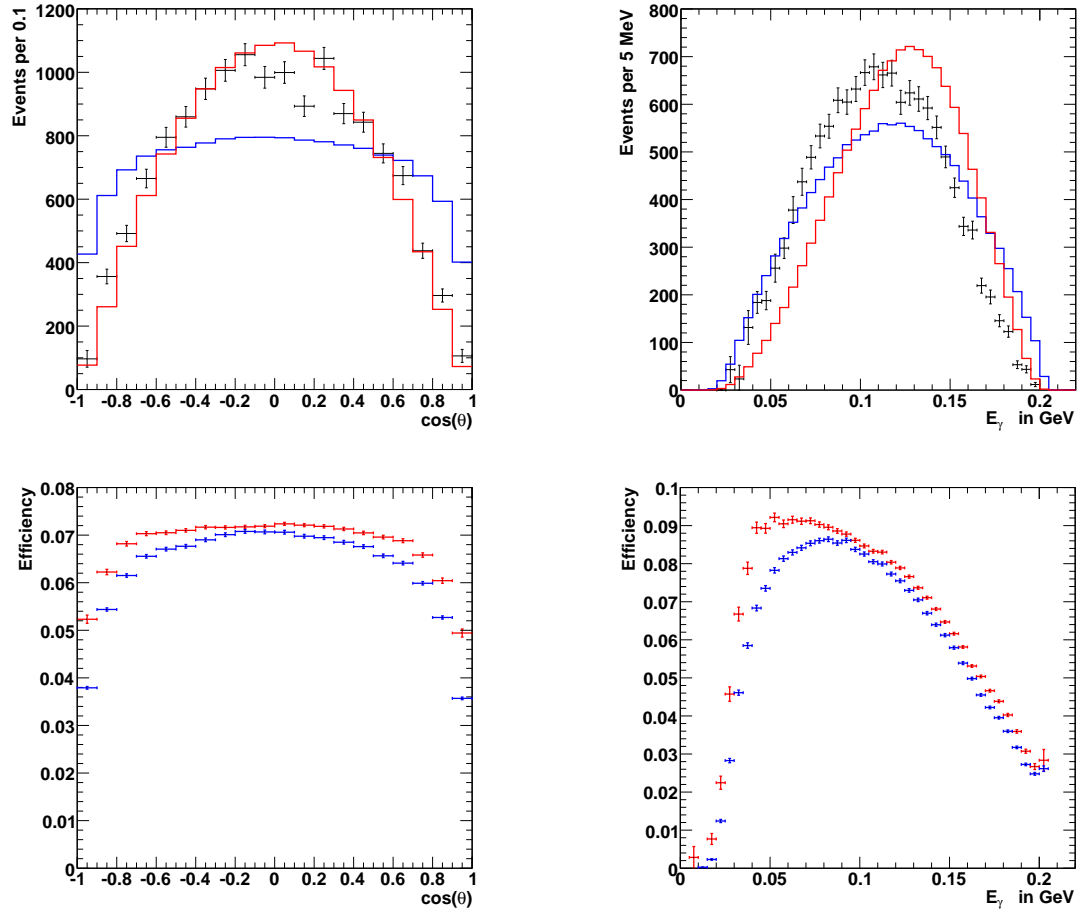
Figure 5.7: The comparison of the experimental angular (upper left) and photon energy distributions (upper right) with Monte Carlo phase space (blue) and the matrix element (red) favors the usage of the matrix element for efficiency corrections as it is able to reproduce the angular distribution and has a higher similarity in shape to the energy distribution. The angular (lower left) and energy (lower right) efficiency is model dependent.

The lower left panel shows the efficiency as a function of angle derived from phase space (blue) and from the matrix element (red). For the matrix element the distribution is flat apart from a small drop at low angles between the photon and the pions. Thus, the angular distribution is essentially not distorted by the efficiency correction. The efficiency extracted from Monte Carlo using homogeneous and isotropic phase space is generally lower compared to the matrix element. In addition, the efficiency is not flat but decreasing from its maximum value at large

opening angles towards smaller opening angles of the photon and either of the
pions. Using the phase space distribution to correct for the efficiency would lead
to an overcorrection of the distribution.

The efficiency as a function of the photon energy is shown in the lower right
panel of Fig. 5.7. Generally, the behavior of the two models is similar. For energies
below 15 MeV the efficiency is 0. Each distribution rises steeply and then drops
slowly with increasing energies. A striking difference between both models is seen
in the energy range of 30 $MeV \leq E_\gamma \leq 90~MeV$. For the matrix element the
maximum efficiency is reached at 40 MeV. The efficiency of the phase space
simulation is significantly lower at this energy. It reaches its maximum efficiency
at 80 MeV. The difference in efficiency between the models is about 20% in this
region, in which the agreement between experimental and phase space distribution
is better. Using the matrix element could thus lead to an insufficient correction
in this region, which is taken into account as a source of systematic uncertainties
in Section 5.2.
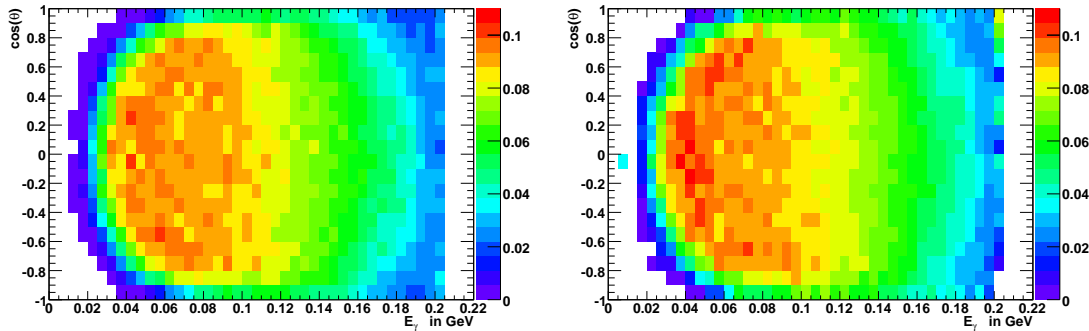
Figure 5.8: The correlation of the energy and angular efficiency shows regions with
zero efficiency at low photon energies and small opening angles between either pion
and the photon for the simulation of phase space (left) as well as for the simulation of
the simplest gauge invariant matrix element (right). The location of the efficiency gaps
indicates that they are caused by the splitoff suppression.

The vanishing efficiency at small energies is correlated with the decreased ef-
ficiency at small opening angles. In Fig. 5.8 the correlation of the energy and
angular efficiency is shown for phase space distributions (left panel) and for
Monte Carlo based on the simplest gauge invariant matrix element (right panel).
The correlation plots reveal that the efficiency is zero for photon energies up to

40 MeV in these regions. This behavior corresponds to the conditions discussed in Section 4.4.3 and used for suppressing events with hadronic splitoffs.

The efficiency correction is model dependent as shown by different efficiencies for phase space and the matrix element. From Fig. 5.7 a better agreement of the distributions of the matrix element with the experimental spectra, especially with respect to the angular distribution, is found. Thus the efficiency correction is performed according to the simplest gauge invariant matrix element. In section 5.2 the model dependence is discussed as a source of systematic uncertainty.
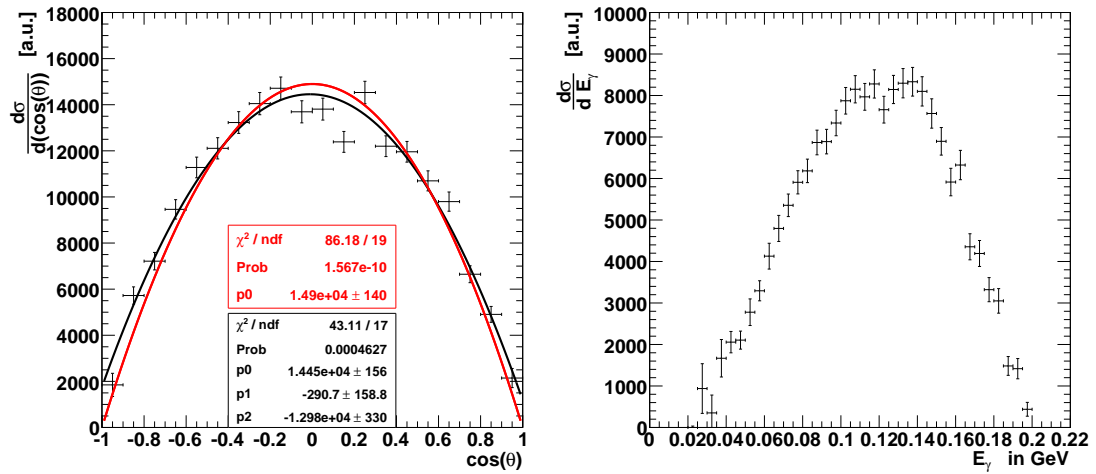
Figure 5.9: Efficiency corrected angular (left) and energy (right) distributions. The angular distribution is compatible with P-wave interaction (red curve). A better fit is achieved allowing for a linear term in the polynomial of second order (black curve), which is caused by the fluctuations in the range of $-0.1 \leq \cos(\theta) \leq 0.4$.

Fig. 5.9 shows the efficiency corrected angular and energy distributions. Due to the mostly uniform efficiency the shape of the angular distribution remains essentially unchanged and is shown in the left panel. The distribution is fitted with a polynomial of the form

$$f(x) = c \cdot (1 - x^2), \tag{5.4}$$

where c is the free parameter of the fit. It describes the shape of the angular distribution in case of the P-wave interaction. The result of the fit is shown with the red curve. Apart from the fluctuations in the region of $-0.1 \leq \cos(\theta) \leq 0.4$ the distribution matches the polynomial, resulting in a reduced χ^2 of 4.54. As a

test, the fit is repeated using a polynomial of second order with 3 free parameters. The result has a lower χ^2 value of 2.54 and is represented by the black line in Fig. 5.9. The constant and quadratic coefficients of the polynomial are identical in their absolute values within the errors. This behavior matches the relation describing p - wave interaction. However, the fit yields a small but non-vanishing linear term. It is influenced by the fluctuations at the center of the distribution, but it might also indicate a flat background in the spectrum, which has not been taken into account. This will be checked in the determination of systematic errors.

The efficiency corrected photon energy distribution is shown in the right panel of Fig. 5.9. At the highest energies the distribution is enhanced, which results in a broader maximum of the distribution in the region of $100 \ MeV \leq E_\gamma \leq 140 \ MeV$. The biggest effect of the efficiency correction should be seen for photon energies below $40 \ MeV$. Since this region is hardly populated after the background subtraction, a distortion of the spectrum is not observed.

Further discussion of the results follows in Section 5.3 after the systematic uncertainties have been determined.

Multi dimensional efficiency correction

As an approach to a multi dimensional correction, a two-dimensional efficiency correction is performed. The correction factors are derived for each bin of the Dalitz plot. In this way the relevant degrees of freedom of the $\pi^+\pi^-\gamma$ system are taken into account.

In the left panel of Fig. 5.10, the efficiency is shown as a function of the Dalitz plot. The maximum efficiency of 9% is found close the center of the distribution at squared invariant masses of $0.05 \ GeV^2/c^4$. At borders of the distribution the efficiency is smallest. The steepest drop in efficiency is found at lowest invariant masses. Here the efficiency decreases from its maximum value to approximately 2%. In the bin corresponding to the smallest kinematically allowed invariant masses the efficiency decreases to 0. The features of the two-dimensional efficiency distribution are in agreement with the one dimensional projections discussed above. Five bins at the rim of the Dalitz plot show an apparently high efficiency. Taking into account the statistical errors, the efficiency in these bins can be neglected. In the efficiency correction, these bins are ignored.
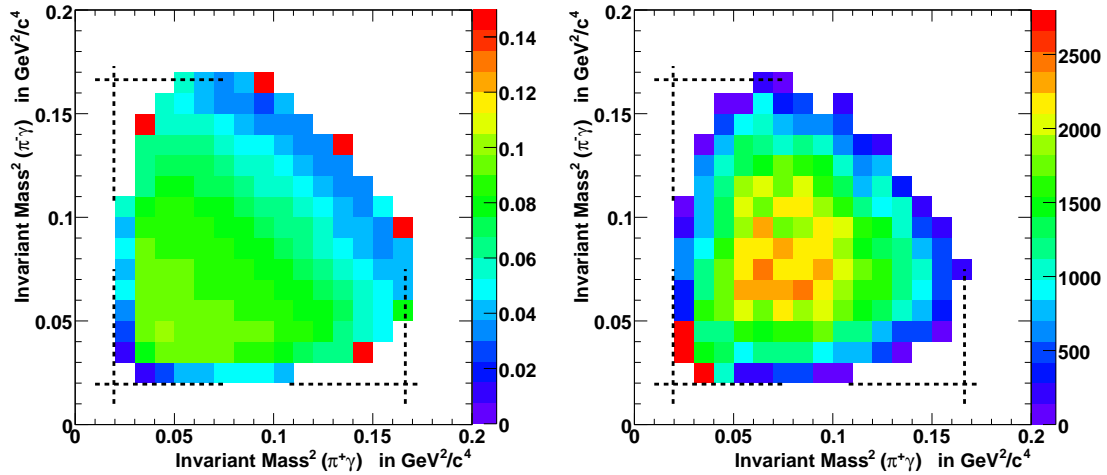
Figure 5.10: The efficiency as a function of the Dalitz plot is shown in the left panel. Zero efficiency is found in the bin at smallest invariant masses. The five bins of apparently high efficiency at the rim of the plot are due to statistical fluctuations and can be ignored due to the errors. In the right panel the efficiency corrected Dalitz plot is shown. The event distribution is compatible with P-wave interaction. The largest entries at smallest invariant masses hint at background which could be not properly subtracted. The dashed lines indicate the kinematically allowed region of the η decay.

The right panel of Fig. 5.10 shows the efficiency corrected Dalitz plot of the $\pi^+\pi^-\gamma$ system. The correction has not distorted the features of the event distribution observed in Fig. 5.4. The population perpendicular to the diagonal is symmetrically decreasing from the center of the plot to the borders. This behavior corresponds to the angular distribution discussed above and indicates a relative angular momentum of $L = 1$ between the two pions. At the lower border of the Dalitz plot, three bins apparently show the maximum of the population. However, in this region the amount of background before subtraction as well as the effect of the efficiency correction is largest. It has to be assumed that the maximum of the distribution is due to background which has not been removed properly.

5.2   Systematic Uncertainties

In order to get an estimate of the systematic uncertainties, every analysis condition is revisited. By varying each condition, its influence on the final result is tested. It is assumed that the sources of systematic errors are uncorrelated, so that only one condition is changed at a time while the others are kept constant. In addition to the analysis chain, some issues of the data taking are considered as sources of systematic uncertainties. The total systematic uncertainty is calculated as the quadratic sum of the individual contributions.

5.2.1   Conditions before kinematic fitting

Conditions based on energy-momentum conservation

The conditions discussed in Sections 4.4.1 and 4.4.2 make use of energy and momentum conservation to suppress background contributions. Events which are rejected due to these conditions should also be rejected after the kinematic fit due to the cut on the probability distribution $P(\chi^2_{kf}, N)$. In order to determine the contribution to the systematic uncertainties, two scenarios are considered.

In a first test, the analysis is repeated omitting all conditions involving energy and momentum conservation before the kinematic fit. These are the condition on missing energy and missing momentum in the events selection (see Fig. 4.7) and the conditions on the missing mass of the $^3\text{He}\gamma$ (see Fig. 4.10) and $^3\text{He}\pi^+\pi^-$ system (see Fig. 4.11). The resulting distributions are shown as open circles in Fig. 5.11. For comparison the result of the original analysis chain is shown as dashed histogram. Energy and angular distributions are reproduced with a small positive offset. The offset is smaller than the statistical errors of the distribution.

In the second test, the condition on the missing mass of the $^3\text{He}\pi^+\pi^-$ system, which was shown to be the most invasive with respect to the signal efficiency, is chosen to be stricter. Only those events are accepted, which have negative values for the missing mass. Background from three-pion final states is removed more efficiently. As the distribution of the signal channel peaks at mass zero the reconstruction efficiency is reduced by a factor two. The solid circles in Fig. 5.11 show the result of this test. For the photon energy as well as for the angular distribution significant deviations from the original result are found. For photon
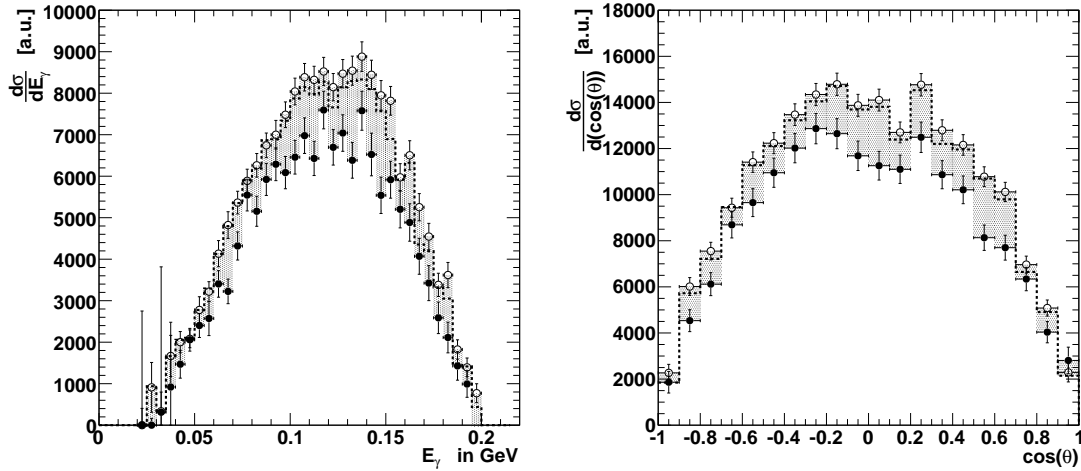
Figure 5.11: Systematic uncertainties in the angular (right) and energy (left) distributions arising from the conditions involving energy and momentum conservation before the kinematic fit. Open circles show the result of an analysis without the conditions. Solid circles result from an analysis with a stricter condition on the missing mass of the $^3\mathrm{He}\pi^+\pi^-$ system. The dashed histogram is the result of the actual analysis.

energies in the range of $80~MeV \leq E_\gamma \leq 160~MeV$ the deviation is larger than the statistical error by a factor 2 to 3. A similar deviation is found in the angular distribution for values of $cos(\theta)$ in the range of $-0.2 \leq cos(\theta) \leq 0.6$. Since the condition now rejects most of the events with three pions in the final state, the large systematic deviation might hint at an incorrect description of the three-pion channels in the Monte Carlo simulations.

Hadronic Splitoffs

In Section 4.4.3, the relation between the energy of a photon candidate and the distance to either of the charged particles was used to suppress the contributions of two-pion production from hadronic splitoffs. As shown in Fig. 4.13, the condition is a compromise between maximum background suppression and good reconstruction efficiency. Two scenarios are investigated in order to estimate the contribution of this condition to the systematic uncertainties.

The analysis is redone using the condition for splitoff rejection of maximum significance. It is given by the hyperbolic relation $E_\gamma > \frac{3.4~GeV \times deg}{\sphericalangle(\gamma,\pi)}$, where E_γ is
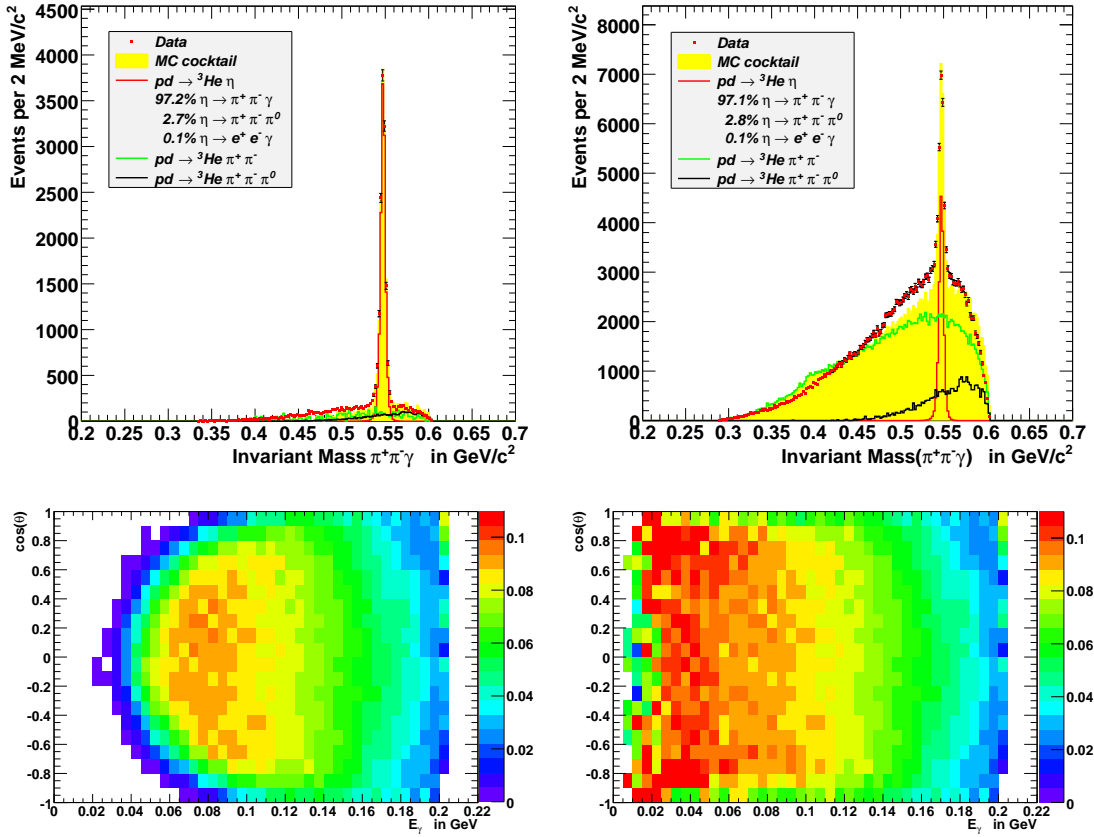
Figure 5.12: To investigate the contribution of the splitoff suppression to the systematic uncertainties the analysis is repeated with a stricter condition (left) and without the condition. A stricter condition improves the signal-to-background ratio, while it becomes worse without the condition. The correlation plots of the efficiencies in the bottom panels illustrate that the suppression of splitoff causes gaps in the efficiency which become larger with stricter conditions.

the photon energy and $\sphericalangle(\gamma, \pi)$ is the opening angle between the photon and the nearest pion in the laboratory frame (see Fig. 4.13). The invariant mass distribution after the kinematic fit is shown in the upper left panel of Fig. 5.12. Here, a peak to background ratio of 5.15 is achieved, which is better by a factor of 3 compared to the result of the actual analysis chain, shown in Fig. 4.20. The improvement in signal purity causes an increased loss of reconstruction efficiency. In the lower left panel of Fig. 5.12 the efficiency correlation of the angular distribution of the pions and the photon energy in the η restframe is shown. The

region without acceptance at low photon energies is increased compared to the actual analysis chain (see Fig. 5.8), so that photons up to 70 MeV cannot be reconstructed. This is directly visible in the resulting photon energy distribution, shown with solid circles in the left panel of Fig. 5.13. The distribution starts only at 40 MeV and has a negative offset up to energies of 120 MeV. For higher energies the result of the actual analysis chain is reproduced almost exactly. In case of the angular distribution of the pions, presented in the right panel, the additional loss of efficiency causes a general offset compared to the actual result shown with a dashed histogram.
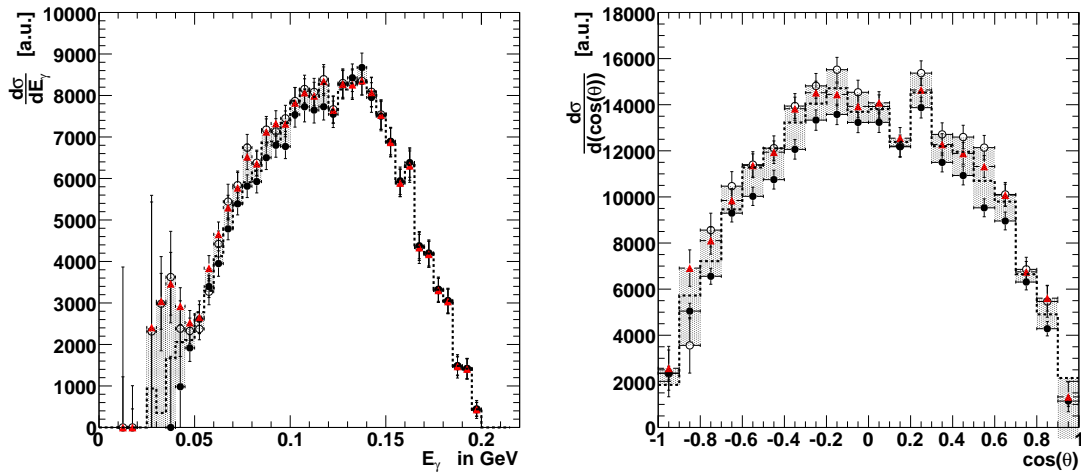
Figure 5.13: Systematic uncertainties in the angular (right) and energy (left) distributions arising from the condition suppressing hadronic splitoffs. Open circles show the result of an analysis without the conditions. Solid circles are the result of the condition with maximum significance. The red triangles illustrate the result of an alternative approach of background suppression by comparing the probability distributions of different hypotheses after the kinematic fit (see text). The dashed histogram is the result of the actual analysis.

In the alternative scenario the analysis is repeated without an additional condition for splitoff suppression. The upper right panel of Fig. 5.12 shows the invariant mass distribution of the $\pi^+\pi^-\gamma$ system after the kinematic fit and the usual condition on the probability distribution $P(\chi_{kf}, N)$. A large amount of two-pion background complies with the condition $P(\chi_{kf}, N) \leq 0.1$, resulting in a ratio of η peak and background of 0.35. This simple condition on the probability distri-

bution does not suppress background effectively. A benefit of this approach is the increased reconstruction efficiency, shown in the correlation plot in the lower right panel of Fig. 5.12. Regions without acceptance are only found for photon energies in the η rest frame below 10 MeV, which can be attributed to the threshold of 20 MeV on photon candidates in the event selection (see Section 4.3). However, the increased amount of multi-pion background is problematic in the background subtraction. This is best seen in the photon energy distribution in Fig. 5.13, where the result of this analysis scenario is shown with open circles. A strong enhancement compared to the result of the actual analysis is visible at energies of 40 MeV. Here, the kinematic limit of the invariant mass region populated by two-pion production is at the η mass, as shown in Fig. 5.3. Background mistaken for a part of the signal peak causes the structure seen in the distribution. For photon energies in the range of 40 $MeV \leq E_\gamma \leq 90$ MeV there is a small offset compared to the result of the original analysis, which can be attributed to the absence of gaps in the reconstruction efficiency. The same argument holds for the angular distribution, which is again reproduced with an offset.

As a variation of this scenario, an additional condition on the probability distribution $P(\chi_{kf}, N)$ is applied after the kinematic fit. As discussed in Section 4.5, every event is fitted twice, testing the hypothesis of the decay $\eta \to \pi^+\pi^-\gamma$ and testing the hypothesis of two-pion production by omitting the photon as splitoff. Background from two-pion production can be reduced on an event-by-event basis, by selecting events which have a larger probability $P(\chi_{kf}, N)$ for the signal decay than for the background reaction, as demonstrated in Fig. 4.21. In the left panel of Fig. 5.14 the invariant mass distribution of the $\pi^+\pi^-\gamma$ system after the selection of the best probability is shown. The continuous background of multi-pion production is reduced showing an η-peak to background ratio of 0.61. This is an improvement of a factor 2 compared to the scenario without any additional condition for splitoff suppression, but still a factor of 3 lower compared to the ratio achieved in the actual analysis chain. In the right panel of Fig. 5.14 the efficiency correlation of the pion angular distribution and the photon energy distribution is shown. A slight reduction in the reconstruction efficiency can be seen in the region of small photon energies, but holes in the acceptance are not created by the additional condition.

The resulting energy and angular distributions are shown with red triangles in Fig.5.13. After background subtraction and efficiency correction the energy
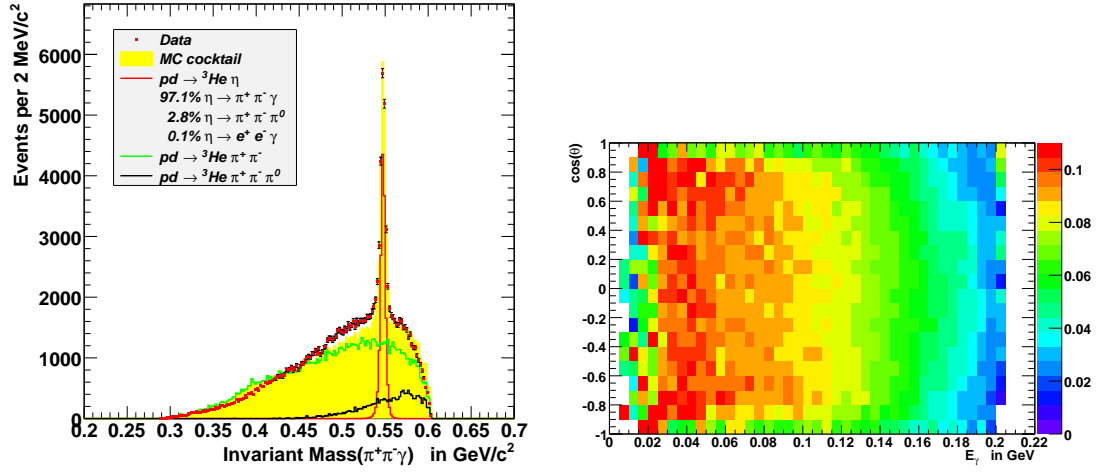
Figure 5.14: Background can be rejected by comparing the probabilities of different hypothesis for the kinematic fit. The left panel shows the invariant mass distribution of the $\pi^+\pi^-\gamma$ system after rejecting the events with a higher probability for two-pion production. This method improves the ratio of η-peak to pion backround by a factor of 2. As shown in the right panel this method does not cause additional gaps in the efficiency.

distribution reproduces the result of the analysis chain without conditions on splitoffs almost exactly. This includes the enhancement at $40\ MeV$ photon energy, which is due to background which could not be eliminated in the background subtraction. For the angular distribution the result of this enhanced alternative analysis agrees with the result of the actual analysis within the statistical errors.

5.2.2 Probability Distribution

The condition on the probability distribution $P(\chi_{kf}, N)$ should select the uniform part of the distribution. In Section 4.5.3 the distribution was considered flat for probabilities $P(\chi_{kf}, N) \geq 0.1$. Here, the effects of different conditions on the probability distribution are evaluated.

In Fig. 5.15 the conditions are indicated by the dashed lines. The lower edge of the accepted region of probabilities is varied in steps of 0.05 from a value of 0.05 to a value of 0.3. An additional condition is introduced at the higher edge. Here, the accepted range is varied from 0.7 to 1 in steps of 0.05. The analysis is

Figure 5.15: The systematic uncertainty introduced by the condition on the probability distribution $P(\chi_{kf}, N)$ is estimated by varying the selected range. The dashed lines show the different conditions used for testing. The top red arrow indicates the actual condition and the lower two indicate the conditions showing the largest systematic deviations.
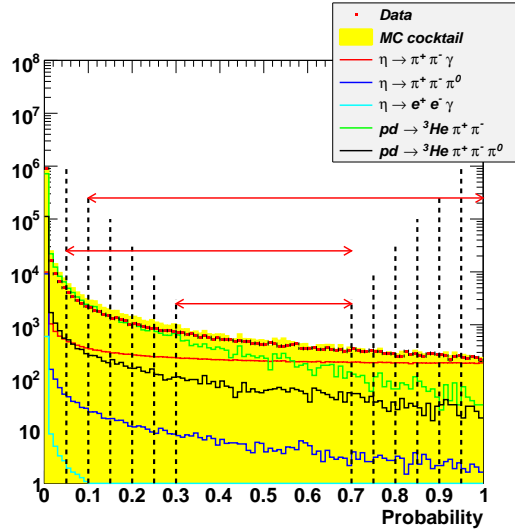
repeated for each possible combination. In Fig. 5.16, the differential distributions of the two conditions are presented which show the largest systematic deviations.
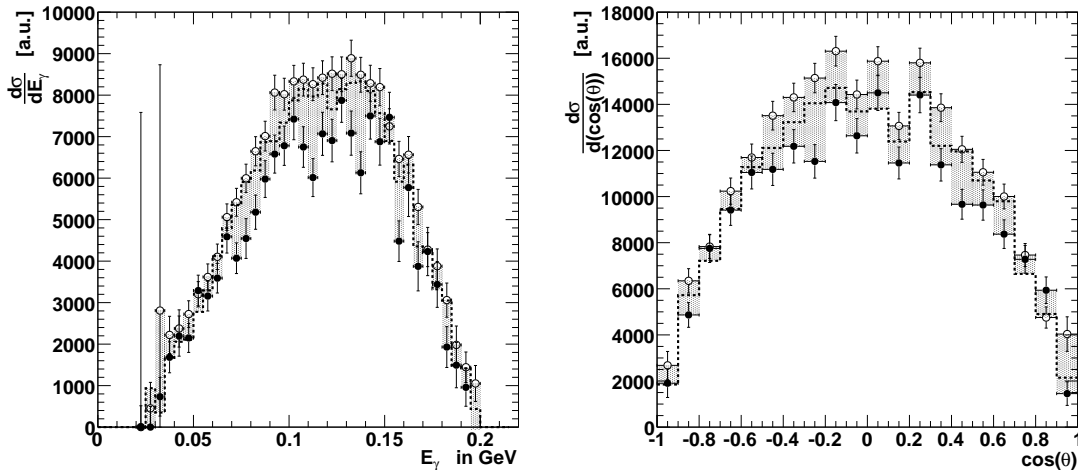
Figure 5.16: Systematic uncertainties in the angular (right) and energy (left) distributions arising from the condition on the probability distribution $P(\chi_{kf}, N)$ of the kinematic fit. Accepting probabilities in the range $0.05 \leq P(\chi_{kf}, N) \leq 0.7$ results in the distributions shown with open circles. For the solid circles events in the range $0.3 \leq P(\chi_{kf}, N) \leq 0.7$ are accepted. The dashed histogram is the result of the actual analysis.

Accepting only events in the probability range $0.05 \leq P(\chi_{kf}, N) \leq 0.7$ results in the distributions shown with open circles. Compared to the result of the original

analysis chain, which is shown with a dashed line, a constant offset is introduced in both distributions. The size of the offset is smaller than the statistical errors of the distribution. As can be seen from Fig. 5.15, rejecting events with probabilities $P(\chi_{kf}, N) \geq 0.7$ reduces the fraction of signal events in the sample, thus, the effects of contributing background are enhanced. The additional background that is included by decreasing the lower edge of the range of accepted probabilities is removed by the background subtraction.

The solid circles in Fig. 5.16 represent the result of accepting events in the probability range $0.3 \leq P(\chi_{kf}, N) \leq 0.7$. A deviation from the original angular and energy distributions by more than a factor 2 to 3 of the statistical error is observed in the ranges of $80 \ MeV \leq E_\gamma \leq 160 \ MeV$ and $-0.2 \leq cos(\theta) \leq 0.6$. Similar deviations have been observed in Section 5.2.1. A higher threshold on the probability distribution rejects more of the contributing background reactions. Thus, the observed systematic deviation might indicate background which is not removed properly in the actual analysis.

5.2.3 Background Subtraction

As discussed in section 5.1.3, background is subtracted by fitting a Lorentz curve to describe the signal peak together with an exponential function or a polynomial of fourth order to describe the background. The signal content is extracted by integrating the fit of the Lorentz curve. To estimate the systematic error which is introduced by demanding a defined shape of the signal, instead of integrating the fit of the signal, the fit of the background is subtracted from the original distribution. The integral number of remaining events is taken to be the signal content. In Fig. 5.17 the results of this method are shown using open circles. The angular distribution reproduces the result of the original method, shown with a dashed histogram, within the statistical errors. A small positive offset indicates that fluctuations in the background have been included into the signal content. This is seen from the individual distributions shown in Appendix B. A similar behavior is seen for the photon energy distribution at values larger $80 \ MeV$. Up to energies of $170 \ MeV$ the deviation from the original distribution even exceeds the statistical error.

This method of background subtraction is still biased by the signal shape. In order to be independent of the distribution of the signal events, the individual
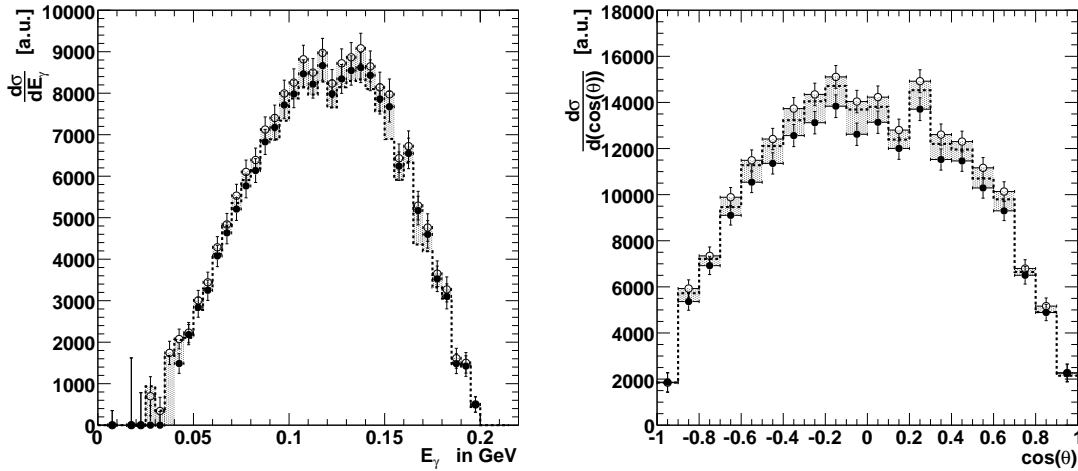
Figure 5.17: Systematic uncertainties in the angular (right) and energy (left) distributions arising from the background subtraction assuming a shape of the signal (open circles) and excluding the signal range from the fit (solid circles). The dashed histogram is the result of the actual analysis, for comparison. Here, the fit of the signal was integrated for signal extraction.

invariant mass distributions are fitted by a function describing the background only. The mass range from 535 MeV/c^2 up to 560 MeV/c^2 is excluded. Again, the number of signal events is obtained from the integral of the spectrum after subtracting the fit of the background. The result is shown with solid circles in Fig. 5.17. The angular distribution is reproduced with a negative offset. In Appendix B the result of this fit of the background is shown with a green line in the individual invariant mass spectra. It can be seen that a larger amount of background is subtracted in the signal region, where in the original method these events belong to the tails of the Lorentz curve fitted to the signal peak. The same effect is observed for the energy distribution of the photon, where the background subtraction assuming a signal shape yields a larger number of entries than the methods discussed here. The excess at energies larger 80 MeV compared to the original result is again due to remaining background which is now inherent in the amount of signal events.

5.2.4   Efficiency correction

Fig. 5.7 demonstrates that the efficiency correction is model dependent. The simplest gauge invariant matrix element is used for the corrections because it is in good agreement with the experimental spectra with respect to the angular distribution. For photon energies smaller than 60 MeV phase space was shown to be in better agreement with data than the matrix element. The difference between the efficiency corrections is regarded as the contribution to the systematic uncertainties.
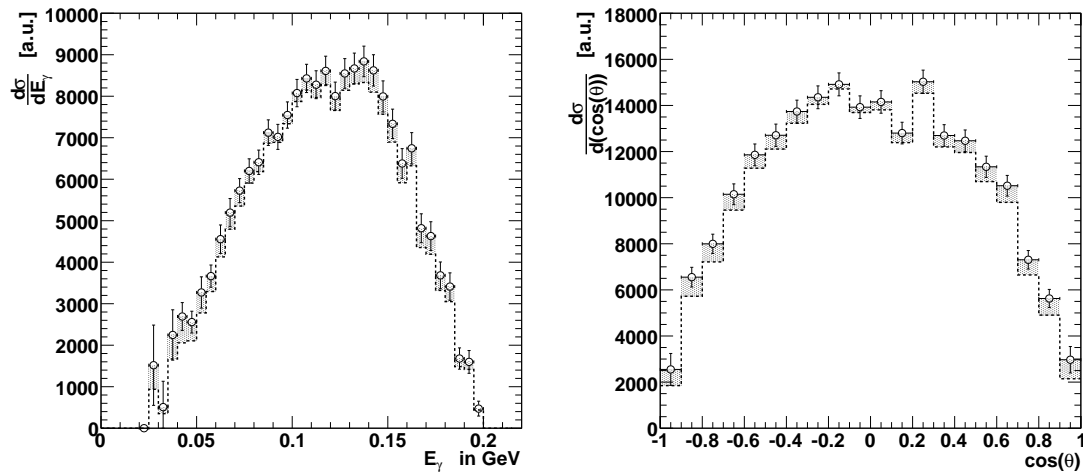
Figure 5.18: Systematic uncertainties in the angular (right) and energy (left) distributions due to the efficiency correction are estimated by comparing the actual result (dashed histogram) with distributions corrected for efficiency using Monte Carlo phase space (open circles).

The open circles in Fig. 5.18 show the resulting energy and angular distributions after the efficiency correction based on homogeneous and isotropic phase space. The deviations from the result of the actual analysis, shown with the dashed histogram, correspond to the differences in efficiency, shown in Fig. 5.7. For energies above 60 MeV the distribution of the photon energy is reproduced within the statistical errors. A small and almost constant positive offset is seen. In the lower energy range the distribution corrected with phase space exceeds the original result, showing a small structure in the low energy tail at 40 MeV. The angular distribution is reproduced with an offset increasing from the center of the

distribution towards the borders. In the center of the distribution the size of the offset is compatible with the statistical errors.

5.2.5   Operation modes of the accelerator

As discussed in Section 4.1, the operation mode of the COSY ring was changed to obtain longer beam lifetimes. Instead of compensating the mean energy loss of the beam with the Barrier Bucket cavity, the beam orbit was allowed to change due to the energy loss and the full acceptance of the COSY ring was exploited. In the analysis, this was taken into account by defining the beam momentum as a function of the cycle time. 48.86% of the data was taken using the Barrier Bucket cavity and the remaining 51.14% were taken with the modified setting of the accelerator. The respective experimental runs are analyzed separately to check for systematic effects due to the change in the beam conditions. The results are scaled according to the fraction of the complete sample.
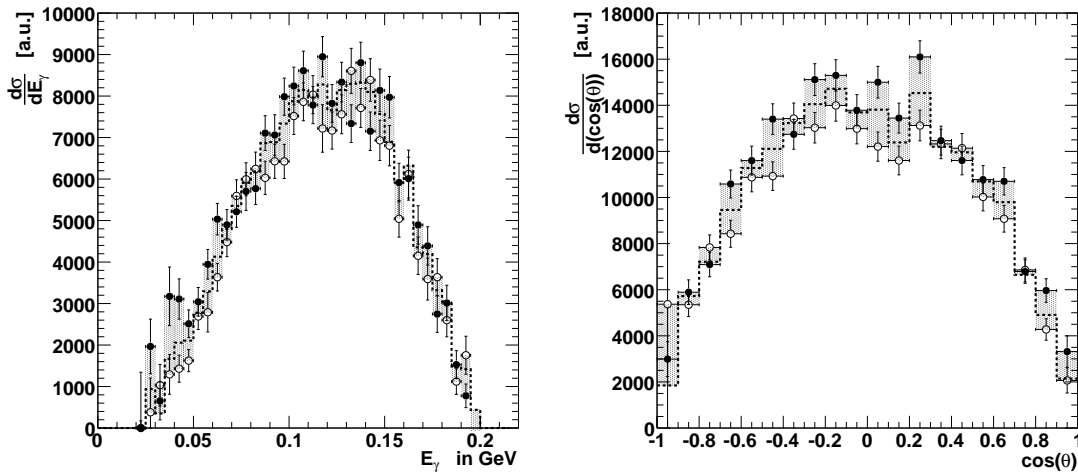
Figure 5.19: Systematic uncertainties in the angular (right) and energy (left) distribution due to the change of the operation mode of the accelerator (see Section 4.1). The open circles represent the results of the period with energy loss compensation of the beam by the barrier bucket cavity and the solid circles show the results of the period with energy loss of the beam. The individual results have been scaled according to the fraction of the complete data set to be compared to the full result, shown as the dashed histogram.

As shown in Fig. 5.19, the data taken with the compensation of the mean energy loss of the beam (open circles) as well as the data with energy loss of the beam (solid circles) reproduce the original result of the analysis (dashed histogram) within the statistical errors. Systematic deviations which might have been introduced by the change of the accelerator settings are smaller than the uncertainties of the analysis chain.

5.2.6 Luminosity dependence

To monitor the luminosity during data taking the trigger *CC1* is used. It demands at least one hit in the first layer of the Range Hodoscope in coincidence with at least one hit in the central part of the Plastic Scintillator Barrel, thus, it is triggering on elastic and quasi-elastic scattering. Fig. 5.20 shows the distribution of average *CC1* rates per run of the analyzed data sample. The mean rate of the distribution is 750 *kHz*. A separated group of runs at rates almost twice as high as the average rate is visible.
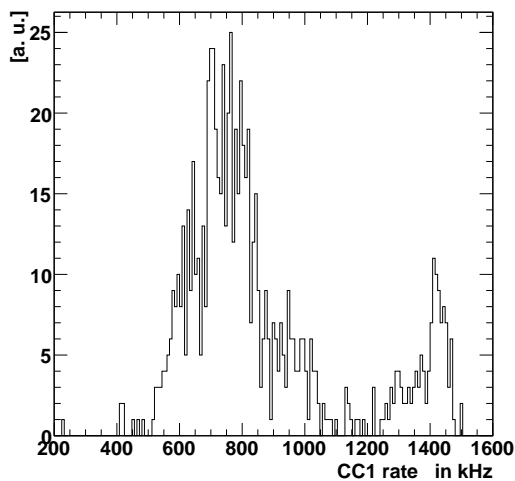
Figure 5.20: The distribution of the average *CC1* rate per run is shown, revealing two separate groups of runs at a mean *CC1* rate of 750 *kHz* and 1400 *kHz*.

The systematic influence of the different luminosities is estimated by dividing the initial sample into three parts. The first part comprises all runs with an average *CC1* trigger rate below the mean value of 750 *kHz*. It contains 46.01% of the analyzed data set. The second subset contains runs with an average trigger rate of 750 $kHz \leq CC1 \leq 1100\ kHz$. This corresponds to 44.69% of the data set. The remaining 9.3% of events form the third subgroup, allowing to study effects at the highest luminosities, with *CC1* rates larger than 1100 *kHz*. Each of the

three subsets is analyzed independently. The results are scaled according to the fraction of the complete data set in order to be compared to the original result.
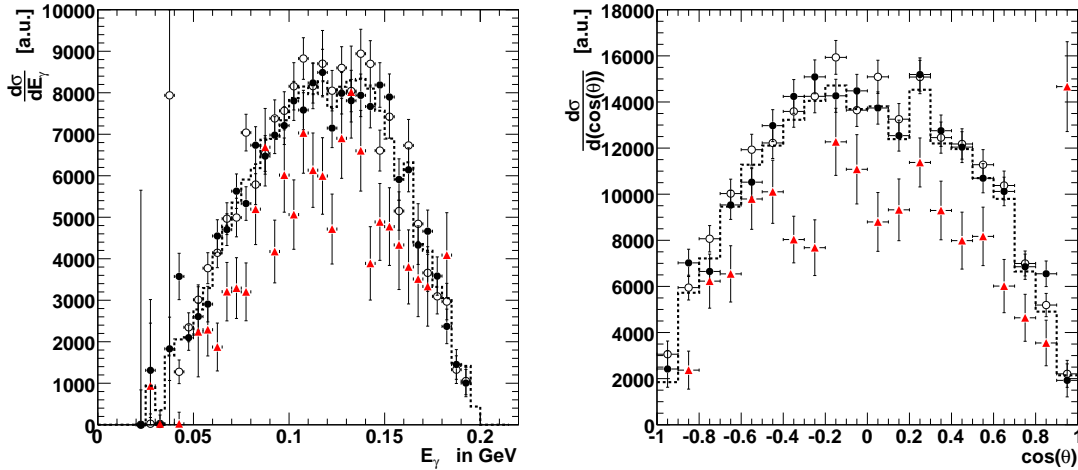
Figure 5.21: Systematic uncertainties in the angular (right) and energy (left) distributions due to different luminosities during data taking, as monitored by the *CC1* trigger rate. The resulting distributions are illustrated by open circles, for luminosities lower than the mean value, solid circles, for luminosities higher than the mean value, and red triangles for highest luminosities. The three distributions have been scaled according to their fraction of the complete data to be compared to the full result, shown with a dashed histogram.

The energy distribution of the photon, displayed in the left panel of Fig. 5.21 is reproduced by the sample of lower (open circles) and medium (solid circles) luminosities. Deviations from the original result (dashed line) are well below the size of the statistical errors. The angular distribution is reproduced with a constant, positive offset which matches the size to the statistical errors. The results of the event fraction taken at highest luminosities (red triangles) shows significant deviations from the original result. On average the energy and angular distributions at the highest luminosity are smaller by two to three times the size of the statistical error. This luminosity dependent deviation might originate from variations in the reconstruction efficiency due to higher rates of chance coincidences.

Summary

The individual contributions to the systematic error are added quadratically. Positive and negative deviations are summed independently, resulting in asymmetric systematic errors. The contribution of maximum rates from the test of luminosity dependence affects less than 10% of the complete data sample, thus, it has been scaled accordingly. Fig. 5.22 shows the distribution of the photon energy in the rest frame of the η meson and the angular distribution of the pions. The error of each bin is indicated by the shaded area. It is the sum of the statistical and systematical errors, where the part of the statistical errors is marked by the error bars shown. Contents and errors of each bin of both distributions are presented numerically in Appendix C.
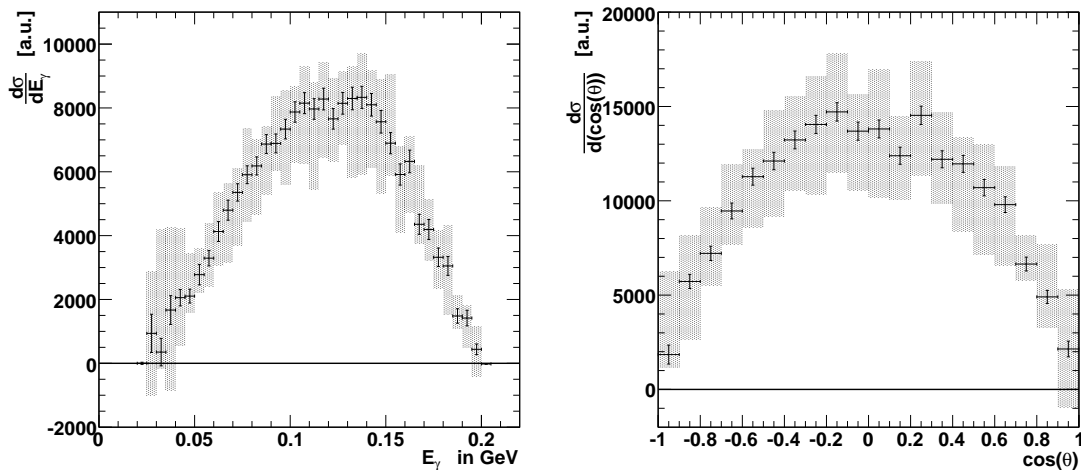
Figure 5.22: Photon energy distribution (left) and angular distribution (right). The shaded area describes the error of each bin, which is the sum of the statistical and systematic errors. The error bars indicate the size of the statistical error.

The systematic uncertainties of the angular distribution are constant over the full range, whereas in the photon energy distribution variations are visible. The largest systematic uncertainties are found for energies in the range of $20\ MeV \leq E_\gamma \leq 50\ MeV$ and $80\ MeV \leq E_\gamma \leq 160\ MeV$. In the low energy region, the uncertainties arise from the possible inclusion of two-pion background depending on the method of splitoff suppression. In the higher energy region the uncertainties are caused by the suppression of three-pion final states before the

kinematic fit and the event selection with respect to the probability distribution after the kinematic fit. Both conditions hint at the subtraction of three-pion background as a special issue. Additionally, it can be seen from Fig. 5.6 that the higher energy region discussed here corresponds to the region where the contribution of the decay mode $\eta \to \pi^+\pi^-\pi^0$ is largest. In the studies presented above the systematic uncertainty arising from the subtraction of this background was not discussed. The fraction of subtracted events is fixed by the relative branching ratio $R_{BR} = \frac{\Gamma(\eta \to \pi^+\pi^-\gamma)}{\Gamma(\eta \to \pi^+\pi^-\pi^0)}$ and the reconstruction efficiency. Here, the PDG value of the relative branching ratio $R_{BR} = 0.203 \pm 0.008$ [A$^+$08] is used and the reconstruction efficiency is determined from simulations based on a realistic matrix element (see Section 3.1.2). In a recent measurement by the CLEO collaboration a different ratio of $R_{BR} = 0.175 \pm 0.007 \pm 0.006$ was found [L$^+$07]. This deviation of 13% in the relative branching ratio results in a systematic uncertainty which is small compared to the effects discussed above, since the subtracted amount of three-pion background is only on the order 2% to 3% of the reconstructed signal events.

5.3   Discussion

5.3.1   Angular distribution

As mentioned in Sections 1.2 and 5.1.4, invariance under charge conjugation demands odd values of relative angular momenta between the two pions. The lowest allowed angular momentum is $L = 1$, P-wave interaction. In the angular distribution P-wave interaction is reflected by the quadratic dependence:

$$\frac{d\Gamma}{d(\cos(\theta))} = A \cdot \sin^2(\theta). \tag{5.5}$$

In Section 5.1.4, the angular distribution was already shown to match this relation. Here, taking into account the systematic errors, the agreement in terms of the reduced χ^2 value of the fit is even better, as shown with the red curve in Fig, 5.23.

In Fig. 5.9 it was shown that a better fit to the histogram is achieved using a polynomial of second order which includes a linear term. In order to test if this observation is caused by contribution of higher angular momenta, terms describing

(a) fit of full range   (b) $-0.1 \leq \cos(\theta) \leq 0.4$ excluded
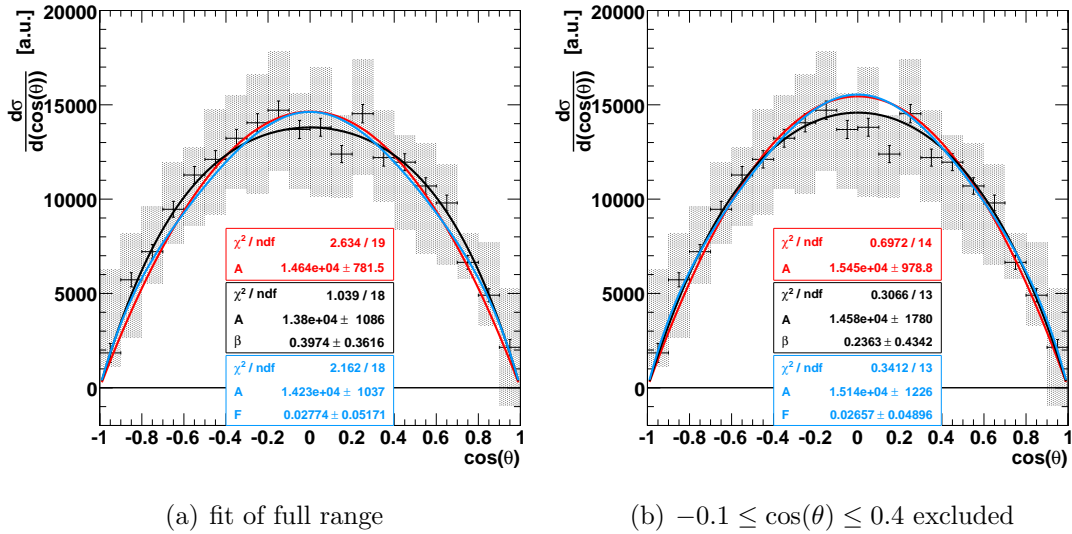
Figure 5.23: The angular distribution of the two-pion system relative to the photon is fitted with relations corresponding to P-wave (red), D-wave (black) and F-wave (blue). The fluctuations in the region $-0.1 \leq \cos(\theta) \leq 0.4$ provoke a possible D-wave contribution, as seen in the left panel. Excluding this range yields a D-wave contribution which is small compared to its errors. It may be concluded that the angular distribution does not show C violating contributions. Larger odd angular momenta (F-wave) are negligible as well.

D-wave and F-Wave interaction are added to the fit of the angular distribution. Including D-wave interaction, allows for terms of relative angular momenta $L = 2$, which are not allowed due to the invariance under charge conjugation. Thus, this is a test for a C violating contribution in the decay $\eta \to \pi^+\pi^-\gamma$.

In order to test for a possible D-wave contribution, the angular distribution is fitted with the function:

$$\frac{d\Gamma}{d(\cos(\theta))} = A \cdot \sin^2(\theta) \cdot (1 + \beta \cdot \cos^2(\theta)), \qquad (5.6)$$

where β is the strength of the D-wave contribution. The result of the fit is shown with the black curve in the left panel of Fig. 5.23. A small, positive value of $\beta = 0.397 \pm 0.355$ is found, which is not compatible with 0 within its errors. However, from the difference between the P-wave (red curve) and the D-wave fit it can be seen that the fluctuations of the angular distribution in the region of

$-0.1 \leq \cos(\theta) \leq 0.4$ bring forward a result of the fit which implies C-violation. In the right panel of Fig. 5.23, the fit of the angular distribution is repeated, excluding the range of fluctuations. Here, the strength of the D-wave contribution $\beta = 0.236 \pm 0.430$ is lower compared to the fit of the full distribution by approximately a factor of 2. Additionally, the value is small compared to its error, so that the angular distribution does not hint at C violation.

In Tab. 5.2 the result of this work is compared to the published measurements of the β parameter as well as the average value of the PDG. The central value of β is larger by a factor of 2 compared to the measurements of Thaler et al. and Jane et al., which reported the largest values of β. Compared to the publication of Gormley et al. and the average value of the PDG, it is even of opposite sign. However, due to its large errors, the result of this work is in agreement with previous measurements.

	Parameter β
Gormley et al. [G$^+$70]	-0.060 ± 0.065
Thaler et al. [T$^+$72]	0.12 ± 0.06
Jane et al. [J$^+$74]	0.11 ± 0.11
PDG average [A$^+$08]	-0.02 ± 0.07
This work	0.236 ± 0.430

Table 5.2: Comparison of the β parameters of previous measurements and the average value of the PDG with the result of this work. Within the errors the result is in agreement with the previous measurements.

The result of Thaler et al. [T$^+$72] is of interest, because the extracted β parameter is not compatible with 0 within its errors. However, this is not interpreted as a possible C violation, because the interference of C allowed P and F-wave interaction may also lead to terms containing $\cos^2(\theta)$, which are characteristic for D-wave contributions.

To test for contributions of F-wave interaction, the angular distribution is fitted with the sum of P and F-wave described by:

$$\frac{d\Gamma}{d(\cos(\theta))} = A \cdot \sin^2(\theta) \cdot (1 + F \cdot (5\cos^2(\theta) - 1)^2), \qquad (5.7)$$

where the parameter F corresponds to the strength of the F-wave contribution. The result of the fit is shown with the blue curve in Fig. 5.23. The size of an F-wave

contribution $F = 0.027 \pm 0.05$ is small compared to the errors and independent of the exclusion of the angular range $-0.1 \leq \cos(\theta) \leq 0.4$. Thus, significant contributions of relative angular momenta larger than $L = 1$ between the two pions are not observed in this work.

5.3.2 Energy distribution

The energy distribution of the photon in the rest frame of the η meson is compared to the distribution given by the simplest gauge invariant matrix element of the decay $\eta \to \pi^+\pi^-\gamma$. The shape of the distribution is described by:

$$\frac{d\Gamma}{dE_\gamma} \propto \left(\frac{E_\gamma}{m_\eta}\right)^3 \cdot \sqrt{1 - \frac{2E_\gamma}{m_\eta} - \frac{4m_\pi^2}{m_\eta^2}}^3 \cdot \frac{1}{\sqrt{1 - \frac{2E_\gamma}{m_\eta}}} \qquad (5.8)$$

The normalization to the measured distribution is done by fitting, as shown with the blue line in Fig. 5.24. Here, a strong deviation of the distributions is observed. Compared to the distribution of the matrix element, the experimental distribution is shifted towards lower photon energies. The same behavior was observed in previous measurements [CP66, C+68, G+70, L+73]. A direct comparison with shape of the published distributions is difficult, as especially in case of the statistically most significant measurements of Gormley et al. and Layter et al. the distributions have not been corrected for efficiency (see Section 1.2.2). However, in the present work events with photon energies below 50 MeV have been reconstructed, which hints at a better reconstruction efficiency compared to the previous measurements, where this energy range is unpopulated (see Fig. 1.3). Additionally, if the bin width of the photon energy distributions of previous measurements ($\sim 10~MeV$) is assumed to reflect the resolution, the resolution of the photon energy achieved in this work is better by almost a factor of 2.

All previous measurements report a good agreement of the experimental photon energy distribution with a purely ρ-dominant matrix element, in which a contact term due to the box anomaly is missing. As pointed out by Holstein [Hol02], the result of this matrix element is not in agreement with recent calculations of Vector Meson Dominance model, in which the amplitude of the simplest gauge invariant matrix element is enhanced by the form factor

$$\mathcal{A}_\eta(s_{\pi\pi}) = \mathcal{A}_\eta(0,0,0)\left(1 - \frac{3~m_\rho^2}{m_\rho^2 - s_{\pi\pi}}\right) \qquad \text{[Pic92, PR93],} \qquad (5.9)$$
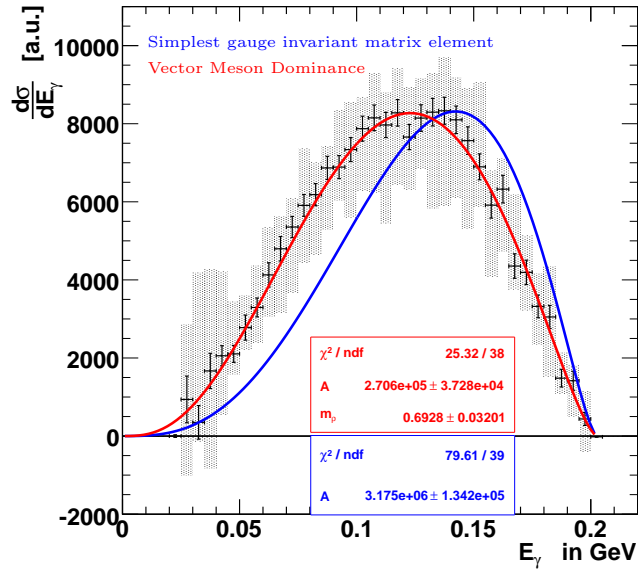
Figure 5.24: The photon energy distribution is compared to the distribution expected from the simplest gauge invariant matrix element (blue) and an additional form factor based on Vector Meson Dominance model calculations [Pic92, PR93, Hol02]. In contrast to the matrix element the Vector Meson Dominance calculation is in good agreement with the data.

where m_ρ is the mass of the ρ meson and $s_{\pi\pi}$ is the squared invariant mass of the two pions. The kinematic range of the η decay is below the pole mass of the ρ meson. For a correct evaluation either the ρ width has to be implemented or a virtual ρ mass is assumed [Wir09]. Here, the latter case will be used by making the mass a free parameter of the fit to the experimental distribution. The result of the fit is shown with the red curve in Fig. 5.24. For a mass of $692.8 \pm 32.0 \; MeV$ of the virtual ρ meson the distribution following the Vector Meson Dominance calculations is in good agreement with the experimental photon energy distribution.

Chapter 6

Summary and Outlook

In this work, background subtracted and efficiency corrected Dalitz plot distributions of the decay mode $\eta \to \pi^+\pi^-\gamma$ have been obtained. The distributions are based on 13738 ± 136 reconstructed events, which is the second largest sample acquired so far. Compared to previous measurements, the resolution of the photon energy in the rest frame of the η meson is improved by a factor two, and due to a better efficiency photon energies below $50\ MeV$ have been measured. The direct comparison of the line shapes has not been performed due to missing efficiency corrections in the publications. However, the reported deviations from the line shape of the simplest gauge invariant matrix element are also observed in this work. Here, the distribution is in good agreement with the calculations of Chiral Perturbation Theory at lowest order matched with calculations of the Vector Meson Dominance model. The angular distribution of the pions is described by P-wave interaction. Significant contributions of higher relative angular momenta have not been found.

The η mesons, analyzed in this work, were produced in the reaction $pd \to {}^3\mathrm{He}\,\eta$ during a production run in the October 2008. In total, $1.1 \cdot 10^7$ η mesons were produced and tagged with the Forward Detector. In August and September 2009 another production run $pd \to {}^3\mathrm{He}\eta$ has been performed. The conditions were similar to the production run discussed in this thesis, yielding $2 \cdot 10^7$ tagged η mesons. Combining the new data with the results of this work will increase the statistics by a factor of three.

However, the systematic uncertainties with the current data set are already larger than the statistical errors. Crucial points in the analysis are the recon-

struction of charged particles and the kinematic fit. Both steps in the analysis chain are responsible for the low overall reconstruction efficiency of 6%. The condition on the probability distribution of the kinematic fit and the condition to suppress three-pion final states, which is strongly dependent on the information of the charged pions contribute most to the systematic uncertainties. The development of the reconstruction routines will bring further improvements with respect to efficiency and resolution.

The physics program of the WASA-at-COSY collaboration includes the investigation of the decays of the η' meson. The box anomaly is involved in the decay mode $\eta' \to \pi^+\pi^-\gamma$. Here, the correct implementation of final state interactions in the theoretical description is even more important than in the η decay, since the dynamic range of the two pions covers the pole mass of the ρ meson. The results of the two statistically most significant measurements [A$^+$97, A$^+$98] are contradictory with respect to the contribution of the box anomaly. A new high statistics measurement will settle this contradiction.

Appendix A

Error Parametrization

$T_{^3\text{He}}/GeV$ θ in deg	0.225	0.275	0.325	0.375	0.425	0.475	0.525	0.575	0.625
3	0.2145	0.1991	0.1818	0.1685	0.1610	0.1547	0.1498	0.1498	0.1498
4	0.2136	0.1960	0.1805	0.1693	0.1623	0.1545	0.1531	0.1531	0.1531
5	0.2153	0.1950	0.1782	0.1671	0.1609	0.1519	0.1491	0.1491	0.1491
6	0.2126	0.1927	0.1768	0.1658	0.1594	0.1540	0.1496	0.1496	0.1496
7	0.2112	0.1915	0.1765	0.1663	0.1589	0.1535	0.1480	0.1480	0.1480
8	0.2112	0.1904	0.1744	0.1635	0.1570	0.1512	0.1489	0.1489	0.1489
9	0.2091	0.1885	0.1750	0.1633	0.1556	0.1511	0.1489	0.1489	0.1489
10	0.2064	0.1876	0.1720	0.1637	0.1562	0.1501	0.1487	0.1487	0.1487
11	0.2035	0.1890	0.1740	0.1617	0.1542	0.1496	0.1463	0.1463	0.1463
12	0.2008	0.1850	0.1708	0.1602	0.1535	0.1497	0.1479	0.1479	0.1479
13	0.1987	0.1831	0.1672	0.1594	0.1516	0.1448	0.1411	0.1411	0.1411
14	0.1925	0.1773	0.1633	0.1531	0.1464	0.1412	0.1405	0.1413	0.1412
15	0.1866	0.1721	0.1582	0.1486	0.1407	0.1364	0.1353	0.1407	0.1407
16	0.1791	0.1632	0.1490	0.1405	0.1362	0.1376	0.1362	0.1360	0.1360
17	0.1722	0.1564	0.1418	0.1381	0.1361	0.1391	0.1363	0.1327	0.1327
18	0.1715	0.1500	0.1394	0.1376	0.1432	0.1409	0.1372	0.1327	0.1327

Table A.1: Measurement errors $\Delta\theta$ of the polar θ angel of ^{3}He in degrees.

$T_{3_{\mathrm{He}}}/GeV$ θ in deg	0.225	0.275	0.325	0.375	0.425	0.475	0.525	0.575	0.625
3	3.5671	3.1932	2.9769	2.8873	2.7625	2.5090	2.7666	2.6382	2.6382
4	2.9429	2.6309	2.3580	2.2490	2.1138	1.9762	1.9830	1.9358	1.9358
5	2.3664	2.1357	1.9090	1.8041	1.6214	1.5900	1.5464	1.5382	1.5382
6	1.9320	1.7007	1.6146	1.4398	1.3824	1.3252	1.3047	1.2723	1.2723
7	1.6587	1.4633	1.3399	1.2585	1.1727	1.1535	1.1191	1.1493	1.1493
8	1.4335	1.2734	1.1764	1.0942	1.0249	0.9598	0.9745	0.9581	0.9581
9	1.2695	1.1432	1.0327	0.9791	0.8972	0.8534	0.8367	0.8406	0.8406
10	1.1247	1.0261	0.9332	0.8554	0.8073	0.7776	0.7651	0.7764	0.7764
11	1.0297	0.9176	0.8425	0.8082	0.7526	0.7078	0.6945	0.6918	0.6918
12	0.9570	0.8609	0.7856	0.7355	0.7017	0.6667	0.6383	0.6370	0.6370
13	0.8780	0.7995	0.7487	0.7006	0.6541	0.6383	0.6249	0.6213	0.6213
14	0.8166	0.7455	0.6915	0.6547	0.6224	0.5989	0.5872	0.6423	0.6423
15	0.7566	0.6971	0.6416	0.6078	0.5796	0.5554	0.5438	0.6384	0.6384
16	0.6943	0.6360	0.5873	0.5560	0.5343	0.5131	0.5068	0.5259	0.5259
17	0.6412	0.5911	0.5498	0.5122	0.4887	0.4756	0.4638	0.5015	0.5015
18	0.6327	0.5808	0.5490	0.5393	0.5084	0.5081	0.4937	0.5748	0.5748

Table A.2: Measurement errors $\Delta\phi$ of the azimuthal angel ϕ of ^{3}He in degrees.

$T_{3_{\mathrm{He}}}/GeV$ θ in deg	0.225	0.275	0.325	0.375	0.425	0.475	0.525	0.575	0.625
3	0.0076	0.0099	0.0132	0.0159	0.0179	0.0189	0.0206	0.0223	0.0240
4	0.0075	0.0099	0.0131	0.0157	0.0177	0.0194	0.0211	0.0228	0.0245
5	0.0074	0.0095	0.0128	0.0155	0.0180	0.0192	0.0209	0.0226	0.0243
6	0.0074	0.0093	0.0130	0.0157	0.0174	0.0203	0.0203	0.0220	0.0237
7	0.0074	0.0093	0.0131	0.0155	0.0176	0.0192	0.0209	0.0218	0.0235
8	0.0074	0.0094	0.0128	0.0158	0.0171	0.0195	0.0212	0.0229	0.0246
9	0.0073	0.0093	0.0129	0.0152	0.0174	0.0187	0.0204	0.0221	0.0238
10	0.0072	0.0093	0.0127	0.0152	0.0176	0.0188	0.0205	0.0222	0.0239
11	0.0075	0.0092	0.0129	0.0156	0.0175	0.0189	0.0206	0.0223	0.0240
12	0.0078	0.0095	0.0130	0.0154	0.0174	0.0189	0.0206	0.0223	0.0240
13	0.0081	0.0095	0.0129	0.0154	0.0173	0.0191	0.0208	0.0225	0.0242
14	0.0085	0.0095	0.0128	0.0153	0.0174	0.0190	0.0207	0.0224	0.0241
15	0.0089	0.0097	0.0127	0.0154	0.0171	0.0189	0.0206	0.0223	0.0240
16	0.0092	0.0096	0.0127	0.0154	0.0171	0.0187	0.0204	0.0221	0.0238
17	0.0095	0.0096	0.0127	0.0154	0.0171	0.0188	0.0206	0.0223	0.0240
18	0.0105	0.0124	0.0182	0.0188	0.0199	0.0209	0.0224	0.0230	0.0247

Table A.3: Relative measurement errors $\Delta E/E$ of the kinetic Energy of ^{3}He.

T_π/MeV θ in deg	25	75	125	175	225	275	325	375	425	475	525	575	625	675	725
21	1.47	1.11	1.11	1.04	0.98	1.09	2.34	1.65	1.01	1.17	2.41	1.39	3.18	3.59	2.26
23	1.52	1.56	1.52	1.28	1.41	1.38	1.31	1.41	1.46	1.28	1.21	1.29	1.48	1.40	0.85
25	2.31	2.10	1.64	1.47	1.41	1.43	1.30	1.31	1.29	1.28	1.23	1.37	1.23	1.35	1.15
27	3.55	2.70	1.85	1.54	1.37	1.31	1.21	1.17	1.24	1.19	1.05	1.18	1.03	1.10	1.10
29	3.21	2.24	1.59	1.42	1.20	1.12	1.10	1.06	1.03	1.07	1.03	1.12	0.98	1.02	0.92
31	2.86	1.78	1.41	1.24	1.13	1.01	1.02	1.06	0.97	0.94	0.93	0.95	0.95	0.98	1.00
33	2.67	1.63	1.32	1.18	1.09	0.99	0.97	0.97	0.91	0.93	0.92	0.97	0.89	0.96	0.94
35	2.55	1.70	1.46	1.27	1.12	1.01	0.95	0.92	0.88	0.88	0.88	0.84	0.82	0.85	0.85
37	2.66	1.83	1.52	1.32	1.15	1.09	0.98	0.95	0.90	0.83	0.82	0.82	0.79	0.82	0.82
39	2.70	1.70	1.37	1.20	1.11	0.98	0.94	0.89	0.81	0.77	0.78	0.79	0.748	0.761	0.72
41	2.79	1.47	1.15	1.02	0.96	0.89	0.85	0.80	0.78	0.76	0.74	0.73	0.738	0.74	0.73
43	2.64	1.40	1.23	1.14	1.00	0.94	0.89	0.81	0.81	0.75	0.72	0.69	0.685	0.69	0.67
45	1.90	1.31	1.14	1.03	0.93	0.87	0.84	0.81	0.77	0.77	0.72	0.71	0.713	0.68	0.70
47	1.84	1.33	1.15	1.07	1.01	0.93	0.88	0.84	0.83	0.79	0.78	0.76	0.761	0.74	0.73
49	1.97	1.34	1.22	1.11	1.05	1.00	0.93	0.89	0.90	0.82	0.81	0.81	0.783	0.80	0.76
51	2.04	1.35	1.27	1.19	1.13	1.03	0.99	0.95	0.90	0.90	0.85	0.83	0.842	0.82	0.83
53	2.13	1.43	1.25	1.21	1.15	1.08	1.04	1.01	0.95	0.93	0.90	0.89	0.877	0.85	0.84
55	2.33	1.46	1.35	1.29	1.21	1.12	1.10	1.05	1.03	0.99	0.95	0.96	0.911	0.89	0.93
57	2.39	1.51	1.44	1.33	1.26	1.19	1.12	1.08	1.06	1.01	0.98	0.94	0.947	0.93	0.93
59	2.27	1.58	1.49	1.43	1.27	1.21	1.14	1.11	1.09	1.05	1.02	0.98	0.976	0.95	0.99
61	2.41	1.57	1.46	1.44	1.33	1.28	1.17	1.16	1.14	1.06	1.06	1.04	1.02	1.02	1.02
63	2.29	1.60	1.52	1.44	1.33	1.28	1.21	1.18	1.12	1.11	1.11	1.06	1.05	1.02	1.03
65	2.30	1.62	1.50	1.48	1.37	1.33	1.24	1.22	1.19	1.17	1.15	1.08	1.09	1.03	1.06
67	2.54	1.66	1.59	1.51	1.42	1.35	1.28	1.23	1.19	1.22	1.15	1.17	1.13	1.10	1.09
69	2.41	1.69	1.66	1.57	1.50	1.42	1.33	1.30	1.26	1.22	1.18	1.19	1.13	1.11	1.11
71	2.51	1.84	1.78	1.60	1.51	1.44	1.38	1.30	1.25	1.20	1.19	1.19	1.14	1.17	1.14
73	2.46	1.89	1.91	1.68	1.59	1.48	1.43	1.32	1.28	1.28	1.24	1.26	1.20	1.19	1.19
75	2.65	1.87	1.88	1.69	1.60	1.48	1.43	1.38	1.29	1.30	1.27	1.26	1.25	1.18	1.20
77	2.61	1.83	1.80	1.64	1.58	1.44	1.44	1.35	1.33	1.32	1.29	1.25	1.26	1.23	1.18
79	2.56	1.86	1.82	1.63	1.60	1.50	1.42	1.39	1.34	1.31	1.30	1.29	1.25	1.27	1.19
81	2.55	1.97	1.80	1.71	1.65	1.49	1.44	1.42	1.36	1.34	1.30	1.28	1.25	1.25	1.22
83	2.59	1.95	1.79	1.67	1.61	1.53	1.48	1.38	1.39	1.35	1.32	1.29	1.29	1.29	1.27
85	2.49	1.96	1.80	1.75	1.65	1.51	1.44	1.49	1.37	1.36	1.38	1.33	1.29	1.23	1.29
87	2.61	1.97	1.86	1.79	1.66	1.52	1.51	1.46	1.42	1.37	1.37	1.31	1.31	1.30	1.32
89	2.56	2.05	1.92	1.77	1.66	1.57	1.53	1.47	1.39	1.37	1.32	1.33	1.34	1.25	1.28
91	2.81	2.09	1.88	1.85	1.70	1.58	1.49	1.43	1.39	1.33	1.35	1.34	1.32	1.29	1.29
93	2.80	1.97	1.88	1.79	1.68	1.56	1.48	1.48	1.38	1.34	1.36	1.31	1.34	1.32	1.31
95	2.82	2.00	1.86	1.75	1.63	1.53	1.49	1.43	1.38	1.37	1.29	1.31	1.28	1.30	1.25
97	2.69	1.98	1.80	1.71	1.64	1.50	1.49	1.43	1.36	1.34	1.32	1.32	1.25	1.26	1.25
99	2.49	1.97	1.76	1.66	1.62	1.52	1.50	1.42	1.34	1.33	1.31	1.29	1.25	1.25	1.22
101	2.63	1.87	1.74	1.64	1.57	1.49	1.42	1.38	1.35	1.37	1.27	1.28	1.21	1.21	1.21
103	2.39	1.86	1.71	1.59	1.58	1.46	1.43	1.36	1.32	1.32	1.28	1.28	1.28	1.18	1.18
105	2.49	1.85	1.77	1.59	1.55	1.46	1.44	1.35	1.30	1.31	1.25	1.28	1.21	1.24	1.19
107	2.43	1.87	1.74	1.63	1.55	1.44	1.42	1.33	1.31	1.23	1.26	1.25	1.17	1.22	1.24
109	2.53	1.81	1.72	1.67	1.55	1.45	1.39	1.31	1.28	1.25	1.19	1.19	1.17	1.13	1.16
111	2.63	1.81	1.71	1.61	1.52	1.40	1.33	1.28	1.24	1.20	1.20	1.17	1.13	1.15	1.13
113	2.50	1.69	1.61	1.57	1.47	1.39	1.34	1.26	1.19	1.19	1.19	1.09	1.12	1.10	1.10
115	2.46	1.65	1.57	1.52	1.45	1.33	1.29	1.25	1.21	1.17	1.18	1.11	1.09	1.09	1.08
117	2.44	1.66	1.51	1.42	1.38	1.29	1.21	1.18	1.16	1.13	1.11	1.10	1.06	1.02	1.04
119	2.38	1.60	1.49	1.41	1.29	1.23	1.24	1.14	1.10	1.11	1.06	1.03	1.01	1.02	1.00
121	2.34	1.54	1.43	1.36	1.25	1.22	1.15	1.10	1.08	1.05	1.02	0.96	0.97	0.97	0.96
123	2.42	1.54	1.37	1.36	1.26	1.19	1.11	1.06	1.04	0.99	0.96	0.95	0.94	0.91	0.94
125	2.55	1.50	1.38	1.31	1.22	1.14	1.09	1.04	1.00	0.96	0.91	0.89	0.91	0.90	0.89
127	2.66	1.46	1.31	1.25	1.16	1.10	1.05	0.99	0.94	0.92	0.89	0.86	0.88	0.88	0.85
129	2.45	1.40	1.24	1.19	1.14	1.02	0.99	0.96	0.88	0.88	0.88	0.83	0.83	0.83	0.83
131	2.64	1.29	1.19	1.12	1.07	0.98	0.91	0.90	0.86	0.82	0.81	0.81	0.78	0.78	0.77
133	2.33	1.29	1.09	1.03	0.99	0.93	0.88	0.86	0.83	0.80	0.78	0.76	0.73	0.72	0.72
135	2.21	1.37	1.12	1.02	0.95	0.88	0.82	0.80	0.78	0.75	0.75	0.72	0.71	0.72	0.67
137	2.33	1.50	1.23	1.07	0.96	0.86	0.83	0.78	0.75	0.72	0.70	0.68	0.67	0.67	0.66
139	2.07	1.58	1.33	1.16	1.06	0.93	0.87	0.83	0.80	0.78	0.74	0.73	0.71	0.71	0.70
141	2.51	1.49	1.23	1.06	0.99	0.87	0.83	0.79	0.76	0.76	0.74	0.73	0.70	0.72	0.72
143	5.39	3.22	2.59	2.14	1.86	1.62	1.46	1.40	1.32	1.34	1.26	1.22	1.15	1.21	1.26
145	2.32	1.61	1.23	1.06	0.96	0.89	0.82	0.83	0.80	0.74	0.76	0.72	0.76	0.71	0.78
147	2.80	1.80	1.46	1.25	1.17	1.04	0.99	0.96	0.91	0.90	0.88	0.80	0.87	0.89	0.89
149	2.53	1.81	1.50	1.20	1.12	1.06	1.06	1.00	0.96	0.93	0.97	0.86	0.93	0.83	0.93
151	2.32	1.62	1.32	1.14	1.05	1.10	1.04	1.04	1.03	1.03	1.06	1.10	1.03	1.03	1.04
153	2.42	1.71	1.37	1.27	1.09	1.08	1.03	1.05	1.05	1.05	1.05	1.01	1.11	1.18	1.06
155	1.93	1.40	1.26	1.22	1.19	1.19	1.13	1.26	1.20	1.19	1.18	1.25	1.23	1.05	1.20
157	1.64	1.42	1.17	1.19	1.12	1.15	1.26	1.21	1.22	1.22	1.18	1.23	1.30	1.16	1.06
159	1.34	1.26	1.16	1.08	1.07	1.08	1.07	1.22	1.15	1.11	1.01	0.95	1.07	2.31	2.76

Table A.4: Measurement errors $\Delta\theta$ of the polar angle θ of the pions in degrees.

T_π/MeV / θ in deg	25	75	125	175	225	275	325	375	425	475	525	575	625	675	725
21	3.35	2.96	3.54	2.74	2.63	2.78	1.71	2.28	1.86	1.70	1.74	1.62	1.16	1.14	1.36
23	3.35	3.14	2.80	2.41	2.26	2.15	1.60	1.50	1.68	1.83	1.52	1.14	1.23	1.18	0.99
25	4.10	3.55	3.10	2.33	2.27	1.73	1.72	1.65	1.64	1.40	1.55	1.67	1.17	1.04	0.95
27	3.73	3.55	2.58	2.17	1.82	1.72	1.40	1.40	1.31	1.44	1.15	1.23	1.13	0.97	1.02
29	3.23	2.97	2.32	1.78	1.77	1.55	1.35	1.29	1.19	1.18	1.20	0.96	0.99	0.80	0.75
31	3.15	2.78	2.31	2.12	1.75	1.43	1.39	1.33	1.30	1.22	1.35	1.04	0.82	0.83	0.74
33	3.14	2.62	2.24	1.97	1.81	1.61	1.45	1.42	1.33	1.27	1.38	0.98	0.81	0.78	0.71
35	2.98	2.42	2.06	1.72	1.62	1.53	1.35	1.32	1.18	1.32	1.25	1.29	1.13	0.82	0.67
37	2.69	2.22	1.91	1.65	1.51	1.41	1.36	1.26	1.22	1.17	1.18	1.19	1.20	0.80	0.61
39	2.62	2.05	1.75	1.52	1.41	1.44	1.36	1.27	1.30	1.14	1.22	1.08	0.96	0.74	0.60
41	2.62	1.95	1.47	1.33	1.28	1.26	1.12	1.14	1.09	1.13	1.22	1.09	0.93	0.74	0.58
43	2.31	1.61	1.39	1.22	1.11	1.09	1.01	0.96	0.94	0.92	0.92	0.88	0.80	0.67	0.57
45	2.14	1.51	1.22	1.10	1.02	0.92	0.90	0.81	0.90	0.87	0.78	0.79	0.75	0.64	0.55
47	1.97	1.41	1.13	1.06	0.95	0.89	0.88	0.82	0.79	0.84	0.78	0.83	0.76	0.64	0.41
49	1.97	1.35	1.17	1.04	0.95	0.89	0.85	0.81	0.78	0.72	0.78	0.77	0.70	0.43	0.40
51	1.85	1.28	1.07	1.01	0.94	0.84	0.85	0.80	0.74	0.76	0.81	0.75	0.47	0.44	0.42
53	1.94	1.25	1.07	0.91	0.91	0.84	0.82	0.76	0.76	0.76	0.76	0.72	0.65	0.42	0.41
55	1.83	1.16	1.01	0.92	0.92	0.83	0.82	0.71	0.79	0.76	0.73	0.71	0.46	0.42	0.43
57	1.78	1.19	0.96	0.92	0.86	0.80	0.81	0.77	0.78	0.77	0.77	0.73	0.45	0.42	0.40
59	1.68	1.13	0.98	0.91	0.83	0.82	0.74	0.74	0.76	0.75	0.71	0.75	0.45	0.41	0.42
61	1.68	1.12	0.98	0.87	0.82	0.79	0.74	0.75	0.73	0.74	0.74	0.46	0.45	0.41	0.40
63	1.59	1.14	0.96	0.89	0.80	0.77	0.77	0.75	0.71	0.76	0.70	0.48	0.46	0.41	0.41
65	1.53	1.11	0.93	0.88	0.79	0.80	0.73	0.77	0.72	0.72	0.72	0.46	0.44	0.41	0.40
67	1.71	1.07	0.92	0.88	0.80	0.78	0.72	0.72	0.78	0.73	0.71	0.47	0.43	0.40	0.41
69	1.58	1.08	0.93	0.85	0.80	0.80	0.70	0.77	0.72	0.75	0.70	0.46	0.44	0.41	0.40
71	1.55	1.07	0.93	0.84	0.80	0.78	0.72	0.73	0.73	0.70	0.47	0.46	0.43	0.40	0.40
73	1.52	1.10	0.94	0.87	0.81	0.78	0.70	0.73	0.69	0.72	0.47	0.47	0.44	0.41	0.41
75	1.56	1.07	0.89	0.84	0.80	0.79	0.71	0.76	0.69	0.76	0.48	0.46	0.43	0.39	0.41
77	1.52	1.02	0.93	0.86	0.78	0.80	0.71	0.73	0.73	0.72	0.47	0.45	0.43	0.39	0.41
79	1.43	1.06	0.91	0.86	0.81	0.77	0.71	0.71	0.71	0.74	0.48	0.48	0.44	0.39	0.42
81	1.42	1.00	0.91	0.87	0.79	0.78	0.70	0.74	0.70	0.74	0.70	0.47	0.44	0.40	0.41
83	1.45	1.02	0.90	0.86	0.80	0.78	0.69	0.74	0.72	0.74	0.47	0.47	0.42	0.39	0.41
85	1.53	1.04	0.93	0.85	0.80	0.80	0.75	0.75	0.76	0.72	0.71	0.46	0.43	0.39	0.41
87	1.45	1.08	0.92	0.87	0.79	0.79	0.73	0.70	0.76	0.73	0.73	0.66	0.41	0.39	0.41
89	1.61	1.04	0.93	0.84	0.80	0.79	0.77	0.72	0.75	0.70	0.48	0.46	0.43	0.40	0.40
91	1.49	1.06	0.93	0.87	0.78	0.81	0.72	0.75	0.74	0.71	0.72	0.48	0.43	0.39	0.40
93	1.56	1.05	0.93	0.87	0.80	0.78	0.72	0.74	0.74	0.72	0.48	0.46	0.42	0.39	0.40
95	1.46	1.04	0.92	0.85	0.80	0.79	0.70	0.74	0.73	0.73	0.47	0.46	0.43	0.38	0.41
97	1.50	1.02	0.93	0.84	0.78	0.80	0.73	0.69	0.71	0.75	0.48	0.47	0.43	0.39	0.41
99	1.39	1.05	0.91	0.86	0.80	0.79	0.76	0.74	0.76	0.71	0.47	0.45	0.43	0.39	0.41
101	1.36	1.04	0.90	0.84	0.78	0.78	0.73	0.72	0.77	0.73	0.49	0.45	0.42	0.39	0.40
103	1.48	1.06	0.90	0.84	0.78	0.82	0.74	0.76	0.72	0.72	0.74	0.47	0.44	0.40	0.40
105	1.51	1.05	0.92	0.84	0.78	0.79	0.72	0.73	0.73	0.72	0.74	0.47	0.43	0.40	0.40
107	1.50	1.04	0.92	0.84	0.77	0.79	0.72	0.75	0.74	0.73	0.47	0.46	0.43	0.41	0.40
109	1.52	1.06	0.89	0.86	0.78	0.79	0.70	0.75	0.72	0.72	0.49	0.47	0.43	0.40	0.39
111	1.64	1.05	0.92	0.85	0.81	0.78	0.70	0.72	0.73	0.75	0.48	0.47	0.43	0.41	0.39
113	1.67	1.06	0.94	0.87	0.78	0.82	0.74	0.71	0.72	0.76	0.49	0.47	0.44	0.40	0.40
115	1.77	1.10	0.93	0.88	0.81	0.78	0.75	0.72	0.74	0.72	0.70	0.47	0.44	0.41	0.40
117	1.70	1.12	0.97	0.87	0.79	0.81	0.75	0.76	0.72	0.75	0.48	0.47	0.45	0.40	0.41
119	1.73	1.12	0.95	0.86	0.80	0.79	0.70	0.72	0.75	0.72	0.72	0.47	0.45	0.41	0.41
121	1.75	1.13	0.94	0.90	0.79	0.80	0.77	0.74	0.72	0.79	0.72	0.47	0.45	0.43	0.41
123	1.84	1.12	0.97	0.89	0.91	0.81	0.78	0.77	0.75	0.77	0.73	0.77	0.46	0.42	0.41
125	1.81	1.19	0.99	0.91	0.90	0.80	0.81	0.79	0.74	0.76	0.80	0.73	0.47	0.41	0.41
127	2.00	1.23	1.07	0.99	0.91	0.84	0.82	0.78	0.74	0.76	0.75	0.76	0.47	0.42	0.40
129	1.98	1.26	1.08	0.98	0.89	0.82	0.84	0.78	0.75	0.81	0.81	0.72	0.74	0.45	0.40
131	2.14	1.36	1.11	1.04	0.93	0.86	0.85	0.83	0.80	0.81	0.77	0.75	0.74	0.63	0.42
133	2.04	1.39	1.13	1.04	0.97	0.87	0.87	0.80	0.85	0.81	0.83	0.76	0.74	0.64	0.40
135	2.20	1.50	1.19	1.07	1.02	0.92	0.89	0.90	0.84	0.80	0.83	0.81	0.72	0.67	0.41
137	2.21	1.58	1.30	1.17	1.05	0.99	0.96	0.96	0.91	0.94	0.84	0.90	0.78	0.70	0.57
139	2.30	1.86	1.42	1.29	1.21	1.21	1.11	1.08	1.01	1.11	1.02	1.01	0.86	0.73	0.56
141	2.49	2.01	1.69	1.40	1.39	1.31	1.14	1.20	1.26	1.22	1.22	1.05	0.93	0.77	0.64
143	3.31	2.47	2.15	1.88	1.71	1.58	1.50	1.35	1.44	1.32	1.24	0.98	0.86	0.76	0.72
145	3.09	2.32	2.13	1.85	1.68	1.48	1.35	1.33	1.31	1.22	1.26	0.99	0.76	0.81	0.69
147	3.02	2.52	2.05	1.73	1.48	1.39	1.33	1.19	1.22	1.09	1.19	0.98	0.81	0.86	0.71
149	3.04	2.73	2.18	1.99	1.77	1.52	1.36	1.34	1.15	1.24	1.32	1.07	0.86	0.81	0.79
151	3.50	3.15	2.44	2.11	1.72	1.58	1.41	1.48	1.26	1.31	1.29	1.20	0.87	0.99	0.84
153	3.38	3.23	2.61	2.04	1.81	1.76	1.69	1.50	1.25	1.38	1.18	1.07	0.96	0.98	0.88
155	3.33	2.90	2.60	2.11	1.76	1.59	1.65	1.41	1.39	1.36	1.44	1.09	1.10	1.07	0.94
157	2.90	2.92	2.31	1.89	1.62	1.77	1.82	1.69	1.54	1.30	1.56	1.46	1.22	1.12	1.05
159	7.35	3.39	2.27	2.53	2.03	2.31	1.91	1.76	1.56	1.48	1.88	2.02	1.87	1.16	1.68

Table A.5: Measurement errors $\Delta\phi$ of the azimuthal angle ϕ of the pions in degrees.

T_π/MeV θ in deg	25	75	125	175	225	275	325	375	425	475	525	575	625	675	725
23	0.29	0.40	0.34	0.27	0.22	0.18	0.17	0.18	0.20	0.21	0.22	0.23	0.26	0.26	0.27
25	0.28	0.30	0.26	0.24	0.19	0.17	0.17	0.19	0.21	0.20	0.22	0.23	0.25	0.25	0.28
27	0.24	0.27	0.26	0.20	0.16	0.17	0.17	0.18	0.20	0.21	0.21	0.25	0.24	0.25	0.28
29	0.21	0.24	0.22	0.18	0.16	0.16	0.17	0.19	0.20	0.21	0.23	0.22	0.25	0.27	0.27
31	0.22	0.21	0.18	0.15	0.15	0.16	0.18	0.20	0.20	0.22	0.23	0.24	0.26	0.25	0.28
33	0.22	0.20	0.16	0.14	0.15	0.16	0.17	0.19	0.20	0.21	0.22	0.25	0.26	0.27	0.29
35	0.19	0.17	0.14	0.14	0.15	0.16	0.17	0.19	0.21	0.22	0.22	0.24	0.26	0.27	0.28
37	0.16	0.15	0.13	0.14	0.15	0.17	0.18	0.19	0.20	0.23	0.22	0.25	0.25	0.25	0.27
39	0.15	0.12	0.12	0.14	0.15	0.17	0.19	0.19	0.20	0.22	0.23	0.24	0.26	0.28	0.26
41	0.14	0.11	0.12	0.13	0.15	0.17	0.18	0.18	0.20	0.22	0.23	0.24	0.24	0.25	0.28
43	0.11	0.11	0.12	0.14	0.15	0.16	0.17	0.20	0.20	0.21	0.24	0.24	0.25	0.25	0.28
45	0.11	0.11	0.12	0.13	0.15	0.17	0.19	0.20	0.22	0.21	0.23	0.25	0.25	0.28	0.27
47	0.10	0.10	0.12	0.14	0.15	0.17	0.18	0.21	0.21	0.23	0.24	0.24	0.27	0.26	0.25
49	0.11	0.11	0.13	0.14	0.16	0.17	0.19	0.20	0.21	0.23	0.24	0.26	0.26	0.27	0.29
51	0.09	0.11	0.12	0.14	0.15	0.17	0.18	0.20	0.21	0.25	0.23	0.24	0.24	0.25	0.26
53	0.09	0.10	0.12	0.14	0.16	0.17	0.19	0.20	0.21	0.21	0.22	0.23	0.25	0.26	0.27
55	0.10	0.11	0.13	0.14	0.16	0.17	0.19	0.19	0.22	0.23	0.25	0.24	0.25	0.23	0.24
57	0.09	0.11	0.12	0.14	0.15	0.18	0.19	0.21	0.22	0.21	0.23	0.26	0.24	0.25	0.25
59	0.09	0.11	0.12	0.14	0.16	0.17	0.19	0.20	0.21	0.22	0.23	0.23	0.24	0.25	0.25
61	0.10	0.11	0.12	0.14	0.16	0.17	0.19	0.19	0.22	0.23	0.22	0.24	0.24	0.25	0.25
63	0.08	0.11	0.13	0.14	0.16	0.17	0.18	0.20	0.22	0.22	0.23	0.23	0.24	0.23	0.24
65	0.09	0.11	0.13	0.15	0.15	0.17	0.19	0.19	0.21	0.22	0.22	0.23	0.24	0.25	0.26
67	0.09	0.11	0.13	0.14	0.16	0.18	0.18	0.20	0.22	0.21	0.23	0.24	0.24	0.24	0.22
69	0.09	0.11	0.13	0.14	0.16	0.18	0.19	0.20	0.21	0.22	0.23	0.24	0.23	0.24	0.24
71	0.09	0.11	0.12	0.15	0.15	0.17	0.19	0.19	0.21	0.22	0.23	0.23	0.24	0.25	0.25
73	0.09	0.11	0.12	0.14	0.16	0.17	0.20	0.19	0.21	0.21	0.21	0.23	0.23	0.25	0.24
75	0.10	0.11	0.13	0.15	0.16	0.18	0.19	0.21	0.22	0.21	0.21	0.22	0.24	0.25	0.25
77	0.08	0.10	0.13	0.14	0.16	0.18	0.19	0.19	0.20	0.21	0.22	0.22	0.22	0.24	0.24
79	0.09	0.11	0.12	0.14	0.16	0.17	0.19	0.19	0.20	0.21	0.23	0.23	0.22	0.23	0.24
81	0.09	0.11	0.13	0.15	0.15	0.18	0.18	0.19	0.21	0.21	0.23	0.21	0.23	0.24	0.25
83	0.09	0.11	0.13	0.14	0.15	0.17	0.19	0.19	0.20	0.20	0.20	0.21	0.23	0.24	0.31
85	0.09	0.11	0.13	0.14	0.16	0.17	0.18	0.19	0.19	0.20	0.22	0.23	0.23	0.25	0.35
87	0.10	0.11	0.12	0.15	0.15	0.17	0.18	0.19	0.21	0.21	0.21	0.23	0.24	0.31	0.36
89	0.09	0.11	0.13	0.15	0.15	0.17	0.18	0.19	0.19	0.21	0.21	0.22	0.25	0.32	0.38
91	0.10	0.11	0.12	0.14	0.16	0.17	0.18	0.18	0.19	0.20	0.21	0.23	0.29	0.35	0.40
93	0.08	0.10	0.12	0.14	0.15	0.17	0.18	0.18	0.19	0.20	0.21	0.23	0.33	0.36	0.41
95	0.09	0.10	0.12	0.14	0.15	0.17	0.17	0.19	0.18	0.21	0.22	0.26	0.35	0.39	0.43
97	0.09	0.10	0.12	0.14	0.15	0.16	0.18	0.18	0.19	0.20	0.22	0.29	0.37	0.40	0.46
99	0.09	0.10	0.12	0.13	0.15	0.17	0.17	0.19	0.19	0.20	0.26	0.34	0.39	0.42	0.47
101	0.10	0.10	0.12	0.13	0.16	0.16	0.17	0.18	0.18	0.22	0.29	0.37	0.41	0.44	0.50
103	0.09	0.10	0.12	0.14	0.15	0.15	0.17	0.19	0.20	0.26	0.31	0.39	0.42	0.46	0.00
105	0.08	0.10	0.12	0.13	0.15	0.16	0.17	0.18	0.20	0.28	0.35	0.41	0.45	0.49	0.00
107	0.09	0.10	0.12	0.13	0.15	0.15	0.17	0.19	0.25	0.33	0.38	0.42	0.46	0.49	0.00
109	0.09	0.10	0.12	0.13	0.15	0.16	0.17	0.20	0.26	0.36	0.39	0.44	0.48	0.47	0.00
111	0.09	0.10	0.12	0.13	0.14	0.16	0.17	0.22	0.32	0.39	0.41	0.47	0.46	0.46	0.00
113	0.09	0.10	0.12	0.13	0.14	0.16	0.19	0.26	0.36	0.41	0.44	0.49	0.45	0.44	0.00
115	0.09	0.10	0.11	0.13	0.14	0.16	0.23	0.33	0.39	0.42	0.45	0.48	0.43	0.42	0.00
117	0.08	0.10	0.12	0.13	0.15	0.18	0.25	0.35	0.40	0.44	0.49	0.46	0.42	0.41	0.00
119	0.09	0.10	0.11	0.13	0.15	0.21	0.26	0.33	0.42	0.45	0.49	0.44	0.41	0.40	0.00
121	0.09	0.10	0.11	0.13	0.16	0.23	0.33	0.35	0.43	0.49	0.47	0.43	0.38	0.37	0.00
123	0.09	0.10	0.12	0.13	0.18	0.27	0.36	0.39	0.45	0.49	0.45	0.42	0.36	0.35	0.00
125	0.08	0.10	0.12	0.15	0.20	0.33	0.38	0.42	0.49	0.48	0.44	0.41	0.34	0.33	0.00
127	0.08	0.10	0.12	0.18	0.29	0.33	0.40	0.46	0.49	0.45	0.41	0.39	0.31	0.28	0.00
129	0.08	0.10	0.13	0.19	0.28	0.37	0.42	0.48	0.45	0.43	0.39	0.37	0.28	0.25	0.00
131	0.09	0.11	0.15	0.24	0.30	0.41	0.44	0.48	0.43	0.42	0.38	0.33	0.26	0.26	0.00
133	0.09	0.12	0.18	0.26	0.38	0.44	0.46	0.46	0.40	0.40	0.37	0.27	0.25	0.24	0.00
135	0.11	0.14	0.21	0.26	0.43	0.43	0.47	0.44	0.38	0.38	0.31	0.25	0.26	0.24	0.00
137	0.11	0.16	0.25	0.33	0.45	0.46	0.45	0.40	0.36	0.34	0.28	0.23	0.24	0.25	0.00
139	0.12	0.19	0.25	0.45	0.47	0.48	0.44	0.38	0.34	0.32	0.25	0.23	0.24	0.24	0.00
141	0.15	0.22	0.29	0.42	0.47	0.45	0.43	0.37	0.34	0.27	0.23	0.23	0.24	0.25	0.00
143	0.16	0.23	0.36	0.47	0.48	0.43	0.41	0.38	0.26	0.23	0.22	0.22	0.25	0.25	0.00
145	0.17	0.27	0.39	0.41	0.44	0.41	0.39	0.33	0.25	0.23	0.22	0.23	0.24	0.25	0.00
147	0.18	0.32	0.39	0.48	0.42	0.39	0.36	0.28	0.22	0.21	0.22	0.23	0.24	0.25	0.00
149	0.20	0.34	0.43	0.47	0.39	0.34	0.29	0.24	0.20	0.22	0.23	0.23	0.24	0.27	0.00
151	0.21	0.34	0.48	0.43	0.35	0.34	0.25	0.21	0.20	0.21	0.23	0.24	0.26	0.25	0.00
153	0.22	0.44	0.45	0.40	0.34	0.27	0.23	0.20	0.20	0.22	0.23	0.22	0.25	0.26	0.00
155	0.20	0.46	0.41	0.40	0.32	0.25	0.21	0.21	0.20	0.22	0.23	0.23	0.26	0.26	0.00
157	0.29	0.43	0.38	0.35	0.27	0.22	0.19	0.19	0.21	0.21	0.23	0.25	0.25	0.27	0.00
23	0.45	0.41	0.35	0.31	0.23	0.20	0.18	0.18	0.21	0.21	0.23	0.24	0.26	0.25	0.00
25	0.45	0.37	0.30	0.26	0.21	0.18	0.18	0.19	0.20	0.22	0.23	0.23	0.24	0.27	0.00

Table A.6: Relative measurement errors $\Delta E/E$ of the kinetic Energy of the pions.

T_γ/GeV SEC Ring	0.025	0.075	0.125	0.175	0.225	0.275	0.325	0.375	0.425	0.475
151	2.1411	2.1945	2.2482	2.0023	1.8612	1.7890	1.6917	1.6169	1.5542	1.4782
152	2.2982	1.9696	1.7923	1.6510	1.5446	1.4510	1.3871	1.3010	1.2479	1.2080
153	2.6173	2.3919	2.1927	2.0405	1.8937	1.7971	1.7375	1.6665	1.6126	1.5766
154	3.1410	2.4716	2.0912	1.8756	1.7206	1.5997	1.5149	1.4364	1.3844	1.2970
155	1.8999	1.6608	1.5180	1.4022	1.2957	1.2270	1.1615	1.1093	1.0782	1.0470
156	1.7995	1.5839	1.4569	1.3233	1.2297	1.1552	1.0875	1.0342	0.9872	0.9625
157	1.8687	1.6684	1.5473	1.4492	1.3734	1.2670	1.2008	1.1483	1.0785	1.0259
158	1.9579	1.7908	1.6551	1.5458	1.4446	1.3411	1.2578	1.1891	1.1355	1.0967
159	2.0516	1.8616	1.7312	1.6034	1.4881	1.4140	1.3291	1.2649	1.1898	1.1521
160	2.0577	1.8984	1.7699	1.6507	1.5404	1.4396	1.3652	1.2809	1.2364	1.1941
161	2.2145	2.0207	1.8667	1.7232	1.6121	1.5176	1.4285	1.3620	1.3002	1.2500
162	2.1984	2.0257	1.9068	1.7611	1.6359	1.5385	1.4260	1.3534	1.2974	1.2370
163	2.2228	2.0299	1.9045	1.7356	1.6163	1.5160	1.4379	1.3680	1.3110	1.2559
164	2.0638	1.9170	1.7956	1.6474	1.5400	1.4468	1.3909	1.3053	1.2378	1.1846
165	1.9881	1.8548	1.7134	1.5945	1.5076	1.4090	1.3251	1.2606	1.2014	1.1506
166	1.8828	1.7607	1.6438	1.5387	1.4308	1.3659	1.2788	1.2022	1.1508	1.0915
167	1.7675	1.6459	1.5640	1.4313	1.3476	1.2632	1.2006	1.1349	1.0902	1.0407
168	1.5716	1.5109	1.4421	1.3709	1.2643	1.1939	1.1268	1.0669	1.0424	0.9902
169	1.4911	1.4807	1.4299	1.3429	1.2667	1.1936	1.1328	1.0944	1.0434	1.0229
170	2.1289	1.8863	1.7756	1.6336	1.5534	1.4682	1.3912	1.3480	1.2798	1.2345
171	1.8447	2.0356	2.0017	1.8413	1.7213	1.6200	1.5372	1.4861	1.4240	1.3825
172	1.6166	1.5979	1.6153	1.5837	1.5210	1.4463	1.3938	1.3313	1.2890	1.2159
173	1.8030	1.5991	1.5591	1.4759	1.3738	1.3391	1.2845	1.2062	1.1738	1.1236
174	1.5243	1.4015	1.3423	1.2921	1.2490	1.2030	1.1802	1.1354	1.0947	1.0714

T_γ/GeV SEC Ring	0.525	0.575	0.625	0.675	0.725	0.775	0.825	0.875	0.925	0.975
151	1.4422	1.3783	1.3309	1.2859	1.2265	1.1870	1.1462	1.1010	1.0551	1.0094
152	1.1685	1.1392	1.0892	1.0695	1.0355	1.0279	0.9863	0.9776	0.9630	0.9452
153	1.5563	1.4989	1.4571	1.4340	1.3809	1.3244	1.2995	1.2074	1.1603	1.1513
154	1.2644	1.1850	1.1528	1.1034	1.0298	0.9518	0.8949	0.8635	0.8144	0.8105
155	1.0193	0.9800	0.9509	0.9227	0.8882	0.8692	0.8547	0.8411	0.8131	0.7953
156	0.9137	0.8797	0.8602	0.8386	0.8188	0.7957	0.7746	0.7703	0.7529	0.7513
157	0.9935	0.9604	0.9232	0.8927	0.8717	0.8415	0.8209	0.8034	0.7921	0.7825
158	1.0517	1.0241	0.9783	0.9503	0.9166	0.8859	0.8744	0.8376	0.8387	0.8201
159	1.1013	1.0659	1.0265	0.9916	0.9657	0.9383	0.9110	0.8817	0.8619	0.8451
160	1.1392	1.0891	1.0504	1.0227	0.9867	0.9599	0.9203	0.9053	0.8936	0.8701
161	1.1957	1.1504	1.1145	1.0666	1.0448	1.0082	0.9769	0.9462	0.9325	0.9013
162	1.1925	1.1506	1.0957	1.0669	1.0348	1.0144	0.9818	0.9465	0.9410	0.9074
163	1.1932	1.1602	1.1271	1.0746	1.0426	1.0159	0.9866	0.9573	0.9278	0.9201
164	1.1494	1.0953	1.0666	1.0282	0.9893	0.9658	0.9405	0.9106	0.8979	0.8764
165	1.1133	1.0678	1.0219	0.9969	0.9734	0.9275	0.8994	0.8714	0.8631
166	1.0713	1.0163	0.9914	0.9551	0.9351	0.9048	0.8786	0.8615	0.8407	0.8277
167	1.0014	0.9593	0.9283	0.8933	0.8711	0.8338	0.8215	0.8089	0.7950	0.7848
168	0.9413	0.9281	0.8871	0.8683	0.8469	0.8230	0.8165	0.7925	0.7756	0.7642
169	0.9670	0.9460	0.9148	0.8919	0.8594	0.8536	0.8287	0.8076	0.7844	0.7783
170	1.1865	1.1667	1.1294	1.1096	1.0648	1.0544	1.0204	1.0054	0.9596	0.9095
171	1.3500	1.2953	1.2532	1.2275	1.1845	1.1954	1.1565	1.1626	1.1559	1.1181
172	1.1895	1.1379	1.1182	1.0837	1.0723	1.0358	1.0152	0.9945	0.9808	0.9427
173	1.0765	1.0599	1.0165	0.9961	0.9891	0.9506	0.9309	0.9189	0.9146	0.8844
174	1.0541	1.0212	1.0100	0.9956	0.9772	0.9641	0.9521	0.9275	0.9111	0.8601

Table A.7: Measurement errors $\Delta\phi$ of the azimuthal angle ϕ of the photons in degrees.

T_γ/GeV SEC Ring	0.025	0.075	0.125	0.175	0.225	0.275	0.325	0.375	0.425	0.475
151	9.1078	7.2375	6.4589	5.9518	5.6544	5.2982	5.0771	4.9128	4.7653	4.5151
152	4.5444	4.2360	4.0111	3.7872	3.5657	3.4323	3.2280	3.0669	2.9975	2.8594
153	4.2287	3.5357	3.1829	2.9695	2.7781	2.6548	2.5372	2.4527	2.3512	2.2688
154	2.3504	2.1858	2.0481	1.9483	1.8328	1.7560	1.6829	1.6143	1.5519	1.4945
155	2.3093	2.0857	1.9546	1.8368	1.7272	1.6155	1.5456	1.4711	1.4118	1.3614
156	2.3019	2.0636	1.9035	1.7358	1.6280	1.5297	1.4440	1.3704	1.3225	1.2618
157	2.3980	2.1448	1.9656	1.8090	1.6687	1.5794	1.4996	1.4221	1.3691	1.3156
158	2.3769	2.1296	1.9670	1.8286	1.6949	1.6073	1.5296	1.4561	1.3813	1.3293
159	2.3298	2.0872	1.9486	1.8098	1.6949	1.5936	1.5257	1.4453	1.3761	1.3352
160	2.2196	2.0794	1.9386	1.8278	1.6901	1.5960	1.5020	1.4316	1.3544	1.3198
161	2.3461	2.0888	1.9615	1.7939	1.6915	1.6104	1.5248	1.4567	1.3761	1.3278
162	2.2857	2.1017	1.9668	1.8367	1.7147	1.6085	1.5362	1.4443	1.3949	1.3495
163	2.3397	2.0860	1.9574	1.8316	1.6918	1.5968	1.5260	1.4409	1.3877	1.3323
164	2.2522	2.0524	1.9517	1.8103	1.6841	1.5866	1.5159	1.4309	1.3674	1.3169
165	2.2745	2.1003	1.9392	1.8128	1.6957	1.6174	1.5081	1.4264	1.3844	1.3253
166	2.3065	2.1197	1.9600	1.8187	1.7035	1.5914	1.5231	1.4385	1.3893	1.3211
167	2.2953	2.1277	1.9777	1.8334	1.7444	1.6041	1.5215	1.4504	1.3980	1.3441
168	2.3353	2.1645	1.9839	1.8902	1.7725	1.6555	1.5737	1.5128	1.4484	1.3787
169	2.4006	2.2513	2.0978	1.9939	1.8807	1.7708	1.7213	1.6102	1.5462	1.5000
170	2.3861	2.2856	2.2189	2.1059	2.0203	1.8989	1.8069	1.7144	1.6478	1.5956
171	3.0222	2.8521	2.7998	2.6181	2.4791	2.3681	2.2648	2.1742	2.1047	1.9965
172	3.0917	3.0270	2.9089	2.7847	2.6222	2.5276	2.3956	2.3310	2.2030	2.1144
173	3.2337	3.3374	3.3107	3.1862	3.0864	2.9272	2.7386	2.6552	2.5515	2.4778
174	3.4350	3.5862	3.6916	3.5748	3.4666	3.3439	3.2354	3.1199	2.9692	2.8847

T_γ/GeV SEC Ring	0.525	0.575	0.625	0.675	0.725	0.775	0.825	0.875	0.925	0.975
151	4.4516	4.2715	4.1931	4.0913	3.9873	3.8702	3.7302	3.6285	3.5340	3.4841
152	2.7479	2.7087	2.5941	2.5539	2.5470	2.4519	2.4209	2.3843	2.3824	2.3906
153	2.2322	2.1787	2.1019	2.1035	2.0554	2.0297	2.0090	1.9835	1.9825	2.0287
154	1.4472	1.4030	1.3817	1.3746	1.3304	1.3020	1.2952	1.2708	1.2728	1.2575
155	1.3090	1.2724	1.2292	1.2133	1.1772	1.1500	1.1414	1.1427	1.1169	1.1145
156	1.2265	1.1827	1.1454	1.1186	1.1015	1.0617	1.0410	1.0274	0.9966	1.0126
157	1.2792	1.2299	1.1992	1.1621	1.1319	1.1053	1.0597	1.0438	1.0361	1.0292
158	1.2753	1.2308	1.2035	1.1786	1.1402	1.1150	1.0679	1.0405	1.0345	1.0218
159	1.2719	1.2377	1.1888	1.1616	1.1476	1.1010	1.0755	1.0505	1.0327	1.0216
160	1.2604	1.2400	1.1808	1.1477	1.1223	1.0991	1.0727	1.0405	1.0329	1.0055
161	1.2700	1.2394	1.2035	1.1767	1.1402	1.1019	1.0783	1.0537	1.0471	1.0112
162	1.2966	1.2586	1.2165	1.1800	1.1446	1.1226	1.0926	1.0647	1.0444	1.0432
163	1.2821	1.2520	1.2006	1.1672	1.1266	1.1147	1.0932	1.0664	1.0428	1.0449
164	1.2753	1.2243	1.1925	1.1517	1.1276	1.0856	1.0575	1.0377	1.0163	1.0073
165	1.2711	1.2325	1.1899	1.1488	1.1327	1.0892	1.0730	1.0496	1.0395	1.0273
166	1.2768	1.2488	1.1874	1.1685	1.1359	1.1080	1.0785	1.0563	1.0402	1.0198
167	1.2901	1.2382	1.2022	1.1675	1.1511	1.1104	1.0847	1.0534	1.0397	1.0140
168	1.3455	1.3162	1.2549	1.2188	1.1837	1.1577	1.1225	1.0987	1.0812	1.0704
169	1.4366	1.4053	1.3518	1.3255	1.2745	1.2616	1.2235	1.2199	1.1904	1.1626
170	1.5371	1.4742	1.4734	1.4271	1.3742	1.3567	1.3227	1.3017	1.2848	1.2509
171	1.9633	1.8960	1.8295	1.7894	1.7369	1.7233	1.6706	1.6617	1.6322	1.6442
172	2.0431	1.9848	1.9104	1.8857	1.8252	1.7829	1.7487	1.7316	1.7139	1.6753
173	2.4059	2.3020	2.2365	2.2172	2.1646	2.0756	2.0404	1.9926	1.9676	1.9322
174	2.8007	2.7178	2.6100	2.5494	2.5268	2.4575	2.4060	2.3158	2.3101	2.2058

Table A.8: Measurement errors $\Delta\theta$ of the polar angle θ of the photons in degrees.

T_γ/GeV SEC Ring	0.025	0.075	0.125	0.175	0.225	0.275	0.325	0.375	0.425	0.475
151	0.2195	0.1599	0.1356	0.1199	0.1158	0.1064	0.0995	0.0918	0.0924	0.0872
152	0.2152	0.1559	0.1285	0.1095	0.1002	0.0943	0.0882	0.0871	0.0849	0.0822
153	0.2152	0.1771	0.1401	0.1283	0.1199	0.1181	0.1156	0.1079	0.1036	0.0983
154	0.2321	0.1734	0.1402	0.1306	0.1194	0.1161	0.1033	0.1070	0.0975	0.0937
155	0.2168	0.1595	0.1331	0.1134	0.1061	0.0972	0.0916	0.0878	0.0837	0.0815
156	0.2270	0.1621	0.1285	0.1123	0.0990	0.0926	0.0895	0.0858	0.0808	0.0789
157	0.2149	0.1503	0.1221	0.1034	0.0918	0.0853	0.0764	0.0712	0.0697	0.0672
158	0.2133	0.1489	0.1200	0.0984	0.0905	0.0807	0.0745	0.0700	0.0655	0.0621
159	0.2140	0.1431	0.1111	0.0997	0.0864	0.0779	0.0716	0.0683	0.0644	0.0596
160	0.2127	0.1457	0.1120	0.0978	0.0840	0.0801	0.0728	0.0666	0.0624	0.0606
161	0.2122	0.1503	0.1127	0.0974	0.0862	0.0766	0.0728	0.0677	0.0636	0.0612
162	0.2046	0.1499	0.1142	0.0969	0.0866	0.0783	0.0733	0.0693	0.0626	0.0597
163	0.2021	0.1525	0.1163	0.1005	0.0895	0.0778	0.0726	0.0687	0.0654	0.0619
164	0.2118	0.1463	0.1128	0.0978	0.0863	0.0786	0.0724	0.0674	0.0624	0.0602
165	0.2126	0.1512	0.1161	0.0968	0.0861	0.0776	0.0714	0.0668	0.0629	0.0596
166	0.2130	0.1455	0.1135	0.0979	0.0852	0.0804	0.0729	0.0678	0.0635	0.0606
167	0.2306	0.1485	0.1157	0.0986	0.0881	0.0754	0.0749	0.0697	0.0630	0.0601
168	0.2191	0.1522	0.1143	0.1012	0.0882	0.0792	0.0755	0.0692	0.0662	0.0625
169	0.2067	0.1442	0.1156	0.0990	0.0868	0.0812	0.0761	0.0703	0.0670	0.0630
170	0.2317	0.1669	0.1381	0.1129	0.1015	0.0938	0.0896	0.0833	0.0819	0.0756
171	0.2169	0.1742	0.1329	0.1098	0.1022	0.0945	0.0861	0.0837	0.0793	0.0761
172	0.2196	0.1564	0.1250	0.1009	0.0894	0.0826	0.0783	0.0716	0.0686	0.0639
173	0.2237	0.1587	0.1242	0.1035	0.0939	0.0841	0.0770	0.0742	0.0678	0.0664
174	0.2518	0.1685	0.1402	0.1250	0.1066	0.0958	0.0890	0.0853	0.0805	0.0805

T_γ/GeV SEC Ring	0.525	0.575	0.625	0.675	0.725	0.775	0.825	0.875	0.925	0.975
151	0.0856	0.0848	0.0890	0.0841	0.0833	0.0743	0.0767	0.0699	0.0459	0.0322
152	0.0805	0.0758	0.0759	0.0759	0.0706	0.0704	0.0651	0.0678	0.0477	0.0338
153	0.0969	0.0949	0.0911	0.0927	0.0875	0.0834	0.0832	0.0728	0.0431	0.0298
154	0.0929	0.0975	0.0945	0.0870	0.0806	0.0830	0.0759	0.0728	0.0470	0.0363
155	0.0793	0.0780	0.0788	0.0770	0.0734	0.0716	0.0657	0.0658	0.0466	0.0359
156	0.0768	0.0753	0.0709	0.0696	0.0688	0.0647	0.0643	0.0620	0.0527	0.0328
157	0.0631	0.0619	0.0607	0.0594	0.0556	0.0559	0.0554	0.0511	0.0516	0.0438
158	0.0585	0.0577	0.0549	0.0537	0.0515	0.0500	0.0483	0.0463	0.0457	0.0449
159	0.0582	0.0550	0.0537	0.0516	0.0497	0.0489	0.0471	0.0464	0.0441	0.0437
160	0.0570	0.0545	0.0529	0.0514	0.0501	0.0476	0.0464	0.0450	0.0424	0.0434
161	0.0569	0.0557	0.0540	0.0521	0.0500	0.0487	0.0470	0.0456	0.0439	0.0438
162	0.0576	0.0554	0.0531	0.0520	0.0497	0.0476	0.0468	0.0453	0.0441	0.0434
163	0.0603	0.0577	0.0543	0.0528	0.0507	0.0489	0.0471	0.0462	0.0452	0.0430
164	0.0577	0.0540	0.0543	0.0509	0.0495	0.0483	0.0472	0.0452	0.0442	0.0429
165	0.0570	0.0551	0.0535	0.0523	0.0493	0.0473	0.0464	0.0461	0.0454	0.0424
166	0.0568	0.0551	0.0527	0.0510	0.0498	0.0485	0.0470	0.0464	0.0444	0.0429
167	0.0584	0.0561	0.0540	0.0519	0.0504	0.0497	0.0480	0.0459	0.0448	0.0442
168	0.0584	0.0564	0.0552	0.0519	0.0514	0.0506	0.0485	0.0467	0.0449	0.0438
169	0.0599	0.0585	0.0556	0.0539	0.0530	0.0513	0.0501	0.0488	0.0473	0.0465
170	0.0764	0.0756	0.0701	0.0721	0.0656	0.0643	0.0599	0.0578	0.0514	0.0422
171	0.0738	0.0734	0.0687	0.0680	0.0643	0.0654	0.0608	0.0574	0.0532	0.0417
172	0.0590	0.0596	0.0565	0.0553	0.0539	0.0512	0.0497	0.0498	0.0493	0.0412
173	0.0638	0.0615	0.0590	0.0568	0.0548	0.0533	0.0538	0.0508	0.0516	0.0383
174	0.0766	0.0745	0.0739	0.0680	0.0689	0.0643	0.0634	0.0626	0.0500	0.0316

Table A.9: Relative measurement errors $\Delta E_{kin}/E_{kin}$ of the kinetic energy of the photons.

Appendix B

Background Subtraction

In this section, the invariant mass spectra of the $\pi^+\pi^-\gamma$ system are presented for each bin of the photon energy distribution and the pion angular distribution. The blue lines illustrate the fit with the Lorentz curve on an polynomial or exponential background, which is performed in Section 5.1.3. The red graphs show the Lorentz curve extracted from the fit, which has been integrated in order to obtain the background-subtracted number of $\eta \to \pi^+\pi^-\gamma$ events. The integrated number is shown for each bin.

The variations of the method of background subtraction, discussed in Section 5.2.3, used in order to estimate the systematic uncertainty, are illustrated with the black and the green graphs. The black graphs correspond to the background contribution of the complete fit (blue graph), whereas the green graphs correspond to the fit of the background only, when the invariant mass range of $535 \ MeV \leq IM_{\pi\pi\gamma} \leq 560 \ MeV$ is excluded from the fit.

Photon Energy
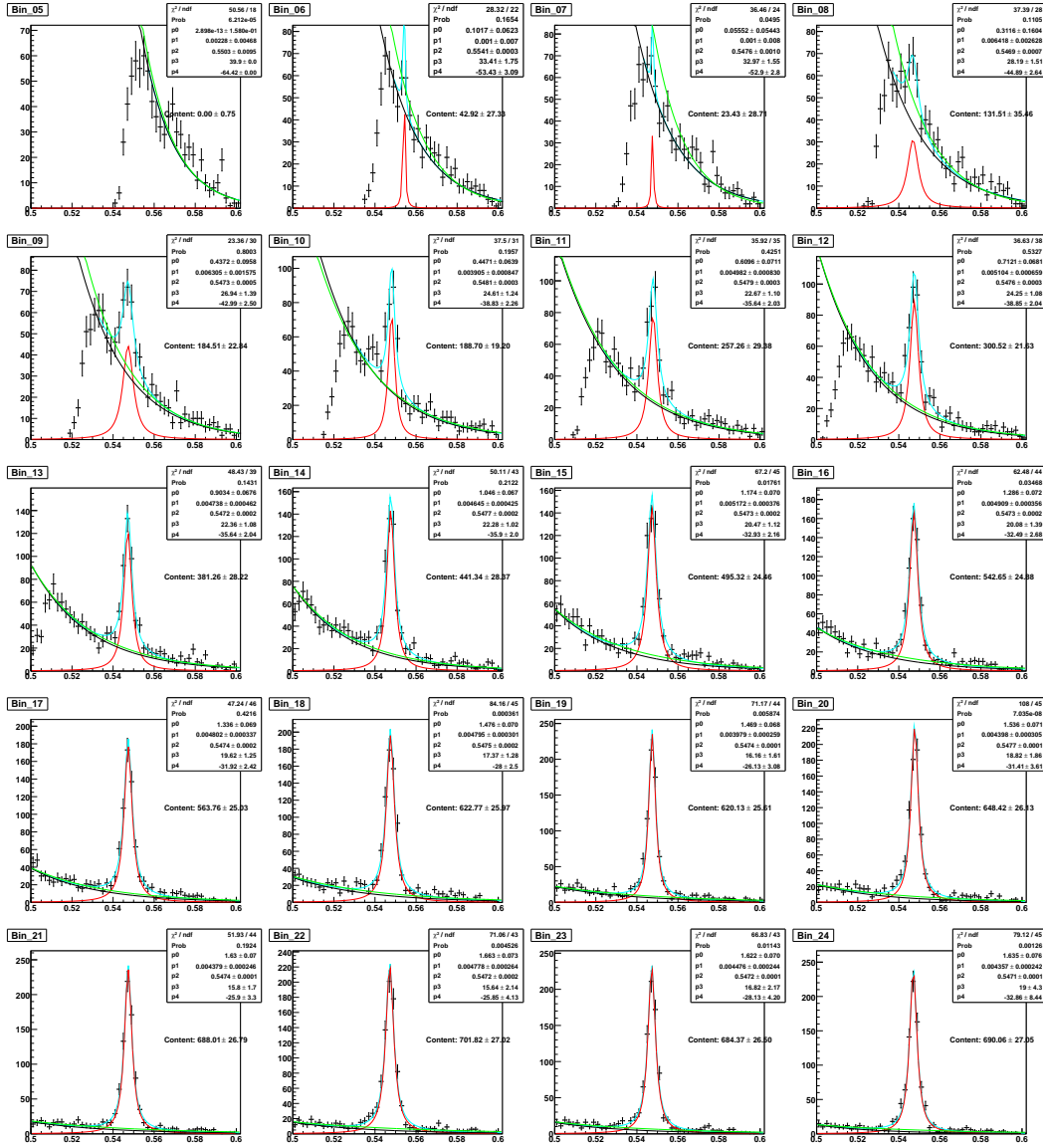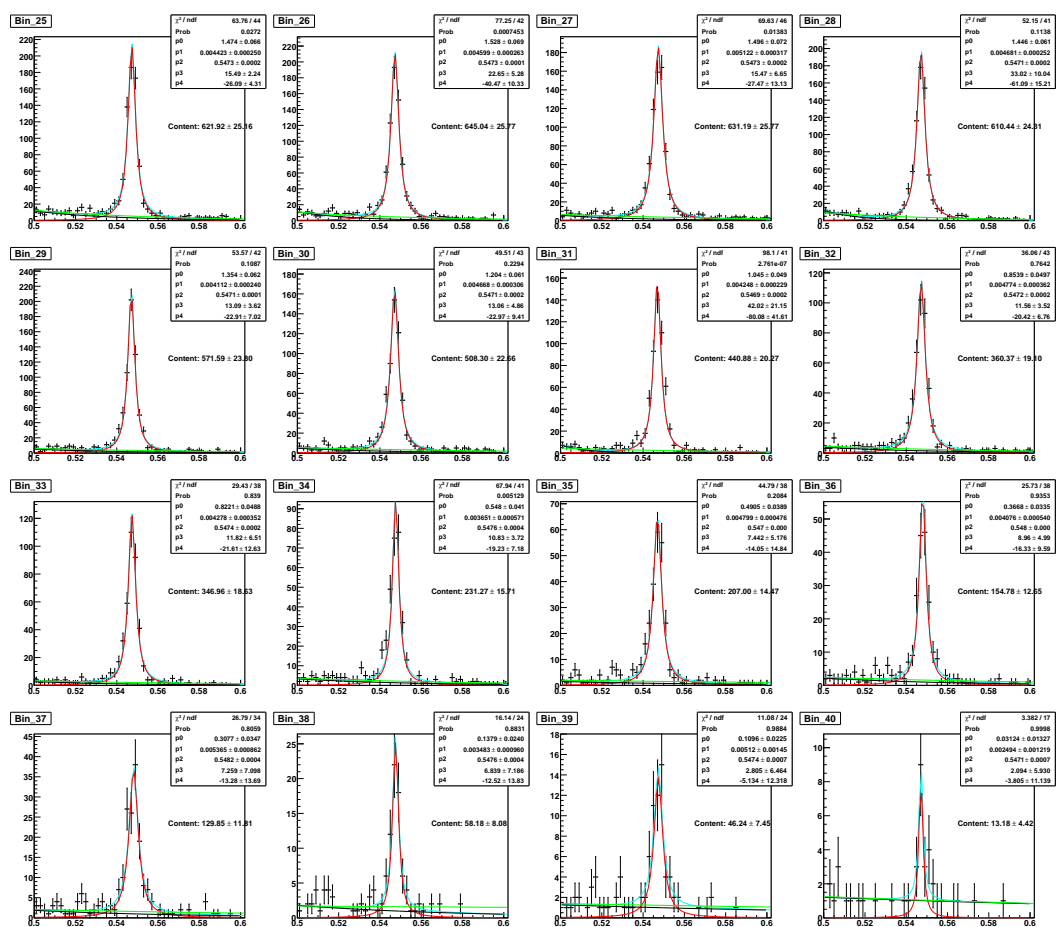
Photon Angle
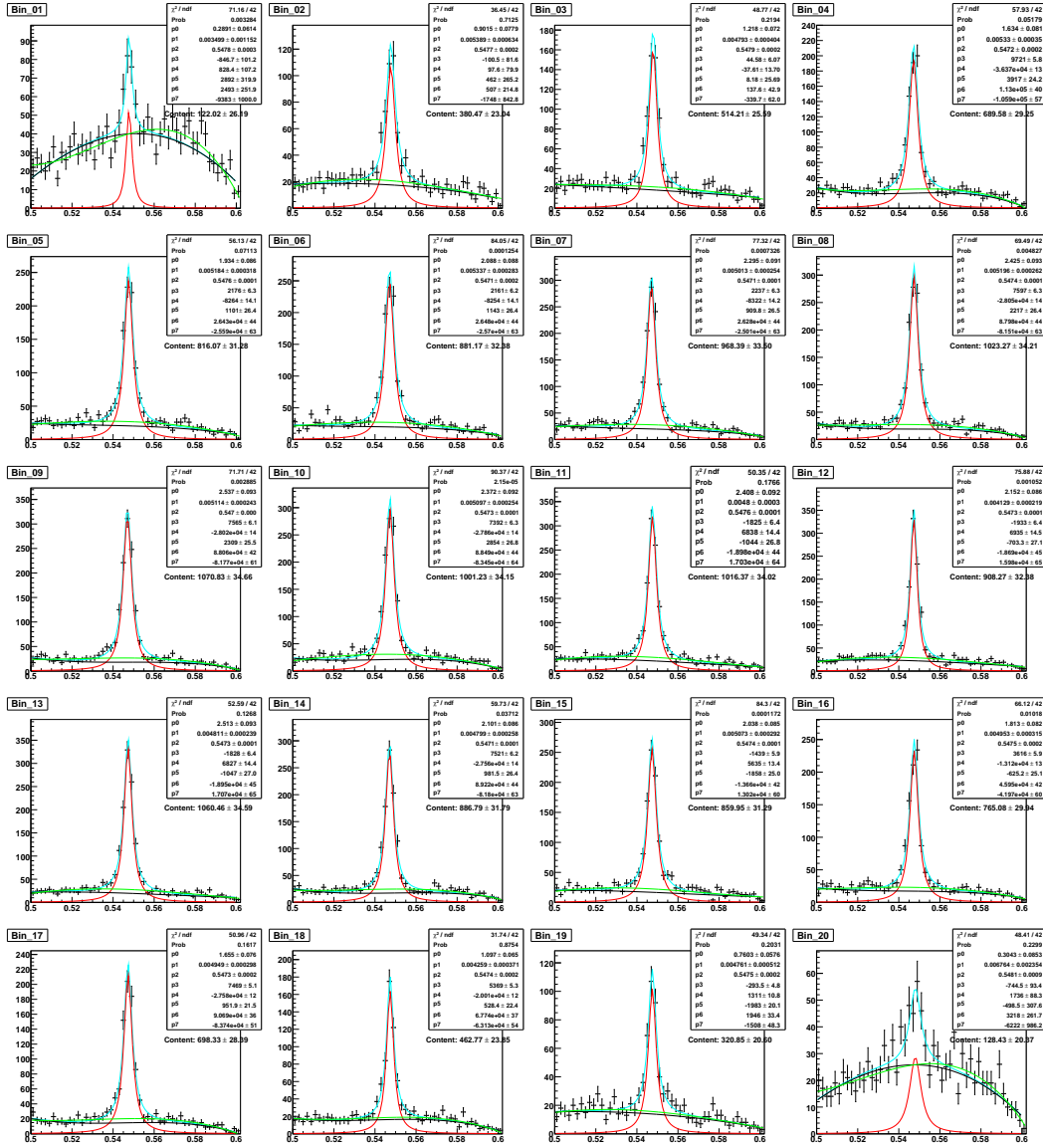
Appendix C

Final Distributions

Pion Angular Distribution

$\cos(\theta)$	Entries [a.u.]	stat. [a.u.]	syst. [a.u.]	
			-	+
-0.95	1847.335	502.313	206.266	3928.477
-0.85	5723.97	374.568	2683.426	2078.701
-0.75	7213.851	379.277	1319.621	2042.344
-0.65	9461.238	420.358	1376.841	2048.228
-0.55	11278.37	448.343	2234.003	998.929
-0.45	12108.88	460.516	2459.858	2200.303
-0.35	13227.46	472.096	2196.75	1817.271
-0.25	14047.84	482.382	3244.228	2067.647
-0.15	14714.04	487.942	2705.286	2612.863
-0.05	13692.58	479.428	2659.261	1447.607
0.05	13809.01	474.465	3174.946	2691.647
0.15	12388.27	452.916	1848.371	1616.154
0.25	14530.22	486.371	2713.84	2380.72
0.35	12200.89	450.106	1867.943	2032.413
0.45	11958.63	448.470	3143.636	949.864
0.55	10697.73	434.624	3124.209	1836.059
0.65	9797.211	417.171	2835.117	1597.782
0.75	6647.102	366.177	515.306	1164.005
0.85	4905.741	344.795	1256.579	2448.362
0.95	2144.631	414.896	2696.583	2728.378

Table C.1: Angular distribution of the pions with statistical and systematical errors

Photon Energy Distribution

Energy [GeV]	Entries [a.u.]	stat. [a.u.]	syst. [a.u.]	
			-	+
0.0225	5.442901e-09	33.493	1.176	0.000715
0.0275	938.116	598.697	1959.616	1922.982
0.0325	351.024	430.231	498.944	3848.785
0.0375	1668.128	451.357	2509.096	2600.731
0.0425	2056.56	257.5444	1491.942	2159.352
0.0475	2105.3	217.171	520.924	1345.389
0.0525	2777.645	320.694	559.32	816.803
0.0575	3293.948	241.823	898.066	1078.573
0.0625	4128.251	310.930	1068.091	1216.651
0.0675	4796.502	314.168	1631.698	824.558
0.0725	5353.873	271.718	1672.647	734.589
0.0775	5908.075	279.500	1457.86	1456.945
0.0825	6183.575	283.119	1522.326	813.684
0.0875	6867.766	297.125	1589.797	552.641
0.0925	6888.961	295.476	860.696	1462.012
0.0975	7337.229	307.039	1744.63	1204.67
0.1025	7873.072	320.299	1585.032	804.176
0.1075	8150.036	328.323	1900.064	1143.279
0.1125	7967.688	322.702	2520.664	824.886
0.1175	8278.436	340.059	1845.423	1147.405
0.1225	7658.214	321.99	1348.748	1268.937
0.1275	8144.917	339.709	1283.972	1000.935
0.1325	8296.021	353.117	2460.223	994.868
0.1375	8331.392	345.441	2414.011	1368.188
0.1425	8099.542	352.873	1979.291	1084.782
0.1475	7566.588	353.520	2247.365	1328.139
0.1525	6895.866	332.086	1003.724	2165.175
0.1575	5914.263	331.348	1828.287	888.186
0.1625	6324.292	353.623	1590.632	774.265
0.1675	4354.41	314.099	597.332	1827.43
0.1725	4192.929	312.801	980.640	952.121
0.1775	3321.156	290.678	986.828	849.877
0.1825	3050.589	295.773	1531.25	1281.696
0.1875	1482.934	226.550	395.894	649.600
0.1925	1417.095	244.083	906.461	391.989
0.1975	438.295	166.585	837.766	701.581
0.2025	-19.598	8.237	4.044	11.985

Table C.2: Distribution of the photon energy in the η rest frame with statistical and systematical errors

Appendix D

List of Acronyms

FZJ	Forschungszentrum Jülich
COSY	Cooler Synchrotron
TSL	The Svedberg Laboratory
CELSIUS	Cooling with Electrons and Storing of Ions from Uppsala Synchrocyclotron
WASA	Wide Angle Shower Apparatus
PDG	Particle Data Group
CD	Central Detector
FD	Forward Detector
FPC	Forward Proportional Chamber
FRA	Forward Absorber
FRH	Forward Range Hodoscope
FRI	Forward Range Intermediate Hodoscope
FTH	Forward Trigger Hodoscope
FVH	Forward Veto Hodoscope
FWC	Forward Window Counters
MDC	Mini Drift Chamber
PSB	Plastic Scintillator Barrel
SCS	Superconducting Solenoid
SEC	Scintillator Electromagnetic Calorimeter

SEB	Backward Part of SEC
SEF	Forward Part of SEC
PM	Photomultiplier
PMT	Photomultiplier Tube
ADC	Analog-to-Digital Converter
QDC	Charge-to-Digital Converter
TDC	Time-to-Digital Converter
FPGA	Field Programmable Gate Array
ASIC	Application Specific Integrated Circuit
ECL	Emitter Coupled Logic
LVDS	Low Voltage Differential Signaling
QCD	Quantum Chromo Dynamics
ChPT	Chiral Perturbation Theory
C	Charge conjugation
CP	Charge conjugation and Parity conjugation
CPT	Charge conjugation, Parity conjugation and Time reversal
FWHM	Full Width at Half Maximum

List of Figures

List of Tables

Bibliography

[A+95]   C. Amsler et al. eta decays into three pions. *Phys. Lett.*, B346:203–207, 1995.

[A+97]   A. Abele et al. Measurement of the decay distribution of $\eta' \rightarrow \pi^+\pi^-\gamma$ and evidence for the box anomaly. *Phys. Lett.*, B402:195–206, 1997.

[A+98]   M. Acciarri et al. Measurement of $\eta'(958)$ formation in two-photon collisions at LEP1. *Phys. Lett.*, B418:399–410, 1998.

[A+04]   H. H. Adam et al. Proposal for the Wide Angle Shower Apparatus (WASA) at COSY-Juelich - 'WASA at COSY'. 2004.

[A+08]   C. Amsler et al. Review of particle physics. *Phys. Lett.*, B667:1, 2008.

[A+09]   C. Adolph et al. Measurement of the $\eta \rightarrow 3\pi^0$ Dalitz Plot Distribution with the WASA Detector at COSY. *Phys. Lett.*, B677:24–29, 2009.

[Adl69]   S. L. Adler. Axial vector vertex in spinor electrodynamics. *Phys. Rev.*, 177:2426–2438, 1969.

[B+67]   C. Baltlay et al. Partial Decay Widths of the η^0 meson. *Phys. Rev. Lett.*, 19:1498–1501, 1967.

[B+02]   R. Bilger et al. Measurement of the $pd \rightarrow^3 He\eta$ cross section between 930 and 1100 MeV. *Phys. Rev.*, C65:044608, 2002.

[B+06]   M. Bashkanov et al. Exclusive measurements of $pd \rightarrow {}^3$He $\pi\pi$: The ABC effect revisited. *Phys. Lett.*, B637:223–228, 2006.

[B+08]   Chr. Bargholtz et al. The WASA Detector Facility at CELSIUS. *Nucl. Instrum. Meth.*, A594:339–350, 2008.

[Bar69]   W. A. Bardeen. Anomalous Ward identities in spinor field theories. *Phys. Rev.*, 184:1848–1857, 1969.

[Bas09]   M. Bashkanov. Universität Tübingen, Germany, Internal Note, 2009.

[BBC90]   J. Bijnens, A. Bramon, and F. Cornet. Three Pseudoscalar Photon Interactions in Chiral Perturbation Theory. *Phys. Lett.*, B237:488, 1990.

[BDD+03]   M. Benayoun, P. David, L. DelBuono, P. Leruste, and H. B. O'Connell. Anomalous η/η' decays: The Triangle and box anomalies. *Eur. Phys. J.*, C31:525–547, 2003.

[BES99]   A. Bramon, R. Escribano, and M. D. Scadron. The $\eta - \eta'$ mixing angle revisited. *Eur. Phys. J.*, C7:271–278, 1999.

[BJ69]   J. S. Bell and R. Jackiw. A PCAC puzzle: $\pi^0 \rightarrow \gamma\gamma$ in the sigma model. *Nuovo Cim.*, A60:47–61, 1969.

[BKY88]   M. Bando, T. Kugo, and K. Yamawaki. Nonlinear Realization and Hidden Local Symmetries. *Phys. Rept.*, 164:217–314, 1988.

[BN04]   B. Borasoy and R. Nissler. $\eta, \eta' \rightarrow \pi^+\pi^-\gamma$ with coupled channels. *Nucl. Phys.*, A740:362–382, 2004.

[BN07]   B. Borasoy and R. Nissler. $\eta, \eta' \rightarrow \pi^+\pi^- l^+ l^-$ in a chiral unitary approach. *Eur. Phys. J.*, A33:95–106, 2007.

[Bur92]   M. Burchell. Hadronic Splitoffs. CB-Note 201, unpublished, 1992.

[C+68]   A. M. Cnops et al. Dalitz Plot Analysis for the Decay $\eta \rightarrow \pi^+\pi^-\gamma$. *Phys. Lett.*, 26B:398, 1968.

[C+94]   E. Chiavassa et al. Measurement of the $pp \rightarrow pp\eta$ total cross-section between 1.265 GeV and 1.5 GeV. *Phys. Lett.*, B322:270–274, 1994.

[CER93]   CERN Program Library Long Writeup W5013. *GEANT – Detector Description and Simulation Tool*, 1993.

[CER10]   CERN. *http://root.cern.ch/*, as of February 2010.

[Cha08]   K. Chandwani. Simulations for a feasibility study of the reaction $pp \to pp\eta \to pp\pi^0\gamma\gamma$ with WASA at COSY. *IKP / COSY Annual Report 2007*, Jül-4262, 2008.

[CMP]   `http://www-hep.phys.cmu.edu/cms`. as of February 2010.

[CP66]   F. S. Crawford and L. R. Price. Study of the Decay $\eta \to \pi^+\pi^-\gamma$. *Phys. Rev. Lett.*, 16:333, 1966.

[Dal53]   R. H. Dalitz. On the analysis of τ-meson data and the nature of the τ-meson. *Phil. Mag.*, 44:1068–1080, 1953.

[F⁺07]   I. Fröhlich et al. Pluto: A Monte Carlo Simulation Tool for Hadronic Physics. *PoS*, ACAT2007:076, 2007.

[FKT⁺85]   T. Fujiwara, T. Kugo, H. Terao, S. Uehara, and K. Yamawaki. Non-abelian Anomaly and Vector Mesons as Dynamical Gauge Bosons of Hidden Local Symmetries. *Prog. Theor. Phys.*, 73:926, 1985.

[G⁺70]   M. Gormley et al. Experimental determination of the dalitz-plot distribution of the decays $\eta \to \pi^+\pi^-\pi^0$ and $\eta \to \pi^+\pi^-\gamma$, and the branching ratio $\eta \to \pi^+\pi^-\gamma/\eta \to \pi^+$. *Phys. Rev.*, D2:501–505, 1970.

[Gib98]   L. K. Gibbons. Measurement of the CKM matrix element —Vub— and exclusive $B\pi$ lepton ν and $B\rho$ lepton ν decays. *Ann. Rev. Nucl. Part. Sci.*, 48:121–174, 1998.

[GRS09]   R. Gebel, Maier R., and H. Stockhorst. Barrier-bucket RF tests. *IKP / COSY Annual Report 2008*, Jül-4282, 2009.

[H⁺08]   V. Hejny et al. Performance issues of the new DAQ system for WASA at COSY. *IEEE Trans. Nucl. Sci.*, 55:261–264, 2008.

[Hej09]   V. Hejny. IKP, FZJ, Germany, Internal Note, 2009.

[HHM03]   V. Hejny, M. Hartmann, and A. Mussgiller. RootSorter: A New Analysis Framework for ANKE. *IKP / COSY Annual Report 2002*, Jül-4052, 2003.

[Hol02]   B. R. Holstein. Allowed eta decay modes and chiral symmetry. *Phys. Scripta*, T99:55–67, 2002.

[J$^+$74]   M. R. Jane et al. A Measurement of the Charge Asymmetry in the Decay $\eta \rightarrow \pi^+\pi^-\gamma$. *Phys. Lett.*, B48:265, 1974.

[Jac04]   M. Jacewicz. *Measurement of the reaction $pp \rightarrow pp\pi^+\pi^-\pi^0$ with CEL-SIUS/WASA at 1.36 GeV*. PhD thesis, Uppsala Universitet, Sweden, 2004.

[Jam68]   F. James. *Monte Carlo Phase Space*. CERN, 1968.

[Jan06]   B. R. Jany. Assembly and Measurements of the Electromagnetic Calorimeter components for WASA-at-COSY setup. Master's thesis, Jagiellonian University Cracow, Poland, 2006.

[K$^+$06a]   H. Kleines et al. Development of a High Resolution TDC Module for the WASA Detector System Based on the GPX ASIC. *IEEE Nuclear Science Symposium Conference Record*, 30:1005, 2006.

[K$^+$06b]   H. Kleines et al. The new DAQ system for WASA at COSY. *IEEE Trans. Nucl. Sci.*, 53:893–897, 2006.

[Kal60]   R. Kalman. A New Approach to Linear Filtering and Prediction Problems. *Trans. AMSE, J. Basic Engineering*, pages 35–45, 1960.

[KMPT97]   M. Komogorov, B. Morosov, A. Povtorejko, and V. Tikhomirov. Track recognition algorithm for WASA Mini Drift Chamber (MDC). WASA memo 97 - 11, 1997.

[KMS09]   W. Krzemien, P. Moskal, and J. Smyrski. Search for eta-mesic helium using the WASA-AT-COSY detector. *Acta Phys. Polon. Supp.*, 2:141–148, 2009.

[Koc04]   I. Koch. *Measurements of $2\pi^0$ and $3\pi^0$ Production in Proton-Proton Collisions at a Center of Mass Energy of 2.465 GeV*. PhD thesis, Uppsala Universitet, Sweden, 2004.

[Koe03]   K. Koeneke. Measurement of the Branching Fraction for the Decay $B^\pm \rightarrow K^{*+-}\gamma$, $K^{*+-} \rightarrow K^\pm\pi^0$ with the BaBar detector. *SLAC-R-841*, 2003.

[Kup09]   A. Kupść. Uppsala Universitet, Sweden, Private Communication, 2009.

[KZ87]   S. Kullander and P. Zielinski. . *Uppsala Accelerator News*, 4, 1987.

[L+67]   P. J. Litchfield et al. Study of the decay mode $\eta \to \pi^+\pi^-\gamma$. *Phys. Lett.*, B24:486–488, 1967.

[L+73]   J. G. Layter et al. Study of dalitz-plot distributions of the decays $\eta \to \pi^+\pi^-\pi^0$ and $\eta \to \pi^+\pi^-\gamma$. *Phys. Rev.*, D7:2565–2568, 1973.

[L+07]   A. Lopez et al. Measurement of Prominent eta Decay Branching Fractions. *Phys. Rev. Lett.*, 99:122001, 2007.

[Leo94]   W. R. Leo. *Techniques for Nuclear and Particle Physics Experiments.* Springer-Verlag, 1994.

[M+97]   R. Maier et al. Cooler synchrotron COSY. *Nucl. Phys.*, A626:395c–403c, 1997.

[Mai97]   R. Maier. Cooler synchrotron COSY: Performance and perspectives. *Nucl. Instrum. Meth.*, A390:1–8, 1997.

[Man04]   R. Mankel. Pattern recognition and event reconstruction in particle physics experiments. *Rept. Prog. Phys.*, 67:553, 2004.

[Mey95]   Curtis A. Meyer. User Guide for CBDROP A Charged Splitoff Supression Package. CB-Note 191, unpublished, 1995.

[P+61]   A. Pevsner et al. Evidence for a three Pion Resonance Near 550 MEV. *Phys. Rev. Lett.*, 7:421–423, 1961.

[P+00]   D. Prasuhn et al. Electron and stochastic cooling at COSY. *Nucl. Instrum. Meth.*, A441:167–174, 2000.

[P+07]   C. Pauly et al. The $pp \to pp\pi\pi$ reaction channels in the threshold region. *Phys. Lett.*, B649:122–127, 2007.

[Pau06]   C. Pauly. *Light Meson Production in pp Reactions at CELSIUS/WASA above the η Threshold.* PhD thesis, Universität Hamburg, Germany, 2006.

[Pau07]   C. Pauly. In-beam efficiency study of the WASA trigger hodoscope. *IKP / COSY Annual Report 2006*, Jül-4234, 2007.

[Pic92]   C. Picciotto. Analysis of eta, $K(L) \to \pi^+\pi^-\gamma$ using chiral models. *Phys. Rev.*, D45:1569–1574, 1992.

[Pod09]   P. Podkopał. Performce of the new Plastic Scintillator Barrel Detector for WASA-at-COSY. *IKP / COSY Annual Report 2008*, Jül-4282, 2009.

[PR93]   C. Picciotto and S. Richardson. Chiral theory calculation of $\eta \to \pi^+\pi^-e^+e^-$. *Phys. Rev.*, D48:3395–3396, 1993.

[Red06]   C. F. Redmer. Groß- und kleinflächige Szintillatorhodoskope in der Teilchen- und Atomphysik. Master's thesis, Ruhr-Universität Bochum, 2006. unpublished.

[Red09]   C. F. Redmer. Analysis of the decay $\eta \to \pi^+\pi^-\gamma$ measured with WASA-at-COSY. *IKP / COSY Annual Report 2008*, Jül-4282, 2009.

[Rub99]   R. J. M. Y. Ruber. *An Ultra-thin-walled Superconducting Solenoid for Meson-decay Physics*. PhD thesis, Uppsala Universitet, Sweden, 1999.

[S+09]   T. Skorodko et al. Two-Pion Production in Proton-Proton Collisions – Experimental Total Cross Sections and their Isospin Decomposition. *Phys. Lett.*, B679:30–35, 2009.

[S+10]   K. Schoenning et al. Production of η and 3π mesons in the $pd \to^3 HeX$ reaction at 1360 and 1450 MeV. 2010. eprint: arXiv:1001.4604 [nucl-ex].

[SBB+95]   P. Salabura, H. Bokemeyer, A. Brenschede, J. Foryciarz, K. Garrow, W. Karig, W. Koenig, F. Lefèvre, H. Schoen, R. Schicker, A. Schröter, and J. Stroth. HADES – A High Acceptance DiElectron Spectrometer. *Nuclear Physics B - Proceedings Supplements*, 44(1-3):701 – 707, 1995.

[T+72]   J. J. Thaler et al. Charge asymmetry in the decay $\eta \to \pi^+\pi^-\gamma$. *Phys. Rev. Lett.*, 29:313–316, 1972.

[TDC01]   TDC-F1 Functional description - scientific version. *Acam Messelectronic GMBH*, 2001.

[TDC06]   TDC-GPX Datasheet. *Acam Messelectronic GMBH*, 2006.

[Vla08]   P. N. Vlasov. *Analysis of the $\eta \rightarrow 3\pi^0$ decay in the pp interaction.* PhD thesis, Ruhr - Universität Bochum, Germany, 2008.

[W$^+$05]   P. Wüstner et al. A new synchronistion system for experiments at cosy. *Proceedings of the 14th IEEE Real Time Conference, Stockholm*, 2005.

[Wir09]   A. Wirzba. IKP, FZJ, Germany, Private Communication, 2009.

[Wit83]   E. Witten. Global Aspects of Current Algebra. *Nucl. Phys.*, B223:422–432, 1983.

[Wol08]   M. Wolke. First Experiments with the WASA Detector. *IKP / COSY Annual Report 2007*, Jül-4262, 2008.

[WZ71]   J. Wess and B. Zumino. Consequences of anomalous Ward identities. *Phys. Lett.*, B37:95, 1971.

[Z$^+$94]   K. Zwoll et al. Flexible data acquisition system for experiments at COSY. *IEEE Trans. Nucl. Sci.*, 41:37–44, 1994.

[Zhe09]   C. Zheng. Matching Trigger Efficiency of Forward Detector of WASA-at-COSY. *IKP / COSY Annual Report 2008*, Jül-4282, 2009.

[Zie08]   M. Zieliński. Feasibility study of the $\eta' \rightarrow \pi^+\pi^-\pi^0$ decay using WASA-at-COSY apparatus. Master's thesis, Jagiellonian University Cracow, Poland, 2008.

[Zło09]   J. Złomańzcuk. Uppsala Universitet, Sweden, Internal Note, 2009.

[ZR09]   J. Zabierowski and J. Rachowski. The Light-Pulser Monitoring System for the WASA detector facility. *Nucl. Instrum. Meth.*, A606:411–418, 2009.

> Dicebat Bernardus Carnotensis nos esse quasi nanos gigantium humeris insidentes, ut possimus plura eis et remotiora videre, non utique proprii visus acumine, aut eminentia corporis, sed quia in altum subvehimur et extollimur magnitudine gigantea.
>
> — John of Salsbury
> Metalogicon III 4 (1159).

Acknowledgments

Finally, here it is, the last chapter[1] of my thesis! Looking at all previous pages, I have to admit that many of the things I reported would not have been possible in this way without the support of a lot of people. I am grateful to everyone of them and I hope they will understand that rather a lack of space then a lack of gratitude is the reason, why I can point out only a few of them.

First and most of all I would like to express my gratitude to Frank Goldenbaum and Susan Schadmand. Your way of supervising me has been an inspiring mixture of outspokenness and never-ending optimism. It helped me to think outside of the box and brought me back on track, whenever I was about to loose confidence or the focus. Thank you, for all your support! There was always an open door I could turn to or if necessary a Skype connection to the other side of the world. You did not even mind to answer my emails even from cocktail parties of strange conferences.

In the same way I am grateful to Volker Hejny and Christian Pauly, two great teachers and even better colleagues. Thank you for providing all those uncountable and highly valuable insights into data analysis, programming, RC-modeling, and Texas hold-em poker as well as all the fun at and apart from work!

I would like to thank Prof. James Ritman for the opportunity to work in the IKP as well as all members of the institute for the nice atmosphere. Special thanks go

---

[1] Dear reader, I have been warned about the possibility that you might mistake my thesis for a Manga, a Japanese comic book, and — even worse — that you would stop reading after the, from your point of view, first chapter. If that really was your intention, you should start again, but this time in the conventional direction and read at least the abstract! The exciting world of hadron physics awaits you! If you read all of this thesis, you will find also some pictures.